NIST Special Publication 1055

Technical Digest: SOFM 2006

A NIST Symposium for Photonic and Fiber Measurements

Sponsored by the National Institute of Standards and Technology
in cooperation with the IEEE Lasers and Electro-Optics Society
and the Optical Society of America

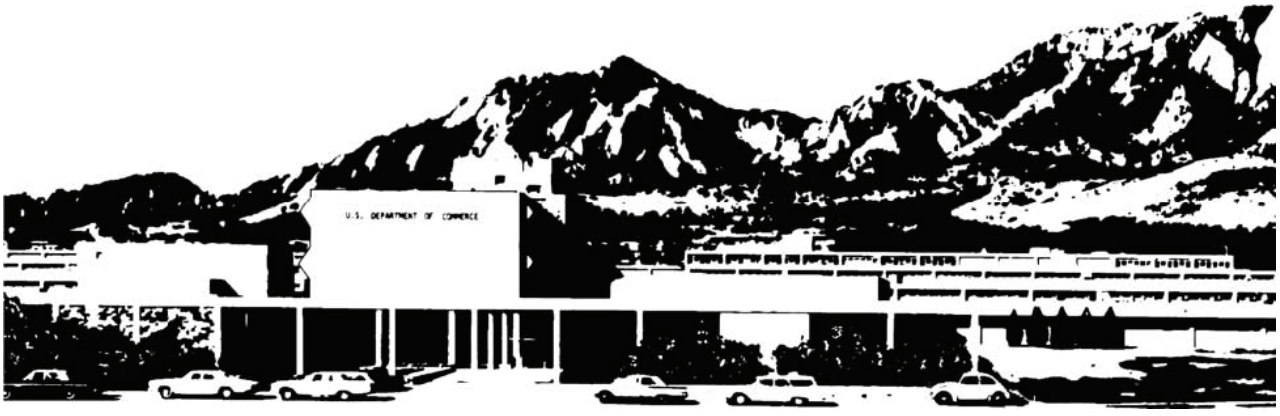

NIST National Institute of Standards and Technology • Technology Administration • U.S. Department of Commerce

The National Institute of Standards and Technology was established in 1988 by Congress to "assist industry in the development of technology ... needed to improve product quality, to modernize manufacturing processes, to ensure product reliability ... and to facilitate rapid commercialization ... of products based on new scientific discoveries."

NIST, originally founded as the National Bureau of Standards in 1901, works to strengthen U.S. industry's competitiveness; advance science and engineering; and improve public health, safety, and the environment. One of the agency's basic functions is to develop, maintain, and retain custody of the national standards of measurement, and provide the means and methods for comparing standards used in science, engineering, manufacturing, commerce, industry, and education with the standards adopted or recognized by the Federal Government.

As an agency of the U.S. Commerce Department's Technology Administration, NIST conducts basic and applied research in the physical sciences and engineering, and develops measurement techniques, test methods, standards, and related services. The Institute does generic and precompetitive work on new and advanced technologies. NIST's research facilities are located at Gaithersburg, MD 20899, and at Boulder, CO 80305. Major technical operating units and their principal activities are listed below. For more information visit the NIST Website at http://www.nist.gov, or contact the Publications and Program Inquiries Desk, 301-975-3058.

Office of the Director
·National Quality Program
·International and Academic Affairs

Technology Services
·Standards Services
·Technology Partnerships
·Measurement Services
·Information Services
·Weights and Measures

Advanced Technology Program
·Economic Assessment
·Information Technology and Applications
·Chemistry and Life Sciences
·Electronics and Photonics Technology

Manufacturing Extension Partnership Program
·Regional Programs
·National Programs
·Program Development

Electronics and Electrical Engineering Laboratory
·Microelectronics
·Law Enforcement Standards
·Electricity
·Semiconductor Electronics
·Radio-Frequency Technology[1]
·Electromagnetic Technology[1]
·Optoelectronics[1]
·Magnetic Technology[1]

Materials Science and Engineering Laboratory
·Intelligent Processing of Materials
·Ceramics
·Materials Reliability[1]
·Polymers
·Metallurgy
·NIST Center for Neutron Research

Chemical Science and Technology Laboratory
·Biotechnology
·Process Measurements
·Surface and Microanalysis Science
·Physical and Chemical Properties[2]
·Analytical Chemistry

Physics Laboratory
·Electron and Optical Physics
·Atomic Physics
·Optical Technology
·Ionizing Radiation
·Time and Frequency[1]
·Quantum Physics[1]

Manufacturing Engineering Laboratory
·Precision Engineering
·Manufacturing Metrology
·Intelligent Systems
·Fabrication Technology
·Manufacturing Systems Integration

Building and Fire Research Laboratory
·Applied Economics
·Materials and Construction Research
·Building Environment
·Fire Research

Information Technology Laboratory
·Mathematical and Computational Sciences[2]
·Advanced Network Technologies
·Computer Security
·Information Access
·Convergent Information Systems
·Information Services and Computing
·Software Diagnostics and Conformance Testing
·Statistical Engineering

---

[1]At Boulder, CO 80305
[2]Some elements at Boulder, CO

NIST Special Publication 1055

Technical Digest: SOFM 2006

A NIST Symposium for Photonic and Fiber Measurements

Digest of a symposium sponsored by the
National Institute of Standards and Technology
in cooperation with the
IEEE Lasers and Electro-Optics Society
and the Optical Society of America

September 19-20, 2006
National Institute of Standards and Technology
Boulder, Colorado 80305

Edited by
T. J. Drapela
P. A. Williams

September 2006

U.S. Department of Commerce
Carlos M. Gutierrez, Secretary

Technology Administration
Robert Cresanti, Under Secretary for Technology

National Institute of Standards and Technology
William Jeffrey, Director

National Institute of Standards and Technology Special Publication 1055
Natl. Inst. Stand. Technol. Spec. Publ. 1055, 148 pages (September 2006)
CODEN: NSPUE2

U.S. GOVERNMENT PRINTING OFFICE
WASHINGTON: 2006

For sale by the Superintendent of Documents, U.S. Government Printing Office
Internet: bookstore.gpo.gov Phone: (202) 512-1800 Fax: (202) 512-2250
Mail: Stop SSOP, Washington, DC 20402-0001

PREFACE

Welcome to SOFM 2006, the fourteenth installment of NIST's biennial symposium dealing with photonic and optical fiber measurements.

In the Fall of 1980, Jimmy Carter was the U.S. President and disco dancing was just past its peak. TV remote controls were just becoming commonplace. Cable, for those lucky few who had it, meant a dozen or so channels—when it was working. The PC was still a couple of years away, while cell phones and the internet were more than a decade away from becoming part of the common vernacular. The prefix "giga" was, at most, a rarely used curiosity, even among scientists, and was virtually unknown to the general public.

At this same time the fiberoptic industry was young and in critical need of metrology development. The National Bureau of Standards (NIST's precursor) speculated that maybe a conference devoted to fiber measurements could be of some utility to this developing industry. It is unlikely that any of the organizers or attendees of that first SOFM could have envisioned this utility to span 26 years! During these years the photonic industry has been through its share of ups and downs, including the exhilarating highs and lows of the last six or so years.

As the fiberoptic industry now seems to have reached a certain level of maturity, the demand for cutting-edge metrology-related research relating to fundamental fiber measurements—the traditional core focus area for SOFM—seems to be leveling off. This is in no way meant, however, to imply that our work as metrologists is done. Rather, crucial metrology needs are now springing up from a wider variety of other related or derived fields of optoelectronics. This is evidenced in the SOFM 2006 technical program, which is as diverse as any in SOFM history, including sessions on fiber sensors, dispersion metrology, power-related metrology, "last-mile" issues, spectroscopic and frequency metrology, systems metrology, and specialty fibers. This diversity is what inspired us to conclude this year's symposium with a "roadmapping" workshop on emerging and anticipated photonic metrology needs. SOFM remains geographically diverse as well, with just over 60 % of this year's accepted papers originating outside the U.S.

It has been a thrilling ride, and we are sincerely glad that you have decided to join us for this iteration. Please enjoy your visit, including SOFM 2006, itself, and all that our Rocky Mountain area has to offer.

Happy reading,

Tim Drapela
Paul Williams
Boulder, Colorado
September 2006

SYMPOSIUM COMMITTEE

P.A. Williams, *NIST*, Symposium Co-Chair

T.J. Drapela, *NIST,* Symposium Co-Chair

A. Barlow, *PerkinElmer*

A. Champavere, *JDSU*

G.W. Day, *NIST*

S.C. Fleming, *Sydney University*

D. Franzen, *NIST*

N. Gisin, *University of Geneva*

M. Hackert, *U.S. Navy*

T.A. Hanson, *Corning*

D. Humphreys, *NPL*

J. Jackel, *Telcordia*

D.Y. Kim, *GIST*

P. Kolesar, *SYSTIMAX Solutions*

D. Krohn, *Light Wave Venture*

G. Kuyt, *Draka Comteq*

A. McCurdy, *OFS*

G.W. Schinn, *EXFO*

C. Shaar, *Photon Kinetics*

H. Takara, *NTT*

CONTENTS

Photonic Sensor Market Evolution, Opportunities and Metrology Needs

David Krohn
Light Wave Venture LLC
7 Cobblestone Drive
Hamden, CT 06518
dkrohn@lightwaveventure.com

Abstract: The fiber optic sensor market has the potential to exceed $1 billion in 2010. Needs in the oil and gas industry, as well as homeland security, will be the primary market drivers. Photonic biochemical sensors have the potential to expand the market potential fivefold. A key part of establishing standards is having metrology procedures in place to allow for conformance to defined specifications. Standards efforts are moving forward with activity by the Fiber Optic Sensor Consortium (OIDA), ASTM and the Petroleum Open Standards Consortium. However, better industry coordination is required to prevent the lack of standards from being a barrier to industry acceptance and growth.

1. Opportunity

There are a broad range of military, homeland security and industrial sensing applications that can be facilitated by distributed fiber optic sensors. These applications include:

- Oil well monitoring
- Pipeline monitoring
- Pipeline security
- Shipboard and avionic health monitoring and damage control
- Industrial processes
- Smart structures (Most applications will be for strain monitoring. However, traffic flow, temperature, toxic gases and icing can also be monitored)
  - Bridges / tunnels
  - Dams
  - Buildings
  - Machines
  - Power lines (Temperature and strain)
  - Transportation
- Oil and gas exploration (seismic)
- Homeland Security
  - Chemical / biological
  - Security / intrusion
  - Wide area surveillance

One of the key drivers in fiber optic sensor market evolution is homeland security [1]. In earlier market studies the need and opportunity for wide areas surveillance was not fully recognized with a much smaller market potential defined. Under current world conditions that need has changed. Many vital assets which cover wide areas, such as pipelines and borders, are under constant threat of being attacked or breached. There is a rapidly emerging need to be able to provide identification of intrusion threats to such vital assets. Similar problems exit for monitoring the basic infrastructure such as water supply, power utilities, communications systems as well as transportation. There is a need to develop a coordinated and integrated solution for the detection of threats. From a sensor standpoint, consideration must not be limited to

detection, but how does detection lead to intervention and deterrence. Also, fiber optic sensor technology must be compatible with integration with other surveillance technologies such as wireless mote technology.

Another key market driver is the oil and gas industry. With the current price of oil up over 300% in the last 5 years and limited supply, smart oil / gas wells as well as reservoir management are very important. A typical well is only 30% efficient. With distributed fiber optic sensors to monitor well health and performance, well efficiencies can be drastically improved providing enhanced oil recovery with potential extraction from reactivation of old oil wells. In addition, seismic sensing systems can better map oil reserves and enhance extraction.

Fiber optic sensors are limited in their ability to monitor biochemical agents. By expanding fiber optic sensors to photonic sensors, the ability to monitor biological agents and chemicals is greatly enhanced [3]. Key market segments include:

- Environmental monitoring
- Homeland security / military
- Industrial process
- Medical diagnostics
- Agriculture
- Food processing
- Drug discovery and processing

2. Market Forecast Potential

Market information sources include:

- OIDA data base
- Supplier, integrator, end user interviews
- Geophysical industry surveys
- Government contracts monitoring

The OIDA (Optoelectronics Industry Development Association) data base was generated through three workshops on sensors that were held in 2005 [2, 3, 4]. Over 125 contacts were made with suppliers and end users from December, 2005 to May, 2006. Significant government funding will be invested in sensor technology. However, markets are in early development stage, fragmented and difficult to forecast.

The fiber optic sensor market potential is shown in figure 1 [5, 6].

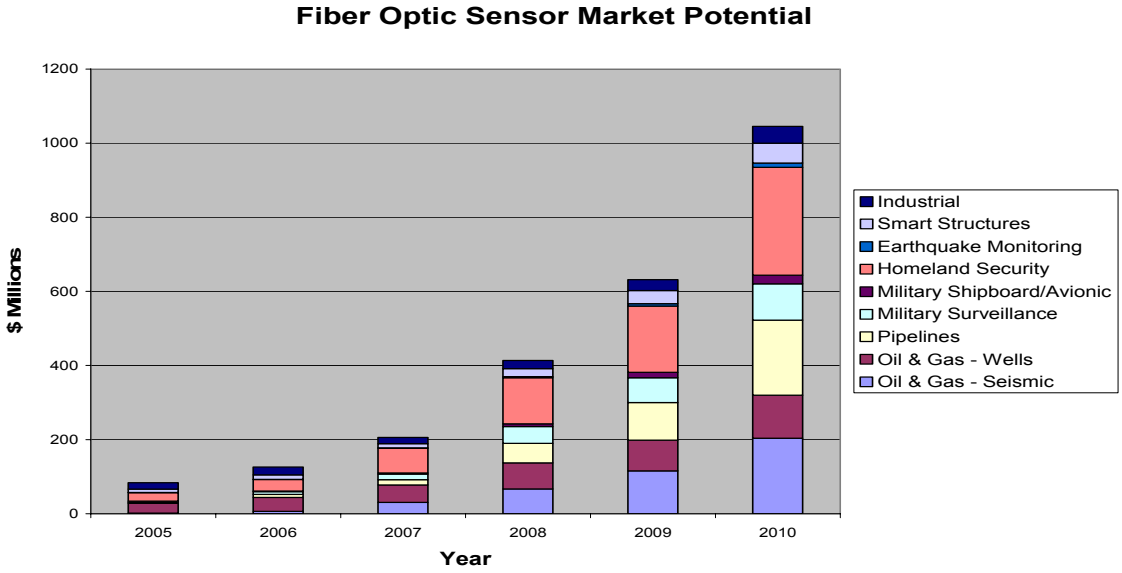

Figure 1 Distributed Fiber Optic Sensor Market Potential

The market analysis for fiber optic sensors indicates that the key market drivers are:

- Smart oil and gas wells
- Seismic sensors for oil well reservoir management and exploration
- Pipeline monitoring
- Homeland security

Military surveillance and smart structures also have good growth potential. The forecast is based on systems cost which includes the sensing elements, packaging, cabling and interrogation. Installation is not included.

The estimate is that approximately 45% of the fiber optic distributed sensing market will use interferometric sensors due to accuracy and speed requirements in seismic applications. About 20% of the distributed sensing market will use Bragg gratings or some form of spectral shift sensors such as Fabry-Perot devices, fluorescence devices or microresonators. Distributed temperature sensing systems (DTS) based on Raman scattering or Brillouin scattering will account for about 15% of the market. Speckle pattern and intensity modulated sensors will have about 10% market share with 5% going to other technologies.

Depending upon the sensing technology used, the interrogation interface represents about 50% to 60% of the sensing system cost (installation not included)

High resolution systems are too costly for many applications. As a result, they will likely tier into two levels

- Higher cost – high resolution systems
- Low cost – reduced resolution systems (Only need to provide an alarm condition in many applications.)

Potentially, more than 60% of the wide areas surveillance applications will be for alarms.

The photonic biochemical sensing market expansion is shown in figure 2 [5, 7]. Clearly, the transition from fiber optic sensors to photonic sensors has a dynamic impact increasing the market potential by a factor of five.

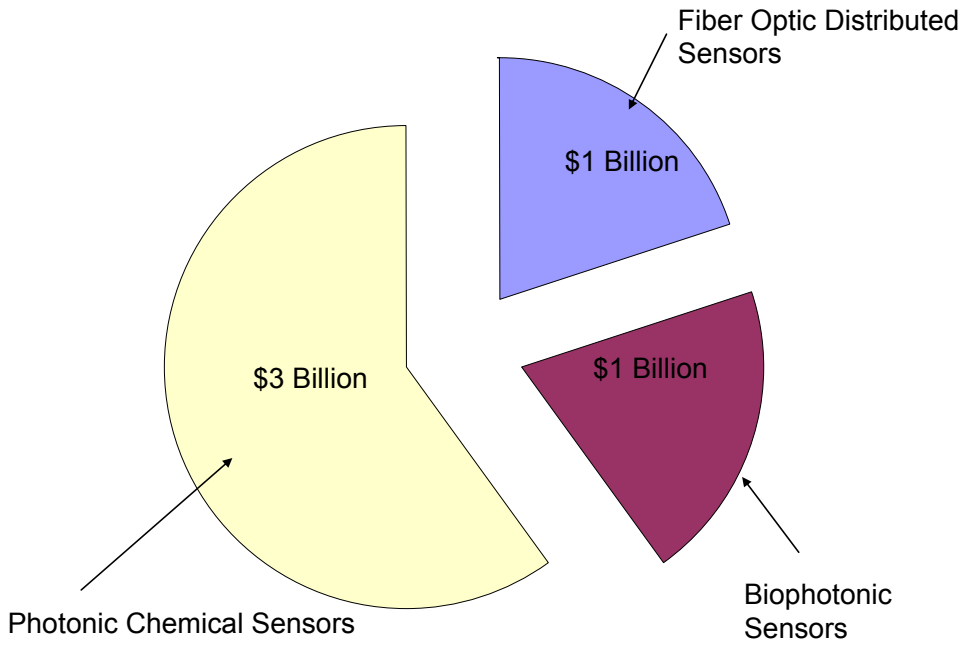

Figure 2 Photonic Sensor Market Potential 2010

3. Barriers

There have been a number of barriers for the acceptance and broad use of smart fiber optic sensors. Compared to telecommunications the volume is low. This fact coupled with proprietary and custom specifications has kept the price of fiber optic sensors high. There is a general lack of a manufacturing infrastructure and lack of standards for packaging and reliability. Also there are several competing technologies; some photonic based and other approaches based on conventional non-photonic technologies. Photonic biochemical sensors face additional barriers. They may need to be functional from UV to mid IR. The industry is plagued with false alarms from various sensing technologies. Compliance requirements may require qualification with several different organizations.

4. Standards and Metrology

There are several groups now involved with standards. The fiber optics Sensor Consortium in conjuction with OIDA and NIST has begun preliminary work on fiber optic sensor metrology and standards. NIST defined the need for standards [8]. Standards facilitate the use of technology as outlined in the following:

- Improve measurement accuracy
- Enable cost reduction
- Promote adoption and market growth
- Allow interchangeability and multi-sourcing
- Foster innovation

Non-standardized items tend to be custom and expensive and slow industry growth.

The Fiber Optic Sensor Consortium has developed a preliminary standard for Bragg grating sensors, a Bragg grating sensor interrogator and an interferometric interrogator. The ASTM Subcommittee E13.09 on Fiber Optics, Waveguides, and Optical Sensors is focused on the formation and development of methods for testing, specifying, and using fiber optics, integrated optics, and other advanced optical and guided-wave techniques for chemical sensing. Currently under development are standards for distributed fiber optic chemical sensors. The Petroleum Open Standards Consortium has drafted a communications standard for DTS (distributed temperature sensing system).

Metrology will play a key role in standards. As an example, the OIDA Fiber Optic Sensor Consortium has prepared a preliminary standard for a Bragg grating sensor interrogator. The interrogator is required to have sensitivity for wavelength shift of 1 picrometer. Standard measurement techniques to ensure compliance need to be defined. Other metrology needs include:

- Bragg grating characterization
- Dynamic strain versus static strain measurements
- Temperature strain discrimination (Bragg grating and Brillouin Scattering)
- Long term drift
    - Strain
    - Vibration
- Biochemical detection threshold

5. Summary

The fiber optic sensor market has the potential to exceed $1 billion in 2010. Needs in the oil and gas industry, as well as homeland security, will be the primary market drivers. Photonic biochemical sensors have the potential to expand the market potential fivefold. Standards efforts are moving forward; but better industry coordination is required to prevent the lack of standards from being a barrier to industry acceptance and growth. A key part of establishing standards is having metrology procedures in place to allow for conformance to defined specifications.

6. References

[1] David Krohn, "Photonic Sensor Opportunities for Homeland Security Applications", PhAST Conference, May, 2006

[2] OIDA, Fiber Optic Sensor Workshop**,** March 22-23, 2005, The Photonics Center at Boston University, Boston, MA

[3] OIDA, Biophotonic Sensors and Smart Fiber Optic Sensor Networks, August 17-18, 2005, Rochester, NY

[4] OIDA, Wide Area Surveillance Workshop, December 13-14, 2005 – Washington DC

[5] David Krohn, "Biophotonic Sensors and Fiber Optic Sensor Networks", OpticsEast, Conference 5594, October 25, 2005

[6] David Krohn, "Market Opportunities and Standards Activities for Fiber Optic Sensors", 18th International Conference on Fiber Optic Sensors, to be published

[7] David Krohn, 2005 OIDA Annual Forum, Washington DC, November 29, 2205

[8] Kent Rochford, Biophotonic Sensors and Smart Fiber Optic Sensor Networks, August 17- 18, 2005, Rochester, NY

Modulation Function Study of Coupling Based Intensity Modulated Fiber-Optic Sensors

Johan Jason[1,2], Hans-Erik Nilsson[1], Bertil Arvidsson[1,3], Anders Larsson[2]
[1]*Department of Information Technology and Media, Mid-Sweden University, SE-851 70 Sundsvall, Sweden*
[2]*Fiberson AB, P.O. Box 1044, SE-824 11 Hudiksvall, Sweden*
[3]*Ericsson Network Technologies AB, SE-824 82 Hudiksvall, Sweden*
johan.jason@miun.se

Abstract: The modulation function for fiber-optic sensors based on coupling between fiber ends is studied for different fiber types and fiber configurations, including multiple fiber passes. Sensitivity aspects are evaluated experimentally and theoretically. It is shown that multiple passes in reality do not result in a significant sensitivity increase due to coupling losses related to fiber alignment and reflection loss.

1. Introduction

Intensity modulated sensors based on coupling between fibers enable simple and cheap displacement sensor solutions (Fig. 1). Such sensors can be used for measurement of position, displacement or vibration [1-5]. Also other parameters can be measured if they have the ability to cause displacement in some way, e.g. temperature changing the deviation of a bimetal strip [6]. In the field of vibration measurement applications, the intensity modulation may be produced by micro-structure cantilevers in the light path [1] or by letting the transmitting fiber itself act as a cantilever [2-3]. Similar sensor designs based on, or combined with, integrated optics have also been realized [4-5].

Some of the most important parameters to consider in the optical design of the sensor are the signal-to-noise ratio, the sensitivity and the linearity of the sensor in the intended measurement range. These parameters are improved, in turn, if the received optical power, the slope (index) of the modulation curve and the linearity of the modulation over the total displacement range are as high as possible. In terms of received optical power, multimode fibers are to be preferred to single-mode fibers. Radial (transverse) displacement gives the most significant change in coupled power [7], and should therefore be considered for sensitivity reasons. Furthermore, the choice of fiber type also affects the sensitivity and the linearity of the sensor.

A way of further improving the sensitivity could be to arrange multiple passes over a connection according to Fig. 2, thus giving a multiple change in coupled power for a certain displacement. The possibility of realizing this, and the practical use, is investigated and analyzed experimentally and theoretically below.

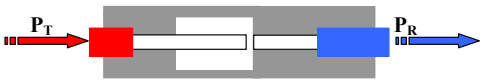

Fig. 1. Principal coupling-based vibration sensor.

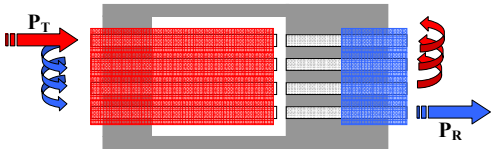

Fig. 2. Multiple pass configuration using fiber ribbons.

2. Experimental pre-study

Measurements of the transmission ratio, i.e. received/transmitted power (P_R/P_T), versus the transverse displacement were performed for 62.5 µm core graded-index (GI) multimode fibers and 4-fiber arrays of the same fiber type, see fiber data in Table 1. The 4-fiber arrays were in the form of encapsulated ribbons (denoted R4), MT-connectors (MT4) and ribbon fibers temporarily put into V-groove arrays (V4). Transmitting and receiving fibers of 5 m length each were coupled to a 1300 nm LED and a HP81521B detector with multimode lens HP81050BL, respectively. An xyz-translator was used to optimize fiber-to-fiber coupling (1 mm free ends with a 10 µm gap), and a transverse scan in 1-2 µm steps was made from +50 to -50 µm.

In Fig. 3 the measured modulation curves are shown. It can be noted that no significant sensitivity improvement is achieved for multiple, in this case four, passes compared with a single one. Here the degree of fiber alignment seems to play an important role: the better alignment, the steeper is the modulation curve, i.e. the higher is the sensitivity. Also the reflection loss at each fiber interface should be considered. A theoretical analysis of the case is performed in the next section.

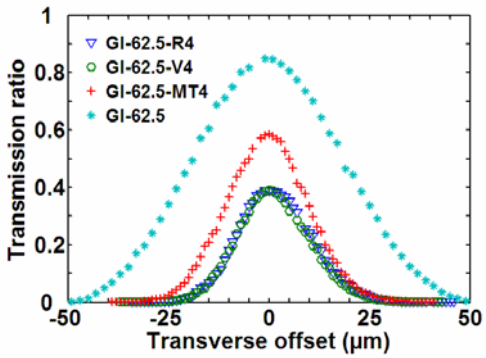

Fig. 3. Experimental modulation curves for 62.5µm core fiber with single pass and for multiple (four) passes with different alignment techniques.

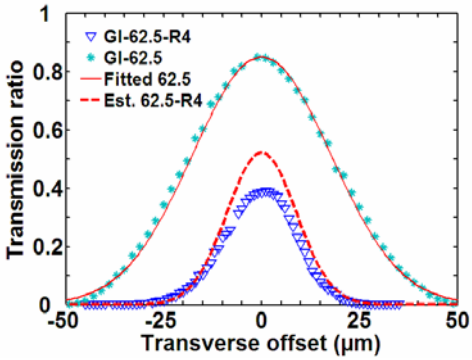

Fig. 4. Fitted modulation curve to experimental data for single pass, and estimated and experimental modulation curves for multiple (four) passes.

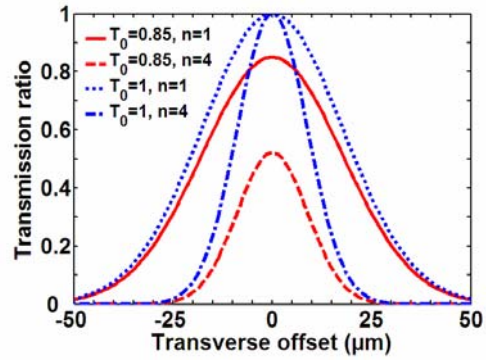

Fig. 5. Theoretical modulation curves for single-pass coupling (n=1) and four-pass coupling (n=4), comparing ideal (T_0=1) and experimental (T_0=0.85) transmission ratio for a single fiber pair.

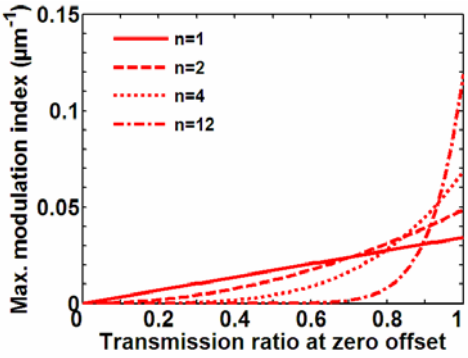

Fig. 6. Maximum modulation index vs. transmission ratio T_0 for α=0.0016 µm^{-2}.

3. Theoretical analysis

There exist a number of models for calculation of the splice loss between two multimode fibers following radial offset [7-9]. The applicability of the models often depends on the actual case, and the models are more or less based on experimental data. For the case presented in this paper, we need a simple expression for the modeling of the modulation curve and for the derivation of an expression for the sensitivity. A simplified way of describing the modulation function is by using a Gaussian expression for the transmission ratio T for n multiple passes as a function of radial (transverse) offset x:

$$T(x) = \left(T_0 \cdot e^{-\alpha x^2}\right)^n = T_0^n \cdot e^{-n\alpha x^2} \qquad (1)$$

where T_0 is the transmission ratio per pass at zero offset. Alternatively, instead of using the α parameter, a characteristic width w can be assigned to the function T(x), such that $\alpha=1/w^2$. The slope S(x) of the modulation curve, also called the modulation index, is given by

$$S(x) = \frac{dT}{dx} = -2n\alpha T_0^n \cdot x \cdot e^{-n\alpha x^2} \qquad (2)$$

with a maximum absolute value S_{max} for $x=\pm 1/\sqrt{(2n\alpha)}$. With $0 \le T_0 \le 1$ and $n \ge 1$, the maximum achievable modulation index S_{max} can be expressed as a function of n and T_0:

$$S_{max}(n, T_0) = T_0^n \cdot \sqrt{(2n\alpha / e)} \qquad (3)$$

With α=0.0016 μm^{-2} and T_0=0.85, T(x) approximates experimental data of a single pass for graded index 62.5µm core fibers, as shown in Fig.4. The fitted curve has been used to estimate the modulation curve for a four-pass connection, provided that T_0 is the same for each pass. This estimated curve is plotted in Fig. 4 together with experimental data for a 4-fiber ribbon coupling.

In Fig. 5, the modeled modulation function T(x) with α=0.0016 μm^{-2} and T_0=0.85 is plotted for n=1 and n=4, also for the ideal case when T_0=1. Fig. 5 gives a picture of what could be expected from an ideal multiple pass case, compared with the experimental result of Fig. 3: a higher slope (higher sensitivity) and a narrower measurable displacement range (smaller measurement range). However, in order to reach the theoretical limit, besides having a good fiber alignment, reflection losses at the fiber ends must be eliminated. This is discussed in the next section. The reflection loss can be modeled by replacing T_0 with $T_F \cdot T_0$ in the expression for T(x), with $T_F=0.96^2=0.92$ being the Fresnel transmission factor per fiber pair, corresponding an approximate 4% Fresnel reflection loss at each glass/air interface.

Fig. 6 shows the corresponding maximum modulation index S_{max} plotted versus T_0 for some values of n, using α=0.0016 μm^{-2}. From Fig. 6 it is clear that a very high T_0 is needed to take benefit from multiple passes. In the case of n=4, a T_0=0.85 just about gives a modulation index higher than for n=1. The more passes, the higher T_0 is needed per fiber pair. This fact flags for problems with end reflections and with fiber alignment as experienced in the experimental pre-study.

Table 1. Fiber sample data

Fiber sample	NA	P_T (µW)
SI 8.3/125 µm	0.11	0.37
GI 50/125 µm	0.20	13.0
GI 62.5/125 µm	0.275	31.2
GI 100/140 µm	0.29	36.0*)
GI 4x62.5/125 µm (ribbon)	0.275	31.9
GI 4x62.5/125 (V-groove)	0.275	35.8
GI 4x62.5/125 (MT-con.)	0.275	17.7
8.3-50-62.5-100 (hybrid rib.)	0.11-0.29	0.32

*) Fiber connected to source with 62.5/125µm fiber

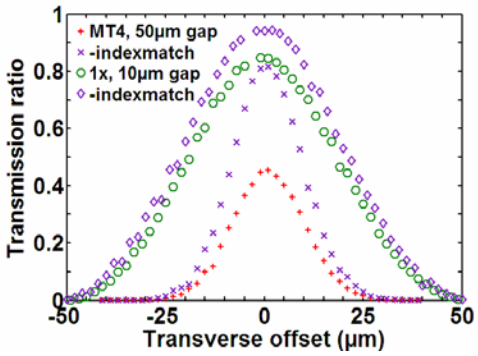

Fig. 7. Effect of index-matching liquid on the transmission ratio.

4. Further experimental work

In order to maximize the transmission ratio further, the practical effect of index matching liquid, in this case glycerol (refractive index ≈1.47), was investigated. As stated above, the Fresnel reflection contribution to the coupling loss theoretically results in a transmission factor T_F of 0.92 per fiber-to-fiber coupling with an air gap. In Fig. 7 the modulation curve for a single 62.5µm core fiber pair with a 10 µm end gap is shown with and without the use of index-matching liquid in the gap. A raise of transmission ratio $T_F \cdot T_0$ from 0.85 to about 0.95 is seen, which gives a transmission factor T_F=0.85/0.95=0.89 if the reflection loss is assumed to be totally eliminated (T_F=1) by the index-matching liquid. The effect of index-matching was also tested on the 4-fiber MT-connector arrangement, here with an end gap of 50 µm. In this case the total change in transmission ratio changed from about 0.45 to roughly 0.8, which would result in a transmission factor T_F=0.87 since T_F^4=0.45/0.8=0.56 under the same assumption as above. Clearly the reflection loss plays an important role when using multiple passes.

Another way of increasing the transmission ratio is to couple the light into a fiber with a higher numerical aperture (NA) and a larger core than the transmitting fiber. With the same experimental conditions, modulation curves were first recorded for other fiber types (see Table 1). The results of these basic measurements are shown in Fig. 8. It is clear from the figure that different fiber types result in different values of α, or characteristic width w, in the modeled T(x). In the next step, hybrid fiber pairs, where the receiving fiber has a larger core diameter and numerical aperture (NA) than the transmitting fiber, were investigated. Finally a hybrid, three-pass fiber array, aligned with V-grooves, was measured on. The hybrid array consisted of a transmitting standard single-mode fiber coupled to a GI 50µm core fiber, further to a GI 62.5µm core fiber and finishing with a receiving GI 100µm core fiber. The result, seen in Fig. 9, is an increase in T_0 for the complete array, and overall more relaxed alignment demands on the fiber pairs. Also it can be noted that the fiber pair with the highest modulation index S_{max} determines S_{max} for the hybrid array, i.e. the same modulation index could be achieved with just a fiber pair, in this case a single-mode fiber to multimode 50µm core fiber coupling.

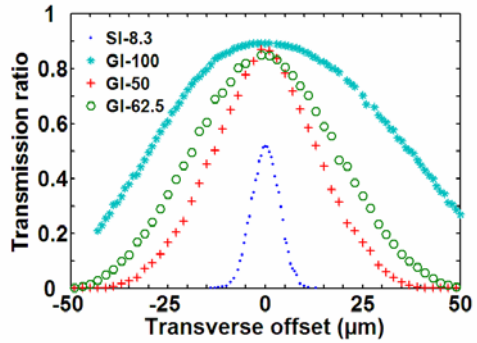

Fig. 8. Experimental modulation curves for single pass (n=1) coupling of some different fiber types.

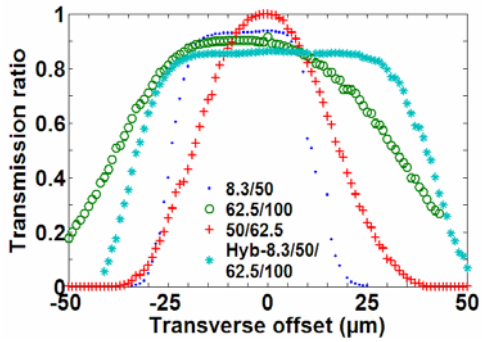

Fig. 9. Experimental modulation curves for hybrid fiber pairs and hybrid fiber array.

5. Discussion

When designing coupling-based intensity modulated sensors a decision must often be made whether sensitivity or measurement range, i.e. measurable range of displacement, should be the priority. Also the coupled power in the system might be an important parameter as well as the fiber alignment possibilities. All these parameters finally determine the most suitable fiber type and fiber configuration of the sensor.

From the experiments (Fig. 8) it can be noted that different fiber types have different modulation indices and therefore result in different sensitivities, but they also have different measurement ranges. By using multiple passes (Fig.3-5), the same effect on the modulation curve is achieved (at its best) as if a fiber with smaller core diameter and numerical aperture was chosen instead: a narrower, steeper curve. Despite possible ways of improving coupling and partly overcoming alignment problems (Fig. 7), increased sensitivity is more easily realized by changing fiber type. In the absence of suitable fiber types though, a multiple pass arrangement may be considered, provided alignment and reflection loss elimination demands are met.

6. Conclusions

We have shown theoretically and experimentally that multiple passes, due to almost unreachable alignment and coupling demands, do not significantly increase sensitivity in practice. Precision alignment and elimination of reflection losses are needed in order to reach a significant sensitivity enhancement compared to a standard single fiber pair arrangement. Also, the multiple pass effect on sensitivity could be realized with the single fiber pair by changing to a fiber type with suitable core diameter and numerical aperture. In reality, fiber types in such a pair should be chosen depending on the displacement range of interest in each sensing application.

7. References

[1] E.Peiner et.al, "A micromachined vibration sensor based on the control of power transmitted between optical fibres", Sensors and Actuators A **65**, .23-29 (1998).
[2] J.M. López-Higuera et.al, "New low cost fiber optic accelerometer system for stator winding monitoring of hydroelectric generating machines", Proc. of SPIE Vol. 2868 (SPIE, 1996), pp.510-515.
[3] M. Kimura and K. Toshima, "A New Type Optical Fiber Vibration-Sensor", in Transducers '97, 1997 International Conference on Solid-State Sensors and Actuators, Chicago (IEEE, 1997), pp. 1225-1228.
[4] K.E. Burcham et.al, "Micromachined Silicon Cantilever Beam Accelerometer Incorporating an Integrated Optical Waveguide", in Integrated Optics and Microstructures, Proc. of SPIE Vol. 1793 (SPIE, 1992), pp. 12-18.
[5] E. Ollier et.al, "Integrated micro-opto-mechanical vibration sensor connected to optical fibres", Electronics Letters **33**, 525-526 (1997).
[6] J. Jason et.al, "Fiber-Optic Temperature Monitoring in Pulp Production", to be published in Proceedings of the 55th IWCS/Focus Conference (International Wire & Cable Symposium, Inc., Eatontown, NJ, 2006)
[7] C.M. Miller, S.C. Mettler and I.A. White, *Optical fiber splices and connectors* (Marcel Dekker, Inc., 1986).
[8] G. He and F.W. Cuomo, "A Light Intensity Function Suitable for Multimode Fiber-Optic Sensors", Journal of Lightwave Technology **9**, 545-551 (1991).
[9] A. Cobo et.al, "More Accurate Coupling Function Approach for Optical Transducers Based on Power Coupling Between Multimode Fibers", Proc. of SPIE Vol. 3746 (SPIE, 1999), pp.442-445.

Characteristics of spun fiber grating sensors

Yong Wang and Chang-Qing Xu
Department of Engineering Physics, McMaster University, Hamilton, Ontario, Canada
wangyong_x@yahoo.com

Abstract: Novel characteristics of spun fiber grating-based sensors are presented in this paper. These gratings were written into special spun fibers with certain intrinsic linear birefringence and short spinning periods. Due to the modal conversion and averaging effect in spun fibers, the introduced linear birefringence enables the spun fibers and spun fiber gratings to have certain resistance to external perturbations, such as transverse pressure and bending. Furthermore, short-period fiber Bragg gratings (FBGs) always exhibit multiple side peaks near the main Bragg peak in their reflection spectra. In term of the main Bragg peak, these spun FBG sensors have similar strain and temperature coefficients to those of traditional FBGs, but weaker polarization dependence. On the other hand, those side reflection peaks have strong polarization dependences, which can be used to simultaneously monitor the change of input polarization state.

1. Introduction

Optical fiber gratings play important roles in both optical fiber communications and sensing [1]. Besides the traditional single-mode fibers, gratings have been successfully imprinted into a variety of optical fibers, in which they have different features, and lead to different applications. Fiber-Bragg-grating (FBG)-based sensors, whose reflected wavelengths vary with the measurands such as temperature and strain, are simple intrinsic sensing elements, and have all the advantages attributed to fiber-optic sensors. In addition, these sensors can also be easily multiplexed in a serial fashion along a single strand of fiber. This type of sensors is highly sensitive and free from the normal fiber transmission losses. Among various fiber gratings, short-period FBGs and long-period gratings (LPGs) are dominant in the sensing field.

It is well known that the core of a traditional optical fiber is not ideally symmetric in its cross section; meanwhile, an external perturbation, such as lateral pressure and macro-bending, usually impacts more on one polarization than the other. As a result, an optical fiber always exhibits a certain polarization dependence on external effects. Furthermore in a fiber grating, nonuniform refractive index change caused by the side UV exposure in a conventional fabrication process can form a polarization-dependent loss (PDL). These factors make traditional FBG sensors polarization-sensitive to some extent. In many high-precision sensing applications, where polarized tunable lasers are adopted as scanning sources, a strong PDL of FBG may deteriorate the interrogation accuracy, and can even cause a failure of measurement due to severe distortions of FBG reflection spectra. Rotating fibers in the manufacturing process, known as spun fibers, can effectively reduce the polarization-mode dispersion and birefringence of fiber [2, 3]. As a result, spun fibers have attracted considerable attention in the fields of both optical communications and fiber sensing [2-4].

It has been found that the spun fibers with millimeter spin periods and certain intrinsic birefringence have many unique characteristics, and the FBGs imprinted in these spun fibers exhibit distinctive properties from those made of the conventional single-mode fibers [5, 6]. In this paper, more characteristics of spun fiber gratings are presented, and their sensing applications are also discussed.

2. Spun fibers and spun fiber gratings

The investigated spun fibers were drawn from an asymmetric preform, which had a D-shaped cladding and a round core in the center. After the drawing process, they have a symmetric structure – a round cladding and a round core at the center – due to the presence of surface tension in the fiber manufacturing process at a high temperature of above 1000 ºC. However, non-uniform stress in the fiber cross section can introduce some intrinsic linear birefringence into the fiber. In these spun fibers, the intrinsic stress has a certain spiral structure at a spin rate of α in the longitudinal direction as schematically shown in Fig. 1(a), where (x, y) is the fixed laboratory coordinate system, and x corresponds to the slow axis. ξ and ζ represent the local rotating coordinates with respect to the slow and fast fiber axes. All these fibers have core diameters of ~8.0 μm and cladding diameters of ~125 μm. To form FBGs and LPGs, these fibers with similar Germanium concentration to the standard fibers were side-exposed to uniform UV light (Excimer laser at 248 nm, ~60 mJ/cm^2) through either a holographic phase mask with a pitch of 1064.82 nm or long-period amplitude masks after two-week hydrogen loading at 1500 Psi. In Fig. 1(b), the stress distribution in the fiber cross section is shown with respect to a fixed exposure direction (x axis).

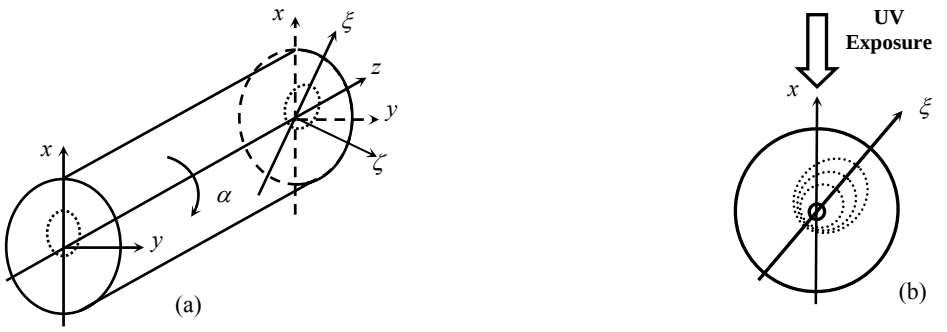

Fig. 1. (a) Schematic of residual stress in a spun fiber. (b) Stress distribution in the cross section against UV exposure.

A variety of FBGs and LPGs have been fabricated in our spun fibers with spin periods of 1~4 mm. Figure 3 shows typical reflection and transmission spectra of a 15-mm long FBG imprinted in the spun fiber with a 2.25-mm spin period, and a transmission spectrum of a 30-mm long LPG in the same kind of spun fiber. The spectra were measured by using a broadband light source and an optical spectrum analyzer (ANDO AQ6317). The UV-induced index change is about $3.0\text{x}10^{-4}$. The LPG period is 300 μm. We can see in Fig. 2(a) that the Bragg peak and four side peaks are dominant with a 0.37-nm spacing between two neighboring peaks in the reflection spectrum, and only one notch at the main Bragg wavelength is apparent in the transmission spectrum. The 3-dB notch width of the LPG is about 13 nm. For spun FBGs, the spectral spacing between two neighboring side peaks is inversely proportional to the spin period. Similar to FBGs in SMF-28, at the wavelength of 1.55 μm, these spun FBGs have a strain coefficient of ~1 pm/με, and a temperature coefficient of 10 pm/ºC for all reflection peaks.

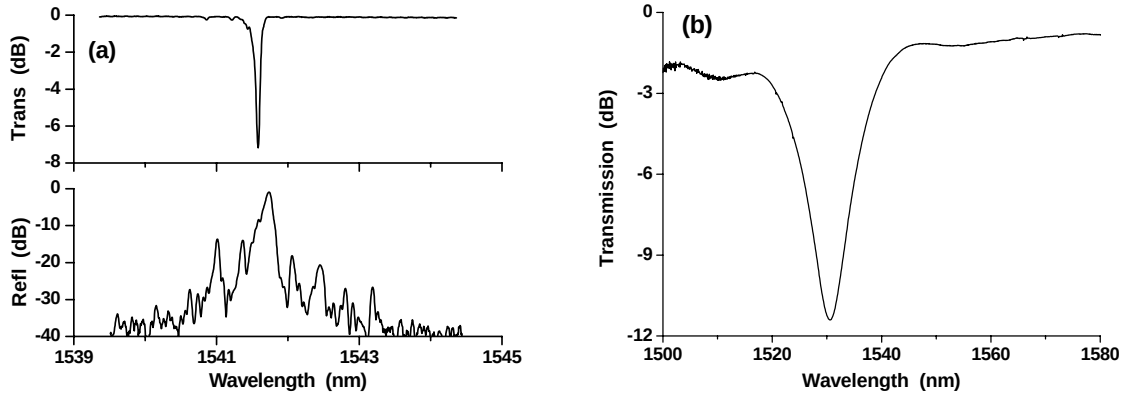

Fig. 2. (a) Transmission and reflection spectra of a spun FBG. (b) Transmission spectrum of a spun LPG.

3. Evolution of state of polarization

These spun FBGs have distinct spectral and polarization characteristics from those imprinted in traditional single-mode fibers, which is attributed to different evolutions of states of polarization (SOPs) in the fibers. This can be verified theoretically. The *x*- and *y*-polarized modes that are mutually orthogonal in an unspun fiber can be coupled to each other in a spun fiber. Regardless of the transmission loss, the modal coupling can be described by [7]

$$\frac{d}{dz}\begin{bmatrix} E_x \\ E_y \end{bmatrix} = -j\begin{bmatrix} \beta_0 + 0.5\Delta\beta_L \cos(2\alpha z) & 0.5\Delta\beta_L \sin(2\alpha z) \\ 0.5\Delta\beta_L \sin(2\alpha z) & \beta_0 - 0.5\Delta\beta_L \cos(2\alpha z) \end{bmatrix}\begin{bmatrix} E_x \\ E_y \end{bmatrix} \tag{1}$$

where E_x and E_y are the amplitudes of two coupled modes polarized in the *x* and *y* directions, respectively. β_0 is the average propagation constant of the two normal modes, and $\Delta\beta_L$ corresponds to the intrinsic linear birefringence (Δn_L).

Due to the presence of strong modal coupling in the spun fibers with millimeter spin periods, these spun fibers cannot be regarded uniformly birefringent [5]. Instead, the two polarization modes can interact and exchange power in a spun fiber. This can be understood from the evolutions of three typical SOPs shown in Fig. 3, where $\Delta n_L = 0.5\times10^{-4}$, $P_s = 2.0$ mm were adopted in the simulation. Despite different higher-frequency components, the three SOP evolutions exhibit the same major spatial period, denoted by the conversion length L_{conv}, at which the optical power converts alternatively between two orthogonal modes. Based on the Fourier transform, the conversion length L_{conv} was then

calculated as a function of spin period and fiber birefringence, and is plotted in Fig. 4. We can see that L_{conv} rapidly drops from hundreds to tens of millimeters with an increase of P_s or Δn_L. This property enables a spun fiber to have a certain resistance to external perturbations, such as lateral pressure or bending, as well as non-uniform refractive index change in a spun FBG. It is often observed in experiments that when a lateral pressure is applied onto a traditional FBG strain or temperature sensor, the FBG spectrum may suffer from a severe distortion. In the case of a split spectrum for the two polarization modes, the measurement may be failed if an interrogation system with a simple peak- or mean-wavelength-tracing method is adopted. Therefore, for those embedded FBG sensors, particularly in civil structural health monitoring, a special design of FBG packaging is usually required [8]. However, for a spun fiber grating, if the fiber section suffering from a lateral perturbation is longer than the aforementioned conversion length, the two orthogonal modes may experience the same perturbation, and consequently weaken the influence of external perturbation. In the experiment, we placed a few bare spun FBGs and other FBGs (SMF-28) in a V-groove, and compared their resistances to lateral forces applied under a certain tension. It was observed that the former can resist a higher lateral pressure than the latter approximately by a factor of 3~10, depending on FBG length and spin period, before a significant distortion of FBG reflection spectrum occurred. This verifies that the spun FBG sensors can take advantage of higher resistance to external perturbations, as compared to the traditional FBG sensors.

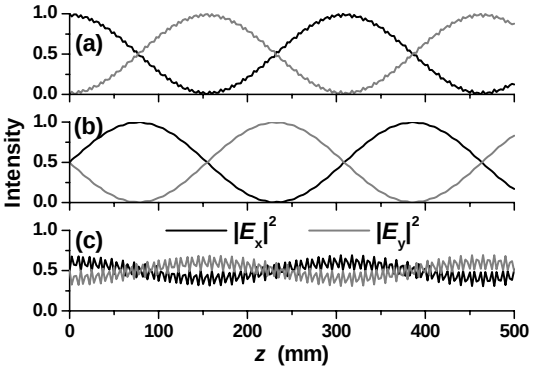

Fig. 3. Evolutions of SOP in spun fibers for different input SOPs. (a) 0° linearly polarized input, (b) 45° linearly polarized input, (c) right-circularly polarized input.

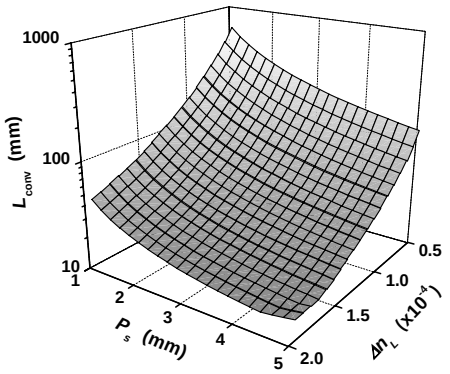

Fig. 4. Polarization conversion length versus linear birefringence and spin period.

4. Polarization dependent loss

To characterize the PDL of spun FBGs, the output SOP was measured using a lightwave polarization analyzer (LPA, Agilent 8509C). Since FBGs may be used in both the reflection and transmission manners, the transmitted and reflected outputs were investigated respectively. The experimental setup is schematically shown in Fig. 5(a) and (b) for the transmission and reflection measurements, respectively. The output from a tunable laser source (TLS, HP 8164A) is linearly polarized, and the SOP test in the reflection manner is obtained through a three-port circulator. The input SOP of an FBG under test is modified through a fiber polarization controller (PC). Note that during the test, only the PC was adjusted to select the required output SOP, and the spun FBGs and their lead fibers were kept unchanged.

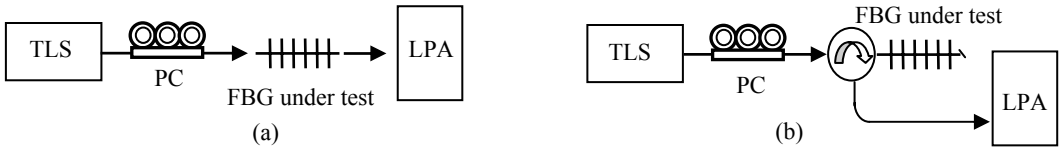

Fig. 5. SOP test setup for (a) transmission and (b) reflection characteristics of polarization. TLS: tunable laser source, LPA: lightwave polarization analyzer, PC: polarization controller.

For the previous spun FBG shown in Fig. 2(a), the reflection spectra under five typical SOPs, i.e. three linear SOPs (0 and ±45º), left-handed circular SOP and an elliptical SOP, were compared in Fig. 6(a). Different variations in amplitude at those reflection peaks can be seen. In particular, the PDL is about 0.1 dB for P_B, 1.5 dB for $P_{\pm1}$, 4.0-6.0 dB for $P_{\pm2}$. Correspondingly from the transmission spectra as shown in Fig. 6(b), the PDL is 0.5 dB for P_B, and < 0.03 dB for other wavelengths out of the FBG stop-band. From the Fourier transform theory, we know that $P_{\pm1}$ and $P_{\pm2}$ correspond to the fundamental spin period and its second harmonic, respectively. Since the UV-induced index change is related to the spiral stress and polarization-dependent, the amplitudes of $P_{\pm1}$ and $P_{\pm2}$ have different sensitivities to the

input SOP. The low-polarization dependence of P_B is due to an averaging effect along the grating. Such strong PDLs at the side peaks and a low PDL at the main Bragg peak in the reflection spectrum provides an outstanding property to spun FBG sensors. In particular, when a spun FBG is adopted as a temperature or strain sensor, temperature or strain information can be read out from the shift of λ_B, while polarization information may be indicated from the intensity variations of the side peaks, and used to monitor the input SOP of the FBG. It is found that for this kind of sensing application, a spin period in the range 0.8 ~ 8.0 mm and an intrinsic birefringence of $> 0.3\times10^{-4}$ are desired.

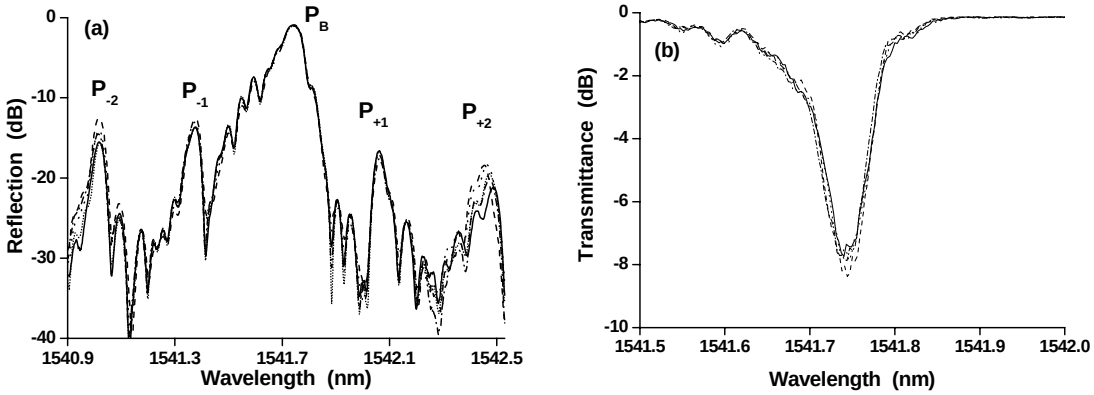

Fig. 6. FBG spectra in (a) reflection and (b) transmission manners for different SOPs. Solid, dashed, dotted, dash-dotted and short-dashed lines correspond to three linear SOPs (0 and ±45º), left-handed circular SOP and an elliptical SOP, respectively.

5. Conclusion

The novel properties of FBGs imprinted into spun fibers with certain intrinsic birefringence and millimeter spin periods have been presented. Due to the modal conversion and averaging effect in spun fibers, the introduced linear birefringence enables the spun fibers and spun FBGs to have higher resistance to external perturbations, such as transverse pressure and bending, than the traditional FBG sensors. Due to the presence of the superstructure in a spun FBG, the multiple peaks appear near the Bragg wavelength in its reflection spectrum. The main Bragg reflection peak has similar temperature and strain coefficients to traditional FBGs, but weaker polarization dependence on input SOP, while the side reflection peaks have strong polarization dependences. These render spun FBG sensors feasible in simultaneous monitoring of the input SOP together with ordinary temperature or strain measurement.

Acknowledgment

This work is supported by the Ontario Photonics Consortium (OPC), the Photonics Research Ontario (PRO), the Natural Sciences and Engineering Research Council of Canada (NSERC) and the Canada Foundation for Innovation (CFI) under New Opportunities program. We would like to thank Dr. Viatcheslav Izraelian for useful discussions.

References

1. A. Othonos, and K. Halli, *Fiber Bragg Gratings: Fundamentals and Applications in Telecommunications and Sensing*, Artech House, Boston, London, 1999.
2. D. N. Payne, A. J. Barlow, and J. J. Ramskov-Hansen, "Development of low- and high- birefringence optical fibers," *IEEE J. Quantum Electron.*, **18**, 477-486, 1982.
3. D. A. Nolan, X. Chen, and M. J. Li, "Fibers with low polarization-mode dispersion", *J. Lightwave Technol.*, **22**, 1066-1077, 2004.
4. J. R. Qian, Q. Guo, and L. Li, "Spun linear birefringence fibres and their sensing mechanism in current sensors with temperature compensation", *IEE Proc-Optoelectron.*, **141**, 373-380, 1994.
5. Y. Wang, C.-Q. Xu, and V. Izraelian, "Characterization of spun fibers with millimeter spin periods", *Opt. Exp.*, **13**, 3841-3851, 2005.
6. Y. Wang, C.-Q. Xu, and V. Izraelian, "Bragg gratings in spun fibers", *IEEE Photon. Technol. Lett.*, **17**, 1220-1222, 2005.
7. J. Sakai and T. Kimura, "Birefringence and polarization characteristics of single-mode optical fibers under elastic deformations," IEEE J. Quantum Electron. **17**, 1041-1051, 1981.
8. S. C. Tjin, Y. Wang, X. Sun, P. Moyo, and J. M. W. Brownjohn, "Application of quasi-distributed FBG sensors in reinforced concrete structures", *Measurement Science and Technology*, **13**, 583-589, 2002.

Metrology of integrated waveguide devices and systems using near-field scanning optical microscopy

Guangwei Yuan and Kevin L. Lear
Electrical and Computer Engineering Department, Colorado State University, Fort Collins, CO, 80523-1317, USA
gwyuan@engr.colostate.edu, kllear@engr.colostate.edu

Abstract: Near-field scanning optical microscopy (NSOM) is a valuable tool for measuring modal propagation parameters including loss, effective index, and coupling coefficients of a variety of waveguide structures. Examples are provided of simple waveguide sections and bends as well as an on-chip optical clock distribution system using an H-tree containing splitters and leaky-mode polysilicon photodiodes.

1. INTRODUCTION

1.1 Motivation

Optical waveguide devices are essential components for photonic integrated circuits, on-chip optical interconnects, and integrated optical biosensors. Near-field scanning optical microscopy (NSOM) is a high resolution alternative to more traditional scatter imaging methods or cumbersome cutback studies for determining waveguide loss. It can easily resolve modal interference signals that can be used to determine propagation constants and related parameters. Several examples drawn from recently published work [1-3] are compiled to illustrate the power of this technique for analysis of integrated waveguide devices and systems.

1.2 Background on Near-field Scanning Optical Microscopy

NSOM is able to simultaneously measure surface topology and the optical intensity on the surface of optical systems. In particular in waveguide systems, the evanescent field at the interface to the air above the waveguide core or upper cladding is readily measured and related to the optical field intensity propagating in the waveguide. The measurements reported here were made using a commercial Alpha-NSOM system from WiTec with simultaneous optical and topological profiling capability. The experimental setup is shown in Fig. 1(a). The combination atomic force microscopy (AFM) and NSOM tip is a hollow aluminum pyramid integrated on a Si cantilever that converts the evanescent field to a propagating wave by locally frustrated total internal reflection. A photomultiplier tube is aligned to a subwavelength diameter pinhole centered in the tip to detect the wave emanating from the tip that is proportional to the evanescent field. A reference laser beam reflecting off the cantilever is directed to a quadrant detector by a dichroic beam splitter and is used to sense tip deflection in AFM mode. As the tip is moved toward the top surface of the waveguide, an exponentially increasing optical field, such as

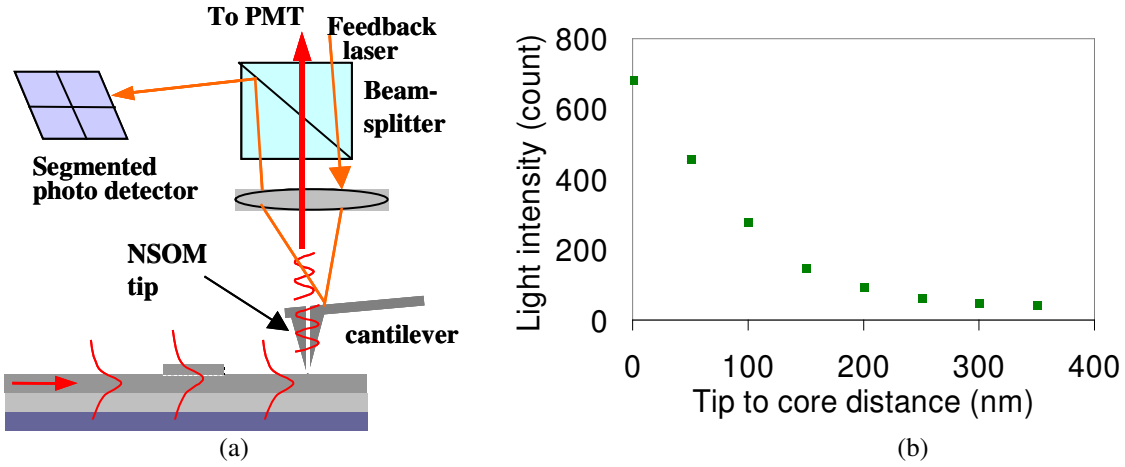

Fig. 1. (a) Schematic illustration of Witec Alpha-SNOM using optical detection of cantilever deflection, after [1]. The sample is scanned laterally. (b) An exponentially increasing optical field as the tip moving away from the top surface of the waveguide.

the measured data plotted in Fig. 1(b), is observed in addition to a constant background signal due to reference beam scattering. During in-plane optical profiling, the NSOM was operated in contact mode so that the field at the top surface of the waveguide was measured [1]. All of the measurements discussed below were performed by coupling a 654 nm laser diode to the waveguides under test using a visible single mode fiber with 4 μm core diameter.

2. MULTIMODE INTERFERENCE IN WAVEGUIDES

2.1 Single mode, straight waveguide

Prior to presentation of modal interference characterization in a few waveguide structures, it is useful to examine the measured topology and optical intensity distribution associated with a segment of straight, single-mode waveguides. The waveguide core was fabricated from a 105-nm-thick SiN film sputtered onto a ~2 μm thick SiO_2 lower cladding supported on a Si substrate. No solid upper cladding was deposited above the SiN to maximize the evanescent field interaction with the region above the core for biosensing purposes. This approach also provides the NSOM ready access to the evanescent field in the air above the core which serves as the upper cladding. Dry etching 21 nm of the SiN outside a ~2 μm-wide ridge defined the lateral extent of the core. The surface topology of the ridge, shown in Fig. 2(a), and the lateral intensity distribution of the evanescent field immediately above the core, illustrated in Fig. 2(b), were simultaneously acquired with the NSOM. The ridge appears wider than the nominal wavguide width due to the blunt nature of the probe tip around the optical aperture. The optical intensity pattern reveals a smooth, fundamental mode distribution without undulations associated with mode beating.

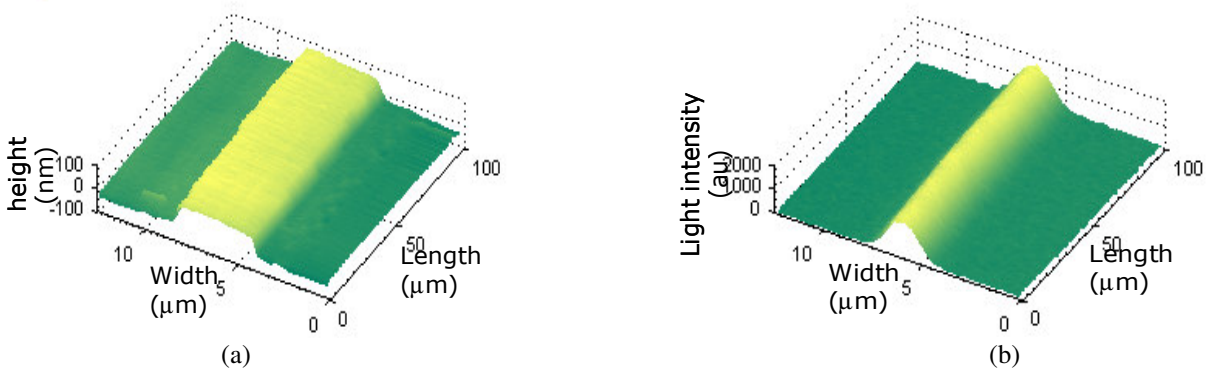

Fig. 2. NSOM measurements of (a) surface topography and (b) optical intensity at the surface. Single mode observation is observed.

2.2 Multimode straight waveguides

Investigations of waveguides with larger dimensions revealed modal interference in waveguides. The surface intensity distribution of a ~4 μm wide waveguide, otherwise identical to the waveguide described above, resulted in multiple horizontally transverse modes seen in Fig. 3(a). The waveguide only supports two TE modes, TE_{00} and TE_{10}, according to modal calculations. The NSOM data in the figure shows the intensity maxima shifting back and forth laterally as the modes travel down the waveguide with different propagation constants. Another waveguide, 500 nm thick with a 250 nm ridge height, displayed interference between multiple orders of vertically transverse modes as seen in Fig. 3(b). The NSOM sees periodic extinction of the surface intensity when the modes are out of phase at the top of the waveguide. The beat distance is much smaller than in Fig. 3(a), indicating a larger difference in effective indices for the two modes.

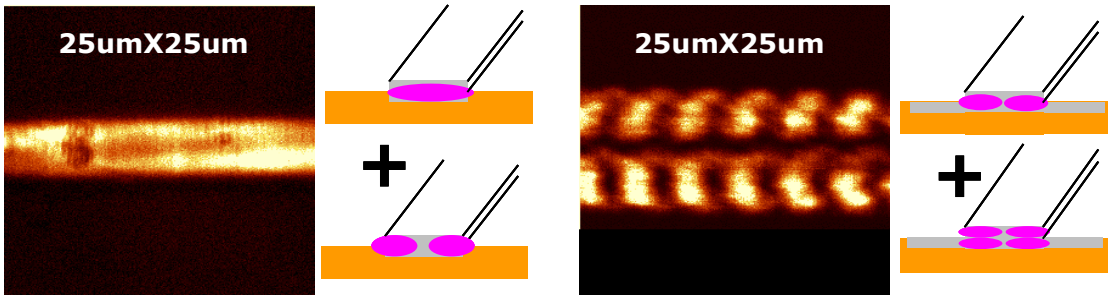

Fig. 3. Surface optical intensity shows modal interference between the schematically illustrated modes for (a) 88 nm thick x ~4 μm wide waveguide core and (b) 500 nm thick x ~10 μm wide waveguide core.

2.3 Nearly single mode waveguide bend

More complicated structures, such as waveguide bends, also present the opportunity to study modal evolution and position and to extract propagation constant information the NSOM measurements [2]. The optical distribution in a ~4 μm wide waveguide similar to that described in Section 2.1 but with a shorter ridge was investigated in a 90° waveguide bend with a centerline radius of 400 μm shown in Fig. 4(a). Two bound modes in the bend determined from conformal mapping techniques matched those observed with NSOM. Simultaneous topography and optical measurements established the shift of the modes to the outside of the waveguide bend as seen in Fig. 4(b). Fitting of the transverse intensity profile at various angles along the bend allowed the determination of the relative intensity and phase of the two modes. The fitting procedure gave attenuation losses of the fundamental and the first order mode as 0.46 dB/90° and 15.1 dB/90°, respectively, demonstrating the effectiveness of planar waveguide bends for mode stripping. Interesting scattering patterns were observed at the exit of the bend to a straight waveguide where the radius of curvature and thus lateral eigenmode peak position shifts abruptly.

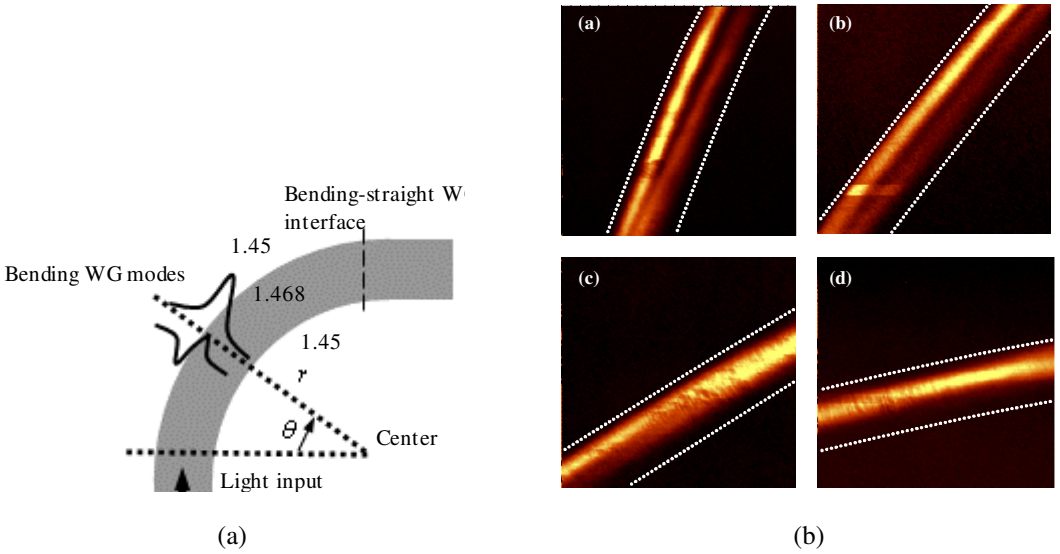

Fig. 4. (a) Schematic diagram (not to scale) of a 90° waveguide bend connected to straight input and output sections. (b) NSOM images of optical intensity at (a) 20°, (b) 40°, (c) 60°, and (d) 80° from the start of the waveguide bend. Dotted lines denote the waveguide core boundaries determined from simultaneous topographical scans. Reproduced from [2].

3. ON-CHIP OPTICAL INTERCONNECTS

A more complicated CMOS based, integrated waveguide optical system for on-chip clock distribution provided an environment for further NSOM studies [3]. The chip contains a series of waveguide straight sections, splitters, and bends in the form of an H-tree as illustrated in Fig. 5(b) to deliver an optical clock signal to 16 nodes where a leaky-mode detector converts the optical signal to photocurrent. Fig. 5(a) depicts the structure of the leaky-mode detector in an initial single metal level chip fabricated in Avago's 0.35 μm CMOS line in Fort Collins, Colorado. Scatter from the waveguides and detectors associated with four nodes is seen in Fig. 5(c). The SiN core waveguides are all 350 nm thick, with the width after the input taper decreases from to 8 μm down to 0.5μm. In contrast to the waveguides described in Section 2, this system did include a thin upper SiO_2 cladding whose minimal 250 nm thickness still provided sufficient evanescent field strength at the air interface to allow NSOM measurements.

Optical intensity recorded along the H-tree was used to extract the loss and performance of the waveguides, splitters, and detectors. NSOM provides a higher resolution alternative to scatter imaging more commonly used for such studies. The first generation splitters had a high excess loss of 2dB or higher with forward scatter, mode beating in the outputs, and undesired unequal branching ratios as seen in Fig. 5(d). Revised designs for a second generation chip now being fabricated are aimed at addressing these issues. NSOM also proved valuable for investigating the coupling of light from the waveguide into the leaky mode detector and in particular determining the effective absorption coefficient of the polysilicon metal-semiconductor-metal detectors. Fig. 5(e) is the NSOM image of the detector region and the waveguide feeding it. Data taken from the centerline intensity is plotted in Fig. 5(f) where the detector portion has been fit to determine the effective absorption coefficient. The measured value of 0.67 dB/μm agrees very well with a calculation of 0.68 dB/μm and is 25 times higher than previously recorded values for leaky mode coupling to Si detectors [3]. Mode beating between the leaky mode centered in the SiN core

and radiation modes generated by the mode mismatch result in a beat signal seen in the decaying optical intensity on the surface above the detector seen in Fig. 5(f).

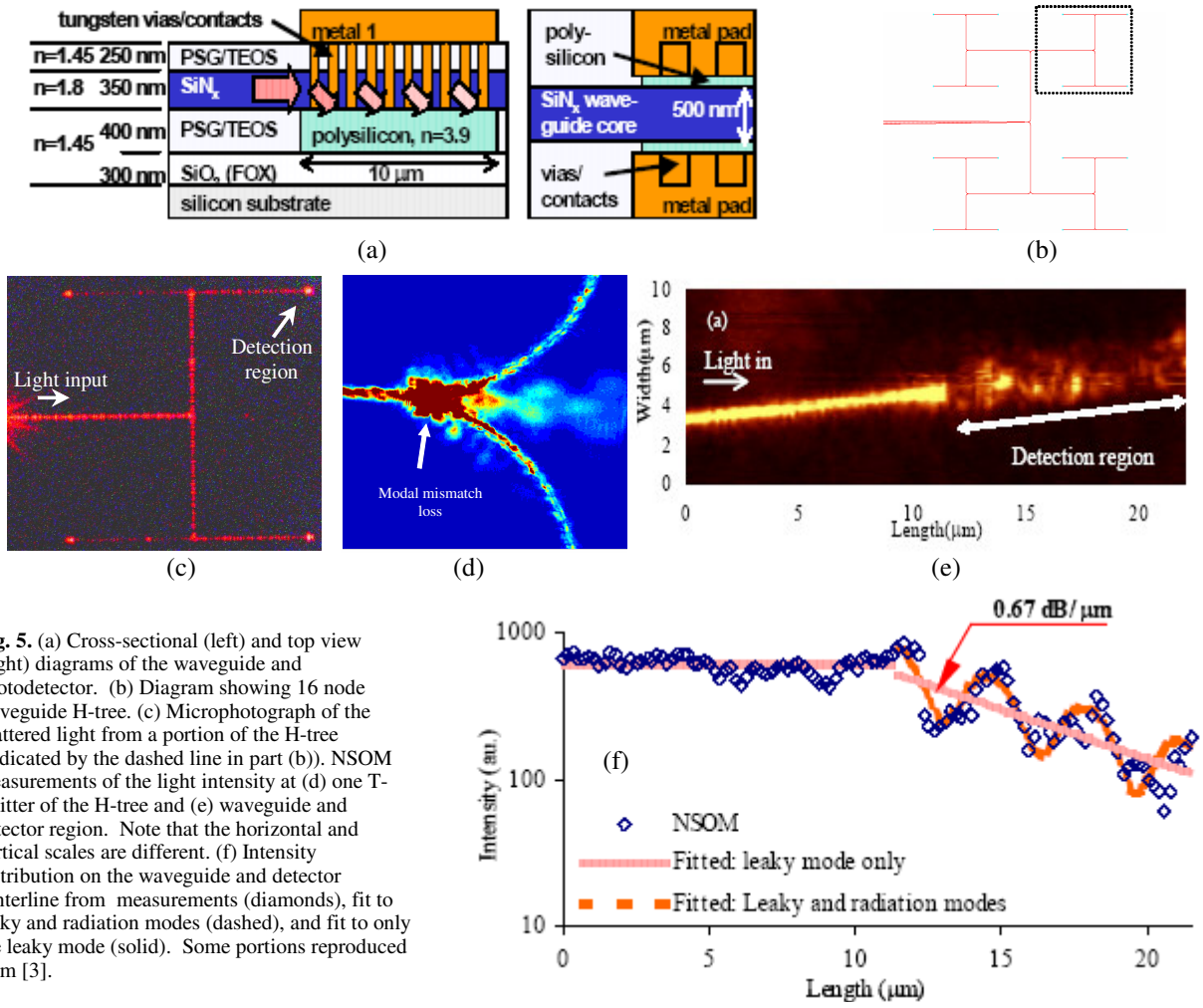

Fig. 5. (a) Cross-sectional (left) and top view (right) diagrams of the waveguide and photodetector. (b) Diagram showing 16 node waveguide H-tree. (c) Microphotograph of the scattered light from a portion of the H-tree (indicated by the dashed line in part (b)). NSOM measurements of the light intensity at (d) one T-splitter of the H-tree and (e) waveguide and detector region. Note that the horizontal and vertical scales are different. (f) Intensity distribution on the waveguide and detector centerline from measurements (diamonds), fit to leaky and radiation modes (dashed), and fit to only the leaky mode (solid). Some portions reproduced from [3].

In addition to the systems described above, NSOM has been used to characterize the performance of a novel integrated waveguide biosensor that relies on local detection of evanescent fields [1], which is very similar to the mechanism of NSOM itself. Further, 1-D effective index models that are in good agreement with wide-angle beam propagation method (BPM) simulations have been developed that offer insight into the function of the leaky mode detectors as well as the new biosensor.

In summary, NSOM is a valuable tool for measuring modal propagation parameters in integrated waveguide structures. Further development of this technique including investigation of methods for accurately relating the surface intensity to the waveguide power in heterogeneous structures is warranted in view of the expected continued development of photonic and optoelectronic integrated circuits.

The authors thank the National Science Foundation for supporting this work under contract number ECS-0323493 and the National Institute of Health for supporting this work under contract number EB00726.

REFERENCES

1. G. W. Yuan, M.D. Stephens, D.S. Dandy, K. L. Lear, "Direct imaging of transient interference in a single-mode waveguide using near-field scanning optical microscopy," *IEEE Photonics Technology Letters*, vol. 17 (no. 11), pp.2382 – 2384, Nov. 2005 and references therein.

2. G. W. Yuan, M.D. Stephens, D.S. Dandy, K. L. Lear, "Characterization of a 90 degree waveguide bend using near-field scanning optical microscopy," *Applied Physics Letters*, vol. 87 (no. 19), Art. No. 191107 Oct. 2005.

3. G. W. Yuan, et al "Characterization of CMOS compatible, waveguide coupled leaky-mode photodetectors," *IEEE Photonics Technology Letters*, in press.

Return Loss Measurement in the Presence of Variable Insertion Loss Using Optical Frequency Domain Reflectometry

Stephen Kreger, Mark Froggatt, Dawn Gifford, Matthew Wolfe, and Brian Soller
Luna Technologies, 2020 Kraft Dr., Suite 2000, Blacksburg, VA 24060

Abstract: The high spatial resolution and high sensitivity inherent to optical frequency domain reflectometery enables precise measurements of distributed insertion loss and return loss events. The ability to compensate return loss for variable insertion loss greatly adds to the accuracy and practicality of measurements. Further, the capability of measuring the Rayleigh backscatter internal to the instrument provides a stable power calibration artifact.

Introduction

Excessive system return loss (RL) negatively impacts source stability and contributes to loss in high-speed fiber optic telecommunication systems. In order to meet system performance goals, precise measurement of return loss in individual components as well as in installed networks is required, especially when temporary mechanical connections are used. Most current return loss measurements are made using optical continuous wave reflectometry (OCWR) and optical time domain reflectometry (OTDR) [1]. One of the primary error sources for RL measurements using these devices is the error induced by variable insertion loss at the connection to the test equipment optical interface. While this error source may be minimized by splicing the device under test (DUT) to the instrument, this procedure is not practical in high volume manufacturing environments or for installed networks.

Both OTDR and optical frequency domain reflectometery (OFDR) are well suited for characterizing networks with some degree of spatial resolution. Both techniques typically have enough sensitivity to monitor the fiber Rayleigh backscatter level which can, in turn, be used to measure distributed loss and gain [2,3]. Typically OTDRs lack sufficient spatial resolution to be useful at the component and module level where one might be interested in, for example, locating a spurious reflection among a concatenation of several components each with multiple elements. OFDR is a tunable laser-based frequency domain technique that has several distinct advantages over time domain and low coherence techniques when the optical systems under test are several tens of meters in length [4,5]. These advantages include sub-millimeter resolution measurements over a few hundred meters of optical length, high sensitivity, and high dynamic range.

The capability of measuring localized insertion loss using OFDR presents a unique opportunity to provide consistent measurements of device RL even in the presence of variable connector loss, even for short lead lengths. Further, the lack of a dead zone and high sensitivity allows our OFDR-based instrument to calibrate return power levels to the Rayleigh backscatter level of fiber within the instrument. This onboard calibration capability provides a highly stable and reproducible reference for RL measurements. This paper outlines the methodology used to establish a value for the scatter in optical fiber, and how this Rayleigh scatter level is used to maintain consistent reflection measurements.

Measurement Apparatus

The optical network used to implement OFDR is shown in Fig. 1. Light from a tunable laser source is split into measurement and reference optical paths. In the measurement path, the light is further split by a 50/50 coupler. A third coupler is used to recombine the light from the measurement path with the light from the reference path. After recombination, the light is split by a polarization beam splitter. Interference is detected at two PIN photodiodes that are connected via amplification circuitry to a data acquisition card. This polarization diverse detection scheme ensures that an interference signal will be present on at least one of the detectors irrespective of the polarization state of the field reflected from the device under test (DUT). Not shown in Fig. 1 is an auxiliary interferometer used to monitor phase error during laser tuning. This technique is called triggered acquisition and is commonly used in OFDR systems to remove laser tuning errors from the data [4]. Also not shown is a portion of the network wherein a Hydrogen Cyanide gas-cell is used to monitor the instantaneous wavelength of the scanning laser.

The network shown in Fig. 1 is used to measure reflected power as a function of wavelength. The back-reflected power as a function of length is obtained via the Fourier transform of the raw data (see reference [6] for details). The maximum measurable length for this instrument is determined by the sampling resolution in the optical

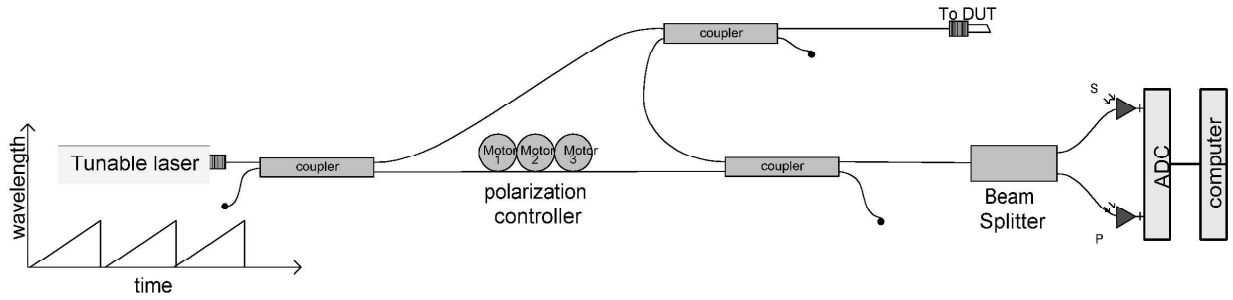

Fig. 1. Optical network used to perform polarization diverse measurements of Rayleigh backscatter.

frequency domain which is in turn determined by the physical delay difference of the auxiliary interferometer used for data triggering. In this paper, the instrument used had a maximum scan range of 30 m with ~20 μm spatial resolution.

To calibrate the measured back-reflection to an absolute RL, the response of a set of polished flat end face connectors was recorded. The expected value of the RL can be calculated using the Fresnel equation:

$$RL = -10\log\left(\left(\frac{n-1}{n+1}\right)^2\right) \tag{1}$$

According to the fiber manufacturer the value for the effective index of refraction n for these connectors is 1.4682 at 1550 nm, resulting in an expected RL of 14.44 dB. Although the above equation is only an approximation and the RL of such connectors is dependent on the surface polish quality and cleanliness, we have observed that the consistency for such connectors manufactured in-house is better than that of most commercially available metal-film fiber reflectors. After the reference set of reflectors was used to scale the return power, the Rayleigh backscatter level for a segment of fiber within the instrument close to the front panel connector was recorded. Upon any subsequent recalibration of the instrument, any drift in detector responsivity or amplifier gain can be corrected for by comparing the measured backscatter level of the fiber segment to the recorded value. Although we have not yet completed an extensive survey, we have found that the repeatability of the Rayleigh backscatter level for the fiber used in our instruments, Corning SMF-28e, is excellent, with a standard deviation less than 0.05 dB for a 1 m integration width.

Making Insertion Loss-Independent Return Loss Measurements

Any measurement of RL involves making a connection to the device under test. If there is loss in the connection, this loss will add directly to the apparent RL. As a practical matter, the insertion loss of the connector to the calibration artifact, component or network is not controllable and typically varies by several tenths of a dB every time a new connection is made. Since OFDR provides a means of measuring this connector loss, reproducible RL measurements are possible even in the presence of variable connector loss.

To demonstrate the repeatability of a RL measurement in the presence of loss, we measured the RL of a polished ST connector at the end of a 1.9 m lead with a FC-APC connection to the measurement instrument. To induce a varying amount of loss, the fiber was mandrel wrapped at roughly 0.3 m after the connection to the instrument. Fig. 2 shows two example scans of this DUT and one scan with no device connected. Because the ST connector has a high RL, two measurements are required to determine the RL. First, the DUT is measured with no alteration. Second, a measurement is taken with the fiber immediately before the ST connector pinched off to reduce the RL from the connector. This reduces the effect of the tails from the reflection peak on the measured data and, thus, enables a measurement of the Rayleigh scatter immediately before the reflection.

Four measurements of the reflected power along the measured traces are required to determine the RL with best accuracy. These measurements are obtained by measuring the integrated normalized power over a defined length centered at a specified location. The first power measurement, P_0, is recorded over a span of fiber inside the instrument and will be the sum of the Rayleigh back scatter P_{RA} and the background noise level P_B. The second power measurement P_1 is recorded over a span of fiber just prior to the reflection event and is given by the sum of P_B and the Rayleigh backscatter level divided by the double pass attenuation factor A. This factor, A, is the

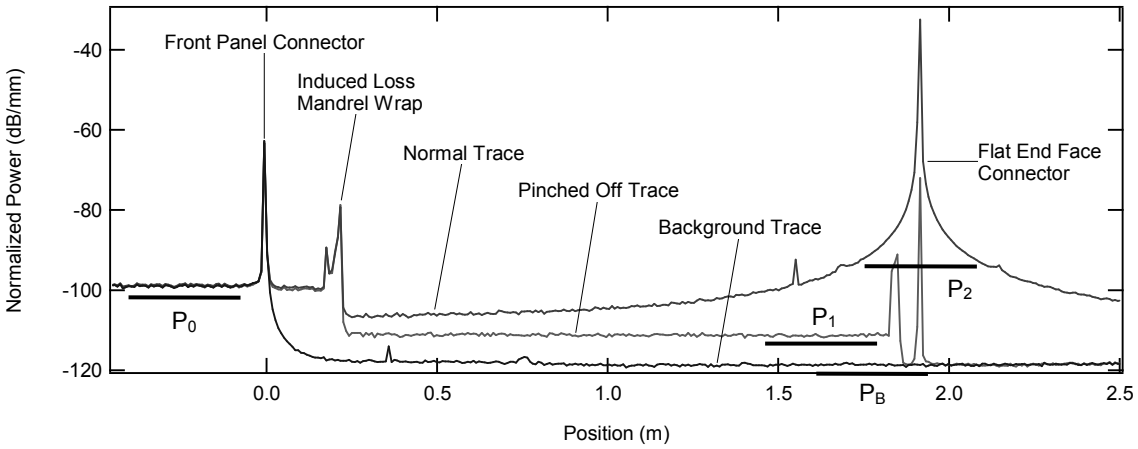

Fig. 2. Sample traces for determining the return loss of a reflection event in the presence of high insertion loss. The four dark lines beneath the traces indicate measurement integration regions for the four measurements.

attenuation caused by the double-pass insertion loss (from the front panel connection and the mandrel-wrap) between P_0 and P_1. Both P_0 and P_1 are measured using the pinched-off trace. If the attenuation is large, it is also necessary to record a value of the background noise level, P_B, by placing measuring the power in the background trace near the locations where P_1 and P_2 are recorded. The expressions describing P_0 and P_1 are,

$$P_0 = P_{RA} + P_B \tag{2}$$

and

$$P_1 = P_{RA} / A + P_B . \tag{3}$$

The power returned from the reflection event P_2 is recorded using the unaltered trace over a span of data centered on the reflection event. In addition to the power from the ST reflection P_{ST}, this measurement will also contain components due to P_{RA} and P_B. P_2 is, then, expressed as:

$$P_2 = \left(P_{ST} + P_{RA} \big/ 2 \right) / A + P_B \tag{4}$$

Using these equations, the IL of the loss events and the RL of the ST connector can be calculated as

$$IL = 10\log(A)/2 = 5\log\left(\frac{P_0 - P_B}{P_1 - P_B}\right) \tag{5}$$

and

$$RL = -10\log(P_{ST}) = -10\log\left(\frac{P_0 - P_B}{P_1 - P_B}(P_2 - P_B) - (P_0 - P_B)/2\right). \tag{6}$$

To demonstrate that the return loss value is repeatable even with high insertion loss, the RL was calculated for the ST connector described above with varying numbers of wraps around a mandrel. The recorded reflection traces without the pinch off applied for each attenuation level are shown in Fig. 3. The results of the measurements are shown in Table 1. The resulting standard deviation for the RL calculation over a range of insertion losses from 0.79 to 14.65 dB was only 0.05 dB.

To demonstrate the repeatability between instruments, RL measurements were taken on a set of seven carefully polished flat end face connectors using four different instruments. The insertion loss at the front panel connection for these measurements was generally less than 0.5 dB. The results are presented in Table 2. The standard deviation is a measure of the combined variations of the RL measurement and the instrument calibration procedure and is equal to or less than 0.15 dB.

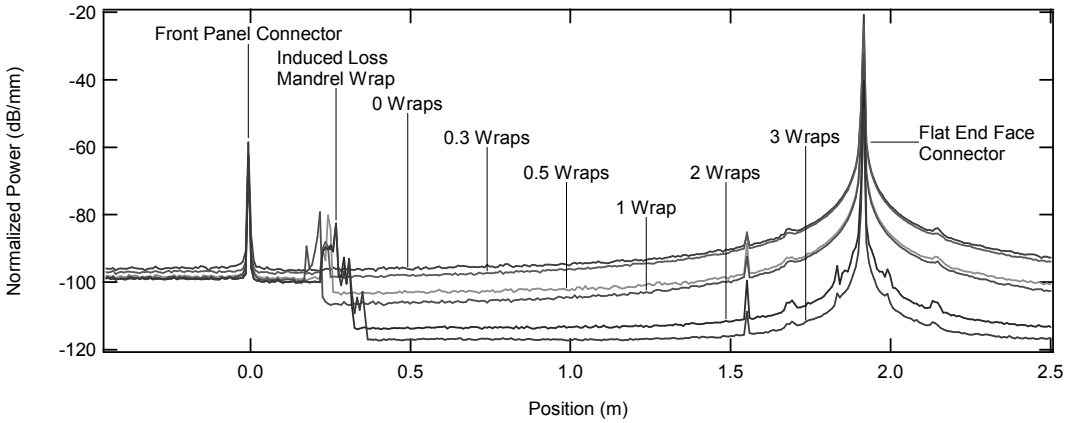

Fig. 3. Traces of a reflection event with varying amounts of insertion loss.

Table 1. Return Loss measurements for the same component for a wide range of Insertion Loss.

	Relative Power Level Measurements				Results	
Mandrel Wraps	P_0 (dB)	P_1 (dB)	P_2 (dB)	P_B (dB)	Insertion Loss (dB)	Return Loss (dB)
0	-76.45	-78.01	-16.09	-96.31	0.79	14.51
0.3	-76.43	-81.20	-19.42	-96.31	2.43	14.57
0.5	-76.44	-84.88	-23.19	-96.31	4.36	14.47
1	-76.41	-88.82	-27.76	-96.21	6.62	14.52
2	-76.48	-93.74	-35.29	-96.31	10.36	14.57
3	-76.48	-95.85	-43.91	-96.31	14.65	14.61

Table 2. Return loss values for a set of flat end face connectors for 4 different instruments.

	Return Loss (dB)						
Instrument	Con 1	Con 2	Con 3	Con 4	Con 5	Con 6	Con 7
OBR 7022	14.21	14.19	14.19	14.37	14.10	14.82	14.36
OBR 7071	14.35	14.39	14.48	14.63	14.45	14.97	14.69
OBR 7078	14.37	14.31	14.30	14.56	14.23	15.01	14.59
OBR 7083	14.55	14.46	14.44	14.70	14.37	15.10	14.66
Std. Dev.	0.14	0.12	0.13	0.14	0.15	0.12	0.15

Summary

We have demonstrated that an OFDR-based instrument is capable of producing repeatable RL measurements even for wildly different values of the insertion loss in close proximity to the reflection event. This capability greatly adds to the utility of the measurement, as the uncertainty due to the insertion loss at the connection to the instrument is eliminated. Additionally, we have shown that our instrument calibration procedure, which ties the RL values for a reference set of flat end face fiber reflectors to the Rayleigh backscatter level for a fiber segment inside the instrument, produces consistent results between instruments. Establishing the consistency of the precise level of the fiber Rayleigh scatter for fiber manufactured under very tight tolerances may eventually allow its use as a widely available, inexpensive, and stable return loss calibration artifact. These are preliminary results and are expected to improve as we continue to refine the calibration process for absolute return-loss measurement.

References

[1] IEC 61300-3-6, Second Edition, "Basic test and measurement procedures - Part 3-6: Examinations and Measurements - Return Loss," 2002.
[2] J. P. von der Weid, R. Passy, and N. Gisin, "Coherent reflectometry of Optical Fiber Amplifiers," *IEEE Photon. Tech. Lett.* **9**, 1253-1255 (1997).
[3] M. Froggatt, B. Soller, D. Gifford, and M. Wolfe, "Correlation and keying of Rayleigh scatter for loss and temperature sensing in parallel optical networks," *OFC Technical Digest*, Los Angeles, March, 2004, paper PDP 17.
[4] U. Glombitza and E. Brinkmeyer, "Optical frequency domain reflectometry for characterization of single-mode integrated optical waveguides," *J. Lightwave Tech.* **11**, 1377-1384 (1993).
[5] J. P. von der Weid, R. Passy, G. Mussi, and N. Gisin, "On the characterization of optical fiber network components with optical frequency domain reflectometry," *J. Lightwave Tech.* **15**, 1131-1141 (1997).
[6] B. J. Soller, M. Wolfe, M. E. Froggatt, "Polarization resolved measurement of Rayleigh backscatter in fiber-optic components," OFC Technical Digest, Los Angeles, March, 2005, paper NWD3.

High-Power Nonlinearity of Optical Fiber Power Meters for Pump Lasers at 980 and 1480 nm

I. Vayshenker and S. Yang
Optoelectronics Division, National Institute of Standards and Technology, 325 Broadway, Boulder, Colorado 80305

R. Swafford
OZ Optics Ltd., 219 Westbrook Rd., Carp, Ontario, K0A 1L0OZ Optics, Canada

Abstract

We describe the nonlinearity of optical fiber power meters at wavelengths of 980 and 1480 nm up to 2 W. We also describe two measurement systems that are based on the triplet superposition method.

1. Introduction

Erbium-Doped Fiber Amplifiers (EDFAs) have revolutionized the field of optical telecommunications. An EDFA uses high-power pump lasers at 980 and 1480 nm. These pump lasers require an accurate measurement of optical power. Current optical fiber power meters (OFPMs) are capable of measuring powers exceeding several watts in an optical fiber. As the demand for higher powers increases, the measurement of OFPM nonlinearity becomes very important. Optical power meter nonlinearity is defined as the relative difference between the response at an arbitrary power and the response at the reference power [1]. While the calibration of an OFPM gives the true input power from the OFPM output reading at the calibration point, the measurement of nonlinearity together with calibration provides the input vs. output relationship at any power for the whole dynamic range of the OFPM. The nonlinearity of some OFPMs could have spectral dependence [2]. This paper also discusses this issue in Section 2.

1.1. Correction factor for nonlinearity and range discontinuity

The true input power P is obtained from an OFPM reading V by

$$P = \frac{V}{F_c CF(P)}, \tag{1}$$

where $F_c = V_c/P_c$ is the calibration factor and CF(P) is a correction factor due to nonlinearity and range discontinuity of the OFPM.

2. Measurement systems and results

To measure the nonlinearity of OFPMs we have built two measurement systems at 980 and 1480 nm. We have based the operation of our systems on the triplet superposition method [3,4], which relies on the principle that, for a linear power meter, the sum of meter outputs corresponding to inputs from two single beams should equal the output when both beams are combined and incident on the meter at the same time. A basic measurement system for both 980 and 1480 nm is depicted in Fig. 1 and described below. Each laser is a laser diode in a butterfly package with an integrated thermoelectric cooler, monitor photodiode, and thermistor. The laser diode is used in a constant-power regime. The output fiber of the first laser diode is aligned with a high-power collimator that produces a beam diameter of approximately 6 mm

(for 980 nm) and 3 mm (for 1480 nm). This beam then propagates through a high-power optical shutter. The shutter is a rotary solenoid with a beam blocker mounted onto the shaft. When the shutter is activated, the beam blocker is removed from the optical path, enabling the beam to pass through.

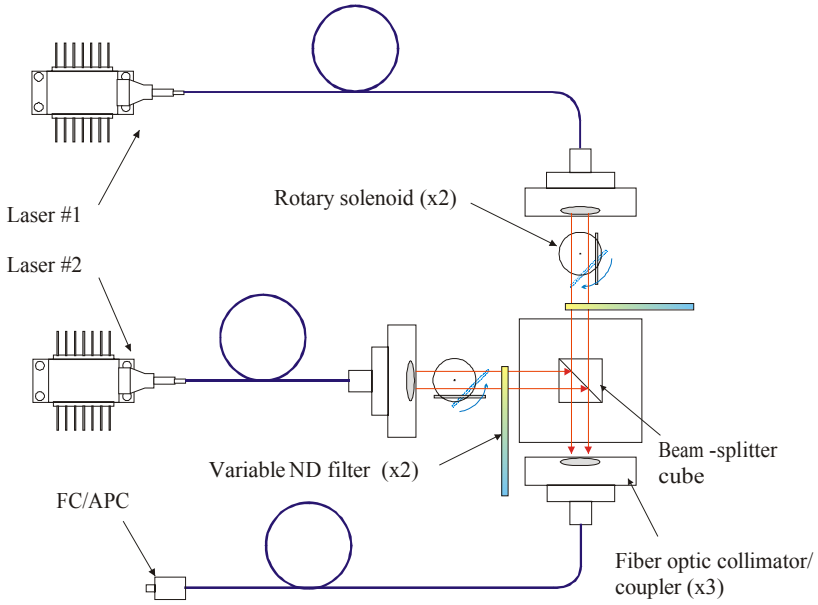

Fig. 1. Measurement system.

The beam then passes through a linear, variable neutral density (ND) filter. The filter density is variable from 0 to approximately 30 dB (for 980 nm) and 40 dB (for 1480 nm). The filter is mounted on a linear translation stage and is driven by a combination of servo motor and encoder. The beam then enters the beam splitter and propagates to the high-power output coupler where the beam is coupled into the output fiber. This fiber is routed to the outside of the case via a 3 mm stainless-steel armored cable (for safety) and is terminated with an FC/APC connector. The second laser transmits, via an identical system, to the beam splitter. The measurement system at 980 nm described in [3] does not use polarization maintaining (PM) fibers; the measurement system at 1480 nm uses lasers with PM fiber pigtails.

The measurements are performed by taking sets of three power readings from the test OFPM: (1) shutter 1 is open and shutter 2 is closed, (2) shutter 1 is closed and shutter 2 is open, and (3) both shutters are open. This sequence is then repeated at different powers. The high-power nonlinearity systems described here and in [3] use two lasers whose center wavelengths are separated by several tenths of a nanometer. Two lasers produce enough power to calibrate high-power OFPMs and compensate for the insertion loss of the system. In contrast, the low-power nonlinearity system in [4,5] uses only one laser whose radiation is divided into two paths.

Fig. 2 and 3 depict correction factors obtained for two commercially available high-power OFPMs, labeled #1 and #2 at 980 and 1480 nm. **Note:** the reference power (where the correction factor is 1) is chosen to be 100 mW (at 980 nm) and 1 mW (at 1480 nm). Each data group (line) represents a separate power range of the meter. At 980 nm, the total nonlinearity of OFPM#2 is approximately 3.5 %, while the total nonlinearity of the OFPM#1 is about 0.5 % for powers from several milliwatts to several watts. At 1480 nm, the total nonlinearity of the OFPM#2 is approximately 1.4 % while the total nonlinearity of the OFPM#1 is less than 0.25 % for powers from 0.2 mW to 0.6 W. Figs. 2 and 3 show that the OFPM#1 is more linear (approximately 7 times) than the OFPM#2 at both 980 and 1480 nm.

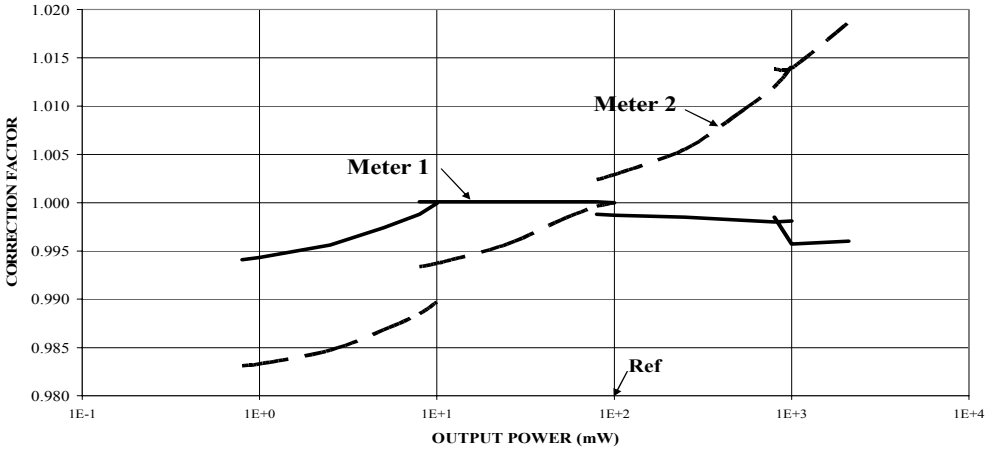

Fig. 2. Correction factor vs. output power at 980 nm.

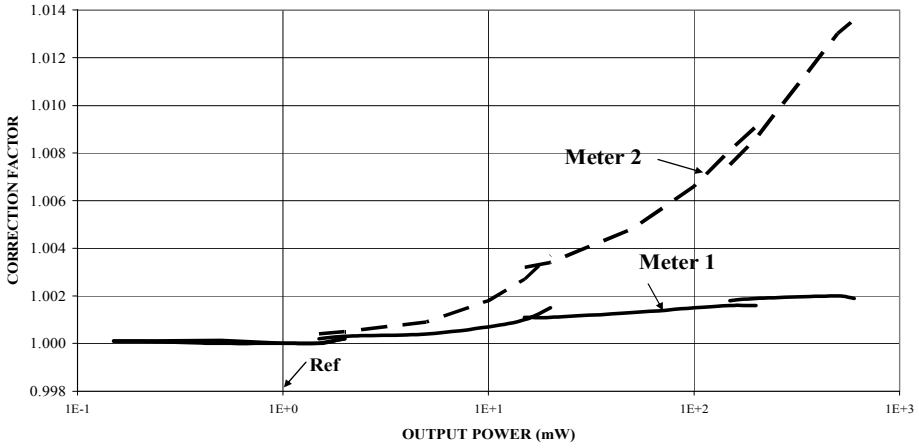

Fig. 3. Correction factor vs. output power at 1480 nm.

3. Conclusions

We have designed and built two nonlinearity systems that allow obtaining correction factors for OFPMs at high powers at 980 and 1480 nm. We showed that the nonlinearity for a given OFPM has spectral dependence at 980 and 1480 nm. Therefore, a user should not assume that if an OFPM were linear at one wavelength, the OFPM would be linear at a different wavelength. The nonlinearity systems are important to characterize OFPMs at high powers. Similar systems could be built at other telecommunication wavelengths and higher powers.

4. References

1. International standard, IEC 61315, Calibration of fibre optic power meters, Ed. 2.0, International Electrotechnical Commission, Geneva, Switzerland, to be released.

2. Boivin, L.P, "Automated absolute and relative spectral linearity measurements on photovoltaic detectors," Metrologia 1993, 30, 355-360.

3. I. Vayshenker, R. Swafford, and S. Yang, "High-power nonlinearity of optical fiber power meters," Natl. Inst. Stand. Technol. Spec. Publ. 1024, 145-148, 2004.

4. I. Vayshenker, S. Yang, X. Li, T. R. Scott, and C. L. Cromer, “Optical fiber power meter nonlinearity calibrations at NIST,” NIST Special Publication 250-56, 2000.

5. I. Vayshenker, S. Yang, X. Li, and T.R. Scott, "Automated measurement of nonlinearity of optical fiber power meters," Proc. SPIE, Vol. 2550, pp. 12-19, San Diego, CA, July 11-12, 1995.

Novel Approach for Non-Intrusive "Clip-on" Fiber Monitoring

Gang HE, Daniel GARIÉPY, Hongxin CHEN, Jean THÉBERGE,
and **Gregory W. SCHINN**
EXFO Electro-Optical Engineering, Inc; 400 av Godin, Québec QC G1M 2K2
CANADA

Abstract: We describe a previously unappreciated "universal" behavior of macrobend-induced loss in singlemode optical fiber. We propose that this could be exploited in a "clip-on"-type instrument that can detect qualitatively and quantitatively the presence of power propagating in an optical fiber or cable, while at the same time essentially guaranteeing that the induced insertion loss on the propagating signal will be a small, known value, independent of signal wavelength or fiber type.

It is often necessary to detect a signal in an optical fiber by extracting a portion of the guided light. For example, one often wishes to be able to distinguish between live (signal carrying) and dark (no signal) fibers, to extract a signal for sampling (e.g. to detect a modulation tone for identification purposes), to perform an approximate measurement of the guided optical power, to perform accurate differential measurement of the guided optical power before and after a possible localized loss such as a splice, and to determine the direction of traffic. It is desirable to perform these operations without disrupting, overly attenuating or distorting the signal, especially in telecommunications systems, as the margins with which many such systems operate sometimes do not permit more than about 1 dB of additional attenuation without the risk of inducing errors on the signal.

It is well known that light can be extracted from an optical fiber by inducing a "macrobend" (i.e. a bend whose radius of curvature is much larger than the fiber diameter) so that a fraction of the propagating light escapes through the cladding [1-4]. The fraction of this extracted light with respect to the total light in the fiber core is known as the "insertion loss" (IL) or "bending loss". When such a macrobend is applied to a fiber, a non-negligible fraction of light may leak out and be detected even if the fiber is cabled, since most buffer and jacket materials are partially transparent at the near-infrared wavelengths used in telecommunications applications. Typical cables found in central offices and outside plant applications frequently use 3-mm- or 1.6-mm-diameter jackets, filler material and a nominal 900-μm buffer about the optical fiber, or simply a 900-μm tight buffer. In addition, one frequently also needs to measure light in 250-μm-diameter acrylate coated fibers.

For a given fiber, the degree of macrobending required to detect a certain amount of leaked light is strongly wavelength dependent: Less bending is required for longer wavelengths and more bending is required for shorter wavelengths. As well, if one wishes to determine the absolute power propagating in the fiber, it is necessary to "know" the induced insertion loss. Moreover, for a given wavelength and macrobend angle, the required detection sensitivity depends upon the fiber type (e.g. standard step-index, depressed clad, etc.) and the types and colors of the coating and jackets protecting the fiber. Clearly, if the propagating signal power is low, and/or if the absorption of the coatings and/or jackets is high, it is desirable to bend the fiber to a relatively tight radius so as to extract as much signal as possible for detection, while remaining well below the loss margin of the system. It is desirable, therefore, to control the bending radius carefully.

A number of commercial clip-on devices exist today that are based upon a fixed-bending structure, i.e. where the bend radius is not changed during the measurement. A disadvantage of this approach is that the insertion loss caused by this fixed macrobending is strongly dependent

upon wavelength, making it impractical to optimize both the IL and sensitivity when the wavelength of the propagating light could be, say, 1310 or 1550nm. Generally, commercial devices choose a bending radius such that the loss at 1310nm is "just" detectable, and the loss at 1550nm is "not too high". However, this induced insertion loss can vary significantly, even at the same wavelength and jacket type, if the fiber type is different.

We report here a new approach that can be applied to a fiber clip-on device that induces a small, known insertion loss, largely independent of signal wavelength, fiber type, or jacket and buffer material. This approach is based upon what appears to be a hitherto little appreciated property of all singlemode optical fibers, namely, that curves representing the rate of change of IL with respect to the macrobend radius R [i.e. d(IL)/dR)], when plotted as a function of IL, are essentially the same for any singlemode fiber type and wavelength.

The measurement setup used to confirm this behavior is shown conceptually in Fig. 1. An optical fiber (or cable) is held in appropriate clamps and the fiber (or cable) is bent in a controlled fashion from an angle of 180 degrees (i.e. no bend, or $R = \infty$) to about 120 degrees, or until the IL became excessive. (Note that in practice, it is generally more convenient to measure a bending angle than the bending radius, although the two are of course directly related.) Care is taken to ensure that the "interaction length", that is the portion of the fiber that is bent, is held approximately constant as the angle is changed. The optical power launched into the fiber, P_{in}, and the optical power propagating through the macrobend and subsequently exiting the fiber (after a short distance, so that the inherent fiber attenuation is negligible), P_{out}, are measured with a standard power meter, as a function of macrobend angle. The insertion loss is defined as IL (dB) = $10\log (P_{out}/ P_{in})$.

Figure 2 shows curves representing IL as a function of angle, for a wide variety of fiber and cable types, and at different wavelengths. One observes that, for a given IL (e.g. -0.7 dB), the slopes of all the curves are approximately constant. This can be seen more explicitly in Figure 3, where the derivatives of these same curves with respect to angle are presented as a function of IL Although there is some spread in the curves according to fiber type, etc., they exhibit a remarkably similar dependence.

From Fig. 3, it can be seen that if one were to monitor only the slope $d(IL)/d\theta$ as the macrobend angle θ were varied, one could ensure that the macrobend-induced loss could be set to fall into, for instance, the range -0.7 ±0.2 dB, independent of the fiber type, wavelength, etc. (Note that in Fig. 3, the independent variable is plotted along the ordinate, whereas the dependent variable is along the abscissa.)

Of course, the underlying motivation for using a clip-on device is to avoid having to measure P_{in} and P_{out} , since these are not normally accessible parameters in practical measurement situations. Only the light escaping from the fiber core, P_e, or a fraction thereof, is available for the measurement.

There is a well-defined relationship between the IL and the power escaping from the fiber core, P_e , which obtains from $P_e = P_{in} – P_{out}$. Expressing P_e and P_{in} in dBm units, and IL in dB, one has

$$P_e = EF + Pin$$

where

$$EF = 10*\log (1- 10^{(IL/10)}) .$$

This can be recast as:

$$\Delta P_e = EF'\Delta IL,$$

where EF' is the derivative of EF with respect to IL.

If one could measure P_e as a function of macrobend angle, one could then plot $dP_e/d\theta$ versus IL and obtain another "universal" curve analogous to that in Fig. 3. Although in practice the photodetector D_1 only detects a fraction of the total escaping light and hence one cannot directly measure P_e, the fact that we are dealing with derivatives of logarithmic quantities renders the results insensitive to collection efficiency to first order. Hence, if the detector in a clip-on device monitors a portion of the escaping light as the bend angle is adjusted (while maintaining a constant interaction length), one can still determine the derivative $dP_e/d\Theta$ as a function of bend angle. (Conveniently, a small dithering of the bend angle could be applied to obtain this derivative directly.)

Figure 4 shows the $dP_e/d\Theta$ vs IL curves for a series of selected fibers with different fiber types and jacket types on both 1310nm and 1550nm. For example, if one wishes to maintain a constant insertion loss of -0.7 ± 0.2 dB, one sets the macrobend angle such that $dP_e/d\Theta$ = -0.9 dB/deg.

In conclusion, we have presented a principle that could serve as the basis for a new generation of "non-intrusive" clip-on instruments for signal monitoring or power measurement. These instruments would be able to essentially guarantee that an excessive bending loss would never be applied to the fiber, independent of its fiber type, jacket, or the propagating wavelength.

References:

1. B.D. Campbell et al, US Patent 4,586,783: "Signal coupler for buffered optical fibers", issued May 6, 1986.
2. S.M. James, "Non-intrusive optical fibre identification using a high-efficiency macrobending `clip-on' optical component", Elec. Lett. 24, 1221-22 (1988).
3. Larry R. Cox, European Patent EP 0639762B1: "Fiber identifier", issued Feb. 22, 1995.
4. Vincent C. So et al, US Patent 4,671,653: "Test instrument for an optical fiber", issued Jun. 9, 1987.

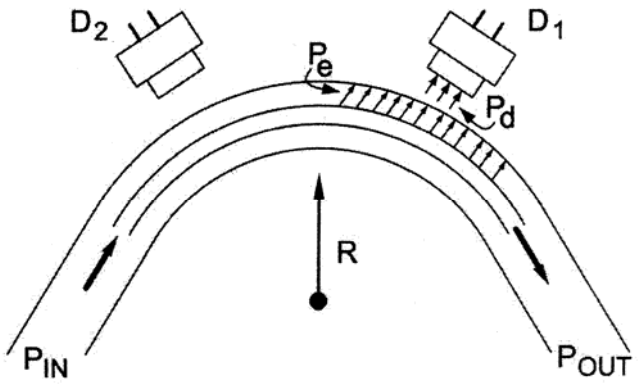

Fig. 1. Schematic illustrating the "clip-on" principle.

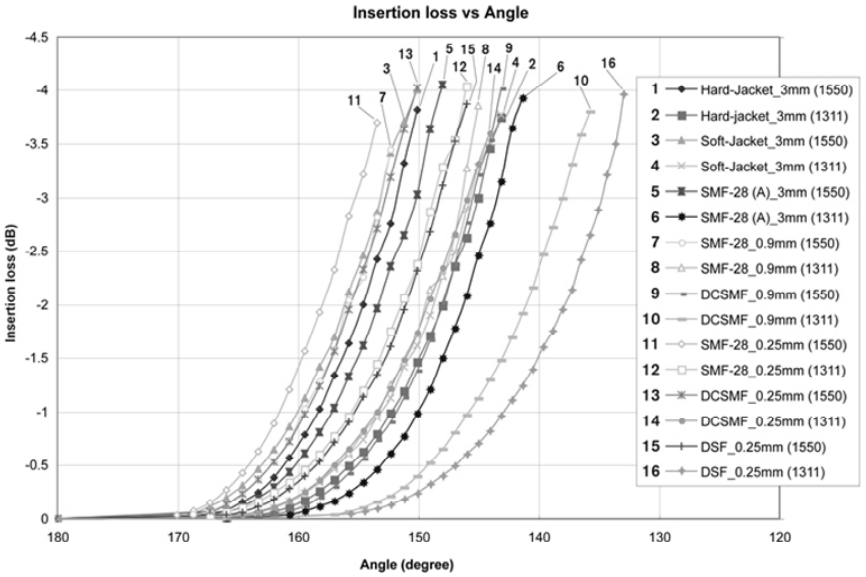

Fig. 2. Measurement data of insertion loss (in dB) versus macrobend angle for a variety of fiber types, jacket and buffer types, and wavelengths of 1311 and 1550nm. (DCSMF: Depressed cladding singlemode fiber; DSF: Dispersion shifted fiber.) This insertion loss was determined by directly measuring P_{out} and P_{in} as a function of angle.

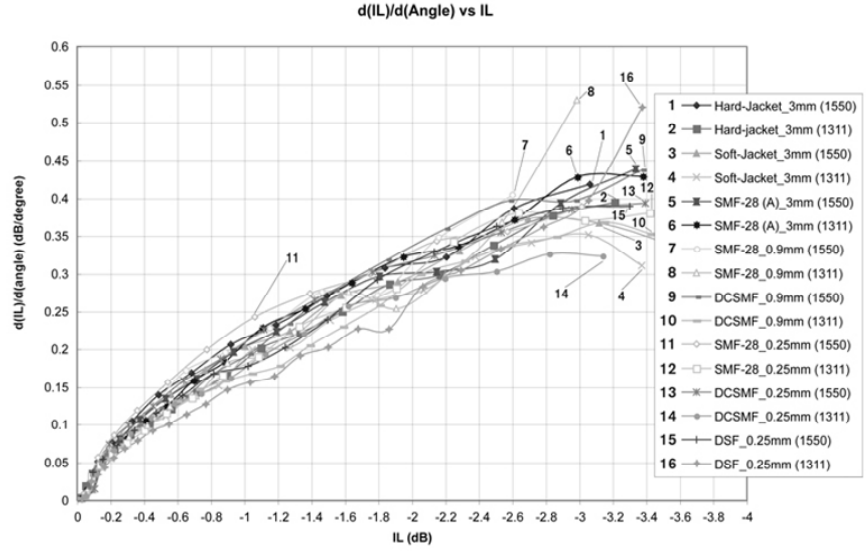

Fig. 3. Derivative d(IL)/dθ of data in Fig.2, but plotted against IL.

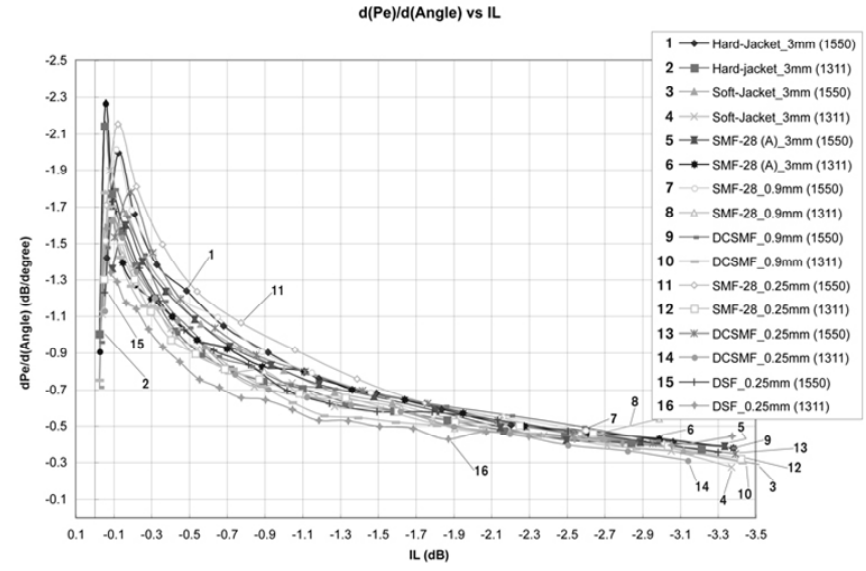

Fig. 4. The derivative $dP_e/d\theta$ vs IL, determined by measuring the escaping power (for each of the data points in Fig. 2) with detector D_1 and plotted against the directly measured IL.

Measurement technique for Stimulated Brillouin Scattering threshold

Per Olof Hedekvist and Anne Andersson
SP, Swedish National Testing and Research Institute
Box 857, SE 50115 Borås, Sweden
Per.olof.hedekvist@sp.se

Abstract

We propose a new technique to measure the SBS critical power. Preliminary results show anticipated effects, and accuracy and repeatability is under investigation. The technique is easy to automate, for simplified multiple fiber testing.

Introduction

The evolving technique for developing optical fibers with tailored properties arise a request for straight-forward characterization methods. Several fibers are manufactured with decreased nonlinearity for transmission of data at high power levels, e.g. the Large Effective Area Fiber (LEAF) [1]. In addition new highly nonlinear fibers, to be used in all-optical processing, are developed with suppressed SBS critical power [2]. There is a huge benefit if this power level could be easily characterized for a batch of fibers, to enable quality control as well as optimized choice of fibers for an installation. This paper addresses this issue, and present results from an ongoing project on measurement technique for accurate estimation of the SBS critical power.

Technique description

The fundamental requirement for the technique is to be reproducible and easily automated. The traditional technique includes cw light launched into the fiber, and the backscattered light measured vs the input power level. This technique was used to present the appearance of SBS in 1972, and is still widely used in scientific work [3].Even though this technique may be adequate with some addition of measurement analysis, it will be influenced e.g. by the thermal noise of the detectors. Furthermore, there are no parameters to adjust for increased interpolation accuracy.

If the input light is modulated with a square wave at small modulation depth, the thermal background can be filtered off. The modulation frequency must be faster than the recombination time of the Erbium doped amplifier, if this is used, but slower than the Brillouin frequency (50 MHz). The modulation depth should be as small as possible, however large enough to still achieve a distinct readout of the critical power.

The fiber under test, FUT, should be connected to the modulated light source, and both launched and reflected light is detected in detectors with a bandwidth exceeding the modulation frequency. For a traceable accuracy, the launched light must be detected in a calibrated device. The important parameters are the high-level of the launched light, and the modulation energy in the back-scattered light. At lower levels, Rayleigh scattering will dominate, but when the high-level reaches the SBS-threshold, the modulation energy will increase. From the second derivative of the measured trace of modulation energy vs launched high-level, the SBS-threshold appears as a peak.

Experiment and results

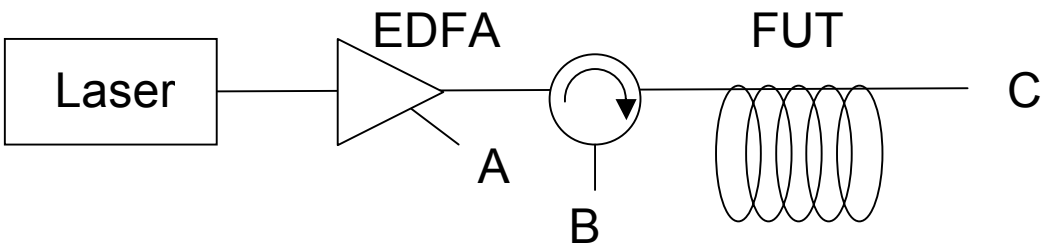

Figure 1: Experimental setup

Figure 1 shows the experimental setup. A narrowband laser is amplified in an Erbium Doped Fiber Amplifier (EDFA) with variable output power, and a calibrated power monitor (A). The solution with a circulator for reflection to (B) is used to avoid influence of reflection in port A, as would be the case with a 2x2 power splitter. Nevertheless, port C at the output of the fiber under t est, FUT, must be prepared to avoid reflections, especially if the fiber length is less than the effective length of the fiber (≈ 20 km for standard single mode fiber).

$$L_{eff} = \left(1 - e^{-\alpha L}\right) / \alpha$$

The first preliminary results of the technique are shown in figure 2, where the FUT was a 25 km standard SMF. The modulation depth is 10% and the oscilloscope trace shows the backscattered light when the high-level is above the SBS-threshold and the low-level is below. The signal will then be filtered in a narrow bandpass filter, and analyzed with respect to the high-level of the launched light. The launched power level into the fiber, calculated from the readout of the photodetector at position A, was 12.5 dBm, indicating an SBS critcal power between 16.9 and 18.7 mW. Through further measurements, including smaller modulation depth and power scanning, in addition to analysis with second derivative of the backscattered power, the accuracy can be improved substantially.

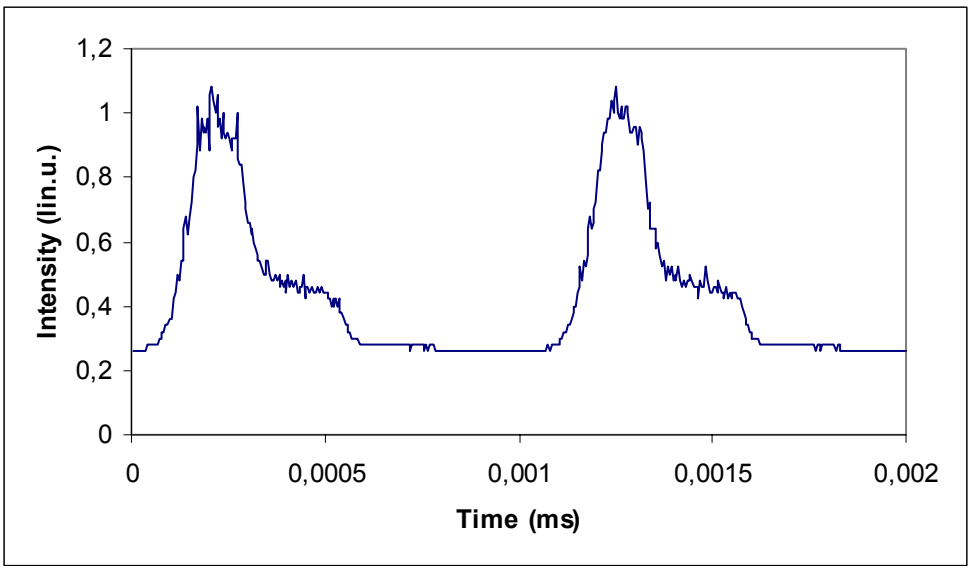

Figure 2: Measured return response of the fiber

The detected trace resembles the response detected by Ippen et al [4], with the difference that the modulation depth is used as a variable, while the reference used 100 % modulation

Conclusion

A new technique for automated fiber testing is proposed, quantifying the SBS critical power. The technique differs from previously presented work through the modulation of the input sugnal, and is easy to automate. It will therefore be suitable for production testing.

The paper describes work in progress, and further results will be presented regarding analysis algorithms and measurement accuracy.

References:

1. "Dispersion-shifted large-effective-area fiber for amplified high-capacity long-distance systems", Liu, Y.-M.; Antos, A.J., *Conference on Optical Fiber Communication. OFC 97*, pp. 69-70, 16-21 Feb. 1997.
2. "New dispersion decreasing fiber with high SBS threshold for nonlinear signal processing", Li, M.-J.; Li, S.; Nolan, D.A.; Achmetshin, U.G.; Bubnov, M.M.; Guryanov, A.N.; Dianov, E.M.; Khopin, V.F.; Sysoliatin, A.A. *Optical Fiber Communication Conference, OFC 2005.* Volume 5, 6-11 March 2005 Page(s):3
3. "Observation of Stimulated Brillouin Scattering in low-loss silica fibre at 1.3 μm", D.Cotter, *Electron. Lett*. Volume 18, pp. 495-496, 1982.
4. "Stimulated Brillouin Scattering in optical fibers", E.P. Ippen, and R.H. Stolen, *Appl. Phys. Lett.* Volume 21. pp. 539-541, 1972

Butt-joint splice with refractive index matching material for high power light in optical fiber communications

Ikutaro Ogushi, Hisashi Izumita, Kuniaki Tanaka, Fumihiko Ito, and Masahito Arii
NTT Access Network Service Systems Laboratories, NTT Corporation.
Hanabatake 1-7-1, Tsukuba, Ibaraki 305-0805, Japan
Tel:+81-29-868-6350, Fax:+81-29-868-6360, E-mail:ogushi@ansl.ntt.co.jp

Abstract

We demonstrated the temporal loss increase of a butt-joint splice with refractive index matching material when using a high power light for optical fiber communication systems. The temporal degradation at the splice as a function of the high launched power arises from the refractive index change caused by the thermo-optic effect. We also proposed the design of a butt-joint splice for high power light by diffusing the heat. Our method reduced the loss increase by 2.3 dB for d = 100 μm and P_{in} = 1 W.

1. Introduction

Recently, the optical power in optical communication systems has been increasing rapidly through the use of wavelength division multiplexing (WDM) and distributed Raman amplification (DRA) technologies. When DRA is applied to WDM systems, a high power light of as much as several watts is launched into optical fibers and devices. This makes it important to know how these optical fibers and devices behave under such high power light input conditions.

In the optical communication systems using high power light, we have to undertake safety engineering to avoid the hazards that the optical power may induce. We must take account of various problems caused by high power light. For example, there is the fiber fuse phenomenon [1], the high power performance of single-mode connectors [2], the influence of a high power light launched into optical fibers in an MT connector [3], the reliability of optical fiber [4, 5] and the optical fiber cord destruction process [6]. The light from optical transmitters is launched into the optical fiber distribution systems in a central office, and is hardly attenuated. So, we must clarify the performance and design of the optical devices of the optical distribution system in a central office for high power light input. The devices are fiber selectors, which are installed in fiber line testing systems, or MT connectors and mechanical splices, which are employed in connection splices. These devices have a butt-joint splice connection mechanism, which often has a function for reducing Fresnel reflection and suppressing optical connection loss by using refractive index matching material [7, 8], for example, silicone oil, silicone resin, or glycerin. In a previous work, we described the optical loss and temperature increase at a butt-joint splice with refractive index matching material when there was a large gap between the two fiber endfaces and a high power light input, and we reported that air bubbles (or oxygen) in the refractive index matching material may cause catastrophic damage [9].

In this paper, we launch a high power light into a butt-joint splice with refractive index matching material and demonstrate its characteristics of the splice. We found temporal degradation at the splice as a function of the launched high power arose from the refractive index change caused by the thermo-optic. We also proposed the design of the butt-joint splice by diffusing the heat.

2. Characteristics of butt-joint splice with refractive index matching material inducing the high power light

Figure 1 shows our experimental setup for exposing a butt-joint splice connection to high power light. We used a laser operated at a wavelength of 1.55 μm and in the CW mode and an EDFA as the high power optical source. We used a V-groove to connect the fibers. The gaps (d) between the two fiber endfaces on the V-groove were 10, 30, 50 and 100 μm. We employed fusion splices for all the splice connections other than the butt-joint splice connection to avoid a fiber fuse and to reduce the connection loss and reflection.

Figure 2 shows the relationship between input power (P_{in}) and exposure time. We launched a constant high power light for 10 minutes and changed the optical power at a rate of ±500 mW/min. The constant optical powers were 250, 500, 1000, 1500, and 2000 mW. In order to investigate the change in the characteristics

against input power at the splice, we measured the optical loss, optical loss fluctuations and maximum temperature changes with and without refractive index matching material on high power input. The optical loss fluctuations were measured by using a digital oscilloscope with an O/E converter via 99:1 couplers as the input power was changed. The temperature change and distribution of the tested butt-joint splice connection were measured with infrared thermography. We used silicone oil, which is commonly used in fiber selectors and MT connectors, as the refractive index matching material.

Figure 3 shows the measured optical loss in the splice with refractive index matching material. In Fig. 3, at 2000 mW and d = 100 μm, the optical loss reached its maximum value of 11.6 dB. The difference between the maximum and minimum optical loss values at d = 10 μm was small (less than 0.3 dB), but at d = 100 μm, it was strongly dependent on the input power P_{in}. We found that the optical losses with the refractive index matching material depended on d and the input power P_{in} and their characteristics were reversible. The measured output power at the splice with refractive index matching material was saturated against the increased optical power when the optical power was increased at the larger gaps (d). These measured optical losses were larger than those calculated using the conventional formula for optical connection loss [10].

Figure 4 shows temperature distribution at the splice with d = 50 μm (a) at 250 mW and (b) 2000 mW. Compared with Fig. 4 (a), there was the clear temperature rise at the splice in Fig. 4 (b). The maximum value of temperature rise was 15.3 °C, and the measured optical loss was 7.0 dB, respectively. The temperature of the refractive index matching material rose as the optical loss increased. As with the optical loss characteristics, the temperature characteristics are reversible. It should be noted that the characteristics of the optical loss increase and temperature rise were reversible and were related each other.

3. Reduction of the optical loss increase due to the thermo-optic effect

The optical loss increase was caused by the temperature increase induced by the high power light. Heat generated by the energy absorbed by the refractive index matching material resulted in a radial thermal gradient, and this led to the distribution of the refractive index in the medium. Using the thermal coefficient $\delta n/\delta T$, a radial refractive index can be derived from the temperature distribution according to

$$n(r) = n_0 + \frac{\delta n}{\delta T}[T(r) - T(0)]$$

where n_0 is the refractive index of silicone oil at r = 0, and $T(r)$ is the radial temperature when the light is launched into refractive index matching material. The thermal coefficient $\delta n/\delta T$ of silicone oil is negative [8] and the temperature distribution plotted in a temperature curve becomes $T(r) > T(0)$. The refractive index distribution of silicone oil has a radial refractive index gradient. This phenomenon is the thermo-optic effect [11]. The refractive index matching material with the radial refractive index gradient behaves like an irradiated lens. As a result, the light propagating in the refractive index matching material degraded, and optical power input into the output fiber was limited as gap (d) increased.

Here, we propose ways of suppressing the thermo-optic effect by cooling refractive index matching material. One measure involves keeping the temperature constant at the refractive index matching material while the splice is exposed to high power light. We conducted the same experiments at d = 10, 30, 50 and 100 μm while cooling the refractive index matching material exposed to 1 W light in order to suppress the temperature increase. The values for the suppression of the increase in the optical loss were 0.1 dB at 10 μm, 0.1 dB at 30 μm, 1.8 dB at 50 μm and 2.3 dB at 100 μm respectively. These values differ with the calculated values according to the conventional formula for optical connection loss [10], and the optical loss increase can be reduced theoretically. However, we need consider appropriate method and conduct quantitative measurements. There are several ways of using the technique to maintain a refractive index without a radial gradient. One example is to diffuse the heat with convection.

4. Conclusion

We demonstrated the characteristics of a butt-joint splice that employed refractive index matching material. We found that the optical loss and temperature increased temporally and reversibly at the butt-joint splice with

refractive index matching material as the input optical power increased. This degradation was mainly caused by the thermo-optic effect of the radial refractive index gradient dependent temperature. We proposed a simple approach for suppressing any optical loss increase, which involved keeping the temperature constant. This work will contribute to the design of butt-joint splices with refractive index matching material for optical communication systems that operate with high power light.

References

[1] R. Kashyap and K. J. Blow, "Observation of catastrophic self-propelled self-focusing in optical fibres," Electron. Lett., **24**, 47-49, (1988).
[2] M. D. Rosa, J. Carrberry, V. Bhagavatula, K.Wagner and T. Uenoya, "High-power performance of single-mode fiber-optic connectors," J. Lightwave Technol., **20**, 879-885, (2002).
[3] K. Hogari, K. Kurokawa and I. Sankawa, "Influence of high-optical power light launched into optical fibers in MT connector," J. Lightwave Technol., **21**, 3344-3348, (2003).
[4] K. Kurokawa, C. Fukai, J. Zhou, K. Tajima, K. Nakajima, N. Yoshizawa and I. Sankawa, "Long-term reliability of pure silica core single-mode fiber when exposed to high-power laser light," Photon. Technol. Lett., **16**, 1110-1112, (2004).
[5] R. M. Percival, E. S. R. Sikora and R. Wyatt, "Catastrophic damage and accelerated ageing in bent fibres caused by high optical powers," Electron. Lett., **36**, 414-416, (2000).
[6] I. Ogushi, H. Izumita, F. Ito and M. Arii, "Catastrophic damage and destructive process induced in optical fiber cord by 33 dBm pump light at 1480 nm in WDM systems," OFC/NFOEC, OME6 (2005).
[7] C. M. Melliar-Smith, P. D. Lazay, G. A. Pasteur, E. A. Chandross and D. L. Wood, "Index matching fluids for long wavelength (1.2 - 1.6 μm) fiber optic applications," Electron. Lett., **16**, 403-404, (1980).
[8] M. Kihara, S. Nagasawa and T. Tanifuji, "Return loss characteristics of optical fiber connectors," J. Lightwave Technol., **14**, 1986-1991, (1996).
[9] I. Ogushi, H. Izumita, K. Tanaka, F. Ito and M. Arii, "Observation of ignition induced by a high power light input at a butt-joint splice with refractive index matching material, " OFC/NFOEC, OFK6 (2006).
[10] D. Marcuse, "Loss analysis of single-mode fiber splices," Bell Sys. Tech. J, **56**, 718, (1977).
[11] M. D. Rosa, and S. Logunov, "Photothermal behavior of an optical path adhesive used for photonics applications at 1550 nm," Applied Optics., **40**, 6611-6617, (2001).

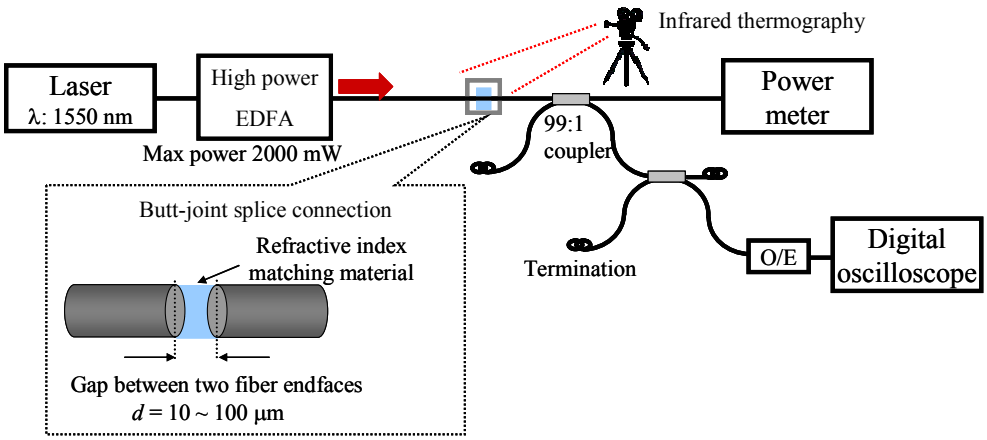

Fig. 1. Experimental setup

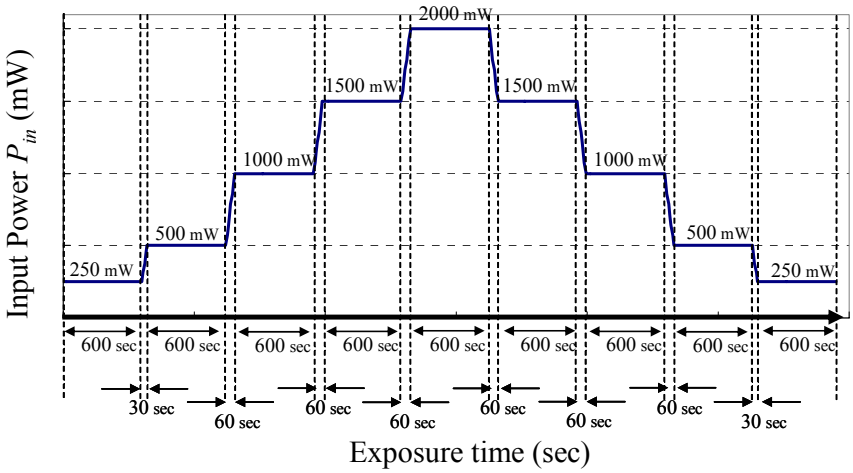

Fig. 2. Input power against exposure time in experiments

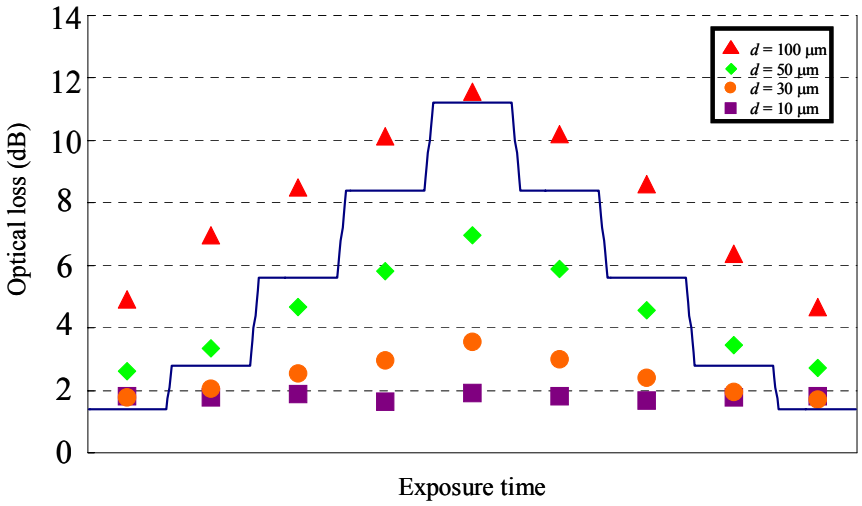

Fig. 3. Measured optical loss in high power light exposure experiments

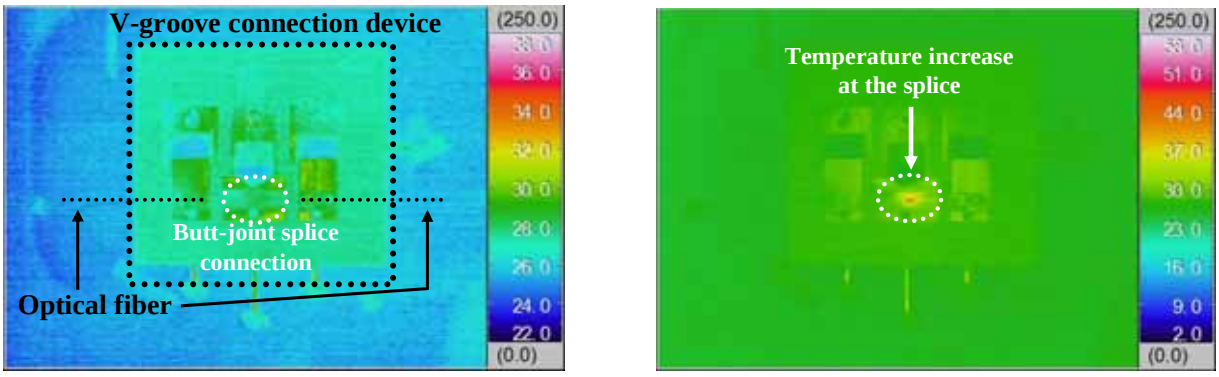

(a) At 250 mW (b) At 2000 mW

Fig. 4. Temperature distribution induced by high power light launched into the butt-joint splice with d = 50 μm

High speed PRBS for detection of defects in fibers and fiber connectors

Rangaswamy. S., Lao, D., and van Doorn, E
Intelligent Automation Inc.
15400 Calhoun Dr, Suite 400
Rockville, MD 20855

Abstract

We present here a high performance OTDR based on Pseudo Random Binary Sequences (PRBS) for solving resolution and dead zone problem associated with fiber and fiber connector inspections. The presented system has the capability of spatial resolution and dynamic range that are compatible with the application and will allow efficient measurement of defects in fiber connectors, independent of the measurement of the airgap reflection. The dynamic range of the system used is 41dB and using components of higher frequency (10 GHz) it could be modified for resolution of 2 cm with atleast 76 dB of dynamic range in a 40ft cable. This capability will allow for independent measurement of airgaps inside connectors, and defect at the backend of the same connectors in aircrafts, and increase the readiness of its fleet at lower cost of ownership.

Introduction

We present here a high performance OTDR based on Pseudo Random Binary Sequence (PRBS) for solving inspection of fibers in dead zones and fiber connectors. In conventional optical time domain reflectometer (OTDR), the impulse response is equivalent to the response of the fiber to a sudden pulse of light. But rather than using a single pulse followed by no injected signal (to listen for echoes), we use a specific binary sequence to detect the reflections from return losses on the fiber. This use of this Pseudo Random Binary Sequence (PRBS) greatly increases the duty cycle of the injected signal, and therefore the ability to average, and achieve great sensitivity. This effect increases with increasing fiber (and sequence) length, but is about a factor of 500 for 30ft fibers inspected with 10Gbit sequences or 100ps pulses!

Rather than injecting a single pulse, and detecting the reflections, we inject a continuous sequence of pulses, and measure the cross correlation between the injected and reflected signals. The impulse response is equivalent to the response of the fiber to a sudden pulse of light, as is the case in conventional OTDR. To do this we first consider the result of a cross-correlation operation between the input and output of a linear system. We then examine this in the case of applying pure Gaussian noise (white noise) to the system as the input signal.

Let $\Psi_{ZY}(\tau)$ be the cross-correlation between the input *Y(t)* and the output *Z(t)* of the system, so that $\Psi_{ZY}(\tau) = 1/T_m \int_0^{T_m} Z(t)Y(t-\tau)dt$. Let $n(t)$ be a random noise function added by the system, so that from the development in the preceding section we can represent the output of the system with system noise as: $Z(t) = \int_0^{\infty} I(\mu)Y(t-\mu)d\mu + n(t)$. That is, we represent the output at t as the convolution of the input with the impulse response function plus the value of the noise at time t. Substituting this expression for $Z(t)$ into the cross-correlation equation, we have:

$$\Psi_{ZY}(\tau) = 1/T_m \int_0^{T_m} \left[\int_0^{\infty} I(\mu) Y(t-\mu)\, d\mu + n(t) \right] Y(t-\tau)\, dt$$

from which, $\Psi_{ZY}(\tau) = \int_0^\infty I(\mu) 1/T_m \int_0^{T_m} Y(t-\mu)Y(t-\tau)dt\,d\mu + \Psi_{nY}(\tau)$, that can be written as $\Psi_{ZY}(\tau) = \int_0^\infty I(\mu)\Psi_{YY}(\tau-\mu) + \Psi_{nY}(\tau)$. Assuming that the system noise is uncorrelated with the input, over many trials $\Psi_{nY}(\tau) \to 0$, and we have finally $\Psi_{ZY}(\tau) = \int_0^\infty I(\mu)\Psi_{YY}(\tau-\mu)$. Now consider the case where the input signal $Y(t)$ is random white noise. The autocorrelation function of random white noise is by definition an impulse over sufficient trials. This may be seen by considering that its correlation with itself is by definition zero except at $\tau = 0$ where it is unity. Therefore we may write $\Psi_{YY}(\tau) = A\delta(\tau)$ where A is some constant. Then, substituting this in the previous development $\Psi_{ZY}(\tau) = \int_0^\infty I(\mu) A\delta(\tau-\mu)d\mu$, which may be written $\Psi_{ZY}(\tau) = A\int_0^\infty I(\mu)\delta(\tau-\mu)d\mu$, which is exactly the convolution of $I(\mu)$ by $\delta(\tau)$ over τ. But we know already that $\delta(\tau) = 0$ if $\tau \neq 0$ and 1 if $\tau = 0$. Therefore, $\Psi_{ZY}(\tau) = AI(\tau)$. Hence the cross-correlation of system input with system output will approximate the system's impulse response function ever more closely over time if the system's input is Gaussian white noise.

Conventional OTDR can also be regarded as a special case of PRBS with only one pulse. In the absence of noise, the performance of PRBS and OTDR would be same. In the presence of random noise and the peak transmit power remaining same PRBS will reduce the noise level. Following the derivation we consider the noise contribution to the correlated output $\Psi_{nY}(\tau) = 1/T_m \int_0^{T_m} n(t)Y(t-\tau)dt$, The noise level is represented by its variance

$$E\left|\Psi_{nY}(\tau)\right|^2 = 1/T_m^2 E\left|\int_0^{T_m} n(t)Y(t-\tau)\,dt\right|^2$$

$$= 1/T_m^2 E\left[\int_0^{T_m}\int_0^{T_m} n(t_1)n(t_2)Y(t_1-\tau)Y(t_2-\tau)\,dt_1 dt_2\right]$$

$$= 1/T_m^2 \int_0^{T_m} E\left|n(t_1)\right|^2 Y^2(t_1-\tau)\,dt_1$$

Since $E\left[n(t_1)n(t_2)\right] = \delta(t_1-t_2)$, $E\left|\Psi_{nY}(\tau)\right|^2 = 1/T_m^2 \int_0^{T_m} E\left|n(t_1)\right|^2 Y^2(t_1-\tau)\,dt_1$

We can assume that $E\left|n(t_1)\right|^2$ is independent of time; and since binary pulses are transmitted, $Y^2(t_1-\tau)$ is constant. Hence $E\left|\Psi_{nY}(\tau)\right|^2 = E\left|n(t_1)\right|^2 Y^2/T_m$. Assuming the pulse width is *T*, and the number of pulses is *N*, then we have T_m=*NT*. We can see the variance of the noise decrease with the increase of *N*.

Comparison of measurements using PRBS and single pulse

The test setup is shown in Figure 1 consists of Anritsu MP 1632C digital data analyzer to generate the PRBS and the signal was sent to the laser that was connected to one end of the 2x1 splitter. The reflected signal was received by the photodiode and amplified and fed to the Tektronix TDS7404B/4M Digital Phosphor oscilloscope. There is no air gap at the connectors. The detector we are using can detect received power as high as 20dBm.

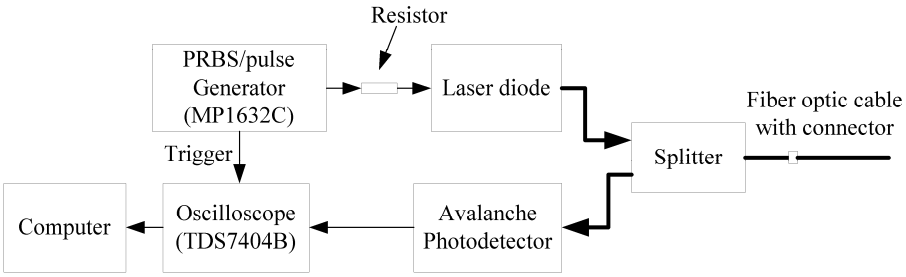

Figure 1: Diagram of the system using PRBS/pulse generator

We compare the performance of using PRBS and a single pulse by measuring the reflection from the end of fiber without reflector. The results are shown in Figure 2. Both curves are obtained by averaging over 64 measurements. We can see the noise floor for results using PRBS is much lower than that using single pulse. This is due to the higher duty cycle of the PRBS.

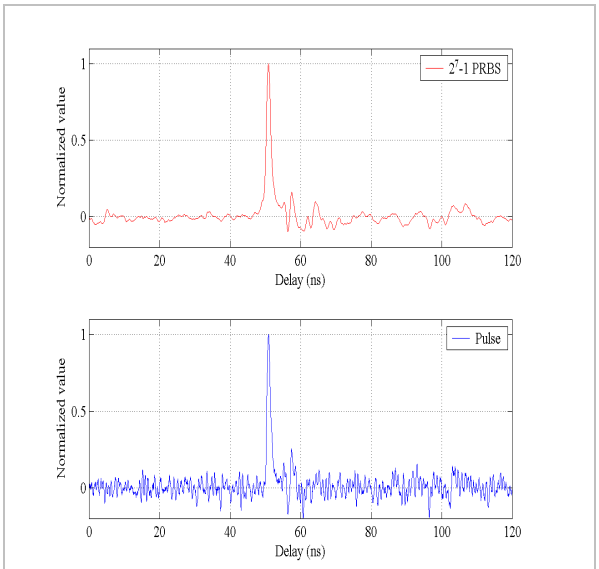

Figure 2: The noise floor using PRBS (top) is much lower than using single pulse (bottom)

Dynamic Range and Sensitivity of PRBS-based OTDR

To understand what the noise figures mean for sensitivity and dynamic range we performed further measurements on a 62.5/125 jacketed 10 ft fiber cable with D38999 mil connector from Glenair, Inc. Since the cable is long, 511 bit PRBS is used. If we use 127 bit PRBS, we can achieve the same SNR by averaging over 4 continuous sequences. With a laser output of 6.29 dBm and the attenuation from the splitter, the possible maximal received power at the detector is 6.29-3.34-3.79=-0.84 dBm (which can be achieved when there is a 100% reflector at the end of the splitter). Therefore the maximal SNR is 0.84-(-40.55) = 41.39 dB.

Combine results using multiple PRBS's

Since we have found that SNR improves with lower frequency, but that spatial resolution decreases simultaneously, one possible scheme is using multiple PRBS's for detection and localization. In this scheme, we would use a low frequency PRBS (with good SNR) for detection. Once we detect and roughly localize a reflection, we would "zoom in" with a higher frequency PRBS to pinpoint the location of the defect. This scheme gives low false alarm rate for detection with accurate localization of defects. We show results for 1, 2, and 4ns pulse widths Figure 3 in a fiber connected having airgaps at the connectors.

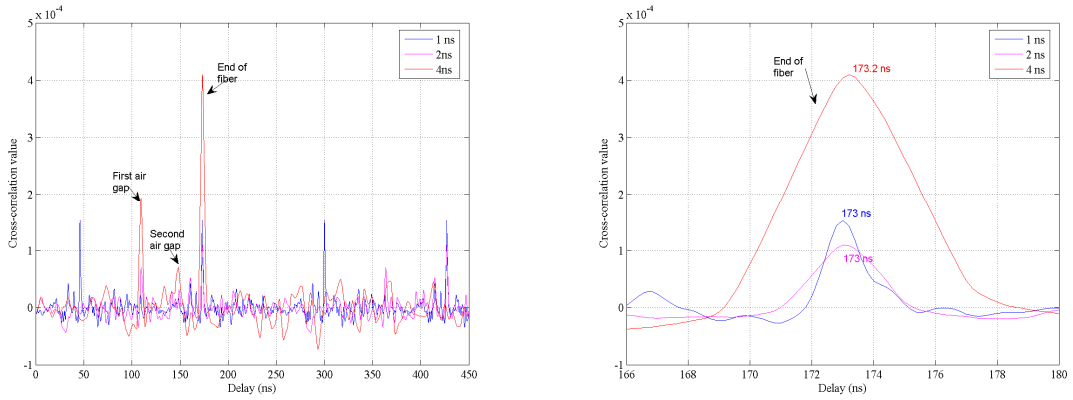

(a) Overall view (b) Close up view

Figure 3: Detection using multiple PRBS

Tests in single mode optical fiber

We tested a single mode optical fiber which has a core diameter of 9µm (Figure 4). Since the receptacle laser diode modules we have right now is not manufactured for single mode cable, we can only transmit at most -4.6 dBm power into the single mode fiber.

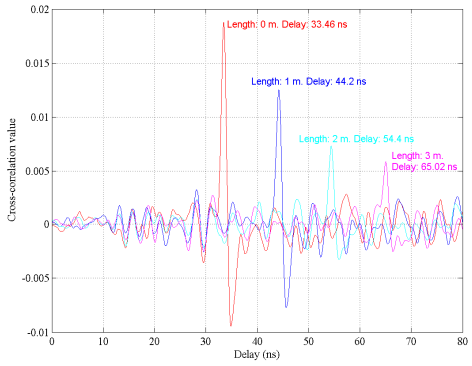

Figure 4: Detection of end of fiber on single mode fiber using multiple PRBS

Low cost High speed PRBS-based OTDR

In previous sections, we have shown that systems using PRBS can achieve excellent performance. We should point out that the results are obtained using expensive oscilloscope with high sampling rate.

To achieve high spatial resolution, it is essential to use a narrow pulse and for even better resolution, we need even faster sampling. To detect the narrow pulse, a high speed digitizer is required for both conventional OTDR systems and systems using PRBS. We are working on a low cost 10GHz PRBS generator that achieves high spatial resolution of 2 cm.

Acknowledgement: We thank the Naval Air Warfare Center (NAVAIR). Lakehurst, NJ, for supporting the work under SBIR phase I 2005 – Fiber optic cables

Experimental Investigation on Special Shaped Fibers Coupling with InP-based Planar Lightwave Circuit Chips

Xu Liu*, Jinbiao Xiao, Xiaohan Sun**

Lab of Photonics and Optical Communications, Department of Electronic Engineering,

Southeast University, Nanjing 210096, P.R.China

Abstract: Special shaped fibers, including tapered and lensed fiber (TLF) and wedge-shaped fiber (WSF), play an important role in planar lightwave circuit (PLC) technology to attain high efficient coupling with the elliptical optical field of InP based multiple quantum well (MQW) waveguide chips. Output optical field of MQW-PLC, TLF, WSF were numerically analyzed using beam propagation method (BPM) and staircase concatenation method (SCM), respectively. The optimum coupling conditions between WSF and PLC were achieved with wedge angle of 45°, cylindrical endface lens curvature radius of 2.5μm, aspect ratio of PLC elliptical optical spot of 5, and misalignment tolerance of 5.5μm. The focused optical spot diameter of TLF and WSF were measured and calculated based on the transformation relationship between object and image Gaussian beams, which differed less than 3.2% from those of the simulation. 1.55μm wavelength signal was injected into PLC-based coupler chip from SMF, TLF, WSF as input fiber separately with the same SMF as output fiber. The coupling efficiency of WSF-PLC-SMF linkage was 24.827dB and 16.22dB higher than that of SMF-PLC-SMF and TLF-PLC-SMF schemes, and therefore an WSF-PLC-SMF experimental prototype was established for pigtailed PLC packaging technique.

Keywords: planar lightwave circuit (PLC); InP; multiple quantum well (MQW); coupling and packaging; special shaped fiber

1. Introduction

Planar lightwave circuit (PLC) promises to be not only a solution to information access and optical signal processing, but it also directly addresses the issues of bandwidth, pincount, reliability and complexity and hence provides foundation for photonic network. As a microphotonics platform PLC technology is being driven by the needs of cost, coupling loss and footprint reduction with increasing functionality [1]. Smart nanopositioning and precision alignment is vitally important in high-efficient connectivity between PLC chips and fiber arrays [2, 3].

Unfortunately refractive-index mismatching between fused silica and Ⅲ-Ⅴ compound, as well as mode field mismatching induced by the output elliptical spot size from PLC, are most serious handicaps. On one hand the tapered spot size converter (SSC) [4] can be added at the ends of the PLC chip to enlarge the output spot laterally so as to partially match the core size of SMF, and in other hand the special shaped fibers, such as TLF [5] and WSF [6], should be used to get the similar output spot as one from the chip through the endface lens.

Application of TLF and WSF in coupling with the elliptical optical field of InP-based MQW-PLC chips was demonstrated and compared to decide the better candidate in this paper. Firstly, we optimized the structures of both TLF and WSF, and discussed their coupling conditions with the chip, respectively. Secondly we observed the compressed spot size of TLF and WSF. Finally the experiment results on the bar state produced by PLC-based coupler chip were obtained using different special shaped fibers and SMF, from which an optimum coupling scheme was devised.

2. Design Considerations

* Xu Liu, presenting author, email: *liuare@seu.edu.cn.*

** Xiaohan Sun, corresponding author, email: *xhsun@seu.edu.cn*

2.1 Output optical field of MQW-PLC, TLF, WSF

Fig.1 showed the optical fields of MQW-PLC with conventional rib width of 2.5μm (Fig.1(a)) and SSC-MQW-PLC with rib width of 8μm (Fig.1b). For the former, the semimajor axis was ω_{0x} = 1.1um， while the semiminor axis was ω_{0y} = 0.8um. For the latter, ω_{0x} = 3.7um, ω_{0y} = 0.7um. Obviously the aspect ratio (AR) of elliptical field ranged from 1.38 to 5.29. Compared with the MQW rib waveguide, the output spot from SSC-MQW-PLC chip matched much better with the core size of SMF along rib width direction.

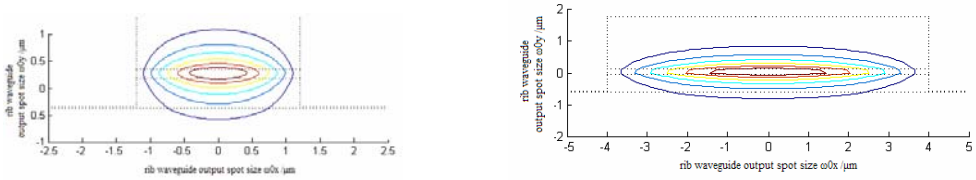

(a) (b)

Fig.1 (a) MQW and (b) SSC-MQW PLC output optical field by SCM simulation

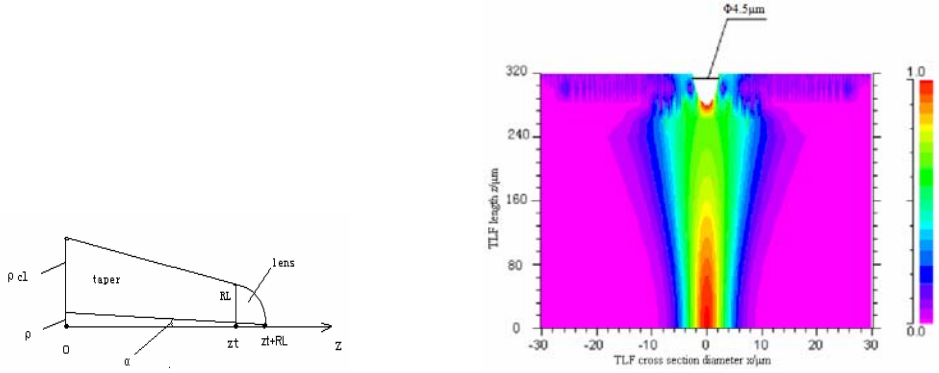

(a) (b)

Fig. 2(a) Upper half of TLF (b) lightwave propagation along TLF by BPM simulation

The structure of TLF can ben seen in Fig. 2a where ρ_{cl} , ρ , z_t , α , R_L represent cladding layer radius, core layer radius, taper length, half core taper angle, thin lens curvature radius [7]. The BPM simulation showed from Fig. 2b that the compressed optical spot diameter for the TLF with certain parameters was 4.5μm.

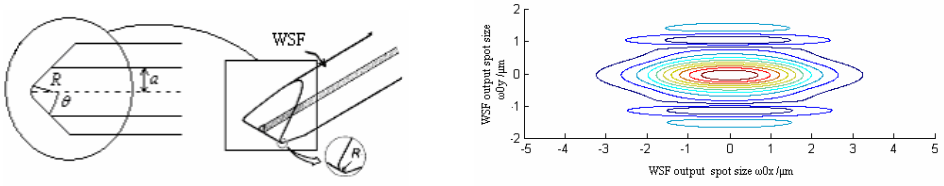

(a) (b)

Fig. 3(a) Illustration for WSF (b) WSF output optical field by SCM simulation

Fig. 3 describes the structure and output spot of WSF simulated by SCM [8], where R, θ, a stand for cylindrical endface lens curvature, wedged angle, core radius of SMF section. The numeric result showed ω_{0x} = 3.2um, ω_{0y} = 1.25um. Therefore, the elliptical field of WSF was closer to the output field distribution from the chip than that of TLF.

2.2 Optimization of TLF and WSF

In general TLF is made from standard SMF (G.652) and taper length varies from 300μm to 400μm. z_t , α , R_L were optimized to 300μm, 0.733°, 13.485μm respectively, and consequently the optical spot diameter was solved to be 4.45μm using a set of empirical equations [9] , which differed 1.11% from that of the BPM simulation.

The coupling circumstance changes with the aspect ratio of PLC elliptical field, the structure of WSF and the axial displacement (D) relationship. The optimum coupling conditions with θ=45°, R=2.5μm, ω_{0x}=3.5μm, AR=5, D=5.5μm were ascertained by calculating the coupling loss between WSF and SSC-MQW-PLC. The vertical displacement tolerance was smaller than that of horizontal. These results supplied a basement for the fabrication of WSF and PLC and the precision adjustment of nanopositioner.

3. Experiment

3.1 Observation on focusing performance

An experimental setup in Fig. 4(a) was established to investigate focusing performance of TLF and WSF. Gaussian beam emitting from He-Ne laser was amplified by 40× object lens and injected into special shaped fibers, digital PC camera received the output optical field. Fig. 4(b) and Fig.4(c) showed computer bitmaps of the TLF and WSF samples when their tips were 20mm apart from PC camera lens. Knowing the percentage the red image bitmap accounted for the blue background and the effective image size of CMOS sensor chip, the actual image size focused on the sensor chip was achieved, subsequently the output optical spot size in object space was calculated out. The measurement result for TLF output spot diameter was 4.31μm. Compared with the theoretical prediction (4.45μm), the error was 3.15%. The values for WSF was 6.2μm×2.5μm ($2\omega_{0x}\times 2\omega_{0y}$), differing from the simulation (6.4μm×2.5μm) within 3.125%.

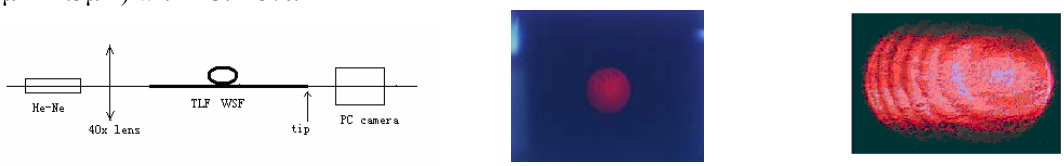

(a) (b) (c)

Fig.4. (a) Output optical field measurement setup , camera acquisition bitmap for (b) TLF and (c) WSF output optical field

3.2 Coupling Experiment

Bar state of InP SSC-MQW-PLC directional coupler chip (Fig. 5(b)) was tested using different input fibers with the same SMF as output fiber. A WSF (wedged angle 45°) stimulated the upper left port of PLC chip 5.5μm apart (Fig. 5(a)), while a SMF received optical field close to the upper right port (Fig. 5(c)). Agilent 86142B Optical Spectrum Analyzer embedded EELED light sources verified the whole transmission power at 1550nm peak to be -45.615dBm (Fig. 6(c)). The output power of SMF-PLC-SMF and TLF-PLC-SMF was -70.442dBm (Fig. 6(a)) and -61.835dBm (Fig. 6(b)). The coupling efficiency of WSF-PLC-SMF linkage was 24.827dB and 16.22dB higher than the above two schemes.

4. Conclusions

We thoroughly investigated the implementation and application of TLF and WSF in PLC chip coupling technology. The optimum coupling conditions were achieved for WSF wedge angle, cylindrical endface lens curvature radius, semimajor axis of PLC elliptical field, aspect ratio of PLC elliptical field, misalignment tolerance between WSF and PLC to be 45°, 2.5μm, 3.5μm, 5, 5.5μm individually. In comparison with the theoretical results, the measurement error of focused spot size of TLF and WSF fell within 3.15% and 3.125%. The coupling efficiency of WSF-PLC-SMF linkage was 24.827dB and 16.22dB higher than that of SMF-PLC-SMF and TLF-PLC-SMF

schemes, and therefore an experimental prototype of WSF-PLC-SMF coupling linkage was validated for pigtailed PLC packaging technique.

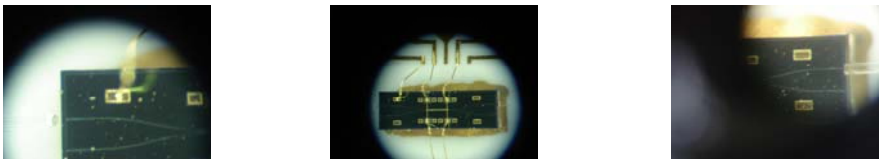

(a) (b) (c)

Fig5. WSF-PLC-SMF experiment photograph

(a) WSF as input fiber (b) directional coupler chip (c) SMF as output fiber

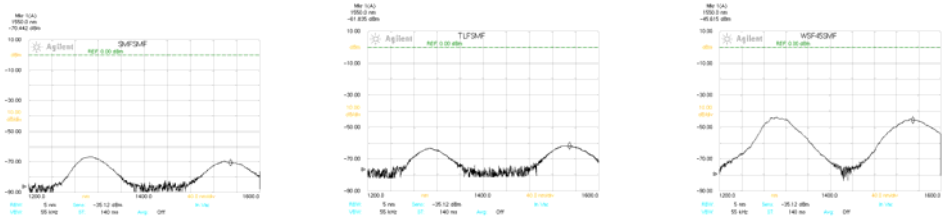

(a) (b) (c)

Fig6. PLC chip bar port test result for different inputs (a) SMF (b) TLF (c)WSF

5. Acknowledgements

The research was partially supported by the National "863'' Project of China (under grant 2002AA31230) and the Jiangsu Hi-Tech Project of China (under grant 7706008020).

6. Reference

[1]. K. Kato and Y. Tohmori, "PLC hybrid integration technology and its application to photonic components," IEEE J. Select. Topics Quantum Electron. **6**, 4-13 (2000).

[2]. David W. Vernooy, Joel S. Paslaski, Henry A. Blauvelt *et al*., " Alignment-insensitive coupling for PLC-based surface mount photonics," IEEE Photonics Technology Letters **16** , 269-271 (2004).

[3]. Rong Zhang and Frank G. Shi, "Manufacturing of Laser diode modules: integration and automation of Laser diode-fiber alignment and RIN characterization," IEEE Transactions on Advanced Packaging **26**, 128-132 (2003).

[4]. T. Mizuno, T. Kitoh, M. Itoh *et al*., "Optical spotsize converter using narrow laterally tapered waveguide for planar lightwave circuits," Journal of Lightwave Technology,**22**, 833-839 (2004).

[5]. T.Alder, A.Stöhr, R.Heinzemann *et al*., "High-efficiency fiber-to-chip coupling using low loss tapered single-mode fiber," Photonic Technology Letter, **12,** 1016-1018 (2000).

[6]. Szu-Ming Yeh, Sun-Yuan Huang, Wood-Hi Cheng, "A new scheme of conical-wedge-shaped fiber endface for coupling between high-power Laser diodes and single-mode fibers," Journal of Lightwave Technology, **23,** 1781-1786 (2005).

[7]. J.D.Love, W.M.Henry, W.J.Stewart *et al*., "Tapered single-mode fibers and devices Part1: Adiabaticity criteria," IEE Proc. **138**, 343-354 (1991).

[8]. Katsunari Okamoto, *Fundamentals of optical waveguides* (Academic Press, 2000), 323-339.

[9]. R.Keil, E.Klement, K.Mathyssek et al., "Experimental investigation of the beam spot size radius in single-mode fiber tapers," Electron. Lett. **20**, 621-622 (1984).

Fiber Frequency Combs: Development and Applications

N. R. Newbury, W. C. Swann, I. Coddington, and J. J. McFerran
National Institute of Standards and Technology, 325 Broadway, Boulder, CO 80305
email: nnewbury@boulder.nist.gov, phone: 303-497-4227, fax: 303-497-3387

Abstract

The output of a femtosecond fiber laser provides a comb of lines in frequency space that can be phase-locked to either a microwave or optical reference to form a stable frequency comb. We discuss the basic configuration of fiber laser-based frequency combs, the underlying physics behind the stabilization of the comb, and some applications of fiber-laser frequency combs to remote sensing and to measurements of the stability and phase noise of optical sources at 1550 nm.

Introduction

The development of frequency combs has led to a revolution in optical frequency metrology.[1-4] Figure 1 shows the basic picture of a frequency comb. It is a set of well defined, evenly-spaced, lines in optical frequency space. The frequency of each line is defined directly in terms of the frequency of a reference oscillator that can be either a microwave oscillator or an optical oscillator. If a microwave reference oscillator is used, then the comb provides the basic, but previously extremely challenging, function of linking optical frequencies directly to microwave frequencies. If an optical reference oscillator is used, the comb provides the basic function of linking that optical frequency directly to other optical frequencies or to microwave frequencies. The importance of frequency combs to atomic clocks and precision spectroscopy is an important factor in the award of the Nobel prize to J. Hall and T. Hänsch in 2005.

The initial development of frequency combs was based on use of femtosecond, solid-state Ti:Sapphire lasers,[1-4] and these systems continue to exhibit the highest levels of performance.[5, 6] However, in recent years, frequency combs using femtosecond, fiber lasers have been developed.[7-13] As they mature, their performance is approaching that of Ti:Sapphire based systems.[13] The interest in fiber laser frequency combs stems from several aspects. First, they can be relatively inexpensive. As a result they are much more attractive for widespread use and there are several commercial products available. Second, they can be relatively compact and robust, since "all-fiber" systems are possible. Third, they cover a wavelength range of 1 to 2 μm, which covers the transparent window of fiber optics. As a result, fiber-laser frequency combs are compatible with the wide range of telecommunication components and Er-based amplifiers. Moreover, the output can be transmitted long distances over optical fiber (although not without impairment of the optical phase stability.)

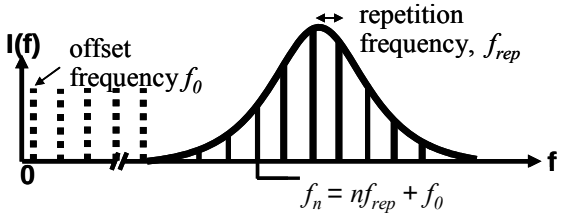

Fig 1: Frequency comb output from a femtosecond fiber laser. The laser output spans ~80 nm directly or 1000 nm after broadening in nonlinear fiber. The comb teeth are separated by the repetition rate of f_{rep} ~ 50 - 375 MHz, depending on the fiber laser. The position of the *nth* mode is given by $f_n = nf_{rep}+f_o$, where *n* is an integer that is ~$4x10^6$ for the comb line near 1550 nm.

The main challenge in stabilizing the frequency comb from a femtosecond fiber laser (or any femtosecond laser) is the detection of the offset frequency, f_0. (In contrast, the repetition frequency, f_{rep}, is easily detected by shining the output onto a photodetector.) The basic method for detecting the offset frequency is through "self-reference" detection with an f-to-2f interferometer,[2] although other methods are possible.[14] This self-referenced detection requires broadening the laser output to form a supercontinuum that spans an octave, i.e., factor of two, in frequency. The long-wavelength end is then doubled and beat against the short-wavelength end, yielding a beatnote at f_0. The difficulty lies in generating from the laser an octave of bandwidth that can provide a f_0 beat signal with sufficient signal-to-noise ratio. The first attempt at stabilizing the frequency comb output of a fiber laser essentially circumvented this problem by using a second Ti:Sapphire frequency comb.[15] However, since the first observations of the offset beat, all current fiber laser frequency combs are based on this self-referencing technique. [7-13]

Below, we first describe the fiber-laser frequency comb and then briefly discuss some of the applications, including basic frequency metrology in support of optical clocks, metrology of narrow-linewidth lasers, and remote sensing.

Configuration

Fiber laser frequency combs are based on passively mode-locked fiber lasers. A number of different laser designs have been successfully used including figure-8 laser[7], soliton[10] or stretched-pulse fiber ring laser[16], and Fabry-Perot laser using a saturable absorber [8]. The exact configuration of the laser does not appear to be important, although it may affect the feedback bandwidth. All these lasers put out ~100 fs pulses of laser light at ~0.1 nJ of energy and repetition rates of ~100 MHz. The spectral width of the pulses can range from 20 nm to 80 nm depending on the laser configuration. As discussed above, a full octave of bandwidth is needed to detect the offset frequency; therefore, this output must be externally spectrally broadened. Because the pulses are so short, the peak powers are significant and one would expect significant spectral broadening in optical fiber due to nonlinear effects. However, for current nonlinear fibers the pulse peak powers are not sufficient to generate a full octave of bandwidth. Therefore, the laser output is first amplified in a dispersion-managed erbium fiber amplifier. The output of the amplifier is then injected into a special highly nonlinear optical fiber that generates an octave-spanning supercontinuum. The development of this optical fiber was a critical step toward achieving fiber laser frequency combs.[17,18]

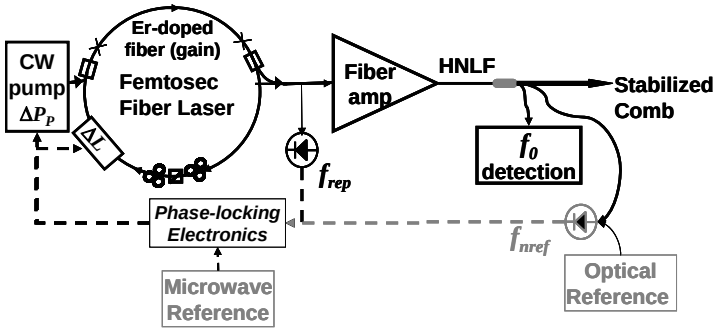

Fig 2: Basic schematic of a fiber laser frequency comb. The femtosecond fiber laser output is amplified and spectrally broadened in highly nonlinear fiber (HNLF). The offset frequency is phase-locked to a microwave reference. The remaining degree of freedom of the comb can be stabilized through (1) phase-locking the repetition rate to a microwave reference or (2) phase-locking one tooth of the comb to an optical reference (shown in gray). Solid lines represent fiber optic paths and dashed lines represent electronic signals.

Once the supercontinuum is generated, the offset frequency f_0 is detected by doubling the ~2 μm portion of the comb and heterodyning it against the ~1 μm end of the comb to generate an rf beat signal at f_0. This signal is phase-locked to an rf synthesizer by feeding back to the pump laser power. In initial efforts, the offset beats signal, f_0, was extremely broad – on the order of 100 kHz or more. While the phase-locking ensured that the average value of f_0 remained fixed with respect to the reference, the broad linewidth indicated that on short time scales there was significant jitter on f_0. It turns out that this jitter arose from intrinsic amplitude noise on the diode lasers that pump the femtosecond fiber laser. In principle, the feedback to stabilize the offset frequency ought to remove this amplitude noise by applying the appropriate correction to the current supply driving the pump diodes. However, the amplitude noise was too large to be totally removed by the simple proportional-integral feedback. Recently we found that by operating the pump diode at high currents, its amplitude noise is considerably reduced. Moreover, by using phase-lead compensation (i.e., derivative feedback) in the feedback loop the feedback bandwidth can be extended considerably further.[19] The end result is a tightly phase-locked offset frequency with ~ 1 radian phase excursions from the reference oscillator (corresponding to an instrument-limited linewidth).[16]

The stabilization of the offset frequency holds the comb fixed in terms of translational motion (see Fig. 1); however the spacing between the comb teeth is still free to change. There are two alternatives to fully stabilizing the comb. First, one can phase-lock the repetition rate to a microwave reference by feeding back to the cavity length (see Fig. 2) through piezoelectric fiber stretchers. In that case, the comb frequencies are given by $f_n(t) = nf_{rep}(t) + f_0(t)$, where we explicitly allow the frequencies to have some slow variation with time, t. This allows one to define the optical frequencies in terms of the microwave reference and is therefore useful for frequency metrology. However, the instantaneous noise on the comb lines can then be quite large. The corresponding frequency noise power spectral density (PSD) as a function of Fourier frequency, ν (conjugate to t), is $S_n(\nu) = n^2 S_{rep}(\nu) + S_0(\nu)$. Here, the PSD, $S_n(\nu)$, is defined as the Fourier transform of the slow time variations in the squared $f_n(t)$. The frequency noise PSD S_{rep} and S_0 in terms of the variations in the squared $f_{rep}(t)$ and $f_0(t)$, respectively, are defined similarly. The frequency noise on the offset frequency and repetition frequency, S_{rep} and S_0, can include both the noise on the microwave reference and noise resulting from imperfect phase-locking of the comb to the reference. Since $n \sim$ (200 THz/ 50 MHz) ~ 4×10^6, any frequency noise on the repetition frequency is "multiplied up" by $n^2 \sim 10^{13}$, which is a very large number. As a result, the optical comb lines will be significantly broadened.

Alternatively, the second method of phase-locking the comb involves stabilizing one tooth of the comb to an optical reference, i.e., a narrow stabilized laser.[6, 20] This approach is shown as the grey line in Fig. 2. The optical reference laser might be stabilized to an optical cavity if only short-term stability is important. It might also be the output of an optical atomic clock if absolute stability is important. If the comb tooth $n = n_{ref}$, is locked to the reference laser with frequency f_{REF} with an offset of f_b, the optical comb frequencies are given by $f_n(t) = (n/n_{ref})(f_{REF}(t)-f_b(t)) + (1-n/n_{ref})f_0(t)$. The phase noise (again ignoring correlations between f_{nref} and f_0) is now $S_n(\nu) = (n/n_{ref})^2 S_{REF}(\nu) + (1-(n/n_{ref})^2)S_0(\nu)$, where $S_{REF}(\nu)$ represents any frequency noise on the optical reference or on the phase-locking to the optical reference. The coefficients multiplying $S_{REF}(\nu)$ and $S_0(\nu)$ are now on the order of unity. For a sub-hertz stabilized optical reference, $S_{REF}(\nu)$ is low, provided that a sufficiently high bandwidth piezo-electric fiber stretcher is used to phase-lock the fiber laser to the optical reference. In that case, very narrow lines can be observed from a fiber laser frequency comb. With IMRA America, we have

demonstrated instrument-limited residual linewidths of less than 100 mHz across the comb spectrum. In essence, by phase-locking the comb to an optical reference, we can transfer the stability and low phase noise of a single optical reference all the way across an optical span of 1 to 2 microns.[20] Additionally, the repetition frequency of the comb is now extremely stable with a projected residual timing jitter of ~ 1 fs or less. This high phase coherence and low timing jitter can be exploited in a number of applications.

Metrology Applications:

The basic application of the fiber-laser frequency comb to metrology involves heterodyning the laser-under-test with the frequency comb. The resulting beat signal is a measure of the frequency difference between the laser frequency, f_{laser}, and the frequency of the nth comb tooth, f_n. Assuming n is known (and there are methods for determining n), the absolute frequency and stability of the laser can be determined with an uncertainty matching that of the comb tooth. If the comb is phase-locked to a microwave reference that is in turn stabilized to a time standard, then the absolute laser frequency can be determined to hertz level accuracy. This accuracy is seven orders of magnitude better than what can be achieved with a state-of-the-art wavelength meter. Experiments have demonstrated that very high levels of stability can be achieved with fiber laser frequency combs.[12, 13]

In some cases, the absolute laser frequency is of less interest than the linewidth or phase noise on the laser under test. In that case, the frequency comb can be phase-locked to a narrow stable optical reference. The beat signal then gives a measure of the absolute linewidth of the laser under test over the given observation time. By demodulating the beat signal with a fast Fourier transform (FFT) device, one can quantify the phase (or frequency) noise spectrum of the laser under test. This approach, which is only just now being developed at NIST, would permit the characterization of the phase noise of optical sources in a quantitative way that is consistent with the current characterization of microwave sources.

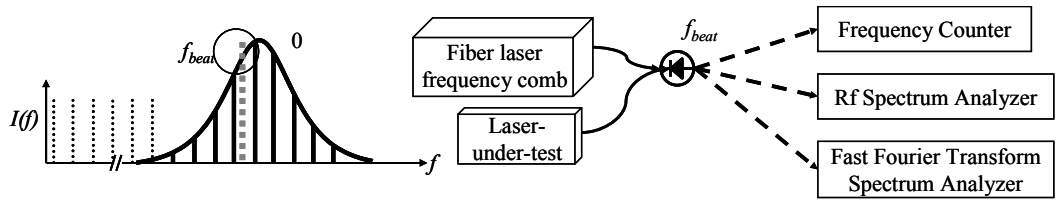

Fig 3: Metrology with a fiber-laser frequency comb. The heterodyne beat note between the laser under test and the frequency comb can be "counted" to measure the absolute frequency stability on long time scales. It can also be directed to an RF spectrum analyzer to measure the linewidth or to a fast Fourier transform spectrum analyzer to demodulate the signal in order to measure the phase noise or frequency noise spectrum.

Remote Sensing Applications:

One advantage of the fiber-laser frequency combs is that the output can be amplified with standard, commercially-available Er-doped fiber amplifiers. The possibility then arises of generating a high power, highly phase-coherent beam useful for remote sensing applications. The high bandwidth of the source implies a very high potential range resolution, while the narrow linewidths imply good Doppler, or vibrational, sensitivity at long ranges. In order to achieve the most sensitivity for ranging experiments, and to achieve any sensitivity for Doppler measurements, one is driven toward a coherent LIDAR system. In coherent LIDAR a strong

laser beam is scattered by a surface. A small fraction of the scattered signal is then collected and heterodyned with a local oscillator (LO), which is typically a frequency-shifted, delayed copy of the original transmitted pulse. For ranging applications with a pulsed transmitter, a range profile of the target is measured from the strength of the heterodyne signal as a function of the LO frequency. For vibrometry applications, the relative longitudinal velocity of the source and target is monitored from the frequency shift of the heterodyne signal.

The difficulties with developing a coherent LIDAR with the femtosecond fiber laser are threefold. First, as with any coherent LIDAR system, the return signal will suffer from speckle, which limits the signal-to-noise ratio for both ranging and vibrometry measurements. Second, the short pulse length of the transmitted signal will provide excellent range resolution, but only if the delay of the LO is precisely controlled. Third, any differential dispersion in the signal arm will degrade the range resolution accordingly. Recently, we devised a frequency-resolved coherent LIDAR (FReCL) system that effectively deals with these issues.[21] The basic setup is shown in Fig. 4 below. By spectrally resolving the returning heterodyne signal we achieve three things. First, we can mitigate the effects of speckle on vibration measurements by incoherently averaging the signals from the N distinct detectors. This speckle-averaging reduces the variance in the Doppler measurement by a factor of N. Second, we can use a fixed delay since the effective delay of the LO can be scanned in post-detection software by applying the appropriate phase shift to the N signals. Third, we can remove any differential dispersion in the signal arm by applying the appropriate phase correction to the N signal channels.

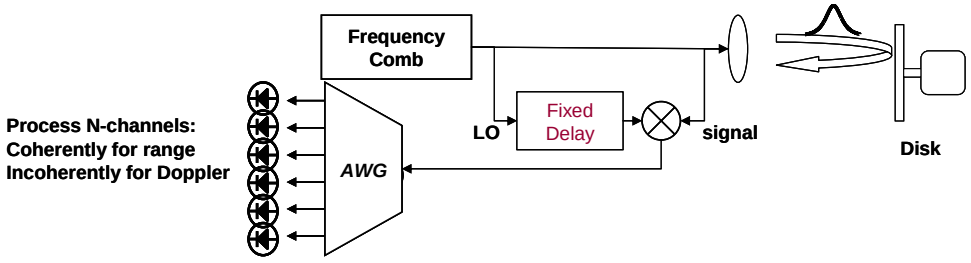

Fig 4: Frequency-Resolved Coherent LIDAR setup. For our laboratory setup, we used a rotating aluminum disk as the "target". The frequency comb in this case was free-running. The return signal was spectrally resolved with an arrayed waveguide grating (AWG). We used six discrete detectors at a 4.8 nm spacing in order to span the 25 nm-wide output pulse.

An example of the range images are given in Fig. 5 below. Fig. 5 compares the results obtained with a conventional setup (without spectrally resolving the return signal) to the results obtained with the FReCL approach. The images are identical, except that the FReCL images are acquired N-times faster, and without physically scanning the delay in the LO path. In these experiments, a single femtosecond fiber laser was used as the transmitter and local oscillator. As a result, the round-trip time to the target needed to be very close to an integer multiple of the laser repetition rate. (In other words, the software scanning of the delay can cover a range of only ~ 1.5 mm, corresponding to the bandwidth of the individual AWG channels.) However, with the recent results in phase-locking to fiber frequency combs to a single optical reference, one can envision a separate fiber laser frequency comb for a transmitter and local oscillator. In that case, arbitrary ranges could be accommodated.

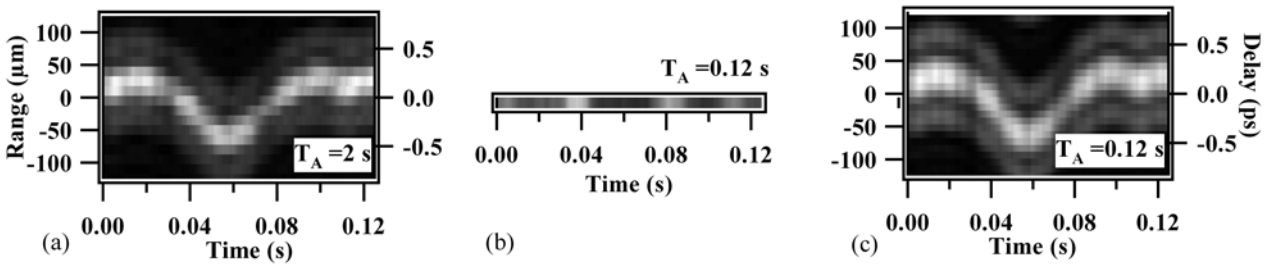

Fig. 5. Range image of the wobbling, rotating disk for one full rotation (0.12 sec) with a 10 ms averaging time. (a) Truth data from conventional system at 20 LO delays. (b) Conventional data for a single delay. (c) FReCL data at the same LO delay. T_A is the total acquisition time.

Conclusion

The output of femtosecond fiber lasers can be stabilized to either a microwave or an optical reference to form a frequency comb. The compatibility of fiber-laser frequency combs with telecommunication equipment should lead to a broad range of applications including frequency metrology, fiber transport of time and frequency, and remote sensing.

References:

1. T. Udem, R. Holzwarth, T. W. Hänsch, Nature, **416**, 233 (2002).
2. D. J. Jones, S. A. Diddams, J. K. Ranka, A. Stentz, R. S. Windeler, J. L. Hall, S. T. Cundiff, Science, **288**, 635-9 (2000).
3. S. A. Diddams, Th. Udem, J. C. Bergquist, E. A. Curtis, R. E. Drullinger, L. Hollberg, W. M. Itano, W. D. Lee, C. W. Oates, K. R. Vogel, D. J. Wineland, Science, **293**, 825 (2001).
4. J. Ye, S. Cundiff, "Femtosecond optical frequency comb technology : principle, operation and application." New York, NY: Springer, 2005.
5. L.-S. Ma, Z. Bi, A. Bartels, L. Robersson, M. Zucco, R. S. Windeler, G. Wilpers, C. Oates, L. Hollberg, S. A. Diddams, Science, **303**, 1843-1845 (2004).
6. A. Bartels, C. W. Oates, L. Hollberg, S. A. Diddams, Opt. Lett., **29**, 1081-1083 (2004).
7. B. R. Washburn, S. A. Diddams, N. R. Newbury, J. W. Nicholson, M. F. Yan, C. G. Jørgensen, Opt. Lett., **29**, 250-252 (2004).
8. T. R. Schibli, K. Minoshima, F.-L. Hong, H. Inaba, A. Onae, H. Matsumoto, I. Hartl, M. E. Fermann, Opt. Lett., **29**, 2467-2469 (2004).
9. H. Hundertmark, D. Wandt, N. Haverkamp, H. R. Telle, Opt. Express, **12**, 770-775 (2004).
10. B. R. Washburn, R. Fox, N. R. Newbury, J. W. Nicholson, K. Feder, P. S. Westbrook, C. G. Jørgensen, Opt. Express, **12**, 4999-5004 (2004).
11. F. Adler, K. Moutzouris, A. Leitenstorfer, H. Schnatz, B. Lipphardt, G. Grosche, F. Tauser, Opt. Express, **12**, 5872-5880 (2004).
12. P. Kubina, P. Adel, F. Adler, G. Grosche, T. W. Hänsch, R. Holzwarth, A. Leitenstorfer, B. Lipphardt, H. Schnatz, Opt. Express, **13**, 904-909 (2005).
13. H. Schnatz, B. Lipphardt, G. Grosche, *in proceedings of Lasers and Electro-Optics/Quantum Electronics and Laser Science Conference (CLEO)*, p. CTuH1, 2006)
14. H. R. Telle, G. Steinmeyer, A. E. Dunlop, J. Stenger, D. H. Sutter, U. Keller, Appl. Phys. B, **69**, 327-32 (1999).
15. J. Rauschenberger, T. M. Fortier, D. J. Jones, J. Ye, S. T. Cundiff, Opt. Express, **10**, 1404-1410 (2002).
16. J. J. McFerran, W. C. Swann, B. R. Washburn, N. R. Newbury, Opt. Lett., in press (2006).
17. J. W. Nicholson, M. F. Yan, P. Wisk, J. Fleming, F. DiMarcello, E. Monberg, A. Yablon, C. G. Jørgensen, T. Veng, Opt. Lett., **28**, 643 (2003).
18. J. W. Nicholson, P. S. Westbrook, K. S. Feder, A. D. Yablon, Opt. Lett., **29**, 2363-2365 (2004).
19. N. R. Newbury, B. R. Washburn, IEEE J. of Quantum Electron., **41**, 1388-1402 (2005).
20. W. C. Swann, J. J. McFerran, I. Coddington, N. R. Newbury, I. Hartl, M. E. Fermann, P. S. Westbrook, J. W. Nicholson, K. S. Feder, C. Langrock, M. M. Fejer, submitted, (2006).
21. W. C. Swann, N. R. Newbury, Opt. Lett., **31**, 826-828 (2006).

GENERATION OF A FREQUENCY COMB BY FWM IN SOAs ENHANCED BY RAMAN

Ana Carrasco-Sanz[a], Sonia Martín-López[a], Miguel González-Herráez[a,b], Pedro Corredera[a], Maria Luisa Hernanz[a] and Laura Abrardi[a]

[a] Departamento de Metrología, Instituto de Física Aplicada, (CSIC). Serrano, 144. 28006 Madrid, Spain. carrasco@ifa.cetef.csic.es

[b] Departamento de Electrónica, Escuela Politécnica Superior, Universidad de Alcalá. Campus Universitario, 28871 Alcalá de Henares, Madrid, Spain.

Abstract: This paper describes and demonstrates a frequency-spacing comb based on four-wave mixing in two semiconductor optical amplifiers enhanced by Raman amplification in a dispersion-shifted optical fiber. As result we have achieved a stable frequency comb with 36 spacing constant channels locked in two absorption lines of the acetylene ($^{12}C_2H_2$).

Introduction

In Dense Wavelength Division Multiplexing (DWDM) systems, the data is transmitted over a single optical fiber using multiple optical frequency channels following a frequency grid centered at 193.1 THz (1552.525 nm) in which the channels are separated by 100, 50 or 25 GHz and specified by the ITU. With such a narrow spacing, accurate frequency stabilization of the optical carrier frequencies is required to ensure a robust transmission system and avoid possible crosstalk between channels and losses in the filtering systems. For this reason, new frequency standards are necessary to calibrate the filters, wavelength meters and optical spectrum analyzers used in the maintenance and characterization of DWDM systems.

An interesting method to generate reference frequencies in the optical fiber communications bands is the stabilization of lasers in the molecular or atomic absorption lines of some specific gases. The absorption lines of gases such as $^{12}C_2H_2$, $^{13}C_2H_2$, $H^{13}C^{14}N$, CH_4, $^{12}C^{16}O$, $^{13}C^{16}O$, or HI provide frequency references that are very stable and have very well understood physical behavior along the telecommunication transmission bands range from about 184 THz to 237 THz (1625-1260 nm) [1], [2], [3] and [4]. Unfortunately with this method the generation is limited to those frequencies at which these gases have well-resolved absorption lines. If we want to obtain reference lines that cover all the ITU's bands it is necessary to use many cells with different gases.

The generation of new frequencies based on standards laser lines using Four-Wave Mixing (FWM) in fiber optic [5] and semiconductor optical amplifier [6] is an interesting method to extend the frequency range.

Other methods have been developed to generate new reference frequencies. One of the most attractive is the creation of a spectrum of discrete, equally spaced and known frequency emissions over the bandwidth of interest, using an optical frequency comb generator. Other systems developed are based on the modulation of a CW laser and extended by the generation of FWM in zero dispersion fiber [7], [8], the modulation of a supercontinuum source [9] and the FWM generation in multicore photonic crystal fibers [10].

In this paper we demonstrate experimentally a frequency-spacing comb based on degenerate four-wave mixing in two semiconductor optical amplifiers (SOAs) enhanced by Raman in a dispersion-shifted optical fiber. The comb is generated by locking two lasers into different absorption lines of acetylene, centered in the zero dispersion region of the optical fiber.

Therefore, the frequency difference between the selected absorption lines sets the spacing of the frequency comb. To assure a good FWM efficiency we use a SOA as nonlinear generation media. Furthermore, since the SOAs are insensitive to phase matching condition, we obtain a wider bandwidth over which the conversion efficiency is significant [6]. We incorporate a Raman enhancement obtained by two Raman fiber lasers getting a comb of 36 frequencies. The spaced of the comb is in our case defined by the separation between P23 (194.743 THz) and P25 (194.566 THz) absorption lines of the $^{12}C_2H_2$ (Δf=176.636 GHz).

Stabilization of the comb in the acetylene $^{12}C_2H_2$ absorptions

Figure 1 shows the experimental setup for the proposed frequency comb that operates stably at room temperature.

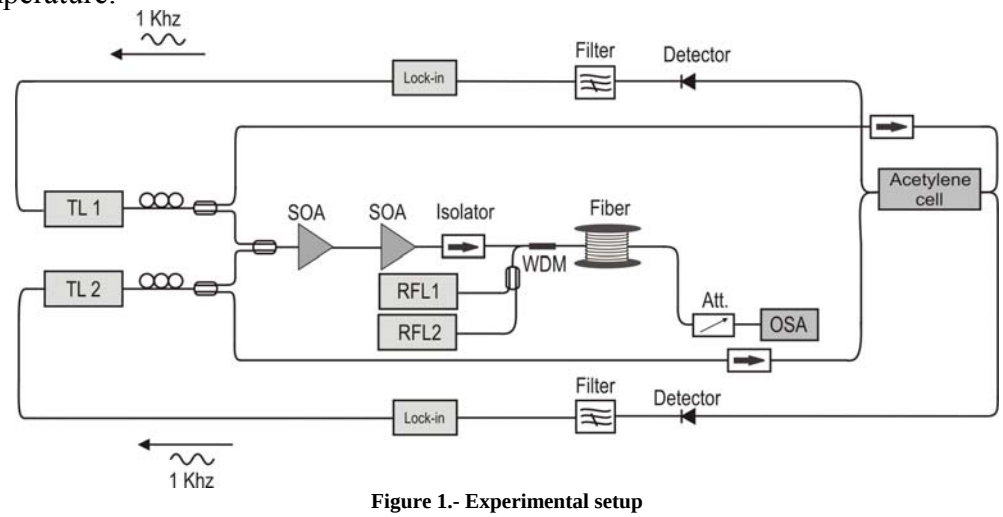

Figure 1.- Experimental setup

The experimental setup consists of two tunable lasers of 150 KHz width, two SOAs with a saturation power of 15 dBm, an isolator, two Raman fiber laser at wavelength 1455 nm and 1427 nm, a 5 Km dispersion-shifted fiber, an absorption acetylene cell (traceable to NIST SRM 2517a [11]), two detectors and two lock-in amplifiers. Two copolarized laser wavelengths are coupled into a SOA with highly non-linear behavior, generating a four-wave product that will be the seed of our comb. The output is injected in a second SOA with higher saturation power in order to enhance the FWM product. Figure 2 shows the waves generated by the first SOA and the mixing product enhanced in the second.

Once we stabilized the lasers at P23 and P25 absorption lines of $^{12}C_2H_2$ respectively, at the output of the first SOA we get six equispaced frequencies (the two original lines and four extra frequencies), and after the second SOA we obtain nine frequencies. The lasers (TL1 and TL2) are locked to the absorption lines using a frequency modulation with a sinusoidal signal of 0.1 V at 1 KHz. The peak-to-peak amplitude of this signal produces a change of 30 MHz in the frequency of the lasers.

The new mixing is introduced in a 5 Km long fiber with a zero-dispersion wavelength λ_0 = 1540 nm (just between the two original laser lines – R23 = 1539.43 nm and R25 = 1540.83 nm –). This fiber was selected in order to improve the FWM generation and to increase the Raman gain.

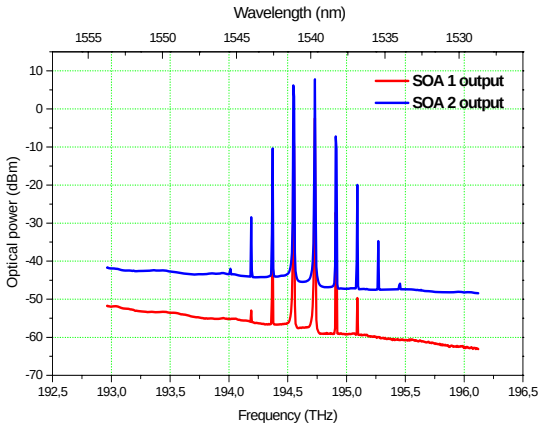

Figure 2.- FWM generated in a high non-linear SOA and enhanced in a high output saturation power SOA.

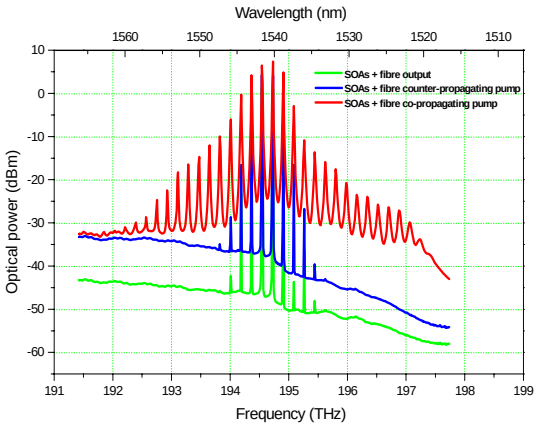

Figure 3.- Frequency comb generation: One Raman pump.

In order to enhance the comb generated we amplified the mixing product using a Raman fiber laser (RFL1) pumping at λ_{p1} = 1455 nm and output power P_{p1}= 1 W. We chose a co-propagating pump configuration for pumping our mixing product since it was more efficient than the counter-propagating pump configuration as Figure 3 shows.

Using one Raman pump, the frequency comb generated consists of 28 equally spaced frequencies (1.4 nm, 176.636 GHz) and covers a wavelength range from 1522 nm to 1561 nm.

As we were increasing the output power, we could not enhance the number of frequencies generated. As Figure 4 shows, pump powers higher than 1 W increase the output power of the comb but diminish the OSNR of the frequencies generated by increasing the noise of the system.

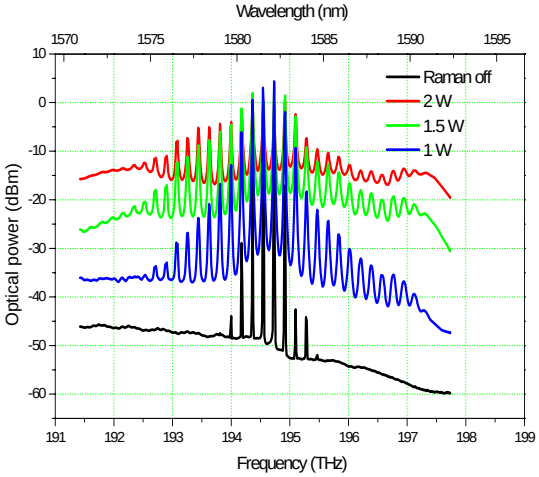

Figure 4.- Effect of the pump power in the frequency comb generation

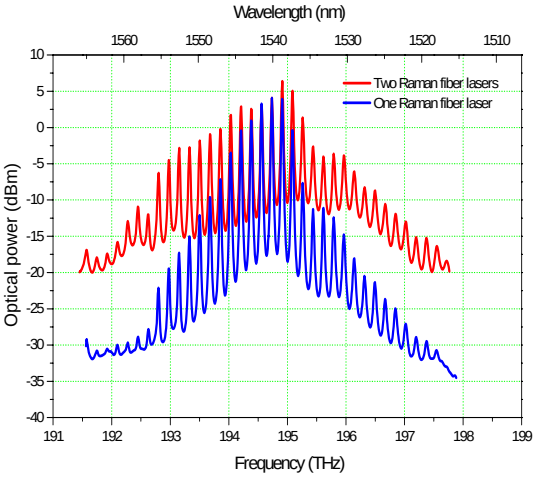

Figure 5 .- Frequency comb generation: Two Raman pumps.

In order to increase the number of frequencies generated we introduced another Raman Fiber Laser, RFL2, pumping at λ_{p2} = 1427 nm and output power of P_{p2} = 1W through a 50/50 coupler. Figure 5 shows the frequency comb generation of the frequency comb obtained from the amplification of the FWM product inside the fiber due to the double Raman amplification. The new frequency comb generated consists of 36 equally spaced frequencies (1.4 nm) covering the wavelength range between 1515 nm and 1565 nm.

The main difficulty found in the generation of this frequency comb arrives from the competition between non-linear effects inside the dispersion-shifted fiber. The linewidth of the lines emitted by our lasers is very narrow (150 kHz bandwidth). This event contributes to generate a strong Brillouin scattering signal. The Brillouin scattering subtracts energy to the system reducing the FWM generation. It would be necessary a dithering of the initial wavelength emitted from the lasers at 10-20 KHz in order to enlarge the linewidth of the lasers and reduce the Brillouin scattering.

The generation of new frequencies by FWM in our comb is limited by the chromatic dispersion of the fiber. Far away from the zero dispersion wavelengths the chromatic dispersion of the fiber introduces a large phase delay that avoids complying with the phase matching condition necessary for the FWM generation.

Conclusions

We have experimentally demonstrated a frequency-spacing comb based on degenerate four-wave mixing in two semiconductor optical amplifiers (SOAs) enhanced by Raman in a dispersion-shifted optical fiber. The new frequency comb generated consists of 36 equally spaced frequencies (176.636 GHz) covering a range from 1515 nm to 1565 nm. The absorption lines of the acetylene set the spacing of the frequency comb. This frequency comb is useful for wavelength metrology to calibrate DWDM systems such as wavelength meters or optical spectrum analyzers, the generation of precise multiwavelength sources employed in DWDM and synchronization of different fiber laser-based frequency comb.

Acknowledgements

This work was supported by Spanish Commision Interministerial de Ciencia y Tecnologia, project TIC2003-01867 and by Comunidad Autónoma de Madrid through project FACTOTEM_CM ref n. S-0505/ESP/0417. A. Carrasco acknowledges support from the CSIC, through the I3P grant program co-supported by the Social European Fund.

References

[1] T. Dennis et al.," Wavelength References for 1300-nm Wavelength-Division Multiplexing". J. Ligthwave Tech., 20, 776-782, (2002)

[2] S.L.Gilbert et al., "Hydrogen Cyanide H13C14N Absorption Reference for 1530-1560 nm. Wavelength calibration- SRM 2519", NIST special publication 260-137

[3] "Carbon Monoxide Absorption References for 1560 nm to 1630 nm. Wavelength calibration-SRM 2514 (12C16O) and SRM 2515 (13C16O)", NIST special publication

[4] W.C. Swann et al., "Pressure-induced shift and broadening of 1510-1540-nm acetylene wavelength calibration lines" J. Opt. Soc. Am. B, 17, pp. 1263-1270. (2000)

[5] D. A. Humphreys, "Synthesis of optical reference frequencies by four-wave mixing in optical fiber", 6th Optical Fiber Measurement Conference (OFMC'01) Proceedings. National Physical Laboratory, Teddington, Middlesex, UK, pp. 69-73. (2001)

[6] A. Carrasco-Sanz et al. "Synthesis of optical standard frequencies in the S, C and L telecommunication bands by use of four-wave mixing in semiconductor optical amplifiers", in press, Opt. Communications

[7] G. A. Sefler, "Frequency comb Generation by Four-Wave Mixing and the Role of the Fiber Dispersion", J. Ligth. Tech., vol.16, No.9, (1998)

[8] Y. Han et al.,"Wavelength-spacing tunable multiwavelength erbium-doped fiber laser cased on four-wave mixing of dispersion-shifter fiber", Opt. Lett., vol.31, No.6, (2006)

[9] H. Takara, "Multiple Optical Carrier Generation from a Supercontinuum Source", Optics & Photonics News (2002)

[10] A. V. Husakou et al., "Frequency comb generation by Four-Wave Mixing in a multicore photonic crystal fiber", App. Phy. Lett., vol.83, No.19, (2003)

[11] Standard Reference Material 2517a, s/n NP013U08. NIST

Comparison of Saturated Absorption Spectra of Acetylene Gas Inside Photonic Bandgap Fibers

K. Knabe, R. Thapa, O. L. Weaver, B. R. Washburn, and K. L. Corwin

Kansas State University, Dept. of Physics, 116 Cardwell Hall, Manhattan, KS 66506
email: corwin@phys.ksu.edu, phone: 785-532-2263, fax: 785-532-6606

Abstract: Saturated absorption spectroscopy is performed inside hollow photonic bandgap fibers, with both 10 μm and 20 μm core diameters. Line width and signal quality depend on the fiber core diameter, as well as pressure and optical power. These parameters are optimized toward the creation of an optical reference. The effect of splicing the fiber to a single-mode fiber is also investigated.

The development of optical frequency standards in the near-infrared spectral region has been motivated in part by the optical telecommunications industry. Acetylene gas offers a series of well-spaced spectral features in the 1.5 μm region, spanning the C band. By pressure-broadening these features to about 1 GHz in width, the National Institute of Standards and Technology (NIST) has created portable standards of moderate uncertainties, between 13 MHz and 130 MHz, that can be built into commercial devices [1, 2]. Meanwhile, sub-Doppler spectroscopy of molecular gases provides high-accuracy infrared optical frequency references. Typically the weak molecular overtone transitions employed at these wavelengths require high powers for saturation, and therefore to date all high-accuracy references have been based on power build-up cavities [3, 4] , which provide power amplification and long effective interaction lengths but are not readily portable. A series of measurements of lines in the $\nu_1 + \nu_3$ band [4-6] led the Comitté International des Poids et Mesures (CIPM) to adopt a value of the P(16) line in $^{13}C_2H_2$ with an uncertainty of 100 kHz [7]. With the advent of frequency comb technology, groups at the National Institute of Advanced Industrial Science and Technology (AIST) in Japan [8, 9], National Physical Laboratory (NPL) in the UK [10], and the National Research Council (NRC) in Canada [11, 12] have measured these lines with greatly increased precision. The CIPM recently reduced the uncertainty of the P(16) transition to 10 kHz, and most recently, 61 lines in the band have been realized with a width of 600 kHz and measured to an uncertainty of 1.4 kHz [13]. However, there are many advantages to performing saturation spectroscopy independent of a power build-up cavity, as described in Ref. [14], where signals with widths ~1 MHz have been observed inside a 1 m long glass cell.

While the science of frequency metrology has been transformed, optical fiber technology has simultaneously been revolutionized by the advent of hollow, low-loss photonic bandgap (PBG) fibers. These optical waveguides allows light to be confined at high intensities in a hollow air or gas-filled region with very low loss [15]. These fibers are vastly superior to capillary fibers for small core diameters [16], and have therefore been used in many recent demonstrations of nonlinear light-gas interactions. Examples include gas sensors [17], Raman scattering in hydrogen-filled fiber as a tunable light source [18], and electromagnetically induced transparency (EIT) in PBG fibers filled with acetylene and rubidium [19-21]. Lasers have been locked to the side of Doppler-broadened transitions in sealed acetylene-filled fibers, toward the development of portable frequency references [22]. Finally, saturated absorption has been observed inside photonic bandgap fibers. Initial observations indicated large background noise arising from interference and mode beating [23, 24], even in an all-fiber configuration [25]. A more complete discussion of these issues appears in Ref. [26].

For PBG fiber cells to be employed as frequency references, the saturated absorption spectrum must be optimized in magnitude and minimized in width. Also, modulation of the transmitted light due to spurious interference or mode beating must be suppressed. In the effort to develop optical frequency references using acetylene filled PBG fiber cells, we have examined the dependence of signal size and width on gas pressure and fiber diameter, among other factors. Furthermore, when the PBG fiber is sealed by splicing SMF solid-core fiber to either side, etalon effects and changes in mode coupling may give rise to spurious signals that must be minimized. Thus we characterize saturated absorption inside a PBG fiber, as a function of gas and fiber dimensions. We also investigate the effects of splicing the fiber on the signal quality.

In Fig. 1a, the experimental setup is shown for measurements of acetylene saturated absorption spectra in an isolated photonic bandgap fiber. Modifications to the experiment made to accommodate a single splice between a step-index single-mode fiber and a photonic bandgap fiber are shown in Fig. 1b. The details of the splicing technique for splicing hollow PBG fiber to step-index fiber are given in Ref. [27]. A 5 mW beam from an extended cavity diode laser (ECDL) is split, and 10% is amplified by an IPG Photonics® Erbium-doped fiber amplifier (EDFA) to up to 500 mW. The remaining power is sent to diagnostics, which include an acetylene-filled glass cell

(as in Ref. [1]), in order to locate the relevant transitions, and a Michelson interferometer, used to monitor the laser frequency as it is swept across the transition under study. The output from the EDFA is split into pump and probe beams, and the probe passes through an acousto-optic modulator (AOM) in order to shift the frequency between the pump and probe beams, minimizing the interference between the probe and any stray pump light. To compensate for polarization rotation inside the fibers, half-wave and quarter-wave plates are used to cleanly separate the pump and probe beams. Also shown are isolators (Iso.), polarization controllers (PC), polarizing beam splitters (PBS), the vacuum chambers (VC), and a photodetector (PD). In Fig. 1b, the second vacuum chamber is obviated by a fusion splice which seals one end of the PBG fiber. Two different PBG fiber types are investigated, as indicated in Fig. 1c and d, with 10 μm and 20 μm nominal core diameters, respectively.

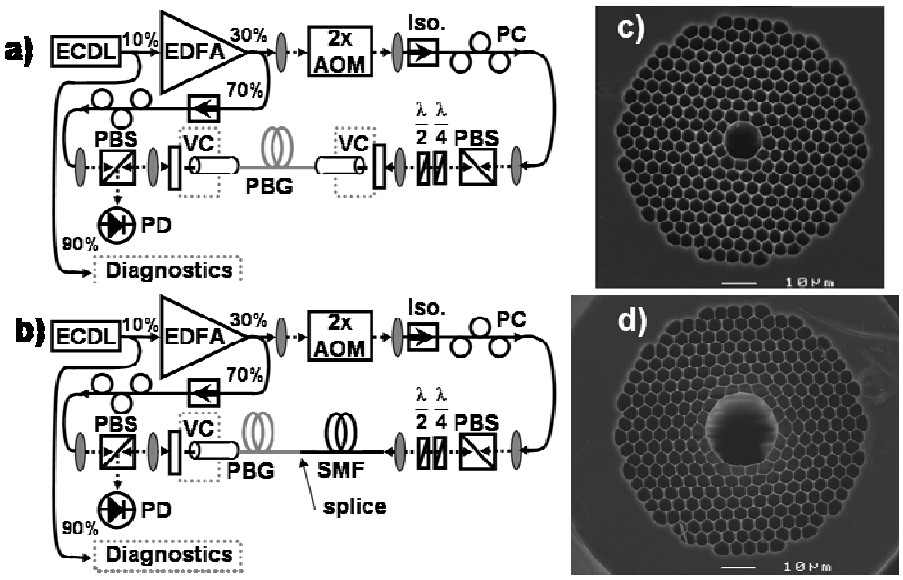

Fig. 1. a) Schematic of the experimental setup, for unspliced fibers. b) Same as a, but with one end of fiber spliced to SMF. c) 10 μm core PBG fiber, made by Crytal Fibre HC-1550-02. d) 20 μm core PBG fiber, made by Crytal Fibre HC19-1550-01. Images of fiber cross-sections provided by Crystal Fibre A/S, www.crystal-fibre.com.

The dependence of the observed signal size inside the 20 μm diameter fiber is shown in Fig. 2a. The central dip in transmitted power is due to the presence of the pump beam, which burns a Bennett hole in the ground-state population of the acetylene molecules. When the probe and the pump are resonant with the same velocity class of molecules, the probe light is less strongly absorbed. A laser may be locked to this feature and used as a frequency reference. Both the strength of the absorption and the width of the saturated absorption feature increase with pressure. Off resonance, the wings are very flat. In contrast, Fig. 2b is taken in a 10 μm fiber, and reveals large interference in the wings, indicative of mode beating. The difference between the two spectra is likely due to a reduced number of surface modes [28] present in the larger-core fiber.

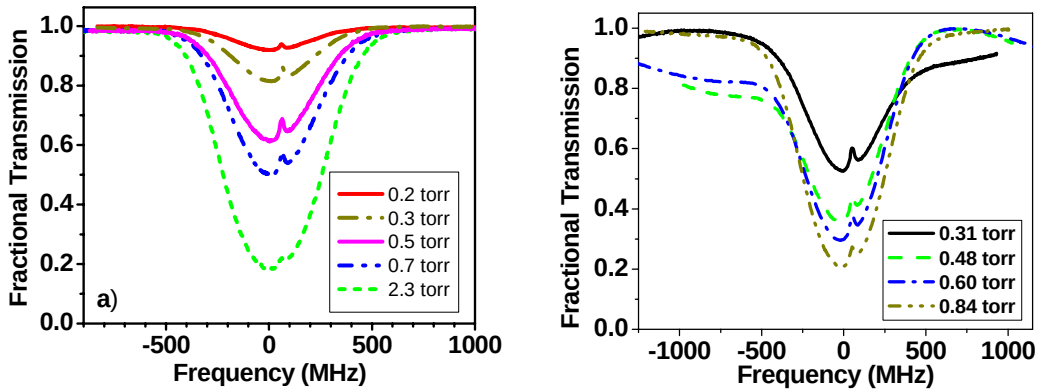

Fig. 2. a) Fractional transmission versus optical frequency detuning at different gas pressures, for the $^{12}C_2H_2$ P (11) transition with a pump power of 29 mW incident on the 0.78 m long fiber. b) Same as a), but in the 10 μm with length 0.90 m long and 30 mW of pump power.

The above spectra are interpreted in terms of Beer's law [29], which describes the transmission of light through a medium as $P = P_0\, e^{-\alpha s(\nu) l}$, where P_0 is the incident power, P is the transmitted power, and l is the length of the medium. From P_0 and P is calculated $l\ \alpha_s(\nu)$, as shown in Fig. 3a. Then $l\ \alpha_s(\nu)$ is fit to an appropriate function, taking into account the Gaussian nature of the Doppler broadened signal and the Lorentzian saturation dip [26]. The full-width-half-maximum w of this Lorentzian feature is plotted as a function of gas pressure in Fig. 3b, for two different pump powers, in the 20 μm fiber with length 0.78 m. Figure 3c shows the frequency discrimination of the saturated absorption feature, which is the signal height in fractional absorption divided by the signal width in MHz. Larger values indicate increased suitability for an optical frequency reference. From Figs. 2 and 3, it is clear that the 20 μm fiber provides cleaner signals and narrower signals than the 10 μm fiber. Thus the 20 μm fiber is more suitable for a frequency reference.

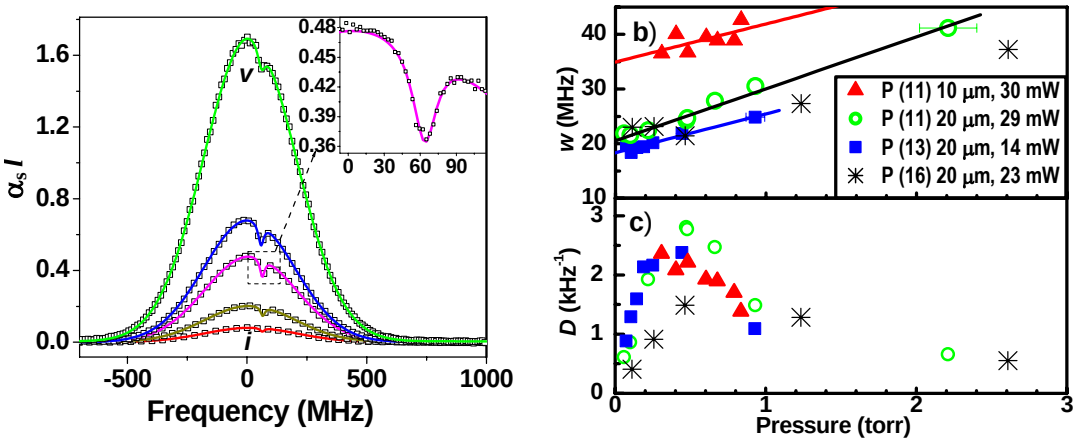

Fig. 3. a) $\alpha_s l$ calculated for the data shown in Fig. 2a, from top to bottom in order of decreasing pressure. Solid lines represent fits to the above equation, using the function described above. b) Width vs. pressure resulting from fits. Circles represent widths of Lorentzian features shown at left. Squares and asterisks represent different transitions interrogated within the same fiber, at the pump powers shown. Triangles represent the widths found in a 10 μm fiber with length 0.90 m. c) Frequency discrimination of the saturation dip, indicating the suitability of the standard for a frequency reference.

In order to employ these PBG fibers as frequency references, they must be sealed by splicing solid-core fiber to each end. Typically this is done with more costly filament heater splicers, but we have demonstrated low-loss splices using a conventional arc splicer [27]. In Fig. 4, spectra taken in spliced fibers are compared to those from unspliced fibers. While the background oscillations in the 10 μm fibers are similar with and without splices, the very flat background offered in the 20 μm fiber is degraded in the presence of the splice. This is most likely due to reflections in the fiber, but may also be due to different coupling into the surface modes of the fiber when using spliced fiber instead of free-space coupling. Further investigation is warranted.

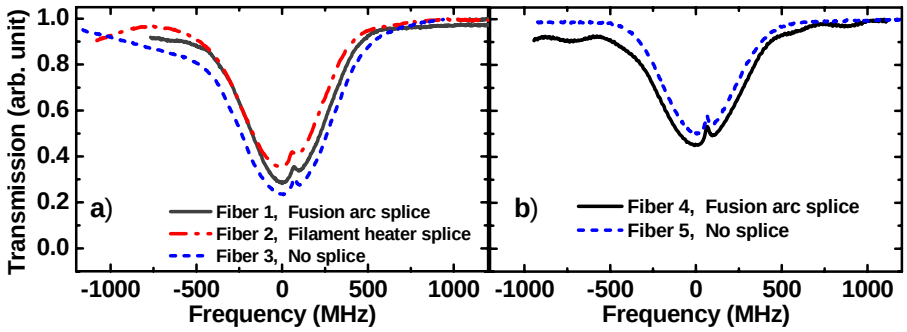

Figure 4. Saturated absorption spectra in a) 10 μm and b) 20 μm diameter PBG fibers. Fiber 1 is 0.78 m long, spliced to SMF using a conventional arc splicer, as described in Ref. [27], and the P(11) spectrum was taken at 29 mW and 0.86 torr. Fiber 2 is 2.0 m long, spliced to SMF by Crystal Fibre A/S using a filament heating splicer, and the spectrum is taken of the weaker P(12) transition at 17 mW and 0.81 torr. Fiber 3 is the unspliced 10 μm fiber of Fig. 2b, of P(11) at 0.69 torr. Fiber 4 is 43.5 cm long, spliced with an arc splicer to SMF, taken of P(11) at 43 mW and 0.8 torr. Fiber 5 is the 20 μm fiber of Fig. 2a, at ~ 0.7 torr.

We gratefully acknowledge funding from AFOSR, and NSF EPSCoR and CAREER. We thank Sarah Gilbert, Dirk Müller, Ahmer Naweed, Bill Swann, and Kurt Vogel for helpful discussions, and Mike Wells and the J. R. Macdonald laboratory staff for technical support.

References

[1] W. C. Swann and S. L. Gilbert, "Pressure-induced shift and broadening of 1510 - 1540-nm acetylene wavelength calibration lines," J. Opt. Soc. Am. B **17**, 1263 - 1270 (2000).

[2] S. L. Gilbert and W. C. Swann, "Acetylene $^{12}C_2H_2$ absorption reference for 1510 nm to 1540 nm Wavelength Calibration -- SRM 2517a," 2001.

[3] M. d. Labachelerie, K. Nakagawa, and M. Ohtsu, "Ultranarrow $^{13}C_2H_2$ saturated-absorption lines at 1.5 μm," Opt. Lett. **19**, 840 - 842 (1994).

[4] K. Nakagawa, M. d. Labachelerie, Y. Awaji, and M. Kourogi, "Accurate optical frequency atlas of the 1.5-μm bands of acetylene," J. Opt. Soc. Am. B **13**, 2718 - 2714 (1996).

[5] A. Onae, T. Ikegami, K. Sugiyama, F. L. Hong, K. Minoshima, H. Matsumoto, K. Nakagawa, M. Yoshida, and S. Harada, "Optical frequency link between an acetylene stabilized laser at 1542 nm and an Rb stabilized laser at 778 nm using a two-color mode-locked fiber laser," Optics Communications **183**, 181-187 (2000), <Go to ISI>://000089153500021.

[6] A. Onae, K. Okumura, K. Sugiyama, F.-L. Hong, H. Matsumoto, K. Nakagawa, R. Felder, and O. Acef, "Optical Frequency Standard at 1.5 μm based on Doppler-free acetylene absorption," in *Proceedings of 6th Sypm on Frequency Standards and Metrology*, P. Gill, (World Scientific, Singapore, 2002) 445.

[7] T. J. Quinn, "Practical realization of the definition of the metre, including recommended radiations of other optical frequency standards (2001)," Metrologia **40**, 103 (2003).

[8] F.-L. Hong, A. Onae, J. Jiang, R. Guo, H. Inaba, K. Minoshima, T. R. Schibli, H. Matsumoto, and K. Nakagawa, "Absolute frequency measurement of an acetylene-stabilized laser at 1542 nm," Opt. Lett. **28**, 2324-2326 (2003).

[9] J. Jiang, A. Onae, H. Matsumoto, and F. L. Hong, "Frequency measurement of acetylene-stabilized lasers using a femtosecond optical comb without carrier-envelope offset frequency control," Opt. Express **13**, 1958-1965 (2005).

[10] C. S. Edwards, H. S. Margolis, G. P. Barwood, S. N. Lea, P. Gill, G. Huang, and W. R. C. Rowley, "Absolute frequency measurement of a 1.5-μm acetylene standard by use of a combined frequency chain and femtosecond comb," Opt. Lett. **29**, 566-568 (2004).

[11] A. Czajkowski, J. E. Bernard, A. A. Madej, and R. S. Windeler, "Absolute frequency measurement of acetylene transitions in the region of 1540 nm," Appl. Phys. B **79**, 45-50 (2004).

[12] A. Czajkowski, A. A. Madej, and P. Dube, "Development and study of a 1.5 μm optical frequency standard referenced to the P(16) saturated absorption line in the (v(1)+v(3)) overtone band of $^{13}C_2H_2$," Optics Communications **234**, 259-268 (2004).

[13] C. S. Edwards, H. S. Margolis, G. P. Barwood, S. N. Lea, P. Gill, and W. R. C. Rowley, "High-accuracy frequency atlas of $^{13}C_2H_2$ in the 1.5 μm region," Appl. Phys. B **80**, 977 (2005).

[14] A. Onae, K. Okumura, Y. Miki, T. Kurosawa, E. Sakuma, J. Yoda, and K. Nakagawa, "Saturation spectroscopy of an acetylene molecule in the 1550 nm region using an erbium doped fiber amplifier," Opt. Comm. **142**, 41 (1997).

[15] R. F. Cregan, B. J. Mangan, J. C. Knight, T. A. Birks, P. S. Russell, P. J. Roberts, and D. C. Allan, "Single-mode photonic band gap guidance of light in air," Science **285**, 1537-1539 (1999), <Go to ISI>://000082359500056.

[16] F. Benabid, J. C. Knight, G. Antonopoulos, and P. S. J. Russell, "Stimulated Raman Scattering in Hydrogen-Filled Hollow-Core Photonic Crystal Fiber," Science **298**, 399 (2002).

[17] T. Ritari, J. Tuominen, H. Ludvigsen, J. C. Petersen, T. Sørensen, T. P. Hansen, and H. R. Simonsen, "Gas sensing using air-guiding photonic bandgap fibers," Opt. Express **12**, 4081 (2004).

[18] F. Benabid, G. Bouwmans, J. C. Knight, P. S. J. Russell, and F. Couny, "Ultrahigh Efficiency Laser Wavelength Conversion in a Gas-Filled Hollow Core Photonic Crystal Fiber by Pure Stimulated Rotational Raman Scattering in Molecular Hydrogen," Phys. Rev. Lett. **93**, 123903-1 (2004).

[19] S. Ghosh, J. E. Sharping, D. G. Ouzounov, and A. L. Gaeta, "Resonant Optical Interactions with Molecules Confined in Photonic Band-Gap Fibers," Phys. Rev. Lett. **94**, 093902 (2005).

[20] F. Benabid, P. S. Light, F. Couny, and P. S. Russell, "Electromagnetically-induced transparency grid in acetylene-filled hollow-core PCF," Opt. Express **13**, 5694-5703 (2005).

[21] S. Ghosh, A. R. Bhagwat, C. K. Renshaw, S. Goh, A. L. Gaeta, and B. J. Kirby, "Nonlinear Optical Interactions with Rubidium Atoms Confined in a Hollow-Core Photonic Crystal Fiber," in *Proceedings of Conference on Lasers and Electro-Optics (CLEO)*, (Optical Society of America, 2006)

[22] F. Benabid, F. Couny, J. C. Knight, T. A. Birks, and P. S. J. Russell, "Compact, stable and efficient all-fibre gas cells using hollow-core photonic crystal fibres," Nature **434**, 488-491 (2005).

[23] M. Faheem, R. Thapa, and K. L. Corwin, "Spectral Hole Burning of Acetylene Gas inside a Photonic Bandgap Optical Fiber," in *Proceedings of Conference on Lasers and Electro-optics (CLEO)*, (Optical Society of America, 2005)

[24] J. Henningsen, J. Hald, and J. C. Petersen, "Saturated absorption in acetylene and hydrogen cyanide in hollow-core photonic bandgap fibers," Optics Express **13**, 10475 (2005).

[25] P. S. Light, F. Couny, F. Benabid, and P. S. J. Russell, "Electromagnetically-Induced Transparency and Saturable Absorption in All-Fiber Devices Based on Acetylene-Filled Hollow-Core PCF," in *Proceedings of European Conference on Optical Communication 2005 proceedings*, 6, 2005) 59.

[26] R. Thapa, K. Knabe, M. Faheem, A. Naweed, O. L. Weaver, and K. L. Corwin, "Saturated absorption spectroscopy of acetylene gas inside large-core photonic bandgap fiber," Opt. Lett. ***(in press)*** (2006).

[27] R. Thapa, K. L. Corwin, and B. R. Washburn, "Splicing Hollow-Core Photonic Bandgap Fiber to Step-Index Fibers Using an Arc Fusion Splicer," in *Proceedings of Conference on Lasers and Electro-Optics (CLEO)*, (Optical Society of America, 2006)

[28] J. A. West, C. M. Smith, N. F. Borrelli, D. C. Allan, and K. W. Koch, "Surface modes in air-core photonic band-gap fibers," Opt. Express **12**, 1485-1496 (2004).

[29] W. Demtröder, *Laser Spectroscopy*: Springer, 1996.

CW SUPERCONTINUUM GENERATION IN STANDARD OPTICAL FIBER OVER THE O, E, S AND C COMMUNICATION BANDS

Laura Abrardi[a], Sonia Martín-López[a], Ana Carrasco-Sanz[a], Miguel González-Herráez[a,b], Pedro Corredera[a] and Maria Luisa Hernanz[a]

[a] Departamento de Metrología, Instituto de Física Aplicada, (CSIC). Serrano, 144. 28006 Madrid, Spain.
[b] Departamento de Electrónica, Escuela Politécnica Superior, Universidad de Alcalá. Campus Universitario, 28871 Alcalá de Henares, Madrid, Spain.
abrardi@ifa.cetef.csic.es

***Abstract**: The generation of a broad CW supercontinuum source spanning from 1286 to 1538 nm is described. The device makes use of a tunable Yb-doped fiber laser, several silica fibers of adequate dispersion and a cascade of FBG mirrors that seed supercontinuum emission at 1318 nm. The source has an output power of 3 W and exhibits >0 dBm/nm spectral density over a range of more than 240 nm.*

1. Introduction

Supercontinuum (SC) generation in optical fibers and waveguides has attracted considerable research interest in the last years [1-12]. Applications of SC generation in optical fibers can now be found in fields such as optical frequency metrology [1,2], optical coherence tomography [3,4], and multiple optical carrier generation for wavelength-division multiplexing [5,6]. This renewed research interest in SC light sources has been made possible thanks to the recent development of special fibers with high nonlinearity, namely photonic crystal fibers [7] and dispersion-tapered fibers [8]. SC is typically obtained in those fibers by pumping them with high peak-power input pulses with durations ranging from several nanoseconds to several tens of femtoseconds. In these cases, SC results from the combined effects of self-phase modulation (SPM), four-wave mixing (FWM), and stimulated Raman scattering (SRS), that together lead to multisoliton generation and collision processes. It is important to realize however that pulsed laser sources are in principle not necessary to generate a broadband SC. SC generation under cw pumping was only achieved recently in optical fibers [9-12]. Of course, since cw sources do not benefit from the high peak-to-average power ratio of pulsed lasers, longer interaction lengths are required. The characteristic fiber lengths used in cw SC generation are in the km range even when highly nonlinear fibers are used [13]. Also, for a given average input power, short pulses produce much wider SC spectra than cw pumps. However, few pulsed lasers are able to generate the multi-watt average output powers that are typical of modern cw lasers such as cascaded Raman fiber lasers. Accordingly, for similar spectral widths, cw SC has a higher average power and exhibits a higher power spectral density than pulsed SC. Mean power densities of typical pulsed-pump SC usually range from -20 to -10 dBm/nm [1,7]. In comparison, we have demonstrated in a previous work a cw SC source with a peak power spectral density in excess of 8 dBm/nm, which represents an improvement of nearly two orders of magnitude [11]. CW SC generation in optical fibers is generally caused by the combined effect of modulation instability (MI) and stimulated Raman scattering (SRS). Efficient generation of a broad modulation instability spectrum can only be achieved in the region of very small anomalous dispersion ($D>0$ or $\beta_2<0$). The use of a long fiber with low loss ensures strong power transfer from pump to MI and a low SRS threshold (~1 W).

In these conditions, SC generation is possible with low peak power sources (and even cw as in this case) while allowing strong pump depletion and high power densities [12] (in the order of mW/nm in our case). In this paper we present a new design of cw-pumped SC source spanning over the O, E, S and C communication bands. The source makes use of a tunable Yb-doped fiber laser, several silica fibers of adequate dispersion and a cascade of FBG mirrors that seed supercontinuum emission at 1318 nm. The source has an output power of 3.0 W and exhibits >0 dBm/nm spectral density over a range of more than 240 nm.

2. Supercontinuum generation

To obtain the new cw SC centered at 1318 nm we use the experimental setup depicted in Fig. 1. The pump used in our experiment was a cw Yb-doped fiber laser tuned at 1104.4 nm. The output is single-mode and the power can be tuned in the range from 0.57 to 20 W. An isolator at the laser output prevents damage in the laser by back-reflected light. To obtain spectral broadening in a conventional fiber, one needs to have the pump tuned at wavelengths in small anomalous dispersion regimes. We seed the spectral broadening process in conventional fibers at 1318 nm by the use of a cascade of Fiber Bragg Grating mirrors (FBG) centered at 1318.0 nm, 1231.8 nm, and 1161.8 nm. These mirrors have reflection bandwidths of 3.12 nm, 1.73 nm, and 1.47 nm and reflectivity of 37.1%, 99.0%, and 99.4% respectively. A 1/99 coupler is inserted between the isolator and the FBG mirrors to monitor the power inserted into the system and the back-reflected light power. The nonlinear medium is a cascade of optical fibers of increasing zero-dispersion wavelengths, as shown in table 1. Finally the output spectrum is analyzed through an optical spectrum analyzer (OSA) after passing through a 10/90 and a 5/95 couplers that only act as fixed attenuators.

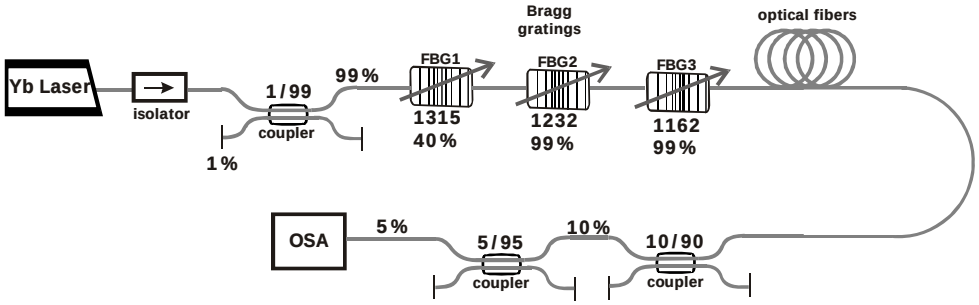

Fig. 1. Experimental setup. FBG: fiber Bragg grating; OSA: optical spectrum analyzer.

The zero-dispersion wavelength λ_0, dispersion slope S_0, loss coefficient α and length L are reported, for each fiber, in the table 1:

	λ_0 [nm]	S_0 [ps nm^{-2} km^{-1}]	α [dB km^{-1}]	γ [W^{-1} km^{-1}]	L [km]
Fiber 1	1302	0.085	0.35	0.4	6.0
Fiber 2	1307	0.087	0.33	0.4	8.0
Fiber 3	1311	0.083	0.34	0.4	2.0
Fiber 4	1312	0.085	0.34	0.4	2.0
Fiber 5	1416.9	0.085	0.34	0.4	2.0

Table 1. Properties of the cascade of optical fibers used in the experiment.

As it has been shown in earlier results [14], the non-linear broadening process that leads to supercontinuum generation is mainly caused by MI and stimulated Raman scattering by pumping high power cw light in small anomalous dispersion regimes. As we have said, the high-power output of our Yb-laser is tuned at 1104.4 nm. Hence, it lies well within the normal dispersion regime of standard fibers. Our experiment has, therefore, two parts: one is to shift the wavelength of the laser emission to around 1318 nm, where the standard fibers have small anomalous dispersion. Then, as the power is increased, the broadening caused by MI becomes more efficient, and the supercontinuum spectrum grows. To seed the emission in the anomalous dispersion regime, we use the cascade of Fiber Bragg Grating mirrors (FBG) described above.

The process of wavelength shift can be qualitatively described as follows: when we increase the laser pump power and we pass the Raman threshold we observe strong stimulated

Raman scattering (SRS). Backward SRS appearing at 1162 nm is reflected back into the fiber by FBG3, and is subsequently amplified as it propagates in the forward direction. The emission at 1162 nm acts as a laser and plays a similar role to the pump laser. The same principle with FBG2 and FBG1 gives rise to cascaded Raman frequency generation. In Fig. 2 we can see the spectrum obtained at the fiber output for different pump powers. The input powers have been measured at the input of FBG1. The isolator losses are approximately 1 dB.

At 3.1 W the first Raman peak at 1162 nm is clearly visible and the next Stokes order appears. At 5.7 W the second Raman peak at 1232 nm is also present, a new Raman peak appears at 1318 nm and depletion of the spectral lines at 1162 and 1232 nm begins to occur. In Fig. 2(b) the blue line represents the output spectrum for a pump power of 7.2 W. We can observe how for this pump power level there is enough power around 1318 nm to generate its own Raman gain curve at 1397 nm. We can see that at power levels higher than 7 W the spectral broadening starts to take place.

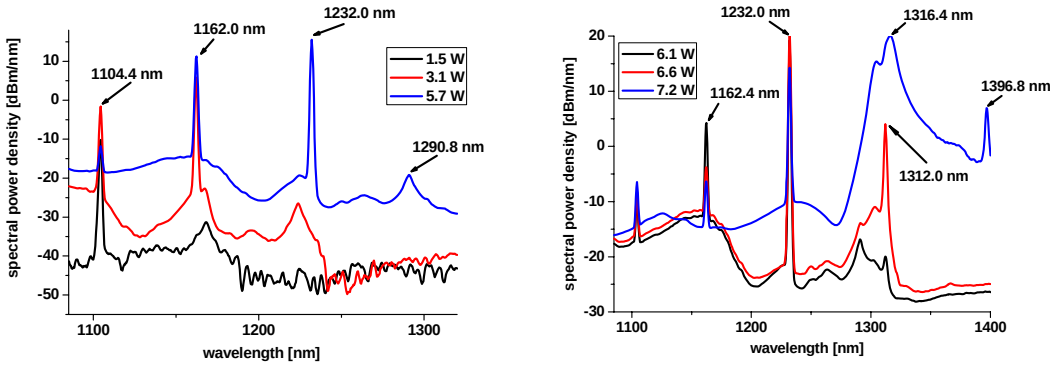

Fig. 2. Normalized output spectrum showing the Raman peaks at the output of the fiber for different input powers. (a) Spectra for input powers of 1.5, 3.1 and 5.7 W. (b) Spectra for input powers of 6.1, 6.6 and 7.2 W; we can observe the pump broadening around 1318 nm.

When the Raman gain curve centered at 1318 nm reaches certain power level the second part of our experiment starts. The first four fibers that we are using as amplifying medium have been chosen with their λ_0 next to 1318 nm as shown in table 1. In fact, the Raman peak at 1318 nm falls in the spectral region of small anomalous dispersion regime. In these conditions the process of supercontinuum generation starts [16,17]. As we can observe in Fig. 2(b), for 7.2 W of pump power, a Raman peak appears at 1397 nm. MI-induced soliton fission and Raman shift is also evident from the appearance of smooth red-shifted tails in the pump spectrum. Soliton generation is done mainly in the first kilometers of the fibers. The fibers are organized so as to have increasing λ_0 order, hence decreasing values of chromatic dispersion at 1318 nm. This organization enhances soliton compression, hence favours a broader supercontinuum. As the pump power grows SRS starts to play a more important role in the broadening process. The components of the Raman peak at 1397 nm are amplified too. The fifth fiber has its λ_0 at 1416.9 nm. We use it to try to reproduce the broadening process of 1318 nm at 1398 nm. In Fig. 3 the two output spectra for four and five fibers are depicted. We can observe how the presence of the fifth fiber improves the spectral width of our SC. The best results show a SC source in the 1300 nm spectral region with >260 nm spectral width when the input pump power grows up to 11 W. This new SC covers the O, E and S bands completely, and partially the C band.

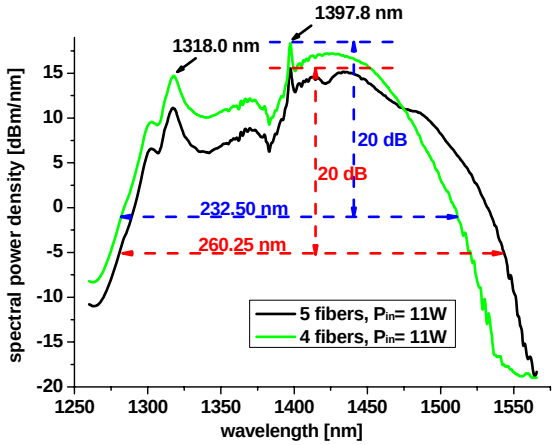

Fig. 3. Normalized supercontinuum spectrum at the fiber output for two different experimental configurations (4 and 5 fibers). Pump broadening covering the O, E, S and C bands is generated over >260 nm as measured 20-dB down from the highest peak.

Conclusions

We have demonstrated pump spectral broadening and supercontinuum generation spanning more than 260 nm over the O, E, S and C bands. This has been achieved by pumping a concatenation of conventional fibers with an Yb-doped fiber laser and a frequency-selective reflective structure that seeds supercontinuum emission at 1318 nm, in the regime of small anomalous dispersion of the fibers used in the experiment.

Acknowledgements

We acknowledge financial support from the Ministerio de Educación y Ciencia through the project TIC2003-01869 and the corresponding FPI contract, the support from the Comunidad Autónoma de Madrid through project FACTOTEM_CM ref n. S-0505/ESP/0417 and the support from the CSIC, through the I3P grant program co-supported by the Social European Fund.

References

[1] S. A. Diddams, D. J. Jones, J. Ye, S. T. Cundiff, J. L. Hall, J. K. Ranka, R. S. Windeler, R. Holzwarth, T. Udem, and T. W. Hansch, Phys. Rev. Lett. (84) 5102-5105 (2000)

[2] D. J. Jones, S. A. Diddams, J. K. Ranka, A. Stentz, R. S. Windeler, J. L. Hall and S. T. Cundiff, Science. (288) 635-639 (2000)

[3] D. L. Marks, A. L. Oldenburg, J. J. Reynolds and S. A. Boppart, Opt. Lett., (bf 27) 2010-2012 (2002)

[4] Hartl, X. Li, C. Chudoba, R. Ghanta, T. Ko, J. G. Fujimoto, J. K. Ranka and R. S. Windeler, Opt. Lett. (26) 608-610 (2001)

[5] T. Morioka, K. Mori and M. Saruwatari, Electron. Lett. (29) 862-864 (1993)

[6] H. Takara, T. Ohara and K. Sato, Electron. Lett. (39) 1078-1079 (2003)

[7] S. Coen, A. Hing Lun, R. Leonhardt, J. D. Harvey, J. C. Knight, W. J. Wadsworth and P. St. J. Russell, J. Opt. Soc. Am B (19) 753-763 (2002)

[8] T. A. Birks, W. J. Wadsworth and P. St. J. Russell, Opt. Lett. (25) 1415-1417 (2000)

[9] M. Prabhu, N. S. Kim and K. Ueda, Jpn. J. Appl. Phys. (39) L291-L294 (2000)

[10] J. W. Nicholson, A. K. Abeeluck, C. Headley, M. F. Yan and C. G. Jorgensen, Appl. Phys. B, (77) 211-218 (2003)

[11] M. Gonzalez-Herraez, S. Martin-Lopez, P. Corredera, M. L. Hernanz and P. R. Horche, Opt. Commun. (226) 323-328 (2003)

[12] A. V. Advokhin, S. V. Popov and J. R. Taylor, Opt. Lett. (28) 1353-1355 (2003)

[13] A. K. Abeeluck, C. Headley, and C. G. Jørgensen, Opt. Lett. (**29),** 2163–2165 (2004).

[14] F. Vanholsbeeck, S. Martin-Lopez, M. Gonzalez-Herraez and S. Coen, Opt. Exp. (13) 6615-6625 (2005)

[15] S.V. Smirnov, J.D. Ania-Castanon, T.J. Ellingham, S.M. Kobtsev, S. Kukarin, S.K. Turitsyn, Opt. Fiber Techn. (12) 122 (2006)

[16] G. P. Agrawal, Applications of Nonlinear Fiber Optics, Academic Press, San Diego (1991)

A C-band optical frequency synthesizer using 1.5 micron NICE OHMS frequency standards and an optical frequency comb generator

C. S. Edwards[1,2], H S. Margolis[1], G. P. Barwood[1], P. Gill[1,2] and W. R. C. Rowley[1]

[1]National Physical Laboratory,
Hampton Road, Teddington, Middlesex TW11 0LW United Kingdom
E-mail christopher.edwards@npl.co.uk
[2]Blackett Laboratory, Imperial College London,
South Kensington Campus, London SW7 2BZ, United Kingdom

Abstract: Two acetylene frequency standards, which make use of the NICE OHMS technique, have been developed in the 1.5 μm region. A summary of their performance will be presented, along with some recently measured frequency values for lines in the $\nu_1 + \nu_3$ combination band of $^{13}C_2H_2$. It is planned to use the standards in conjunction with an optical frequency comb generator to demonstrate arbitrary frequency synthesis with kHz absolute accuracy in the spectral region 1.52 to 1.56 μm.

1. Introduction

There is considerable interest in the use of semiconductor lasers as frequency standards for optical telecommunications in the 1.5 μm region using Doppler-free acetylene spectra [1-7]. The most commonly used experimental arrangement utilises conventional cavity-enhanced saturation absorption spectroscopy [1-6], where an acetylene cell is placed inside an enhancement cavity. Relative stabilities of a few parts in 10^{12} at 1 s have been reported using this method [4-6], falling to a floor of a few parts in 10^{14} for a few thousand seconds averaging time [5, 6]. The relative frequency stability of these systems is limited by the residual differential frequency variation between the laser and the enhancement cavity resonance, which introduces amplitude noise on the transmitted light, thus degrading the signal-to-noise ratio of the acetylene features. The technique of Noise Immune Cavity-Enhanced Optical Heterodyne Molecular Spectroscopy (NICE OHMS) was developed to address this problem [8]. Although this technique has been used before for acetylene spectroscopy at 1.54 μm [3], the performance achieved was not superior to that demonstrated with conventional cavity-enhanced spectroscopy. This paper describes work aimed at improving on the best relative frequency stability results reported to date [4-6]. It is planned to use the NICE OHMS systems in conjunction with an optical frequency comb generator (OFCG) [6] to demonstrate arbitrary frequency synthesis in the spectral region 1.52 to 1.56 μm, with the potential for long-range dissemination of reference frequencies via fiber-optic network to end users in industry. In addition, as transportable local oscillators with a relative stability superior to that of a GPS-disciplined quartz oscillator, the NICE OHMS standards are candidates for use in a transportable fiber laser femtosecond comb system for *in situ* frequency metrology and other applications.

2. NICE OHMS Standards

The experimental arrangement of one of the NICE OHMS standards is shown in Fig.1. The output of the diode laser is directed through a Faraday isolator and via a polarizing beamsplitter through two electro-optic phase modulators. One of these adds a pair of 8 MHz sidebands to the carrier frequency (with modulation index β = 0.7) which are used for Pound-Drever-Hall (PDH) locking to the enhancement cavity. The PDH locking narrows the laser linewidth from 2 MHz to 50 kHz full-width-at-half-maximum (FWHM). The enhancement cavity has a finesse of ~ 150 and contains a

sealed 200-mm Brewster-windowed cell containing 1.0 (3) Pa of $^{13}C_2H_2$ controlled at a temperature of 25.0 ± 0.5°C. The one-way intra-cavity power density is typically 0.20 Wmm^{-2}. The cavity length is dithered via a piezo-electric transducer (PZT) at 800 Hz, and this modulates the laser frequency to a depth of 1 MHz peak-to-peak. The other electro-optic modulator adds another pair of sidebands at 490 MHz (β = 0.3), this frequency corresponding to the free-spectral range of the enhancement cavity. These sidebands are transmitted through the cavity and are used in the NICE OHMS detection scheme [8]. Interference between the carrier and these sidebands gives rise to an acetylene signal at 490 MHz which is demodulated using a double-balanced mixer (DBM) and subsequently demodulated at the second harmonic (1.6 kHz) of the cavity dither frequency to give a locking discriminant. Any differential frequency noise between the cavity resonance and the carrier frequency affects the transmitted sidebands in the same way, and so there is a high degree of common mode cancellation of this noise on the observed acetylene signal. This "noise immune" character is the principal advantage of the NICE OHMS technique. A summary of the systems' relative stability and parametric sensitivities will be presented in this paper, as well as an assessment of their longer term reproducibility.

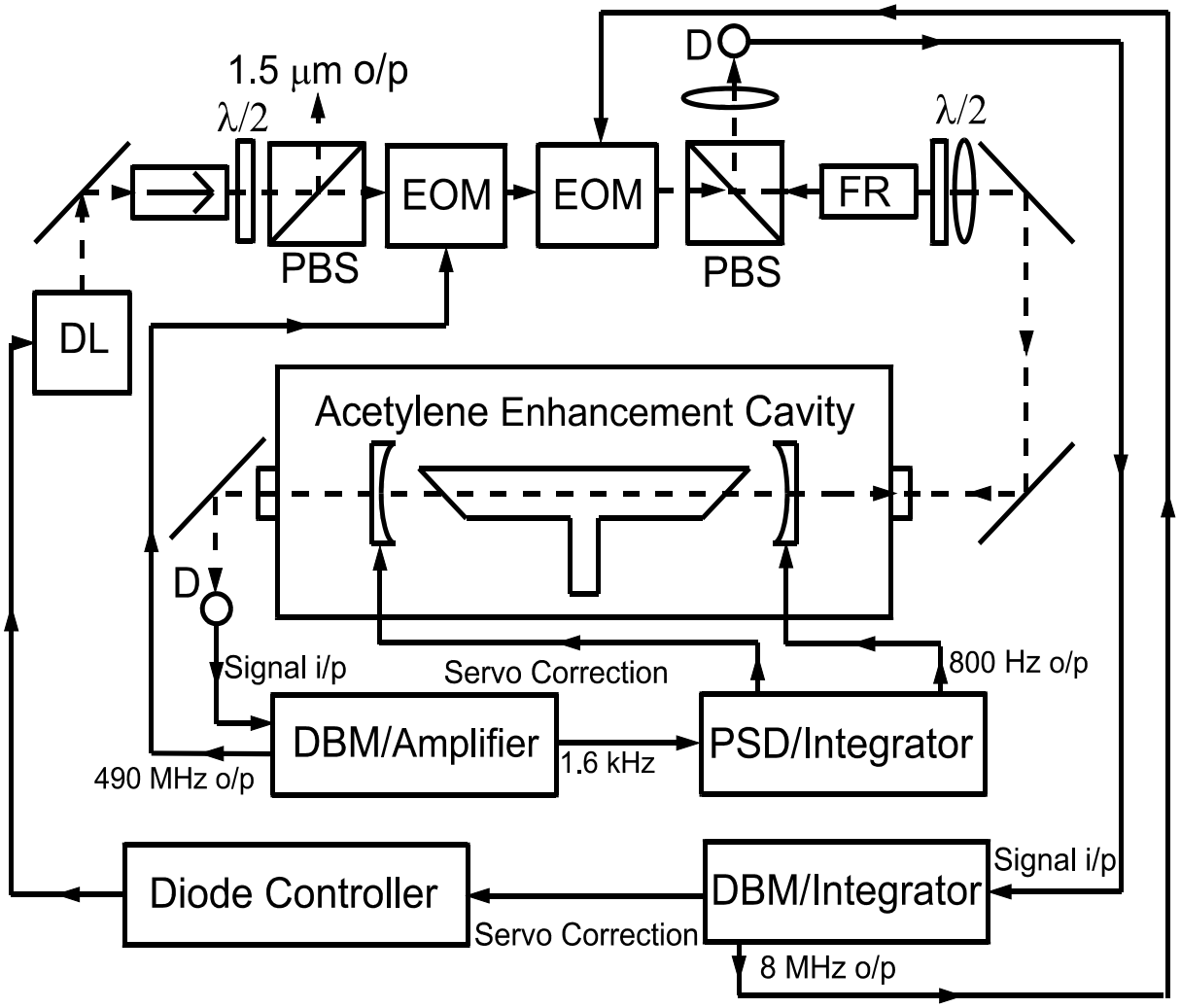

Fig. 1: Experimental arrangement of a NICE OHMS acetylene standard. Key:- DL ≡ diode laser, PBS ≡ polarizing beamsplitter, EOM ≡ electro-optic modulator, FR ≡ Faraday rotator, D ≡ photodiode, DBM ≡ double-balanced mixer, PSD ≡ phase-sensitive detector.

3. Absolute Frequency Measurements and Synthesis

Three experimental techniques are used to measure the acetylene transition frequencies. In the first, a combined frequency chain and self-referenced TiS femtosecond comb system [5] have been used to determine a few reference frequencies. Using these reference frequencies, an acetylene standard is used to drive an OFCG, resulting in a comb of known frequencies which can be used to measure some unknown acetylene frequencies [6]. Thirdly, it is planned to use a fiber femtosecond comb [9] to make direct absolute frequency measurements. The measurements to date have resulted in a set of acetylene frequency values with fractional uncertainties in the range 10^{-11} to 10^{-12}, limited only by the reproducibility of the standards.

The experimental arrangement for optical frequency synthesis is shown in Fig. 2.

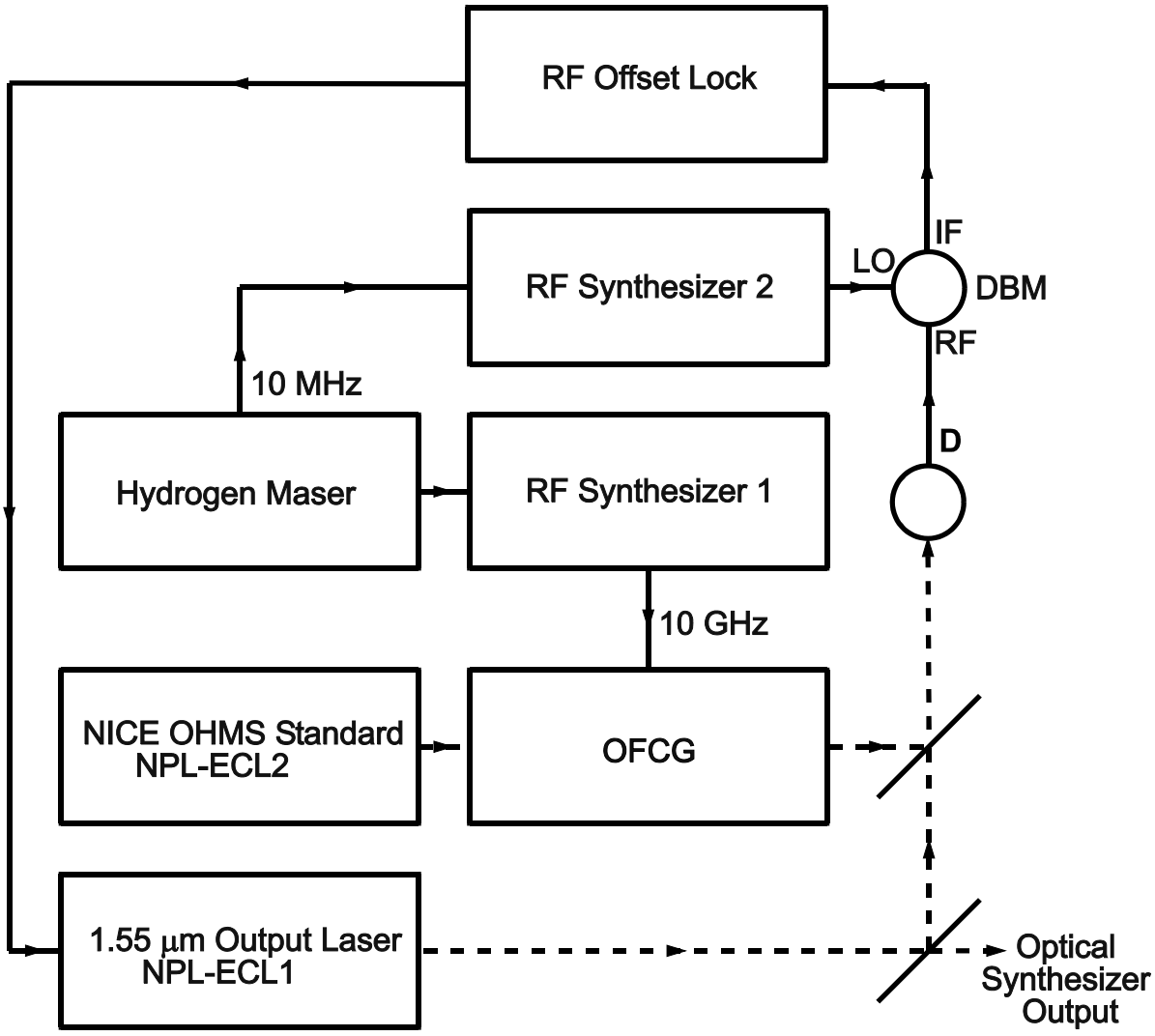

Fig. 2: Optical Synthesizer Set-Up.
Key:- D ≡ photodiode, DBM ≡ double-balanced mixer

The OFCG used in this work has been described in detail elsewhere [6]. An electro-optic modulator is placed in a build-up cavity whose free spectral range is a sub-harmonic of the applied rf drive frequency

of 10 GHz. An applied rf power of 1 W gives a modulation index $\beta \sim 0.3$. This results in a comb of modes with a usable span of ~ 800 GHz. The comb is driven by NPL-ECL2 operated as a NICE OHMS acetylene standard, and the output of the comb is mixed with light from NPL-ECL1, which provides the optical synthesizer output. The detected beat frequency is mixed with the output of rf synthesizer 2 to give a residual beat frequency which is stabilized at 50 MHz using the rf offset lock electronics. As the absolute frequency of the NICE OHMS standard is known, together with the comb order number, the rf synthesizer frequency and the offset beat frequency, the optical synthesizer frequency of the output laser is determined by the choice of acetylene line and the frequency of rf synthesizer 2, and so the optical output frequency can be arbitrarily chosen in the range 193 to 197 THz.

Summary

A pair of NICE OHMS acetylene standards have been developed for use as frequency standards in the 1.5 μm region. The frequencies of various acetylene transitions have been measured with uncertainties in the range 10^{-11} to 10^{-12}, corresponding to an uncertainty range 0.02 to 0.002 fm in vacuum wavelength. When combined with an OFCG, they will form an optical frequency synthesizer capable of sub-kilohertz accuracy.

Acknowledgements

This work was funded by the National Measurement System Length Programme. C S Edwards would like to acknowledge useful discussions with Prof R C Thompson of Imperial College London (UK).

References

[1] K. Nakagawa, M. de Labachelerie, Y. Awaji and M. Kourougi, “Accurate optical frequency atlas of the 1.5 μm bands of acetylene,” *J. Opt. Soc. Am. B*, vol. 13, pp. 2708-2714, 1996.

[2] A. Onae, K. Okumura, J. Yoda, K. Nakagawa, A. Yamaguchi, M. Kourogi, K. Imai and B. Widiyatomoko, “Toward an Accurate Frequency Standard at 1.5 μm Based on the Acetylene Overtone Band Transition,” *IEEE Trans. Instrum. Meas.,* vol. 48, pp. 563-566, 1999.

[3] T. Kurosu and U Sterr, "Frequency-stabilization of a 1.54 micrometer DFB-laser diode to Doppler-free absorption lines of acetylene," *Proc. SPIE*, vol. 4269, pp. 248-254, 2001.

[4] A. Czajkowski, J. E. Bernard, A. A. Madej and R. S. Windeler, "Absolute frequency measurement of acetylene transitions in the region of 1540 nm," *Appl. Phys. B*, vol. 79, pp. 45-50, 2004.

[5] C. S. Edwards, H. S. Margolis, G. P. Barwood, S. N. Lea, P. Gill, G. Huang and W. R. C. Rowley, "Absolute frequency measurement of a 1.5-μm acetylene standard by use of a combined frequency chain and femtosecond comb," *Opt. Lett.*, vol. 29 , pp. 566-568 , 2004.

[6] C. S. Edwards, H. S. Margolis, G. P. Barwood, S. N. Lea, P. Gill and W. R. C. Rowley, "High-accuracy frequency atlas of $^{13}C_2H_2$ in the 1.5 μm region," *Appl. Phys. B*, vol. 80, pp. 977-983, 2005.

[7] P. Balling, M. Fischer, P. Kubina and R. Holzwarth, "Absolute frequency measurement of wavelength standard at 1542 nm: acetylene stabilized DFB laser," *Opt. Express*, vol. 13, pp. 9196-9201, 2005.

[8] J. Ye, L.-S. Ma and J. L. Hall, "Ultrasensitive detections in atomic and molecular physics: demonstration in molecular overtone spectroscopy," *J. Opt. Soc. Am. B*, vol. 15 pp. 6-15, 1998.

[9] P. Kubina, P. Adel, F. Adler, G. Grosche, T. W. Hänsch, R. Holzwarth, A. Leitenstorfer, B. Lipphardt and H. Schnatz, "Long term comparison of two fiber based frequency comb systems," *Opt. Express*, vol. 13, pp. 904-909, 2005.

PMD: Measurement method linkages

T.A. Hanson, Corning, Inc.
27-Mar-06

Introduction

The study of polarization mode dispersion (PMD) in terms of both measurements and system impairments has gone on for over fifteen years in Standards developments as well as other venues. Some open issues remain, but many were closed with the Consent of ITU-T Recommendation G.650.2 in December, 2004. This Recommendation clarified the definitions and relationships of the different measurement methods for first order PMD. Since then, the IEC Standards have been in an update process. See for example, 60793-1-48 for measurement of fiber and cable, or the general theory and guidance document, 61282-9. This paper will try to illuminate the main mathematical aspects of the learnings obtained in this convergence process. Although numerous references exist, only a few will be cited here.

Background

PMD measurements can be considered as falling into two broad categories: the frequency domain methods such as Stokes Parameter Evaluation (JME and PSA) and the time domain methods such as Interferometric or the Fixed Analyzer FFT methods. As a parameter, the PMD value is representative of a wavelength or optical frequency range. For the frequency domain methods, a parameter called differential group delay (DGD) is determined for individual optical frequencies in the range. The PMD value is reported as either the linear average or root-mean-square (RMS) of these values. For the time domain measurements, the aggregate of PMD effects across the frequency range is measured all together and the relationship to RMS PMD value for the frequency range of the source is deduced.

System impairments are most easily considered in the frequency domain. The field of the signal that would be obtained without PMD, but with the inclusion of other effects such as chromatic dispersion can be considered in the time domain as f(t). The Fourier transform of this complex scalar function can be considered as F(ω) where ω is the angular frequency deviation about some central frequency, ω_0. This is multiplied with the two dimensional complex output Jones vector, $\hat{j}(\omega)$, representing PMD induced variance in the neighborhood of ω_0. Inverse Fourier transformation yields the composite time domain image of the signal as a complex two dimensional vector. Conversion to power yields the time domain PMD adjusted signal. Differences in the result, with or without PMD effects, gives an indication of the impairment. This impairment is due only to variation in the output Jones vector with optical frequency and power variations that could arise from polarization dependent loss, which will not be discussed in this paper.

Many aspects of PMD can be simplified by considering coordinate transformations. The situation for first order PMD can be stated as: There is a coordinate system where the

output Jones vector can be expressed as: $\hat{j}(\omega)^T = \left[c_x e^{-i\gamma'\omega} \quad c_y e^{i\gamma'\omega}\right]$, where c_x and c_y represent the complex output Jones vector at ω_0.

When this vector is multiplied with the signal in the frequency domain and then the results are converted back to the time domain one obtains the vector function, $\hat{f}_{PMD}(t)^T = \left[c_x f_{PMDx}(t) \quad c_y f_{PMDy}(t)\right]$.

The functions $f_{PMDx/y}(t)$ are shifted up and down by $\pm\Upsilon$' from the center which would be seen without PMD. The time domain power function, $P(t) = \hat{f}^*_{PMD}(t)\hat{f}_{PMD}(t)$, is the weighted total of the two split signals (where * represents the transpose complex conjugate). The constants can be adjusted so one or another of the split signals disappears – or so that both have equal power. In the latter case, the impairment is maximal. The difference between the centers of these two split signals is called the differential group delay, $\Delta\tau = 2\gamma'$. The reason for keeping a separate parameter, Υ', is to facilitate a more general description given in terms of a rotation angle.

The variance of the output Jones vector can include higher order effects – which can be described as more complicated output variance functions which might be needed for a consideration of a broad signal spectrum. The signal bit rate and format can therefore affect the range of frequencies that are important and therefore the importance of higher order PMD. This paper will focus on first order PMD.

Stokes and Jones relationships

Poole [1] described PMD in terms of the normalized output Stokes vector, $\hat{s}(\omega)$, a rotation matrix, R(ω), and an input normalized Stokes vector, $\hat{s}_{IN}$, assumed to be frequency invariant. Jones [2] described PMD in terms of an output Jones vector, $\hat{j}(\omega)$, a transfer matrix, T(ω), and an input Jones vector, $\hat{j}_{IN}$. One may wonder why the Stokes representation is important. Reasons include:

- One does not measure Jones vectors, one measures Stokes vectors
- The Stokes vector representation will be important for the development of the interferometric method

The normalized Stokes vector is a three dimensional vector that moves on the Poincaré sphere. The values are obtained by measuring the power through a polarizer set at three pairs of orthogonal settings. The three values are the differences in power between the two orthogonal settings for each pair. The relationship between the Stokes and Jones vectors can be expressed in terms of a polar coordinate system defined as:

$$\hat{j} = \begin{bmatrix} e^{-u/2}\cos\theta \\ e^{i\mu/2}\sin\theta \end{bmatrix} \quad \Leftrightarrow \quad \hat{s} = \begin{bmatrix} \cos 2\theta \\ \sin 2\theta\cos\mu \\ \sin 2\theta\sin\mu \end{bmatrix} \tag{1a}$$

The three polarizer pairs used to measure the Stokes vectors are:

$$\begin{bmatrix}\theta\\ \mu\end{bmatrix}=\left\{\begin{bmatrix}0\\ 0\end{bmatrix},\begin{bmatrix}\pi/2\\ 0\end{bmatrix}\right\},\left\{\begin{bmatrix}\pi/4\\ 0\end{bmatrix},\begin{bmatrix}-\pi/4\\ 0\end{bmatrix}\right\},\left\{\begin{bmatrix}\pi/4\\ \pi/2\end{bmatrix},\begin{bmatrix}\pi/4\\ -\pi/2\end{bmatrix}\right\} \tag{1b}$$

The first two pairs are called linear states and the last are circular states.

The parallelism of Jones and Stokes are shown as the following pairs, which are also defined in terms of the output vectors at the central frequency, $\hat{j}(\omega_0)$ and $\hat{s}(\omega_0)$:

$$\hat{j}(\omega)=T(\omega)\hat{j}_{IN} \qquad \hat{s}(\omega)=R(\omega)\hat{s}_{IN} \tag{2a}$$

$$\frac{d\hat{j}(\omega)}{d\omega}\Big|_0=\frac{dT(\omega)}{d\omega}\Big|_0 T^{-1}(\omega_0)\hat{j}(\omega_0) \qquad \frac{d\hat{s}(\omega)}{d\omega}\Big|_0=\frac{dR(\omega)}{d\omega}\Big|_0 R^{-1}(\omega_0)\hat{s}(\omega_0) \tag{2b}$$

For first order PMD, these can be further expressed as the following, which will be further elaborated.

$$\frac{d\hat{j}(\omega)}{d\omega}\Big|_0=-\frac{i}{2}\begin{bmatrix}\Omega_1 & \Omega_2-i\Omega_3\\ \Omega_2+i\Omega_3 & -\Omega_1\end{bmatrix}\hat{j}(\omega_0) \qquad \frac{d\hat{s}(\omega)}{d\omega}\Big|_0=\hat{\Omega}\times\hat{s}(\omega_0) \tag{3}$$

Ω_x are the elements of the three dimensional polarization dispersion vector (pdv), $\hat{\Omega}$, which is related to the differential group delay, $\Delta\tau$, and principle state of polarization (PSP) vector, $\hat{p}$, as $\hat{\Omega}=\Delta\tau\bullet\hat{p}$. If the output state is aligned with the PSP, there is, to the first order, no change with respect to frequency.

The jump from (2b) to (3) is done by representing T and R with polarimetric coordinates, θ_T, μ_T, rotation angles $2\Upsilon_T=\Upsilon_R$, and rotation vector, y. The matrix, T, is represented as an orthogonal decomposition where the elements of S are the eigenvalues:

$$T=VSV^* \text{ where } V=\begin{bmatrix}\cos\theta_T e^{-i\mu_T/2} & -\sin\theta_T e^{-i\mu_T/2}\\ \sin\theta_T e^{i\mu_T/2} & \cos\theta_T e^{i\mu_T/2}\end{bmatrix},\ S=\begin{bmatrix}e^{-i\gamma_T} & 0\\ 0 & e^{i\gamma_T}\end{bmatrix} \tag{4}$$

$$R=\hat{y}\hat{y}^T(1-\cos\gamma_R)+I\cos\gamma_R+[\hat{y}\times]\sin\gamma_R\ ,$$
$$\hat{y}^T=\begin{bmatrix}\cos 2\theta_T & \sin 2\theta_T\cos\mu_T & \sin 2\theta_T\sin\mu_T\end{bmatrix} \tag{5}$$

$$T=\begin{bmatrix}\cos\gamma_T-iy_1\sin\gamma_T & -(y_3+iy_2)\sin\gamma_T\\ (y_3-iy_2)\sin\gamma_T & \cos\gamma_T+iy_1\sin\gamma_T\end{bmatrix} \tag{6}$$

Using the Jones/Stokes association defined in (1a), T and R are equivalent in that: The Stokes vectors given by the conversion of Jones input and output vectors derived from T are also given by R. When the first column of the matrix, V, is converted to a Stokes vector using (1a), the result is the rotation vector, y.

Expansion of (2b) results in the following differential equation, which can also be written out in polarimetric coordinates to yield both expressions in (3). This differential equation follows from (2b) and allows writing (3).

$$\hat{\Omega} = 2\frac{d\gamma_T}{d\omega}\hat{y} + \sin 2\gamma_T \frac{d\hat{y}}{d\omega} + 2\sin^2\gamma_T\left(\hat{y}\times\frac{d\hat{y}}{d\omega}\right) \tag{7}$$

If one sets $\Delta\tau/2 = \Upsilon'$, one can write the left part of (3) as an orthogonal decomposition:

$$\frac{d\hat{j}(\omega)}{d\omega}\Big|_0 = V_P D V_p^* \hat{j}(\omega_0),\ V_p = \begin{bmatrix} \cos\theta_p e^{-i\mu_p/2} & -\sin\theta_p e^{-i\mu_p/2} \\ \sin\theta_p e^{i\mu_p/2} & \cos\theta_p e^{i\mu_p/2} \end{bmatrix},\ D = \begin{bmatrix} -i\gamma' & 0 \\ 0 & i\gamma' \end{bmatrix} \tag{8}$$

The first column of V_p converts to the PSP vector, $\hat{p}$. Assuming that this vector is locally fixed, one has a local solution for the output Jones vector given as:

$$\hat{j}(\omega) = V_p S_J(\omega) V_p^* \hat{j}(\omega_0) = J(\omega)\hat{j}(\omega_0),\ \text{where}\ S_J(\omega) = \begin{bmatrix} e^{-i\gamma'\omega} & 0 \\ 0 & e^{i\gamma'\omega} \end{bmatrix} \tag{9}$$

Equation 9 is in the same form as what is used to describe the first order PMD impairment. The change in coordinates can be done by pre and post multiplying J by V_p^* and V_p. This concludes the connection between the Stokes and Jones formulations for the first order PMD and differential group delay. This equation is also associated with a Stokes vector rotation which increases as the frequency deviation increases. The rotation angle on the Poincaré is equal to $2\Upsilon'\omega$. The rotation vector is the PSP.

Stokes parameter analysis measurements

Both these methods, Jones Matrix Eigenanalysis (JME) and Poincaré Sphere Analysis (PSA), are based on measuring the normalized Stokes vectors at multiple optical frequencies, incremented with $\Delta\omega$. For each frequency, three orthogonal input states are sampled to obtain three orthogonal output states. The states are normally given by the (θ,μ) pairs: (0,0), $(\pi/4,0)$ and $(\pi/4,\pi/2)$, but others are possible.

For JME, the output states are converted to Jones vectors using (1a) and an assumption that $0\le\theta\le\pi$. The ratio of the x and y elements is taken to eliminate the one π ambiguity and the application of the left part of (2a) yields estimates of the T matrix at the different frequencies. Using (9), one can then write:

$$T(\omega_0+\Delta\omega) = J(\Delta\omega)T(\omega_0) \tag{10}$$

The argument of the ratio of the eigenvalues of $T(\omega_0+\Delta\omega)T^{-1}(\omega_0)$, divided by $\Delta\omega$, yields $2\Upsilon' = \Delta\tau$ for frequency ω_0. The eigenvalues are the elements of $S_J(\Delta\omega)$.

For the PSA method, the rotation on the Poincaré sphere is considered. From (9) and a consideration that this relates to such a rotation, we have that the rotation angle swept out

is equal to $\Delta\tau\Delta\omega$. The change in output Stokes vectors from one frequency to the next is related to the angle, α, of the output state to the PSP, which is the frequency-domain rotation vector. The following output difference applies to each input state:

$$\left|\Delta s\right| = 2\sin\alpha\sin\left(\frac{\Delta\tau\Delta\omega}{2}\right) \tag{11}$$

If the three orthogonal input/output states are designated as $\hat{h}$, $\hat{q}$ and $\hat{c}$ for both ω_0 and $\omega_0+\Delta\omega$ they can be combined to yield:

$$\left|\Delta\hat{h}\right|^2 + \left|\Delta\hat{q}\right|^2 + \left|\Delta\hat{c}\right|^2 = 4\sin^2\left(\frac{\left|\hat{\Omega}\right|\Delta\omega}{2}\right)\cdot\left[\sin^2(\alpha_h)+\sin^2(\alpha_q)+\sin^2(\alpha_c)\right] \tag{12}$$

The sum of $\sin^2$ terms on the right side expression is equal to two because of the orthogonality of the vectors. The arcsine formula follows.

Interferometric measurements

Gisan [3] and later Cyr [4] elaborated on the interferometric measurement method. Most of what is given in this section is a paraphrasing of the work of Cyr.

From Chamberlain [5], equation 4.17 gives the formula for the measured interferogram for a polychromatic source, $S(\omega)$. It is the sum of a constant and the Fourier cosine transform of the source.

The measurement of a single interferogram involves setting up a polarizer at the input and one at the output and usually uses a broadband source. The field that emerges from the output can be considered as $S_0^{1/2}(\omega)P(\theta_{POL})T(\omega)\hat{j}_{IN}$, where $P(\theta_{POL})$ is the output polarizer with setting θ_{POL}, T is the Jones transfer matrix, and $S_0(\omega)$ is the power spectrum before the output polarizer. The output spectrum going into the inteferometer, $S(\omega)$, is equal to this vector multiplied with its transpose complex conjugate. The non-constant part of the interferogram, $R(\tau)$, and this spectrum are related as:

$$R(\tau) = \sqrt{\frac{2}{\pi}}\int_0^\infty S(\omega)\cos(\omega\tau)d\omega \text{ and } S(\omega) = \sqrt{\frac{2}{\pi}}\int_0^\omega R(\tau)\cos(\omega\tau)d\tau \tag{13}$$

Invoking the Parseval theorum, it can be shown that (13) is equivalent to:

$$\int_0^\infty S^2(\omega)d\omega = 2\int_0^\infty R^2(\tau)d\tau \quad \text{and} \qquad \int_0^\infty\left[\frac{dS(\omega)}{d\omega}\right]^2 d\omega = \int_{-\infty}^\infty \tau^2 R^2(\tau)d\tau \tag{14}$$

The spectrum out of the polarizer can also be written as the sum of the input and a normalized Stokes vector product, of the output Stokes vector and the Stokes vector associated with polarizer, $x(\omega) = \hat{s}(\omega)\bullet s_{POL}$.

$$S(\omega)=\frac{1}{2}\left[S_0(\omega)+S_x(\omega)\right]=\frac{1}{2}\left[S_0(\omega)+x(\omega)S_0(\omega)\right] \tag{15}$$

The definition of $S_0(\omega)$ and $S_x(\omega)$ allow the definition of their Fourier cosine tranform pairs, $R_0(\tau)$ and $R_x(\tau)$.

Rotation of the output polarizer to 90° from initial results in a new set of variables designated here with subscript $\perp$ as $x_\perp(\omega)$, $R_\perp(\tau)$, $S_\perp(\omega)$, $S_{x\perp}(\omega)$, and $R_{x\perp}(\tau)$. Because $x_\perp(\omega) = - x(\omega)$:

$$\frac{1}{2}\left(R(\tau)+R_\perp(\tau)\right)=R_0(\tau) \qquad \frac{1}{2}\left(R(\tau)-R_\perp(\tau)\right)=R_x(\tau) \tag{16}$$

The RMS relationships of these function are given as the following, where the expected value operator is with respect to random input and output polarizer settings, which can be assured by polarization scrambling:

$$\sigma_x^2=\frac{\int_{-\infty}^{\infty}\tau^2\left\langle R_x^2(\tau)\right\rangle d\tau}{\int_{-\infty}^{\infty}\left\langle R_x^2(\tau)\right\rangle d\tau}=\frac{\int_0^{\infty}\left\langle\left(\frac{dS_x(\omega)}{d\omega}\right)^2\right\rangle d\omega}{\int_0^{\infty}\left\langle S_x^2(\omega)\right\rangle d\omega} \qquad \sigma_0^2=\frac{\int_{-\infty}^{\infty}\tau^2\left\langle R_0^2(\tau)\right\rangle d\tau}{\int_{-\infty}^{\infty}\left\langle R_0^2(\tau)\right\rangle d\tau}=\frac{\int_0^{\infty}\left\langle\left(\frac{dS_0(\omega)}{d\omega}\right)^2\right\rangle d\omega}{\int_0^{\infty}\left\langle S_0^2(\omega)\right\rangle d\omega} \tag{17}$$

From equation 15, we have $\frac{dS_x(\omega)}{d\omega}=\frac{dx(\omega)}{d\omega}S_0(\omega)+x(\omega)\frac{dS_0(\omega)}{d\omega}$, which leads to:

$$\left\langle\left(\frac{dS_x(\omega)}{d\omega}\right)^2\right\rangle=\left\langle\left(\frac{dx(\omega)}{d\omega}\right)^2\right\rangle S_0^2(\omega)+2\left\langle x(\omega)\frac{dx(\omega)}{d\omega}\right\rangle S_0(\omega)\frac{dS_0(\omega)}{d\omega}+\left\langle x^2(\omega)\right\rangle\left(\frac{dS_0(\omega)}{d\omega}\right)^2 \tag{18}$$

A consideration of the random relationship of the polarizer to the output Stokes vector lead to (19) and then to (20), which is a simplification of (18):

$$\left\langle\left(\frac{dx(\omega)}{d\omega}\right)^2\right\rangle=\frac{1}{3}\left\langle\left|\frac{ds(\omega)}{d\omega}\right|^2\right\rangle \text{ and} \qquad \left\langle S_x^2(\omega)\right\rangle=\frac{1}{3}S_0^2(\omega) \tag{19}$$

$$\left\langle\left(\frac{dS_x(\omega)}{d\omega}\right)^2\right\rangle=\frac{1}{3}S_0^2(\omega)\left\langle\left|\frac{ds(\omega)}{d\omega}\right|^2\right\rangle+\frac{1}{3}\left(\frac{dS_0(\omega)}{d\omega}\right)^2 \tag{20}$$

The relationship to the DGD is based on the following:

$\hat{\Omega}(\omega)=\Delta\tau(\omega)\hat{p}(\omega)$ and (21a)

$$\frac{d\hat{s}(\omega)}{d\omega}=\hat{\Omega}(\omega)\times\hat{s}(\omega)=\Delta\tau(\omega)\left(\hat{p}(\omega)\times\hat{s}(\omega)\right)=\hat{u}(\omega)\Delta\tau(\omega)\sin\theta \tag{21b}$$

where θ is the angle between the PSP and output Stokes vector, and $\hat{u}$ is a vector orthogonal to both.

The random relative orientations of the PSP and output Stokes vector lead to the expected value relationship:

$$\left\langle \left| \frac{d\hat{s}(\omega)}{d\omega} \right|^2 \right\rangle = \Delta\tau(\omega)\left\langle \sin^2(\theta) \right\rangle = \frac{2}{3}\Delta\tau^2(\omega) \tag{22}$$

The results of (17), (18), (20), and (22) are combined to yield:

$$\frac{3}{2}\left(\sigma_x^2 - \sigma_0^2\right) = \frac{\int_0^\infty \Delta\tau^2(\omega) S_0^2(\omega) d\omega}{\int_0^\infty S_0^2(\omega) d\omega} \tag{23}$$

The square root of (23) is the spectrally (squared) weighted RMS of the DGD, which is one way to represent the PMD. Simulations have shown that the statistics resulting from this method are equivalent to those from using the JME in the case of random mode coupling, where Δτ is a random variable that is independent of frequency.

One of the key results of [4] is the segregation of the autocorrelation function from the cross-correlation functions that is done with the orthogonal polarizer setting and (16). Another is the linkage to DGD that is seen in (22).

Fixed analyzer method (FFT)

This method is conceptually very similar to the interferometric method. Instead of a broadband source, however, wavelength range is sampled discretely using a monochromator or tunable filter. The spectra, $S_{0F}(\omega)$ and $S_F(\omega)$, before and after the output polarizer are measured at discrete frequencies for a fixed output polarizer (analyzer) setting. The resulting ratios, $S_F(\omega)/S_{0F}(\omega)$, are Fourier transformed. The power spectrum of the Fourier transform is analyzed to report an RMS value that would possibly be present if the autocorrelation function were not included. The Fourier transform is normally done after multiplying the ratio with a windowing function, $W(\omega)$, to reduce the ringing associated with a finite sampling window. For this method, the spectrum before the output polarizer is nominally constant.

If, instead of doing a Fourier transform, a Fourier cosine transform were done, the result would be equivalent to the interferometric method using a source that is constant across the frequency range. The multiplication with the windowing function plays the same role as the shape of the power spectrum, $S_0(\omega)$, for the interferometric method.

Make the following associations to the functions defined in the interferometric method:

$$S_0(\omega) = W(\omega) \qquad \text{and} \qquad S(\omega) = W(\omega) S_F(\omega) / S_{0F}(\omega) \tag{24}$$

Application of the Fourier cosine transform will yield the associated $R_0(\tau)$ and $R(\tau)$ functions – although these are discrete vs. optical. Making the measurement with the polarizer at a 90° offset will allow the additions and subtractions defined in the interferometric method to remove the autocorrelation function. After this, the equations defining σ_0 and σ_x can be applied to obtain the result from (23).

Conclusions

The results leading up to (9) are key to understanding the main PMD measurement methods and the relationship to system impairments. Methods such as the phase shift method are also easily understood in this context.

Understanding the results of [4] are key to understanding the linkage between frequency domain methods and time domain methods.

The combination of a modified form of (9) and (10) can be used to characterize second order PMD using matrix that maps not only to $T(\omega_0+\Delta\omega)$ but also back, to $T(\omega_0-\Delta\omega)$, by using a quadratic function for $\Upsilon(\omega)$ and, for example, linear functions for θ_p and μ_p.

Given a measured or simulated pdv function, all orders can be investigated with a solution for $T(\omega)$ derived from (7).

References

[1] Poole, C.D. and Wagner, R.E., "Phenomenological approach to polarization dispersion in long single-mode fibres", Electron. Lett. 22(19), 1029-1030 (1986)

[2] Jones, R.C., "A new calculus for the treatment of optical systems. VI: Experimental determination of the matrix", J. Opt. Soc. Am. 37, 110-112 (1947)

[3] Gisin, N., Passy, R., and Von der Weid, J.P., "Definitions and measurements of polarization mode dispersion: Interferometric versus fixed analyzer methods", J. Lightwave Tech. 6, 730-732 (1994)

[4] Cyr, N., "Polarization-mode dispersion measurement: generalization of the interferometric method to any coupling regime", J. Lightwave Tech., 22 (3), 794-805 (2004)

[5] J. Chamberlain, The principles of interferometric spectroscopy, John Wiley & ` Sons, 1979.

PMD measurements using Fixed-Analyzer technique on a 1000km amplified link that includes ROADMs

Vincent Lecœuche, Fabien Sauron and André Champavère
JDSU Commtest Division, Saint-Etienne, France

Alexey Turukhin and Enrico Gonzales
JDSU Optical Network Research, Eatontown, New Jersey

Abstract : We report PMD measurements, performed on an amplified network with Reconfigurable Optical Add Drop Multiplexers (ROADMs) and a total fiber length exceeding 1000km, using a commercially available setup based on the Fixed Analyzer Fourier Transform (FA-FT) technique. We have implemented straightforward numerical filtering that removes the inter-channel spectral data as well as dropped channels and demonstrated the improvement brought to the SNR. We show that this enhancement would allow one to maintain reliable PMD readings in Agile Optical Networks with transmission pass-bands affected by ROADMs.

Introduction

Measurement of the polarization mode dispersion of Agile Optical Network represents new challenges for Test & Measurement equipments. Not only do the signal paths depend on wavelength and time, but the wavelength span available for actually performing the PMD measurement into channels may get so limited that measurement accuracy is compromised. This latter fundamental limitation, associated with the statistical nature of PMD, applies to any of the available measurement techniques [1]. Some methods would indeed allow a precise measurement of the instantaneous DGD at the exact channel wavelength, but this information alone is not really valuable as the DGD varies over time, even with relatively short spans of buried cables [2]. In this context, we focused our attention on the only truly representative parameter that can be measured, i.e. the most stable over time, which is the average DGD over the available wavelength span.

We have conducted laboratory experiments on an amplified network that includes commercial ROADMs, using the FA-FT technique implemented into our field test mainframe. We showed that this method provides a meaningful reading of the mean DGD over the available wavelength span, provided that a sufficient number of channels are passing through the link under test.

In section 1, we will first briefly describe our experimental setup. In section 2, we will describe our experimental results, observed both on a "regular" amplified link and one that does include ROADMs.

1 - Experimental arrangement

The FA-FT technique is a well documented measurement tool and JDSU's implementation of it strictly follows the recommendations of the standards on PMD measurements [3]. The measurement block diagram is shown in Figure 1. A broadband polarised source (BBS) is launched into the Device Under Test (DUT), and the transmitted signal is analysed spectrally through a polarizer, integrated into the OSA and commutable. Manual polarisation controllers are added before and after the DUT in order to improve measurement accuracy.

Note that a reference spectrum is first performed without the polarizer, and the signal through the polarizer is normalized to this reference signal before performing the FFT, so that the FA-FT is intrinsically immune to any source/amplifier spectral shape features. This direct normalization procedure in the frequency domain is mathematically equivalent to other means that have been proposed in order to compensate for the corresponding auto-correlation peak in the time domain, as observed on interferometric setups. We will see hereafter that the direct access to the spectral data also allows the analysis of the ROADM passing channels information, yielding an improvement on the measurement accuracy.

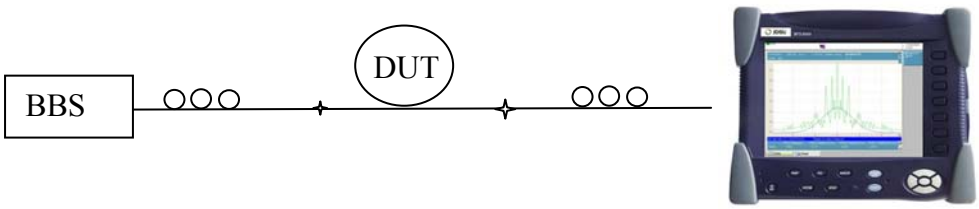

Figure 1: Measurement equipment

The link under test is described in Figure 2. This C-band link is fully functional and normally populated with 40 WDM channels with 100GHz spacing, modulated at 10Gb/s using NRZ format. The Multi-port Wavelength Switches, used as ROADMs have been configured to allow traffic for all channels through the express port. Measurements have been performed both on the whole link, i.e. from launch point A to detection point C, including the 3 ROADMs to imitate a fragment of AON, and from point B to C to consider the case of a regular point-to-point amplified network.

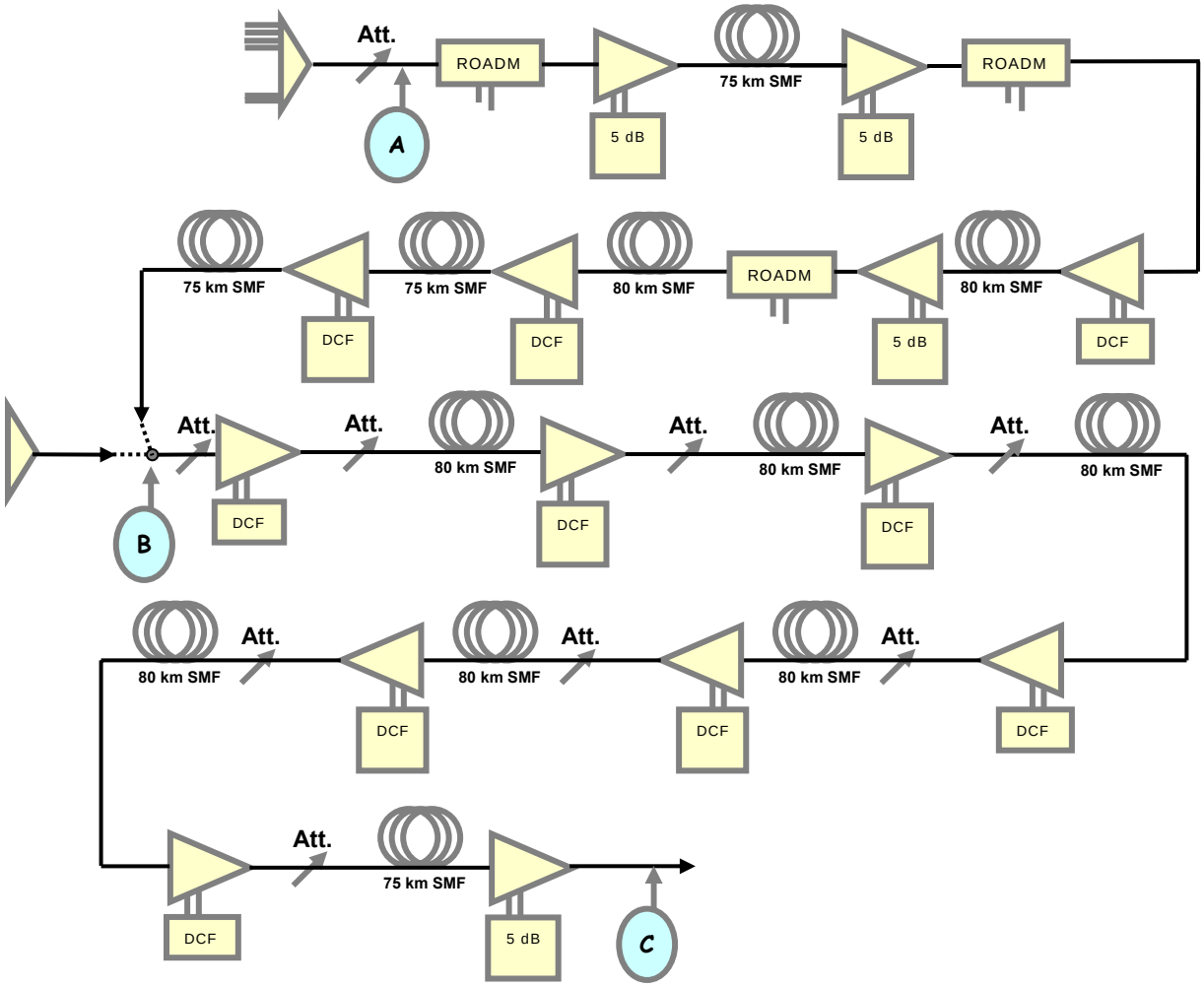

Figure 2: Link under test, including 3 ROADMs (MWS1X6+2), 14 EDFAs (OA3500), 940kms of SMF and 140kms of Dispersion Compensating Fibre

2 - Measurements

a) PMD measurements on a regular amplified link

The first test was performed on the link from point B to C. The value of the mean DGD, averaged over 50 successive measurements while manually changing the input/output polarisation launch conditions between successive scans, was found to be 1.32ps with a standard deviation of 0.16ps. Figure 3-a) shows the measurement distribution, while Figure 3-b) shows a typical Fourier transform.

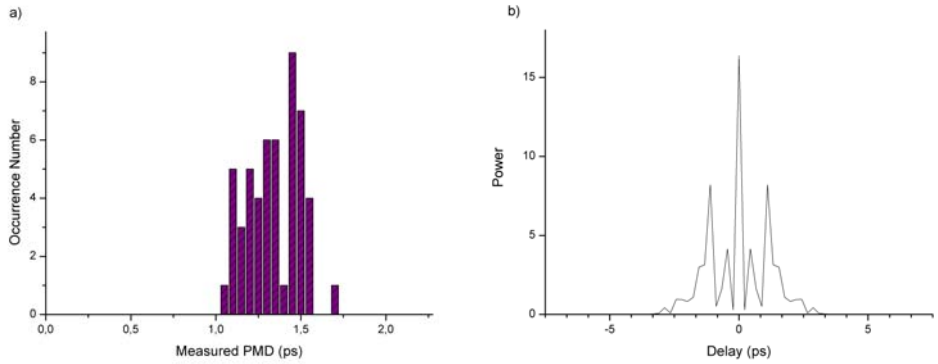

Figure 3: a) Histogram of the 50 measurements recorded while changing input/output polarisation launch conditions and b) typical FFT measured from point B to C.

For comparison, we used a commercial bench top instrument based on the Jones Matrix Eigenanalysis (JME) method. The use of a JME on WDM amplified network brings some difficulties associated with transmitting a single test channel, which is using the total power of the amplifiers. To avoid nonlinear issues, the amplifiers must somehow be loaded with an additional signal. To do so we used a broadband ASE source combined with the tunable laser. While the degree of polarisation at the output of the network was of only 10%, which is low to conduct reliable polarimetric measurements, the JME instrument was robust enough to take a reading. We ran 3 successive measurements without changing the launch conditions (the JME method being mostly insensitive to these changes), and the mean DGD over 1527-1563 band was found to be 1.33, 1.23 and 1.38 ps.

b) PMD measurements through a ROADM

The second experiment was performed on the total link represented in figure 2 from point A to C. The 3 ROADMs are set to let all the channels pass through. The spectrum of the BBS transmitted by the network is shown in Figure 4.

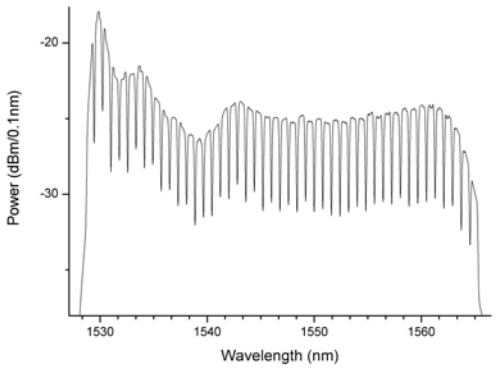

Figure 4: spectral transmission of the BBS from A to C, with ROADMs set in passing mode for all 45 channels.

The mean DGD was found to be 1.63ps, averaged over 50 successive measurements while manually changing the input/output polarisation launch conditions between successive scans, with a standard deviation of 0.18ps. With the JME setup, we have obtained a mean DGD of 1.71ps after manually removing the inter-channel DGD points that were totally wrong as one could expect. Figure 5-a) shows the measurement distribution, and Figure 5-b) shows a typical Fourier transform.

We would like to emphasize that our standard test tool without any modification was able to provide reliable PMD measurements despite the peculiar shape of the transmission associated with ROADM's pass-bands. However, we must consider that conditions were quite favourable, and in particular the value of the PMD of the link was quite advantageous here. A close look at Figure 5-b) reveals the

presence of signals at several harmonics of 10ps which directly arises from the 100 GHz spacing of the ROADM channels. If the PMD of the link had been slightly higher with components close or above 10ps, these perturbations would have been integrated into the width calculation and the result would probably have been overestimated. The signal to noise ratio would also decrease if some channels are dropped on the line or if the output Degree Of Polarization decreases.

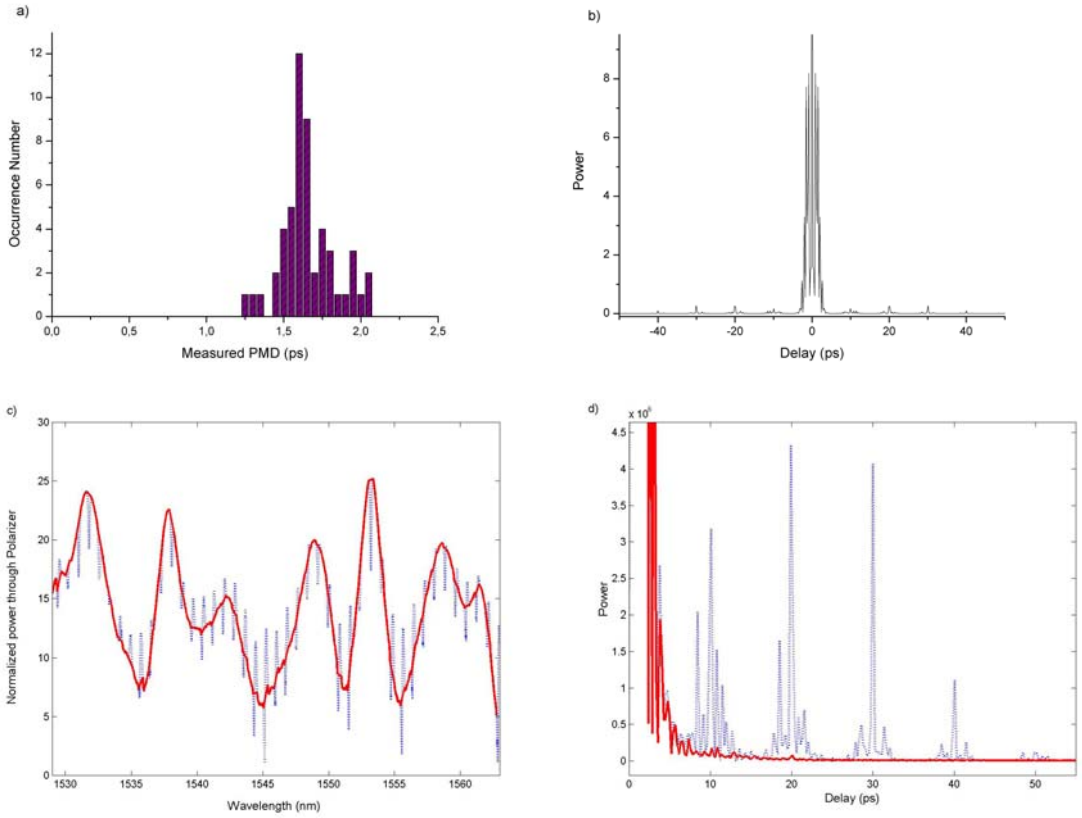

Figure 5: a) Histogram of the 50 measurements recorded while changing input/output polarisation launch conditions. b) typical FFT measured from point A to C. c) Normalized spectrum through polarizer (dotted line), with inter-channel filtering applied (solid line). d) zoom on the ROADM perturbations in the FFT (dotted line) removed with the inter-channel filtering applied (solid line).

As the FA-FT does a reference signal similar to the one shown in Figure 4) at every scan, we can use this information to locate the passing channels and simply remove the inter-channel signals. Channels are on the ITU grid, and we have located the passing bands with a power drop criteria of 0.3dB compared to the channel centre value. The second step is to replace the inter-channel signals with straight lines as shown in Figure 5-c). By doing so the 10ps component and its harmonics are clearly removed on the FFT as can be seen in Figure 5-d). Without filtering, the reading on this scan was 1.54ps, with filtering, the reading was 1.48ps, confirming that the ROADM influence on our measurement remains minor in this experiment.

Conclusions

We have demonstrated PMD measurement capability on an amplified network using the FA-FT technique. We showed that for this particular setup the measurements were not significantly affected by the presence of ROADMs in-line, and we proposed a software enhancement that would allow one to maintain valuable readings in more critical conditions. While this method is not meant to replace polarimetric methods that allow high-resolution DGD readings, it provides a simple, cost effective and field dedicated alternative when a sufficient number of passing channels are available.

References:

[1] Gisin et al, IEEE Photonics Technology Letters **8**, n°12, p. 1671 (1996)
[2] Allen et al, Journal of Lightwave Technology **21**, n°1, p. 79 (2003)
[3] see for example IEC 60793-1-48, IEC61280-4-4, ITU-T G.650.2 or TIA 455-113

Chromatic dispersion measurement technique utilizing an unstable supercontinuum pulse source

Sucbei Moon and Dug Y. Kim
Gwangju Institute of Science Technology (GIST)
Buk-gu, Gwangju 500-712 Republic of Korea
dykim@gist.ac.kr

Abstract: We report a time-domain chromatic dispersion measurement scheme that can analyze a very short (down to 10 meters) optical fiber by using a supercontinuum pulse source. An ultra-wideband supercontinuum pulse source that spans the entire range of the communication wavelength bands from 1,250 nm to 1,700 nm were generated by using an amplified diode-laser pulse source combined with a dispersion-shifted fiber. Wavelength dependent temporal delays for a spectrum-sliced supercontinuum pulses were measured after transmitting through a sample fiber with a differential reflectometric configuration. A monochromator was used to do spectrum slicing, and a high-speed photodetector with an oscilloscope were used to measure temporal delays. In order to increase the measurement precision, the measurement system used reflecting configuration and a differential measurement technique. This enabled us to measure the dispersion of a 10-m-long single-mode fiber with good precision.

1. Introduction

Chromatic dispersion (CD) or group-velocity dispersion (GVD) is a key characteristic of a single-mode fiber. In fiber-optic communications, it determines the transmission capacity and should be carefully measured before the fiber is installed. In nonlinear-optic applications such as supercontinuum generation and parametric amplification, zero-GVD wavelength is a crucial parameter that determines the efficiency of the process. Time-of-flight measurements and modulation phase-shift methods are standardized and commonly used for evaluating fibers longer than hundreds of meters.[1] The measurement wavelength ranges for these methods are normally limited within 100 nanometers around C+L-band due to the limited availability of suitable light sources outside this band. In analyzing specialty fibers like photonic-crystal fibers (PCFs) where short fibers need to be measured outside the band, interferometric methods have been usually used with white light sources.[1] However, those methods are not able to measure fibers longer than a few meters because it is hard to construct a long reference arm in an interferometer. Thus the fiber should be cut in order to be analyzed.

Supercontinuum (SC) generation is a powerful method to obtain high-power ultra-wideband pulses. As the output spectrum of an SC source can cover the entire wavelength range of single mode fiber's (SMF) applications, time-of-flight measurement technique with a pulsed SC source has been studied so far for wide-band capability and simplicity in dispersion measurements.[2] However, this technique traditionally has been considered to be less precise because the relative temporal delay of a pulse is usually hard to be determined when the required precision is much less than the measured pulse-width of an output pulse. In principle, the temporal precision of the time-of-flight measurement method can be much better than the output pulse-width because it does not have to resolve pulses but only measures the pulse position. However, many supercontinuum sources generate pulses with randomly varying pulse

shape and unstable pulse position in time-domain when they are spectrally sliced. This problem has made the GVD measurement schemes based on supercontinuum sources difficult to be utilized in the real-world applications.

In this paper, we report on an ultra-wideband time-of-flight measurement scheme that can measure the GVD of a fiber with high precision and accuracy even with an relatively unstable SC source. Because the spectrum of the supercontinuum source used in the experiment covered the entire transmission band of an ordinary single-mode fiber, the scheme could measure the full GVD characteristics. Well-known differential measurement technique was used, in which difference in temporal delay between two different wavelengths is detected simultaneously. This alleviates the problem of the group velocity variations induced by possible temperature changes. In addition, reflectometric configuration was used in order to minimize effects induced by the instability of an SC source. As in OTDRs, back-reflected pulses from both ends of a sample fiber are detected by a high-speed photodetector. And measured temporal delay between these two pulses in arrival time corresponds to the group delay of the sample fiber at the wavelength. So, absolute accuracy can be obtained without calibration. Furthermore, this temporal delay is independent with the stability of an SC source. As the standard deviation of this differential temporal delay was only 0.35 ps in our measurement, even a 10 m long single-mode fiber sample can be measured successfully. It proves that this measurement scheme exhibits very high accuracy such that it can be used for the GVD measurement of a very short length fiber sample, which is considered to be measurable only by an interferometric measurement method.

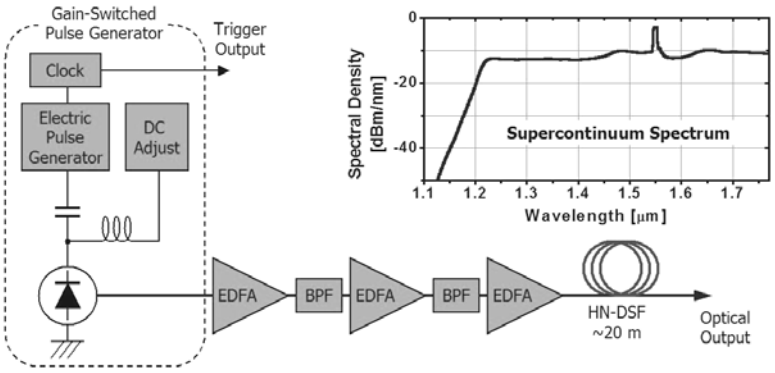

Fig. 1. Schematic diagram of the supercontinuum source based on an ADP source and an HN-DSF. The inset graph shows the output spectrum.

2. Supercontinuum

We had demonstrated a supercontinuum generation method based on an amplified diode-laser pulse (ADP) source and a dispersion-shifted fiber in our previous report.[3] The original pulse was generated by gain-switching a distributed-feedback laser diode (DFB-LD) at 1,550-nm wavelength and was amplified by 3 concatenated erbium-doped fiber amplifiers (EDFAs) in order to obtain a high peak power. The amplified high-power pulse was launched into a dispersion-shifted fiber (DSF) for supercontinuum generation. The same kind of the supercontinuum source had been used in this experiment. In order to get higher efficiency, a highly-nonlinear DSF (HN-DSF) was used as a supercontinuum fiber inside the

source. Fig. 1 shows the schematic diagram of the supercontinuum source based on the ADP source and the HN-DSF. The inset graph shows the output spectrum that covers the entire communication band from 1,200 to 1,700 nm.

Since the pulse was generated by an electric triggering signal, the pulse repetition rate can be controlled freely in this source. The repetition rate was set to be 12.00 MHz in our experiments. The spectral densities were above –13 dBm/nm or 50 μW/nm for a wavelength band between 1,250 nm and 1,700 nm. The pulse-width of the spectral slice with 5-nm-bandwidth was about 200 ps. Therefore, the estimated peak power is over 100 mW for every 5-nm-bandwidth pulse. Significant pulse-to-pulse power and shape variations had been observed. Because the supercontinuum generation process was based on the cascaded effects of the 3rd-order nonlinearity, small changes in the pump pulse properties such as power, shape and polarization state would result in significant variations of the output. This SC source is composed of the low-cost fiber-optic components only and is easy to be constructed and maintained.

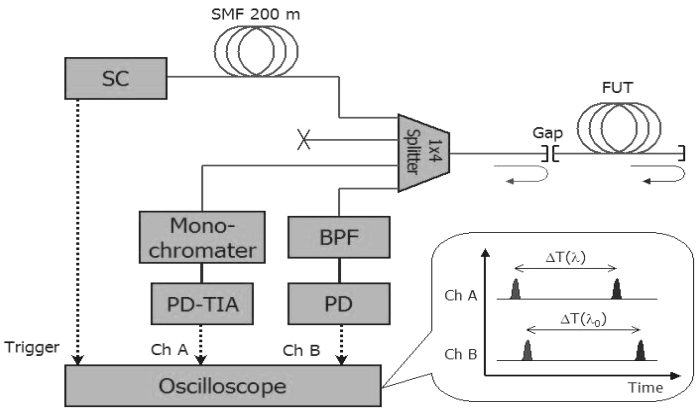

Fig. 2. Experimental setup of GVD measurement.

3. Measurement setup

We have built a wavelength-dependent group delay (GD) measurement system based on a differential reflectometric configuration. Fig. 2 shows the experimental setup of our GD measurement system. Ultra-wideband pulses from the SC source were stretched in time-domain by a 200 m single-mode fiber (SMF) in order to reduce the peak power and minimize possible nonlinear effects in the following fibers. After a 1x4 fiber-optic splitter, the pulse was launched into a fiber under test (FUT). A significant amount of back-reflection was made at the input end of the FUT after making a slight gap between two fiber connectors used for the FUT. Another 4% back-reflection was made naturally at the other cleaved end of the FUT. Lights from these two reflected points were split into four parts by the fiber splitter. In one channel of the splitter, the reflected lights were spectrum-sliced by a monochromator with a 5-nm bandwidth. The monochromator produced ~20-dB insertion loss. And an InGaAS p-i-n photodetector plus transimpedance amplifier (PIN-TIA) converted the spectrum-sliced optical pulses to electric signals. This signal was acquired by Ch A of an oscilloscope. In another channel of the 1x4 fiber splitter, the reflected wideband pulse from the FUT were also spectrum-sliced by a fixed band-pass filter whose center wavelength and bandwidth were 1,550 nm and 2 nm, respectively. A p-i-n photodetector and Ch B of the

oscilloscope were used to measure these spectrum-sliced pulses. This channel works as a reference for our GD measurement system. The bandwidth of the photodetection system used in our experiment was ~2 GHz. By changing the center wavelength of the monochromator, GDs were measured as a function of wavelengths.

4. Results and discussion

Fig. 3 shows a typical set of oscilloscope traces captured simultaneously by Ch A and Ch B in an equivalent-time sampling mode. Ch A detected the pulses spectrum-sliced by the monochromator with center wavelength of 1,500 nm while Ch B did those of the reference at 1,550 nm. Each trace has 32,768 data points in a 50-ns interval after averaging 64 waveforms. In order to increase the signal-to-noise ratio (SNR), the acquired data were smoothened by adjacent averaging (N = 128), which corresponds to digital low-pass filtering. A 10-m-long single-mode fiber was used as an FUT. The position of a pulse was determined as the center of two half maximum points within the pulse duration. The first pulses on the left-hand side of a trace are due to the reflected light from the connector gap, and the second pulses on the right-hand side are due to the reflected light from the cleaved fiber end. Hence, the group delays are the time differences between the first and second pulses. The differential group delay is the difference between the group delays of Ch A and Ch B.

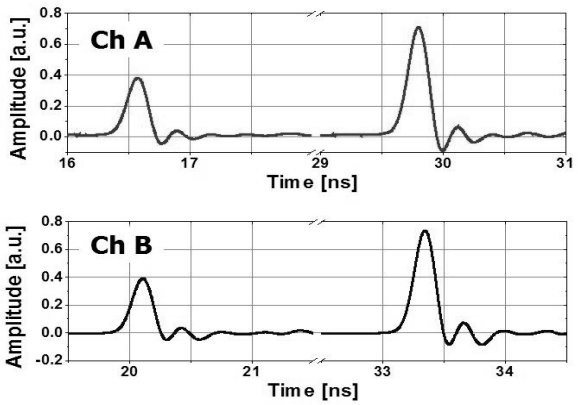

Fig. 3. Measured oscilloscope traces for λ = 1,500 nm (Ch A) and λ_0 = 1,550 nm (Ch B). The data were smoothened by adjacent averaging (N=128) for a better SNR.

When we have repeatedly measured in the same condition, we have obtained a standard deviation of 0.35 ps for differential group delay. Note that the pulse generation period exceeded the time range of the measurement. Thus the actual absolute delay for 1,550 nm was the sum of the observed delay (13.238 ns) and a period of the pulse generation (83.333 ns) and was calculated to be 96.571 ns. The delay corresponded to 19.72 meters, assuming the group index at the wavelength is 1.4682. Thus the fiber length was measured to be the half i.e. 9.86 meters. The standard deviation of the length determination was 0.015 mm i.e. 1.5 ppm. These results demonstrate that relative group delays as well as absolute temporal delays could be measured precisely with this scheme.

GVD of a 10-m-long single-mode fiber that complies ITU-T G.652 standard (Corning SMF-28^{TM}) was measured. Only 9 group delays were acquired with a ~50 nm wavelength interval. Fig. 4 shows these 9

measured group delays, their 3rd-order polynomial fitting curve. The calculated GVD from the fitting curve is also plotted on the same graph. The GVD measurement was repeated twice. The measured chromatic dispersion and slope at 1,550 nm wavelength were 0.3094 ps/nm and 0.0016 ps/nm^2, respectively in the first measurement. In the second measurement, they were 0.3112 ps/nm and 0.0015 ps/nm^2, respectively. The deviation was only 0.6% for the measured chromatic dispersion values. The GVD coefficient for this fiber was calculated to be 15.7 ps/nm.km at this wavelength. The zero-GVD wavelengths were calculated to be 1,316 nm and 1,319 nm.

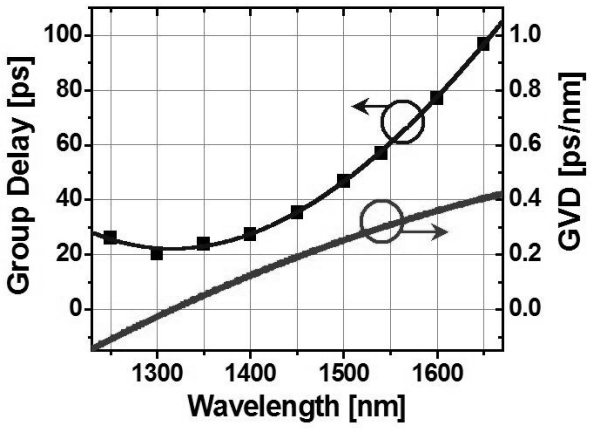

Fig. 4. Measured group delays (rectangular spots), their 3rd-order polynomial fit curve (black line) and the calculated GVD from the curve (gray line).

5. Conclusion

A new time-domain GVD analysis method with a pulsed supercontinuum source was proposed and demonstrated with a differential reflectometric-configuration for better accuracy and precision. The full dispersion characteristic of a sample fiber in the entire transmission band of an SMF from 1,250 to 1,700 nm was analyzed with a single pulsed source. The differential reflectometric configuration guarantees the accuracy of the measurement as well as the precision. A fiber as short as 10 meters could be analyzed successfully with the scheme. This method must be useful in characterizing short-to-medium-length fibers of which dispersion characteristics outside the C+L band are of prime interest.

References

[1] D. Derickson, **Fiber Optic Test and Measurement,** Prentice Hall PTR, 1998.

[2] K. Mori, T. Morioka and M. Saruwatari, **"**Group velocity dispersion measurement using supercontinuum picosecond pulses generated in an optical fibre," Electronics Letters, vol. 29, **987** – 989 (1993).

[3] S. Moon and D. Y. Kim, "Generation of octave-spanning supercontinuum with 1550-nm amplified diode-laser pulses and a dispersion-shifted fiber," Optics Express, vol. 14, 270-278 (2006).

Accurate Measurement of Chromatic Dispersion Distribution along Dispersion Managed Transmission System

Mirza IMRAN Baig* Tohru MIYAUCHI and Masaaki IMAI**

Dept. of Electrical & Electronic Engineering, Muroran Institute of Technology
27-1 Mizumoto-cho, Muroran, Hokkaido, 050-8585 Japan
s1261027@mmm.muroran-it.ac.jp,* mimai@mmm.muroran-it.ac.jp**

Abstract: **In this paper, a nondestructive measurement technique, which uses a four wavelength bidirectional optical time domain reflectometer (OTDR) to measure the chromatic dispersion distribution along a dispersion managed transmission system, has been presented. A new formulation has been developed to enhance the correction factor, which leads to an improvement in the measurement results of a pre-existing method and the obtained experimental results are in good agreement with those obtained by the other techniques.**

I. INTRODUCTION

The advent of optical repeaters based on erbium-doped fiber amplifiers (EDFAs) has opened the new era of optical transmission technologies, allowing us to use wavelength-division-multiplexing (WDM) technologies with simple, compact, and economical approaches. Infact, the demonstrated capacity for long-haul optical transmission has been growing remarkably, and more than a thousand fold increase in capacity has been achieved. The price we have to pay for such success is to combat with the accumulated impact of fiber nonlinearity, interplay with the chromatic dispersion (CD) of the transmission fiber, which grows with the transmission distance and therefore becomes significant for ultra-long-haul system. Dispersion management technologies have been invented to overcome such inherent problems in optically amplified transmission systems [1].

Chromatic dispersion results from the difference in propagation velocity associated with different wavelengths of light traveling down the fiber. In a transmission system, it gives rise to pulse broadening. The need for the distributed measurement of chromatic dispersion along an optical fiber transmission system comes from the increasing diffusion of wavelength division multiplexing (WDM) transmission systems. Nonlinear effects, such as four wave mixing or cross-phase modulation seriously affect WDM transmission. For this reason, not only an average estimation of CD along the fiber is required, but a distributed evaluation is also essential. The OTDR based techniques have been established in these respects [2], which are based on the analysis of OTDR traces acquired bi-directionally at different wavelengths.

II. THEORETICAL BACKGROUND

A. Backscattered Power:

For an optical fiber supporting single-mode with a Gaussian field distribution the optical power *P(?,z)*, of backscattered light from an input pulse of power P_o and duration *W* launched at one end of optical fiber at time *t=0* can be expressed as [3],[4].

$$P(l,z) = P_0 a_s(z) W B(l,z) \frac{c}{N} \exp\left[-2\int_0^z g(x)dx\right] \qquad (1)$$

where P_0 is the input power,
W is the pulse width,
$a_s(z)$ is the local scattering coefficient,
$B(l,z)$ is the backscatter capture fraction,
c is the speed of light,
N is the group refractive index,
g(x) is local attenuation coefficient .

The backscattered signal has two components. The first is an exponential decay due to scattering and absorption in the glass and is insensitive to the fiber end from which the pulse is launched. When it is displayed on a semi-log scale, this decay with distance is usually a straight line whose slope represents the fiber attenuation in dB/km. The second signal component is sensitive to local imperfections, which result from changes in MFD and a_s. This portion of backscattered signal does depend on the launching end. The OTDR semi log trace is the sum of these two contributions. A reliable means of separating the effects of optical power decay and waveguide imperfections from OTDR signals has been reported in [3] and [5].

B. MFD Evaluation:

$S_1(z)$ and $S_2(L-z)$ are the backscattering traces read, respectively, from the origin, and from the end of the fiber, which can be obtained as follows:

$$S_1(\lambda, z) = 10\log[P_1(\lambda, z)], \quad (2)$$

$$S_2(\lambda, L-z) = 10\log[P_2(\lambda, L-z)], \quad (3)$$

By using above two equations, the waveguide imperfection contribution $I(\lambda,z)$ can be expressed as

$$I(\lambda, z) = \frac{S_1(\lambda, z) + S_2(\lambda, L-z)}{2}, \quad (4)$$

$$I(\lambda, z) = 10\log[a_s(z)B(\lambda, z)] + a_o. \quad (5)$$

where a_o, which is a constant independent of distance z, is expressed as

$$a_o = 5\log(P_{01}P_{02}) - 10\log\left[\exp\left(\int_0^L g(x)dx\right)\right]. \quad (6)$$

$B(\lambda,z)$ is expressed in terms of refractive index of the core *n* and the mode field diameter $2W(\lambda,z)$ as [2]

$$B(\lambda, z) = \frac{3}{2}\left\{\frac{\lambda}{2\pi n W(\lambda, z)}\right\}^2. \quad (7)$$

The variation in the local scattering coefficient a_s is negligible compared to that in the mode field diameter $2W(\lambda,z)$ [2],[6]. Therefore, the imperfection contribution *$I_n(\lambda,z)$* normalized by the value at $z = z_o$ is

$$I_n(\lambda, z) \equiv I(\lambda, z) - I(\lambda, z_o) = 20\log\left[\frac{W(\lambda, z_o)}{W(\lambda, z)}\right]. \quad (8)$$

When the mode field diameter $2W(\lambda,z_o)$ at $z = z_o$ is given, the mode field diameter distribution $2W(\lambda,z)$ can be obtained as [6]

$$W(\lambda, z) = W(\lambda, z_o)10^{-\left\{\frac{I_n(\lambda, z)}{20}\right\}}. \quad (9)$$

C. MFD Evaluation with Correction Factor:

In the above section, by assuming the variation in the scattering coefficient $a_s(z)$ along a fiber is negligible compared to the variation in the MFD, the distributed MFD can be obtained from (9). However, when the scattering coefficient changes greatly along a fiber, its length dependence must be taken into account. It has been considered a measurement procedure for the transmission line composed of different types of fiber, by taking into account the difference between the scattering coefficients of each fiber.

When the scattering coefficient and the refractive index change along the fiber are taken into account, the MFD can be evaluated as [2]

$$W(\lambda, z) = W(\lambda, z_0)10^{-\left\{\frac{I_n(\lambda, z) - K}{20}\right\}}. \quad (10)$$

Using this relation, correction factor *K* is rewritten as

$$K = 10Log\left[\left\{\frac{1+0.62\Delta(z)}{1+0.62(z_o)}\right\}\left\{\frac{50-\Delta(z)}{50-\Delta(z_o)}\right\}\right]. \quad (11)$$

where $\triangle$ is the relative index difference of SiO_2 glass in %.

D. Improved Correction Factor K:

The backscattered power received by the OTDR also influenced by the group refractive index of fiber under test. Therefore, it is taken into account in literature [3] and [4] and can be witnessed from (1). Group refractive index can be expressed in terms of refractive index of optical fiber as [7]

$$N = n - \lambda\frac{dn}{d\lambda}. \quad (12)$$

where *n* is the refractive index of fiber and λ is the operating wavelength.

By neglecting the second term on the right hand side of (12), it can be assumed that the group refractive index is nearly equal to the refractive index of fiber. Therefore, (8) yields

$$I_n(\lambda, z) = 10\log\left[\frac{a_s(z)\ n^3(z_o)}{a_s(z_o)\ n^3(z)}\right] + 20\log\left[\frac{W(\lambda, z_o)}{W(\lambda, z)}\right] \quad (13)$$

and finally, the correction factor *K* has to be altered as [8,9]

$$K = 10Log\left[\left\{\frac{1+0.62\Delta(z)}{1+0.62\Delta(z_o)}\right\}\left\{\frac{50-\Delta(z)}{50-\Delta(z_o)}\right\}\left\{\frac{50-\Delta(z)}{50-\Delta(z_o)}\right\}^{1/2}\right]. \quad (14)$$

Thus, we have improved the correction factor *K*, which then affect on the measurements of MFD and consequently the measurements of chro matic dispersion.

E. Chromatic Dispersion Evaluation:

The chromatic dispersion σ is the sum of the material dispersion σ_m and waveguide dispersion σ_w, given by

$$\sigma = \sigma_m + \sigma_w \quad (15)$$

Where σ_m and σ_w are expressed as [7],[10]

$$s_m = -\frac{l}{c}\frac{d^2}{dl^2} \quad (16)$$

$$s_w = \frac{l}{2p^2cn}\frac{d}{dl}\left(\frac{l}{W^2}\right) \quad (17)$$

The material dispersion s_m can estimated from the dopant concentration in an optical fiber by using Sellmeier`s relation [11]. On the other hand, the waveguide dispersion s_w can be estimated by determining the wavelength dependence of the mode field diameter. The empirical relationship between the mode field diameter $2W$ and the normalized frequency V has been reported by Marcuse as [12].

$$\frac{W}{a} = b_o + b_1V^{-1.5} + b_2V^{-6} \quad (18)$$

$$\frac{W}{a} = c_o + c_1\left(\frac{l_c}{l}\right)^{-1.5} + c_2\left(\frac{l_c}{l}\right)^{-6} \quad (19)$$

where a is the core radius and $?_c$ is the cutoff wavelength. Here, wavelength dependence of mode field diameter $2W$ can be approximated as

$$W(l,z) = g_o(z) + g_1(z)l^{-1.5} + g_2(z)l^{-6} \quad (20)$$

Equation (20) has been used to approximate the distribution of the derivative of MFD in (17) at the wavelengths of interest.

By substituting (20) into (17), the waveguide dispersion s_w can be obtained from

$$s_w(l,z) = \frac{l}{2p^2cnW^2(l,z)} \times\left\{1-\frac{2l}{W(l,z)}\left(\frac{3}{2}g_1(z)l^{0.5}+6g_2(z)l^5\right)\right\} \quad (21)$$

Here, the coefficients, $g_o(z)$, $g_1(z)$ and $g_2(z)$ are determined by solving (20) with the least squares method, when mode field diameters are given at more than three wavelengths [9].

III. EXPERIMENTAL RESULTS

A. Bidirectional Measurement:

Two OTDR traces have been acquired bi-directionally. The pulse width and averaging time were 1.0μs and 20 minutes per wavelength, respectively, during the experiment and all four available wavelengths of the equipment were used. The OTDR took 50,000 samples for averaging with 1 meter resolution.

Four wavelengths of 1.31, 1.45, 1.55 and 1.625μm, were available for measuring the backscattered signal power with the Anritsu MW9076 OTDR. The experiment has been performed around a fusion-spliced optical transmission link. The transmission link composed of two different kinds of optical fibers, i.e. 2, 15 and 10km long single mode fiber (SMF) and 20km long Reverse Dispersion Fiber (RDF). The specifications of the fibers used in our experiment are listed in Table I.

TABLE-I
FIBER SPECIFICATION

Parameters	Fiber A	Fiber B	Fiber C	Fiber D
MFD @ 1.31 (μm)	9.53	9.32	9.59	
MFD @ 1.55 (μm)	10.69	10.35	10.71	5.59
CD @ 1.55μm (ps/nm/km)	19.5	19.1	19.7	-26.7
Fiber Length (km)	2	15	10	20

B. Mode Field Diameter Measurement:

Fig.1 shows experimental results for the mode field diameter distribution of the dispersion managed transmission line. Here, in order to normalize the imperfection contribution, a 2km single mode fiber had connected in front of the link under test. The value of MFD at the reference point z_o i.e. after 2km long reference fiber, on the available set of wavelengths, should be known in advance. Therefore, the reference fiber shall be fully characterized in terms of MFD by one of the standard methods [13], e.g., the far field pattern (FFP) technique or variable aperture far field (VAFF) technique. A comparable results are presented in Fig.1, with previous and our proposed new correction factor K. The difference between two results can be observed from the expanded view. Black line shows results with new correction factor and pink line

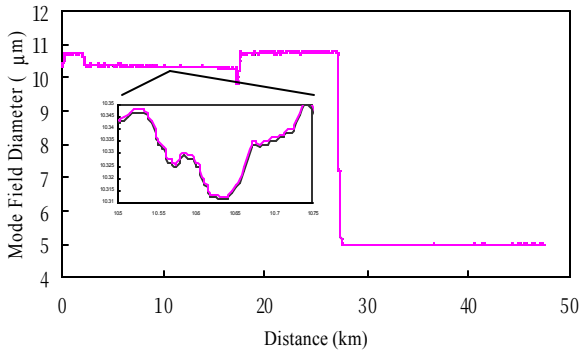

Fig.1 Measured mode field diameter distribution at 1550nm.

shows results with old correction factor. An average MFD measurement can be observed from Table II.

C. *Chromatic Dispersion Measurement*:

The measurements of chromatic dispersion distribution are shown in Fig.2. These results are calculated from the results of MFD measurements depicted in Fig.1. Here, the results are also presented with previous and our newly proposed correction factor *K*. The two different colors of line are separating the two results. Black line shows results obtained from new correction factor and pink line shows results with old correction factor. A clear difference between two results is evident through an exp anded view shown in Fig.2. An average CD measurement is depicted in Table II.

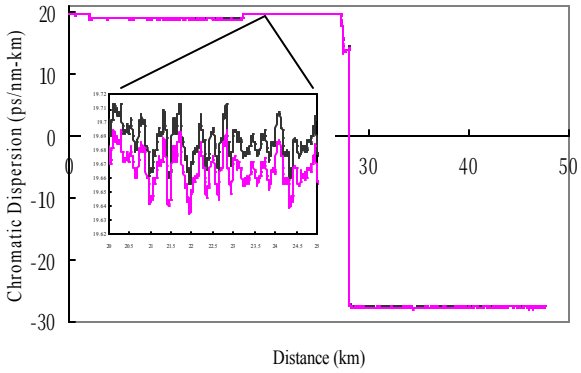

Fig.2 Measured chromatic dispersion distribution at 1550nm.

TABLE-II
AVERAGE MEASUREMENT

Fibers		MFD 1.55μm (μm)	CD 1.55 μm (ps/nm/km)	Fiber Length (km)
A	Old K	10.6534	19.6653	
	New K	1065454	19.6451	2
B	Old K	10.25473	19.1597	
	New K	10.25582	19.1382	15
C	Old K	10.65177	19.7872	
	New K	10.65291	19.767	10
D	Old K	5.000725	-26.4762	
	New K	5.001254	-26.5721	20
Accumulated CD	Old K		-4.9259	
	New K		-7.4088	47

In this table the accumulated CD is defined as a sum of the dispersion occurred at each of the fiber sections A, B, C and D that construct the dispersion managed system. Her, it is noted that the combination of fibers used in our experiment made not exactly zero but almost zero accumulated dispersion.

IV. CONCLUSION

The described, OTDR based nondestructive technique with our proposed enhanced correction factor clearly improved the measurement of the chromatic dispersion distribution along the optical fiber transmission system. The technique was compared with the previously established technique with old correction factor *K*. The results are in good agreement with the fibers specifications shown in table-1.

ACKNOWLEDGEMENT

The authors would like to thank Dr. I. Morita of KDDI R&D laboratories Inc. for providing us the fiber samples used in their experiments. They are also grateful to Mr. Y. Hinata of A-Tic company for his assistance in splicing of different kinds of fiber.

REFERENCES

[1] M. Suzuki and N. Edagawa, *J. of Lightwave Technology,* vol. 21, no. 4, April 2003.

[2] K.Nakajima, M.Ohashi and M.Tateda, *J. of Lightwave Technology*, vol. 15, No.7, pp.1095-1101,July 1997.

[3] M.S. O`Sullivan and R.S. Lowe, "Interpretation of SM fiber OTDR signatures," *Proc. SPIE`86* vol. 661, Optical Testing and Metrology (1986), pp 171-176.

[4] Luc B. Jeunhomme, *"Single –Mode Fiber Optics Principles and Applications,"* optical engineering/vol. 23, second edition,pp. 187.

[5] P. Di. Vita and U. Rossi, *Electron. Lett*., vol. 15, pp. 467-469, July, 1979.

[6] M. Ohashi and M. Tateda, *Electron. Lett.,* vol. 29, pp. 426-427, 1993.

[7] John M. Senior, *"Optical fiber communications principles and practice,"* Prentice-Hall,1985.

[8] A. Rossaro, M. Schiano, T. Tambosso, and Davide D`Alessandro, *IEEE J. on Select. Topics in Quantum Electronics*, vol. 7, no.3, pp.475-483, May/June 2001.

[9] M. Imran Baig, T. Miyauchi and M. Imai, *Proc. of WFOPC 2005*, IV.2, pp. 146-151, June 2005.

[10] M. Imran Baig, T. Miyauchi, M. Imai and S. Sato, *Optical Engineering,* 2006 (to be published).

[11] J.W. Fleming, *Electron. Lett.,* vol. 14, no. 11, May 1978.

[12] D. Marcuse, Bell System Technical Journal, vol. 56, pp. 703-718, 1977.

[13] "ITU-T Contribution G.650," Dec. 1997. Definition and test methods for the relevant parameters of SM fibers.

Assessment of the potential accuracy of a four wavelength OTDR to measure Chromatic Dispersion.

David Ives, Joan Hall and Christian Hart, Photonics Group
National Physical Laboratory, TW11 0LW, United Kingdom.

Abstract: Modern multi-wavelength Optical Time Domain Reflectometers (OTDRs) are capable of measuring chromatic dispersion of installed links. This paper describes the sources of uncertainty associated with this measurement along with techniques to assess each contribution. The potential accuracy based on the assessment of one four wavelength OTDR is calculated.

Introduction

OTDRs can be used to measure the total chromatic dispersion of a fibre link. The technique is a bi-directional version of the Spectral Group Delay in the Time Domain technique[1] and relies on measuring the variation in the time of flight of the optical fibre with wavelength. In the case of OTDRs the distance to a well-defined end reflection is measured at a number of wavelengths (typically four). These distances are converted back to time of flight, $\tau(\lambda_i)$, for each of the discrete measurement wavelengths, λ_i. These time of flight data points are fitted to a time delay model and the resulting model parameters are used to calculate the chromatic dispersion. In this paper only three term models have been considered, the three-term Sellmeier equation, and the three-term quadratic equation,

$$\tau(\lambda) = a_{-2}\lambda^{-2} + a_0 + a_2\lambda^2 \text{ and } \tau(\lambda) = a_0 + a_1\lambda + a_2\lambda^2, \quad (1) \& (2)$$

where a_i are the fitted parameters. The accuracy of the chromatic dispersion depends on accurate measurements and accurate fibre time delay models. The critical measurement is the change of time delay for the different wavelengths. This depends on the ability to repeatably locate a well-defined end reflection while ensuring that there is no zero offset between the different laser sources. The latter is only important if the OTDR does not perform a cut back measurement. It is also necessary to know the wavelength of each laser source and less critically the overall distance scale uncertainty.

Assessment of OTDR

The source wavelengths can be measured using a calibrated optical spectrum analyser (OSA). It is necessary to operate the lasers in their normal pulsed mode since a continuous wave mode can change the operating temperature and thus wavelength. This means that care must be taken not to overload the OSA even though the average power may be quite low. As a test a variable attenuator is inserted between the OTDR and OSA and the attenuation increased in steps until the total power measured on the OSA decreases in sympathy. The uncertainty of the wavelength measurement is combined with the deviation of the measure centre wavelengths from their internal OTDR software values to calculate the OTDR wavelength uncertainty, σ_λ. For the OTDR tested σ_λ was found to be 0.75 nm although by adjusting the OTDR software values this could be reduced.

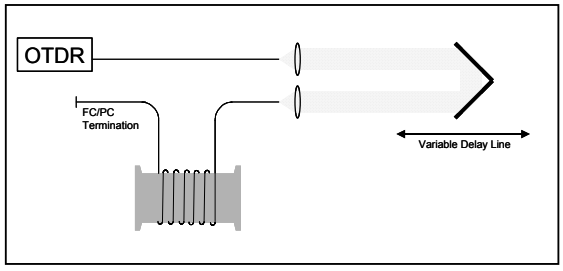

Figure 1 Experimental arrangement to assess the distance resolution and repeatability of the automated event recognition software

The distance resolution and the repeatability of the automated event recognition software were assessed using the experimental arrangement in Figure 1. The OTDR was connected through a variable optical delay to a 35 km fibre sample. Since the OTDR sample resolution was stated to be 50 mm the variable optical delay was scanned in small, 5 mm, steps over a 100 mm range and the distance to the end reflection recorded for each OTDR wavelength. The OTDR was operated in its automated chromatic dispersion measurement mode allowing it to optimise the pulse width and event recognition features. The OTDR used a 10 ns pulse and determined the position of the end reflection from the position of the peak of the reflected signal. The OTDR measured distance was converted into time delay using the OTDR assumed group index for each wavelength. The variable optical delay time was subtracted from the OTDR time delay for each measurement to leave the fixed time delay of the 35 km fibre. The standard deviation was taken for each wavelength and combined with the uncertainty of the variable optical delay to calculate the OTDR time resolution, σ_{TR}. For the OTDR tested σ_{TR} was found to better than 0.05 ns.

The zero offset distance of the different wavelengths is critical to avoid biasing the chromatic dispersion results. This was determined using the same set up of Figure 1 but by replacing the 35 km fibre with a 4 m patch lead. Again the OTDR distance to the end reflection was recorded, using the automated chromatic dispersion software, for each wavelength while the optical delay was incremented in 5 mm steps over a 100 mm range. The OTDR measured distance was converted into time delay using the OTDR assumed group index for each wavelength and the variable optical delay time subtracted as before. The standard deviation was taken for the whole data set, all the wavelengths together; to obtain the zero offset uncertainty, σ_{ZO}. For the OTDR tested σ_{ZO} was found to be 0.5 ns. This uncertainty could be removed by carrying out a cut back measurement and this would have reduced the uncertainty contribution to 0.05 ns due only to the short length repeatability, however the OTDR tested did not have this feature.

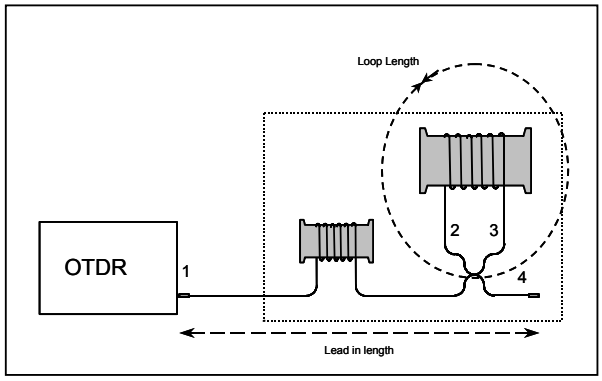

Figure 2 Assessment of OTDR distance scale deviation using a re-circulating delay line.

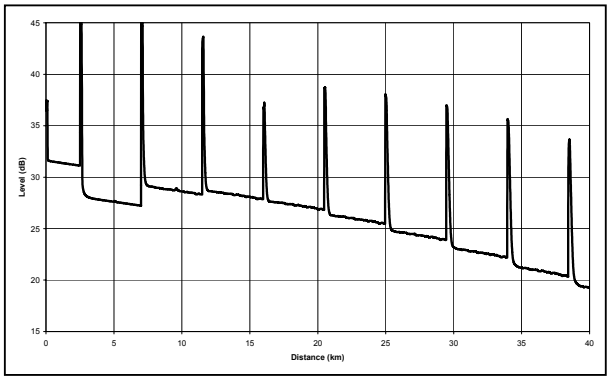

Figure 3 Typical OTDR trace.

The distance scale deviation affects the overall distance accuracy and thus the overall chromatic dispersion accuracy. The distance scale deviation can be easily assessed using a re-circulating delay line[2]. The re-circulating delay line consists of a lead in fibre connected to a 50/50 coupler which is joined back on itself by a loop fibre. The fourth port of the coupler is given a flat end face to provide a well-defined reflection event, see Figure 2. The OTDR trace, Figure 3, shows a sequence of reflection events spaced at half the loop length. The distance to these events is fitted by linear regression to obtain the spacing, which is compared to the loop length to obtain the distance scale deviation. The distance scale deviation is combined with the uncertainty in its measurement to obtain distance scale uncertainty, σ_X. For the OTDR tested σ_X was found to be 0.00003 $m.m^{-1}$. This is likely to be the least significant uncertainty contribution to the measurement of chromatic dispersion.

Fitting Equations

The uncertainty due to the fitting equation can be estimated by comparing the chromatic dispersion calculated from a three term fit to time delay data at the four measurement wavelengths with chromatic

dispersion calculated from a high order fit to a larger time delay data set measured using the phase shift technique. The latter is taken as a true estimate of the chromatic dispersion of the fibre under test. The best three term fits for calculating the chromatic dispersion in the two wavelength ranges and for five fibre types are shown in the Table 1 (It should be noted that this is based on very limited measurements, one fibre of each type and is for guidance only. Further work is required.).

Fibre Type	Zero Dispersion Wavelength (nm)	Chromatic Dispersion at 1550 nm ($ps.nm^{-1}.km^{-1}$)	Best three term fit for Chromatic Dispersion results in wavelength window (nm)	
			1250 – 1450	1450 - 1650
SMF28 ™	1313	16.8	Sellmeier	Sellmeier
DSF	1547	0.3	Quadratic	Quadratic
LEAF ™	1575	-2.9	Quadratic	Quadratic
TRUEWAVE ™	1449	4.4	Sellmeier	Quadratic
DCF	-	-106.7	-	Quadratic

Table 1 Fibre type vs best three term fit. This is the best three term fit for calculating the chromatic dispersion in the range shown using all four wavelength points.

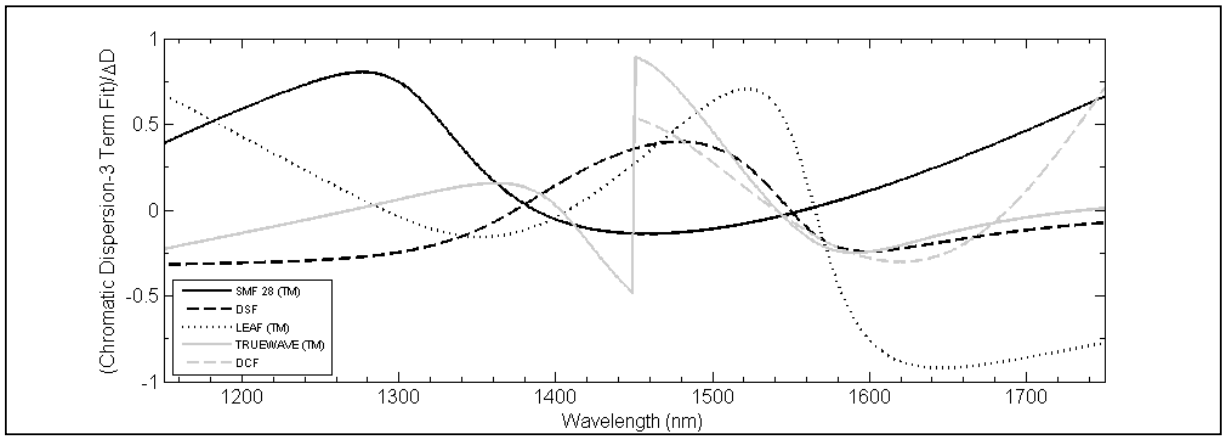

Figure 4 Difference between the chromatic dispersion and the best fit 3 term equation divided by the empirical derived error of equation 3 or 4. The discontinuity in the curve for the TRUEWAVE™ fibre is caused by a change in the best 3 term fit equation, see Table 1.

An empirical relation of the maximum difference between the chromatic dispersion and the best three term fit was developed and found to be correct for the five fibres in the ranges shown in Table 1. For the three term Sellmeier this was found to be

$$\left|\Delta D_{CD-3T\ Sellmeier}\right| < \sqrt{0.25^2 + 0.05^2 D^2 + 0.0025^6 (\lambda - <\lambda>)^6} \quad (ps.nm^{-1}.km^{-1}), \tag{3}$$

where $<\lambda>$ is the mean of the four measurement wavelengths (nm), λ is the wavelength (nm) where the difference is being calculated and D the chromatic dispersion ($ps.nm^{-1}.km^{-1}$). For the three term Quadratic the maximum difference was found to be given by

$$\left|\Delta D_{CD-3T\ Quadratic}\right| < \sqrt{0.25^2 + 0.05^2 D^2 + 0.007^6 (\lambda - <\lambda>)^6} \quad (ps.nm^{-1}.km^{-1}). \tag{4}$$

Figure 4 shows the difference between the chromatic dispersion and the best three term fit as a fraction of the empirically derived error of equations 3 and 4. This is less than ±1 showing that the empirically derived maximum error is correct over this wavelength range for these fibres.

Uncertainties

The uncertainty in the chromatic dispersion due to the OTDR is calculated by combining the OTDR resolution, offset and wavelength uncertainties into a single relative time uncertainty for each wavelength,

$\sigma_\tau(\lambda)$ ps.km^{-1},

$$\sigma_\tau(\lambda)^2 = \frac{\sigma_{TR}^{\ 2}}{L^2} + \frac{\sigma_{ZO}^{\ 2}}{L^2} + D(\lambda)^2\,\sigma_\lambda^{\ 2}, \quad (5)$$

This relative time uncertainty is used to calculate the chromatic dispersion uncertainty, σ_D ps.nm^{-1}.km^{-1}, through the statistics of the fitting process. The uncertainty in the zero dispersion wavelength, $\sigma_{\lambda 0}$ nm, is calculated through the dispersion slope, $S(\lambda)$ ps.nm^{-2}.km^{-1} and

$$\sigma_{\lambda 0} = \frac{\sigma_D}{S(\lambda)}, \quad (6)$$

The measurement uncertainty is combined with the distance scale deviation, the effect of the assumed fitting equations, the temperature dependence of the fibre[3] and the overall repeatability of the measurement. The measurement uncertainties are dominant for short fibres (<50 km) while the effect of the fitting equations become dominant for longer fibres (>50 km).

Measurements

Table 2 show the zero dispersion wavelength and chromatic dispersion at 1550 nm measured by the NPL phase shift system and by the OTDR with their 95% confidence intervals. The results are within the 95% confidence intervals.

Fibre	Zero Dispersion Wavelength (nm)		Chromatic Dispersion at 1550 nm (ps.nm^{-1}.km^{-1})	
	Phase Shift	OTDR	Phase Shift	OTDR
SMF28 ™	1313.1 ± 0.1	1331.4 ± 19.0	16.76 ± 0.25	18.2 ± 1.5
DSF	1546.6 ± 0.1	1542.0 ± 12.6	0.26 ± 0.01	0.7 ± 1.0
LEAF ™	1574.7 ± 0.1	1574.7 ± 21.1	-2.95 ± 0.05	-3.2 ± 2.0
TRUEWAVE ™	1448.8 ± 0.1	1454.6 ± 21.3	4.36 ± 0.07	4.3 ± 2.1

Table 2 Zero dispersion wavelength and chromatic dispersion at 1550 nm measured using both phase shift and OTDR techniques. Uncertainties shown are 95% confidence intervals. 3 term fit as suggested in Table 1.

Conclusion

The significant uncertainties in the calculation of the zero dispersion wavelength and chromatic dispersion from OTDR data are the accurate measurement of time at known wavelengths and the quality of the fitting equation. Techniques to assess the OTDR accuracy have been described. An empirical relationship for the error due to the fitting equation has been developed and compared for five fibre types.

For short fibres the accurate measurement of the time of flight is the dominant component while for longer fibres the error between using a three term fit and the true curve is the dominant component. The best uncertainty on the zero dispersion wavelength in the long fibre regime is expected to be around ± 3 nm, while the best dispersion uncertainty is expected to be around ± 0.3 ps.nm^{-1}.km^{-1}.

Acknowledgements

We gratefully acknowledge the financial support of the UK Department of Trade and Industry.

References

[1] "Optical fibres. Measurement methods and test procedures. Chromatic dispersion" IEC 60793-1-42:2001
[2] "Calibration of optical time-domain reflectometers (OTDRs)" IEC 61746:2005
[3] M C Wicks, "Temperature dependence of Zero Dispersion Wavelength in Single Mode Optical Fibres", NPL Report, June 1996.

Critical Issues Relating to FTTH/PON Testing

by

Dr. Andre Girard

Senior Member of Technical Staff

EXFO E.O. Engineering, Inc.
400 Godin Avenue, Quebec City, QC Canada G1M 2K2
Tel.: 1-418-683-0913 #3138; Fax: 1-418-683-2170
E: andre.girard@exfo.com; Web: www.exfo.com

Presented at SOFM 2006, Boulder, CO, USA, September 19-20, 2006

Summary

Fiber-to-the-home (FTTH) Passive Optical Networks (PON) is currently in major deployment or demonstration around the world. The technology is currently being supported by international standards organizations such the International Telecommunication Union (ITU-T), the Institute of Electrical and Electronic Engineers (IEEE) and the International Electrotechnical Commission. This paper will address the following issues:

- Market and driving application motivation compared to other access technologies together with the related bandwidth requirements.
- Description of PON topologies and architectures
- Critical aspects and challenges during PON installation, operation and maintenance.
- Technical challenges having forced the development of new test instrumentation.

A textbook, Girard, A. “FTTx PON Technology and Testing”, 191pp, © 2005 will be distributed in conjunction with the presentation.

1 Market and applications

PON is one of many solutions for supporting bandwidth and services provisioning in the access network as shown in Figure 1. Typical modern basic triple-play applications and future ones make the total downstream bandwidth demand at levels between 30 to 40 Mbit/s, as shown in Table 1. PON represents an attractive solution for bringing these high-bandwidth consuming applications to home and small office, home office (SOHO) residences. PON is considered a cost-effective and very long-term maintaining solution because it uses no active elements between the service provider’s central office and the subscriber’s premises, as shown in Figure 1. Totally passive components are used in the field; and consequently they substantially contribute to improve the network reliability, decrease maintenance costs, and provide a much better life cycle cost and return on the investment.

FTTH PON is based on two basic architectures: point-to-point (P2P) (Figure 2) and point-to-multipoint (P2MP) (Figure 3), with the later further divided in broadband PON (BPON), Ethernet-ready PON (EPON) and gigabit-capable PON (GPON).

The P2P architecture operates on the same downstream and upstream wavelength (1310 nm) and has no bandwidth provisioning limitation. However, it has a poor premises count per cable and is consequently considered more expensive and less cost effective than the P2MP architecture for the FTTH market.

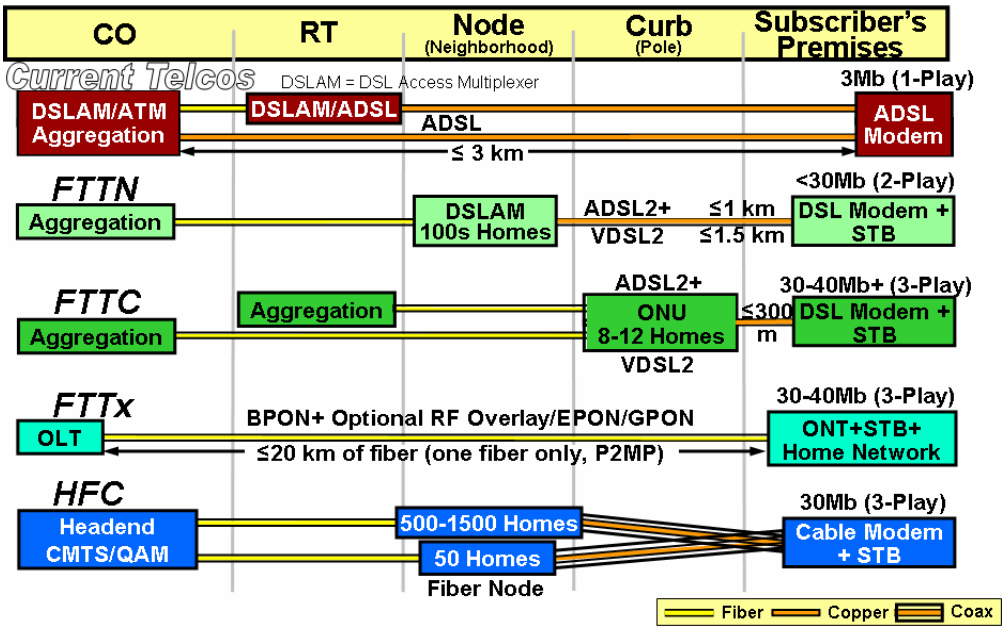

Figure 1 –Solutions for bandwidth and service provisioning in the access network

Applications			Bandwidth (Mbit/s) Single appl.	Maximum MPEG-2	Maximum MPEG-4 WM 9
Voice *(per channel)*			0.064	0.5 (Multi-lines)	
Web browsing			1 – 2	5-10 (2 PC's)	
File download *(10s-6Mpixel JPEG picture*)*			2		
TV Broadcasting *(per channel)*	**SD**	*MPEG-2*	4 – 6	10/2TV	
		MPEG-4	2		5/2TV
	HD	*MPEG-2*	20	20/1TV	
		MPEG-4	9		8-10/1TV
		Windows Media 9	8		
Others *(e.g. e-health/e-safety probing/monitoring)*				*5*	*10*
TOTAL (per premises)				***~40***	***~30***

J/MPEG: Joint/Motion Picture Experts Group * Real-time = 50 Mbit/s minimum

Table 1 – Typical home applications and related bandwidth demand

The P2MP architecture operates on different downstream (1490 nm + 1550 nm if RF analog video overlay is used as shown in Figure 4) and upstream (1310 nm) wavelengths and provides bandwidth on a shared basis. Even with the additional use of a power splitter between the CO transmitter and the premises, it has a very large premises count per cable (a 144-fiber cable serves 4608 homes) and is consequently considered the most attractive solution for the FTTH PON market.

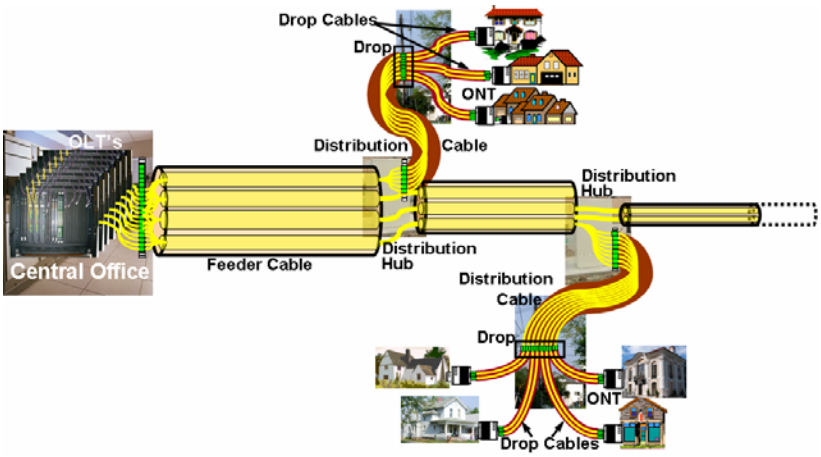

Figure 2 – Point-to-point (P2P) PON architecture

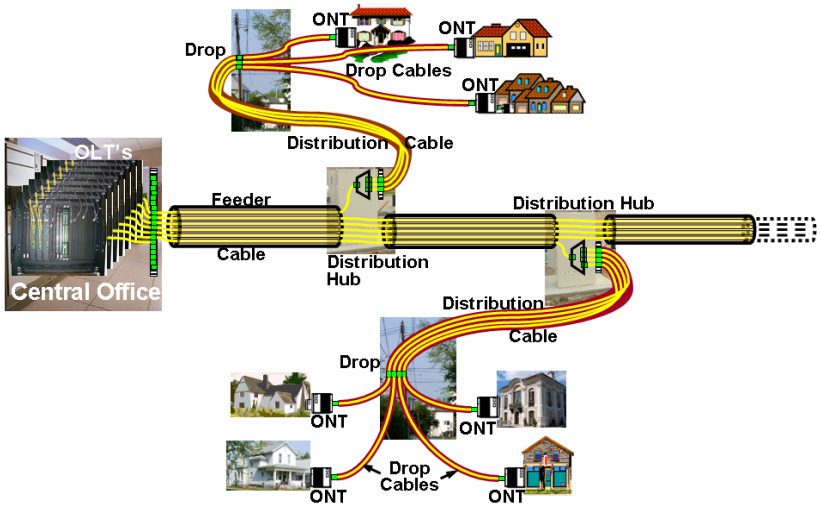

Figure 3 – Point-to-multi-point (P2MP) PON architecture

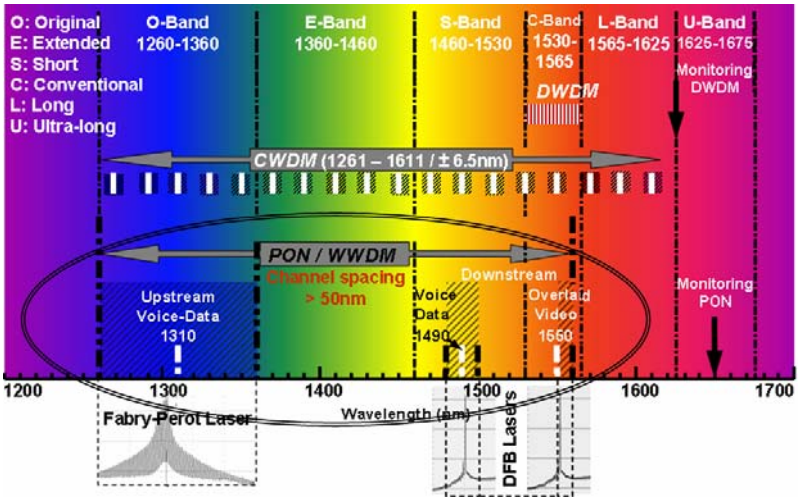

Figure 4 – Spectral bands used in telecommunication networks

2 Critical PON issues

Even if PON is an attractive business solution for the premises access network, there are some technical issues that installers and operators will have to take into consideration in order to ensure successful deployment and avoid market disruption if anything goes wrong.

The choice of transmitting video on analog RF signal using 1550 nm separate wavelength brings a certain number of critical issues such as human safety, stimulated Brillouin scattering non-linear effect and composite second-order beat noise all due to the very high power used. Furthermore, an expensive transmitter is required together with narrowband filtered cooled DFB laser with external modulation. Localized laser heating may also happen especially in case of very high power RF video transmission together with dirty or bad connection.

In order to keep the cost of the premises equipment down, an inexpensive transmitter and receiver are used. However the choice of a Fabry-Perot laser also brings technical issues such as mode partitioning noise and mode hopping due to the multi-frequency nature of that laser.

Macrobending is another issue related to excessive fiber curvature such as in fiber management system causing loss of light. It is mostly workmanship-related. It is defined in fiber specifications as in the ITU-T Recommendations G.65x series. The longer the wavelength the more sensitive it is and could reach 0.5 dB at 1550 nm. Apart of fiber discontinuity, voids, gaps, misalignment, mismatch, and angular cracks, one of the worst issue related to network performance is still related to connector cleanliness or lack of verification that connectors are in fact clean before connecting.

3 Testing requirements

3.1 Physical layer

Adequate testing during network construction, installation and commissioning will always minimize costly and time-consuming afterwards troubleshooting efforts. The following is a list of areas in which particular attention should be provided.

(1) Construction and installation

- Qualification of installed outside plant equipment through optical loss and optical return loss (ORL) measurement using OTDR and automated optical loss test set
- End-to-end link characterization assessing splices and cable plant, connectors and splitters with bidirectional loss and ORL measurement

(2) Service activation and troubleshooting

- Verification of each optical signal power to be within specification
- Problem source/location identification

PON link characterization using an OTDR has however created new OTDR requirements and consequently a new product development. For instance, a much shorter dead zone is required in order to detect the closest drop terminal from the premises (see Figure 3). A much larger dynamic range is also required to go through the lossy splitter (see Figure 3). The OTDR should also be able to measure through the splitter, distinguishing between the splitter loss (approximately 17.5 dB for a 1x32 splitter) and the end of fiber, in order to characterize the link after the splitter. Finally, high resolution is required to characterize closely-spaced events.

These have brought the development of a new handheld-type PON-optimized OTDR operating at

1650 nm for in-service activation and troubleshooting.

Optical power measurement at the CO is required to ensure that sufficient power is delivered to the premises. This is done only during the initial activation because it cannot be repeated without interrupting service for the entire network. A new wavelength-isolating PON power meter measures the power of each wavelength simultaneously without traffic interruption. Power thresholds may be used in order to provide pass, warning or fail status for each wavelength simultaneously.

Each time new premises are added to the PON, downstream and upstream optical powers at the drop terminal and at the premises should be measured. Because of the bursty nature of the upstream 1310-nm traffic, the new wavelength-isolating PON power meter must be capable of simultaneously measuring the continuous downstream power at 1550 nm and 1490 nm, and the bursty upstream power at 1310 nm each for BPON, EPON and GPON.

3.2 Protocol layer

On of the advantages of using ATM in PONs (BPON and GPON) is that it includes management features to guarantee quality of service (QoS). This allows network service providers to guarantee transmission rates, error rates, and other characteristics to their customers. Two types of testing can be performed with ATM-based PONs for ensuring QoS. Those are non-intrusive testing (in-service) used to monitor live traffic for service-affecting faults, and intrusive testing (out-of-service) used for circuit turn-up and troubleshooting faults. An end-to-end QoS test can be run in order to determine if performance will degrade over time.

There are two levels to ATM testing. One is cell level testing which requires wire-speed ATM traffic generation and cell analysis. The second is packet level analysis which requires reassembly of cells into packets and analysis of upper layer protocol layers. The packet latency and loss measurement is an example of the later.

In case of EPON, Ethernet was not designed with QoS in mind and, originally, offered no means to differentiate between low and high priority data. This made it difficult to combine different types of services, such as email and voice communications, over the same link while ensuring that transfer rates met pre-established criteria. Various solutions have been proposed since then to overcome this shortcoming. One improvement is to manage network traffic by grouping similar types of traffic together (for example, email, streaming video, voice, large document file transfer) and treating each type as a class with its own level of service priority. This technique is called class of service (CoS).

Regardless of the CoS specified for any particular type of data, various factors such as network congestion can affect the actual rate at which the data is transferred. For this reason, specific tests are required to verify Ethernet performance in order to ensure that the SLA requirements are met.

The data-communication industry has put together a test methodology to address the issues of performance verification at the layer-2 and layer-3 levels. The Internet Engineering Task Force (IETF) has developed RFC 2544 (“Benchmarking Methodology for Network-Interconnect Devices”, IETF, Ed. S. Bradner & J. McQuaid, The Internet Society, March 1999) in order to specify the requirements and procedures for testing the network performance characteristics. When these measurements are performed, they provide a baseline for service providers to define SLAs with their customers.

3.3 Component testing

Characterizing PON passive components in manufacturing is a critical step in ensuring the optimum PON performance. Important parameters such as insertion loss, spectral uniformity, bandwidth, isolation (for passive WDM components while called crosstalk for systems) central channel wavelength, polarization dependence, and optical return loss must be controlled and tested during development, engineering and production.

Three test methods are currently available depending on the device complexity and performance requirement: one based on broadband light sources (BBS), one based on swept delay system and a test method based on swept-wavelength (or frequency) system. A possible compromise between testing time and system complexity may be a system using a tunable scanning laser, a polarization controller and multi low-polarization-dependent response (PDR) detectors, capable of performing IL, ORL and PDL measurements.

For active components, the most critical parameters to be considered in production testing are:

- Center wavelength
- Bandwidth (spectral distribution and linewidth)
- Frequency stability/temperature control (when applicable)
- Output power stability/control
- Life time (failure in time - FIT).

4 Conclusion

FTTH PON has never provided before such service applications and bandwidth provisioning to residences and SOHO. However there are still and will be technical and market issues that will need to be looked at and in some cases overcome. Proper testing, measurement and monitoring strategy and instrumentation will have to be carefully implemented. The following five market conditions will have to be met before FTTH PON becomes a wide spread reality:

- A growing telecommunication market
  - Opened, highly competitive market
  - No single dominant service provider
- Favorable Government FTTH policy / regulations
- Educated middle-class population knowing, accepting and desiring telecommunication technologies
- Optical fiber used as a marketing incentive
- Favorable conditions for consuming HDTV

When these conditions will be met together with yet-to-be-found killer applications, FTTH PON will become the only long term suitable transport solution.

WDM-PON for FTTx

Wayne V. Sorin[1], Chang-Hee Lee[2], Byoung Y. Kim[1],

[1] *Novera Optics, Inc., 2620 Augustine Dr., Santa Clara, CA 95054*
[2] *Korea Advanced Institute of Science and Technology, Daejeon, Korea*

Introduction

WDM-PON is a general purpose and extremely efficient future-proof optical transport technology for use in Access and Metro transport networks. It enables highly efficient use of the outside fiber plant by providing point-to-point optical connectivity to multiple remote locations through a single feeder fiber.

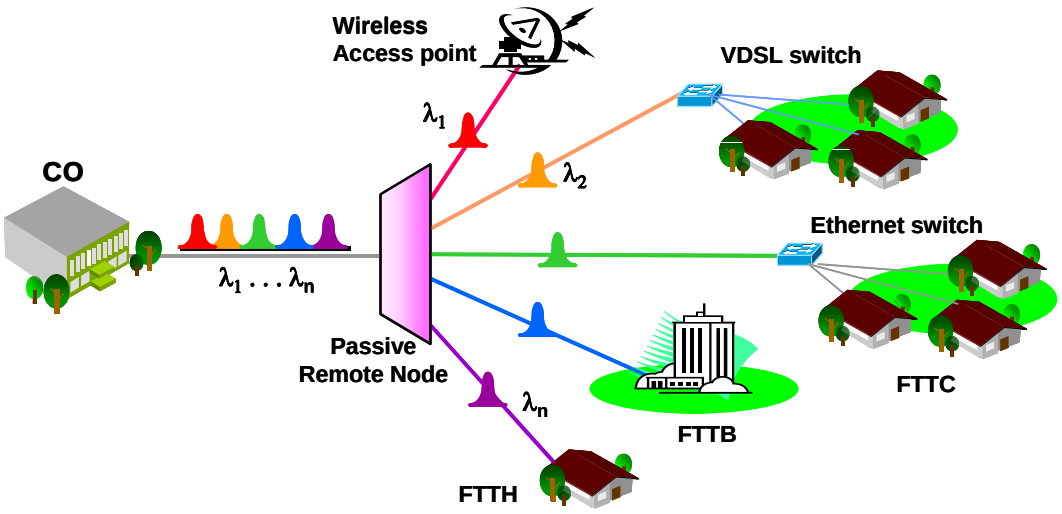

Figure 1. WDM-PON supports multiple services

Figure 1 illustrates the general FTTx (Fiber-to-the-x) architecture using a WDM-PON (Wavelength Division Multiplexed Passive Optical Network). As can be seen in the figure, this general-purpose architecture can serve multiple applications for both the business and residential customer. This functionality is possible since each end point is connected to the central office through a dedicated bidirectional optical channel. This virtual point-to-point PON architecture enables large guaranteed bandwidths, bit rate independency, protocol transparency, graceful upgradeability, high QoS with excellent security and privacy.

Until recently, WDM (i.e. dense WDM) has been used only for long-haul and metro applications and was not thought to be economical for the access market. One reason for this

is that each remote site would have needed a unique transceiver (i.e. a wavelength-stabilized DFB laser) to match the WDM channel defined by the optical transport layer. These differently "colored" transceivers raised concerns regarding the high operational costs (installation, management and inventory) associated with managing each remote access location.

This limitation has been solved through the development of an innovative technology that has eliminated the need for complex wavelength-stabilized lasers [1, 2]. By utilizing an "optical injection seeding" technique, simple and identical Fabry-Perot lasers can now be used at all the remote ONU (Optical Network Unit) locations. Although all the transmitters are identical, each one operates at a different DWDM wavelength through the use of a novel automatic wavelength-locking technique. The term "wavelength-locked" WDM-PON will be used to describe a WDM-PON system that utilizes identical transceivers by means of automatic wavelength locking. In this paper we will review the concepts behind a wavelength-locked WDM-PON and will discuss a measurement instrumentation opportunity for this future-proof access architecture.

Comparison with Conventional WDM system

It is useful to first describe how a wavelength-locked WDM-PON differs from a more conventional long-haul WDM transmission system. Conventional WDM systems, as illustrated at the top of figure 2, typically carry unidirectional traffic over each fiber transmission link. This allows the use of unidirectional optical amplifiers that are normally required in long-haul applications. Therefore, bidirectional traffic requires two separate data links, one for eastbound traffic and another for westbound traffic. In contrast a WDM-PON provides the same functionality using only a single bidirectional data link. This is possible by using a cyclic or periodic AWG that can support both a separate upstream and downstream wavelength on each of its "n" output fibers. To achieve this functionality the AWG must be designed to operate on a high diffraction order (just as in a classical bulk-optics diffraction grating). By requiring only single fiber connections at each location, this simplified architecture becomes much more suitable for access network applications.

Another important difference is eliminating the need for "n" different laser sources (i.e. multiple wavelength-stabilized DFB lasers) at the "n" transceiver locations. By using automatically wavelength-locked FP-LDs (Fabry-Perot laser diodes), each remote transceiver can be identical and interchangeable with all the other remote transceivers. Identical transceivers are critical for minimizing inventory and management costs in an access network application. Wavelength locking of FP-LDs will be described in the following section.

Also of importance is the recent development of athermal AWGs that enable the remote node to be completely passive. Previously AWGs required heaters to keep their WDM channels locked onto the ITU wavelength grid. This active power requirement was acceptable in conventional long-haul applications since the AWGs (together with the temperature stabilized DFB lasers) could be located in temperature-controlled environments (i.e. central offices).

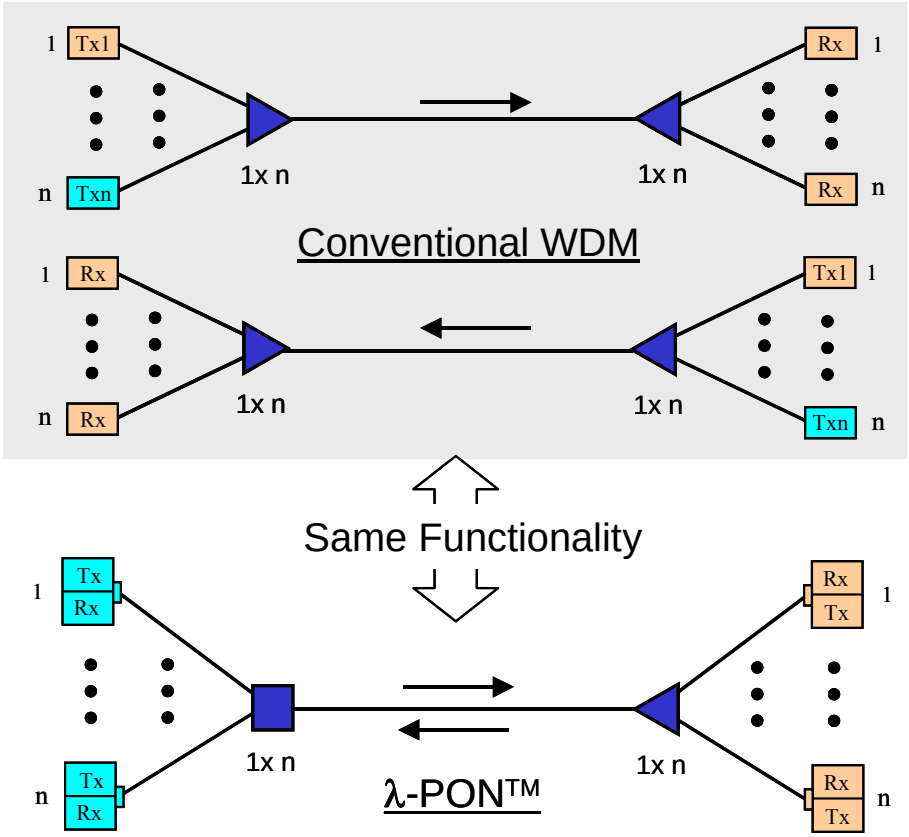

Figure 2. Comparison with a conventional WDM system.

In summary, a wavelength-locked WDM-PON differs from a conventional WDM long-haul system by (i) enabling bidirectional transmission over each of its optical fibers, (ii) providing a point-to-multipoint architecture through a passive and environmentally hardened remote Mux/DeMux, and (iii) using identical and interchangeable automatically wavelength-locked FP-LDs.

Automatic Wavelength Locking in a WDM-PON

Figure 3 illustrates the operation of automatic wavelength locking in a WDM-PON system. An un-modulated BLS (Broadband Light Source) located at the OLT (Optical Line Terminal) in the central office is used to generate seeding signals for "locking" the wavelengths of the remotely located identical FP-LDs. The BLS seeding signal is transmitted downstream through the single feeder fiber into the passive remote node containing the athermal and cyclic AWG. At this location the BLS wavelength spectrum is divided or "sliced" into "n" narrowband DWDM (dense WDM) channels by the demultiplexing function of the AWG. Each spectral slice is then transmitted through a single distribution fiber and injected into a remotely located FP-LD. When the FP-LD is current modulated with the electrical data signal, the injected seed signal forces the laser to operate in a narrow wavelength range

defined by the optical passband of the DWDM transmission link. This wavelength locking process can be easily understood when one realizes that the FP-LD basically acts as an optical amplifier that modulates, amplifies and reflects the injected BLS seeding signal. The FP-LD is not capable of free-lasing due to the gain saturation caused by the amplified seeding signal. This results in a stable narrow-band output data signal, free from any of the noise associated with mode-hopping found in standard free-running FP-LDs.

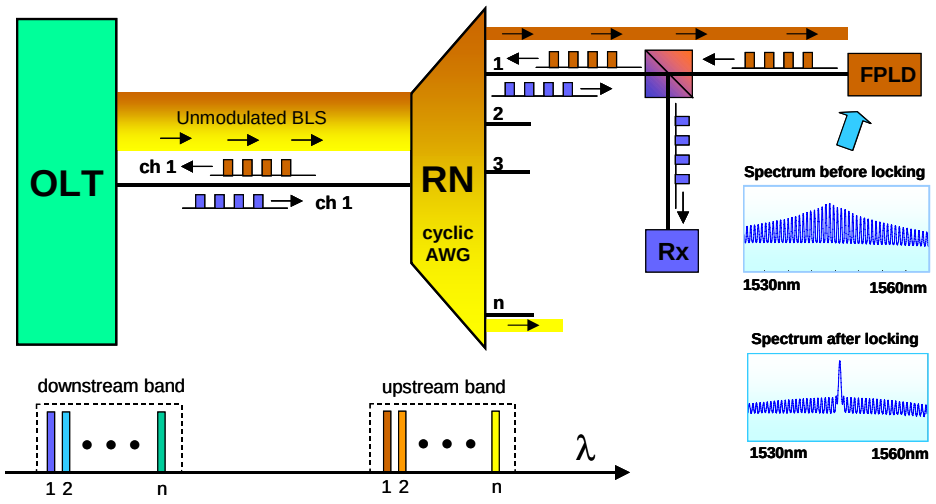

Figure 3. Basic description of automatic wavelength locking

The lower right hand side of figure 3 shows the FP-LD wavelength spectrum before and after applying the seeding or "locking" signal. Without the application of the locking signal, the FP-LD lases in multiple wavelength modes (see top insert on the right). This spectrum is unsuitable for data transmission through the DWDM transmission link due to the generation of mode partition noise caused by the wavelength filtering of the AWG. After injection of the locking signal the multimode spectrum is transformed into a quasi single-mode signal (see bottom insert) similar to that of a DFB laser. This "DFB-like" signal is automatically aligned to the DWDM channel defined by the optical transport layer. This wavelength locking process results in a "plug and play" functionality where all the remote FP-LDs are identical and interchangeable but can operate at different wavelengths without the need of any complex control or locking circuitry.

Figure 3 also illustrates the bidirectional functionality of a WDM-PON. Simultaneously along with the downstream BLS signal, "n" independent downstream data wavelengths are transmitted in a different wavelength band (shown at bottom left of figure 3). Due to the cyclic nature of the AWG, both a spectral slice of the BLS and one downstream data wavelength are demultiplexed and sent to each remote ONU. Each ONU transceiver uses an identical dichroic band-splitting filter which separates the two bands, directing the downstream BLS seeding wavelength into the FP-LD and the downstream data wavelength into a standard optical receiver. The modulated upstream data signal generated by the

wavelength-locked FP-LD returns along the same optical path as the downstream BLS seeding signal.

System Description

Figure 4 shows a typical configuration for a wavelength-locked WDM-PON. Wavelength-locked FP-LDs are used at both the central office and the remote ONUs. All the ONU transceivers are identical and interchangeable. The central office OLT houses the BLS, a Mux/DeMux and the "n" downstream wavelength-locked laser sources.

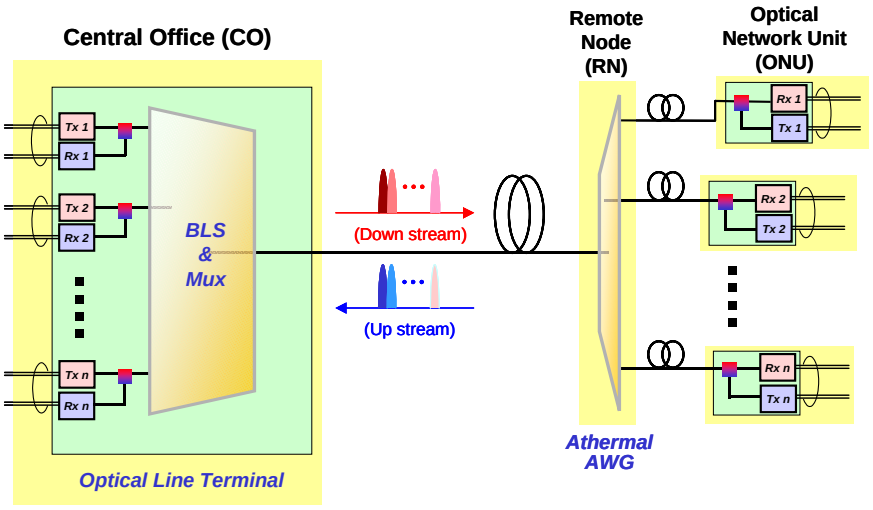

Figure 4. Wavelength-locked WDM-PON system configuration

A single feeder fiber is used to connect the OLT to the environmentally hardened passive remote node. From the remote node, "n" distribution fibers are used to connect to "n" remote ONUs. In summary, over a single feeder fiber this WDM-PON architecture provides a dedicated and bidirectional optical point-to-point connection between "n" transceivers in the central office and "n" remotely located ONUs. There are no special requirements for addressing or managing the multiple remote ONUs.

One important advantage of the WDM-PON architecture is the ability to completely characterize all the optical fiber paths by using a single tunable-wavelength OTDR located at the central office [3]. This is possible since the different DWDM wavelengths provide a unique and low-loss optical path to each remote ONU which can be used to measure individual Rayleigh backscatter signals. This level of optical characterization is not possible in a more conventional TDM-PON (Time Domain Modulation) due to the remote node power splitter that prevents unambiguously identifying the backscatter signatures from the individual fibers after the power splitter. It is expected that a demand for wavelength-tunable OTDRs will emerge as WDM-PONs grow in popularity [4].

Summary

A wavelength-locked WDM-PON is an efficient and future-proof WDM transport architecture optimized for the access network. It provides a point-to-point optical connection over a shared fiber plant by allocating a pair of dedicated wavelengths for each ONU. To reduce both capital and operating costs, a newly developed optical seeding technique enables the use of automatic wavelength locking of identical low-cost Fabry-Perot laser diodes. The benefits of a wavelength-locked WDM-PON access system are; identical wavelength-independent DWDM ONT/ONUs, simple point-to-point dedicated connectivity, bit-rate and protocol independency, high security and privacy, simple future data-rate upgradeability, and complete fiber characterization through use of a wavelength-tunable OTDR.

References:

[1] H. D. Kim, S. G. Kang and C. H. Lee, "A Low-Cost WDM Source with an ASE Injected Fabry-Perot Semiconductor Laser," IEEE Photonics Technology Letters, vol. 12, pp 1067-1069, Aug. 2000

[2] D. J. Shin, Y. C. Keh, J. W. Kwon, E. H. Lee, J. K. Lee, M. K. Park, J. W. Park, Y. K. Oh, S. W. Kim, I. K. Yun, H. C. Shin, D. Heo, J. S. Lee, H. S. Shin, H. S. Kim, S. B. Park, D. K. Jung, S. T. Hwang, Y. J. Oh, D. H. Jang and C. S. Shim, "Low-Cost WDM-PON With Colorless Bidirectional Transceivers," IEEE Journal of Lightwave Technology, vol. 24, pp. 158-165, Jan 2006

[3] J. H. Park, J. S. Baik and C. H. Lee, "Fault-localization in WDM-PONs," Optical Fiber Communications Conference, paper JThB79, Mar. 2006

[4] S. J. Park, C. H. Lee, K. T. Jeong, H. J. Park, J. G. Ahn and K. H. Song, "Fiber-to-the-Home Services Based on Wavelength-Division-Multiplexing Passive Optical Network," IEEE Journal of Lightwave Technology, vol. 22, pp. 2582-2591, Nov. 2004

FTTx Deployment Issues

Jimmy Salinas
AT&T
Senior Manager-Technical Support
js5906@at&t.com

FTTx is talked about in many forms, (FTTN, FTTP, Brown Field, Green Field, Fiber to the Curb, and Fiber to the Home) an the forms all are just FTTx technology applied to match the surrounding. A good example of this is the FTTH Council report of April 25, 2006 covering the 936 communities in 47 states already being served Via Fiber-to-the – Home technology today. Everything from small developments to entire communities, ILEC to DEV/CLEC joint ventures.

In this presentation we will start with FTTP technology and then jump to FTTN technology with an understanding that FTTP technology is only applied to the local loop out of the serving Central Office, excluding the backbone network and local rings needed to get the signal to the local office serving the local loop. FTTP networks are made of an Optical Line Termination unit in the Central Office, the PON local loop including the splitter, and a H-ONT Gateway unit. There are many issues with FTTP technology, but the main issue is "Fiber and Connector Cleaning" with 75% of all troubles being due to dirty connector related issues. This is followed by a misunderstanding of the maximum and minimum PON Loss allowed.

Optical link loss budgets for FTTP PON systems are in two parts, the first being the maximum allowed Optical Link Loss of about 25.0 dB followed by a minimum Optical Link Loss of -14.0 dB. In fact if the optical loss is to low attenuation will need to be added to keep the signal from overdriving the receivers. The Optical Link Budget includes items like fiber loss per Kft, Fusion Splice loss, Connector loss, and 1x32 or 1x16 Splitter loss. Within the Central Office the P-OLT is connected to the world by items like Voice Gateways and Broadband Optical Boxes that connect all other services to the P-OLT unit. Within the Optical OSP Link you have the fiber, a splitter (1x32 or 1x16) and the Fiber Serving Terminal that serve the Home. The FTTP local loop network is finished by the application of a Home-Optical Network Terminal (H-ONT) which serves as a gateway to the customer providing POTS, Ethernet, VoIP, and IPTV service.

Trouble issues with the application of PON technology are the following
1. Dirty Connectors and Bad Splice Points
2. Micro Bending
3. Max Light Loss Budget exceeded
4. Minimum Link Loss not maintained
5. 120 AC needed to power the H-ONT and to charge the back up battery

FTTN systems come with a difference set of problems including the following

1. A max of 12 Kft between the CO and the SAI (Based on 26 GA NL-Loaded Cable) and a max of 9.0 dB loss between the CO and the NID for the POTS Lines
2. A max of 4 Kft (of Drop) between the SAI and the NID for Data
3. Depending on the VDSL/POTS drop length, Bridge Tap cable can be an issue

As with FTTP technology, the FTTN NID (H-ONT) converts the POTS and Optical Data signal from the network into POTS and VDSL services on the customer's side of the NID using a VRAD/HPNA signal that is further converted into Data and Video through a deplexer / router unit.

Due to the fact that FTTX technologies are all built on local loops, short to medium in length and newer type fibers, as well as the improvements in fiber manufacturing (Core placement and Core shaping) and splicing equipment doing automatic alignment, testing and splicing simultaneously, problems like dirty connectors, optical loss, optical return loss, and reflectance can be minimized and detected using tools like Fiber Scope, Bi-directional Power Meters, and Optical Time Domain Reflectometers to test and correct all trouble issues. As well as Jitter and Propagation Delay are not being major issue when FTTx/PON technology is correctly applied.

Other problems like Chromatic Dispersion and Polarization Mode Dispersion (PMD) should not be issues with FTTx technology. This being the case because of the fiber manufacturing methods used today to create a more uniforme shape, size, and placement of the core within the center of the fiber. As well as most FTTx systems being designed today to work in a 10M and 1.0 M range with both problems only being an issue above the 10Gb/s range of operation.

Place note that the Local and Backbone networks being used to support the local loop FTTN or FTTP application are a different matter. Because of the bandwidth and technologies being used to transport the signal between the SHE (Super Head End), VHO (Video Hub Office), and the Local Central Office, extensive system and fiber testing will be required to insure overall system performance requirements.

Fiber system testing requirements can be reduced by following a few of the design items

1. No cable manufactured before 1997
2. No Depressed Clad Fiber or Dispersion-Shifted Fiber
3. All Fusion spliced cable, no mechanical splices
4. No damage cable that has been restored
5. No cable that has temperature induced cable loss
6. No Biconic connectors, replace with SC type connectors
7. Clean all fiber connection points every time accessed

FTTx is the future with the ability to deliver greater bandwidth and data rates (20 to 25M), with lower installation and maintenance cost along with the ability to grow as the customer's need grow.

If proper design, application, and engineering guide lines are applied when creating your FTTx network of the future along with the supporting interoffice network. There is no reason for your network of the future to not grow with your customer's needs at a minimal cost to you the network provider. In fact this network should be ready for all your customer's anticipated future needs (1 to 24M and up) for many years to come.

Thank You for Your Attention and Time
Jimmy Salinas

Special requirements for measurement techniques used for POF and thick glass fibers

Olaf Ziemann, Polymer Optical Fiber Application Center
University of Applied Sciences Nürnberg, Wassertorstraße 10, 90489 Nürnberg/Germany
Ph./Fax: ++49 911 5880-1060/ -5060
e-mail: olaf.ziemann@pofac.fh-nuernberg.de, web: www.pofac.de

Summary

Optical fibers are well established in the field of data communication and local area networks. It is obvious, that a high number of different measurement technologies and devices for optical fiber have been developed and produced over the last years. Examples are spectrometers, reflectometers and dispersion measurement setups. The fibers typically used in these areas are made from silica glass having core diameters between 10 µm (single mode) and 62.5 µm (graded index multi mode). Operation wavelengths are around 850 nm, 1,300 nm and 1,550 nm. Of cause, all the measurement devices are optimized for these conditions.
In a number of new applications, fibers are used newly for short-range data communication as well. The high reach and transmission capacity of communication glass fibers is not required here. On the other hand side, special attention must be taken for easy installation and low cost components. The solution is the use of large core diameter optical fibers like POF (Polymer Optical Fiber) and PCS (Plastic Clad Silica).
The measurement problems for thick fibers are different sometimes. The existing devices can be used only in a limited manner, due to deviating parameters. This paper will give an overview to typical problems, existing solutions an open questions of measurement techniques for thick optical fibers (detailed overview: [1], [2], [3]).

1. Thick optical fiber overview

We like to define “thick” optical fibers as all versions with a core diameter higher than the classical telecommunication fibers (10 µm for single mode and 50 µm for multi mode. The following list includes some of the most important fibers.

- Step index type POF: core diameter: 1 mm, NA: 0.30 to 0.65; core material: PMMA; single ore double optical cladding
- Multi core type POF: core diameter: 1 mm, NA: 0.19 to 0.50; core material: PMMA; 19 to >600 connected cores; single or double coating
- Multi core glass fibers: developed by Schott Glas as an example; about 400 single fibers (each 50 µm diameter) as a loose bundle; NA about 0.50 (see [4] and [5])
- PMMA-GI-POF: core diameter: 0.5 to 1 mm, NA: 0.30 to 0.40; core material: doped or copolymerized PMMA
- SI- and semi-GI-PCS: 200 µm diameter silica glass core with a polymer optical cladding, NA: 0.30 to 0.50; also available with a week graded index profile in the core ([6], [7])
- PF-GI-POF: the core diameter is 120 µm for all existing fibers (62.5 µm and 200 µm included in the standard; core material is CYTOP® by AGC; graded index profile is formed by dopants (detailed description of measurement problems in [8])

Cross-areas of the different fibers with a comparison of the size of communication fibers are shown in Fig. 1.

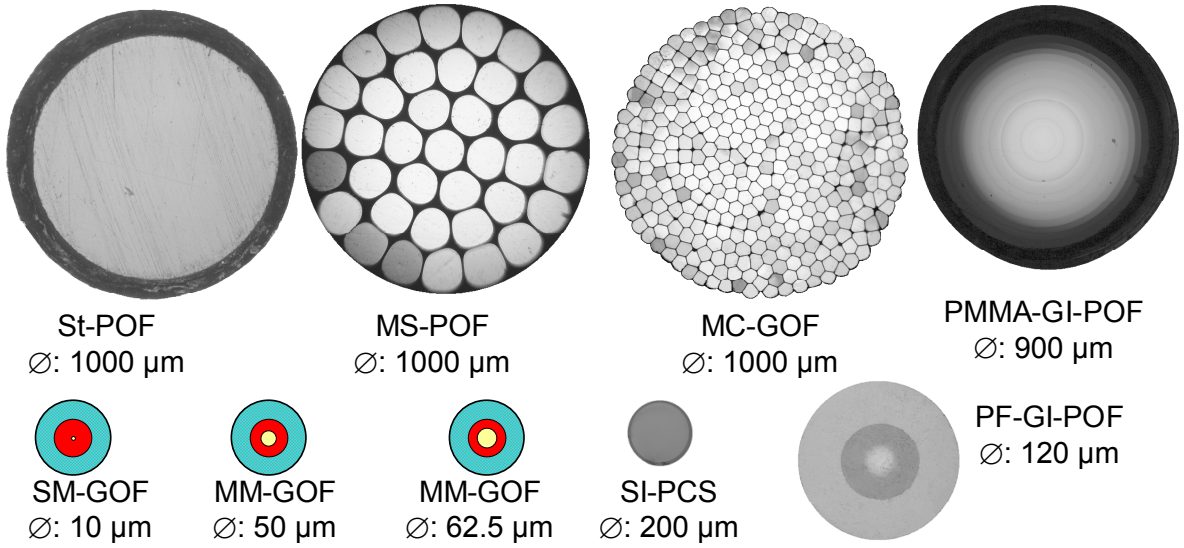

Fig. 1: Comparison of different optical fibers

On a first view, on can see the big differences in the core diameters of the fibers. This influences the requirements for measurement technique, first of all the size of detectors. But there are even more differences existent. The Numerical Aperture (NA) and the core diameter of different available fibers s presented in Fig. 2.

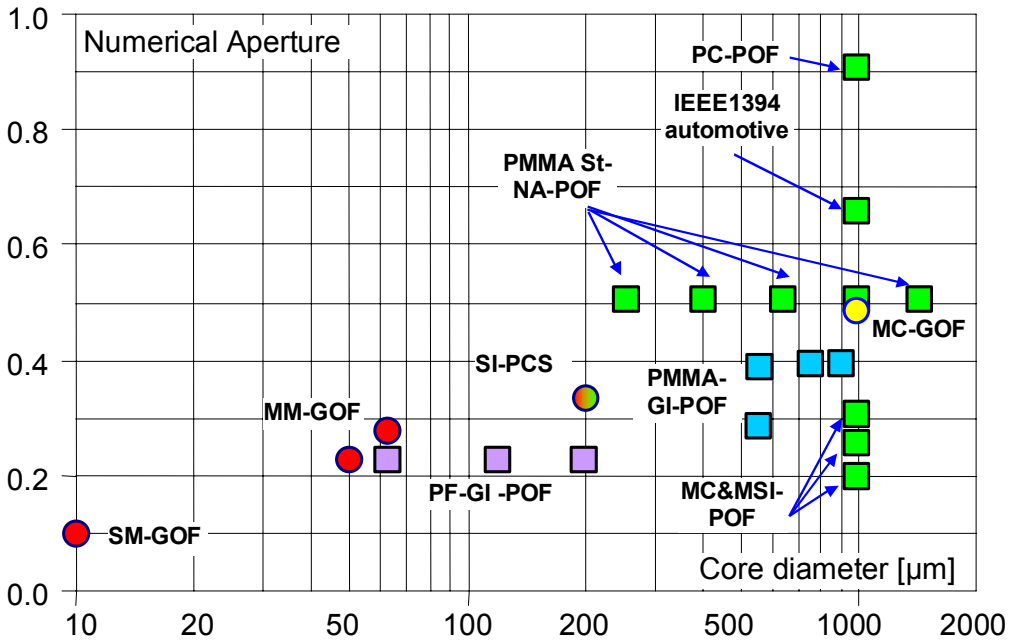

Fig. 2: Comparison of different optical fibers

The perfluorinated GI-POF is more or less comparable with glass multimode fibers. Most of the existing measurement devices, optimized for MM-GOF can be use with small changes. But for MC-GOF, PMMA based POF and the PCS the situation is different, even more, if one take into account, that the operation wavelength is between 450 nm and 780 nm, which is an unused range for silica glass fibers.

If a standard optical device is used for thick fibers, the most frequent error is, that only center low order modes are detected. This leads to a incorrect measurement of loss, bandwidth, bending behavior and more or less all other optical parameters ad described in the next chapter.

2. Light propagation in multimode fibers

Light passes through multi mode fibers along many different ways (about 50 for a MM-GOF, but 2,000,000 for a St.-POF). For MM-GOF, these paths are more or less identical, but in thick fibers there a very strong mode dependent processes. First of all, for POF and PCS the cladding has a much higher attenuation than the core. This gives a high mode dependent loss. The results of mode dependent loss for a POF and two different PCS (with a step index and a semi-graded index profile) are shown in Figs. 3 and 4.

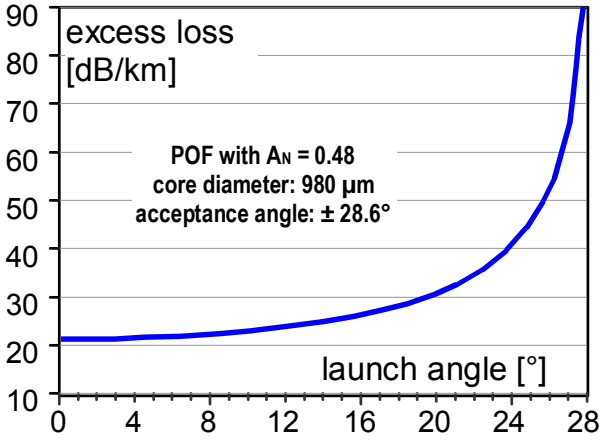

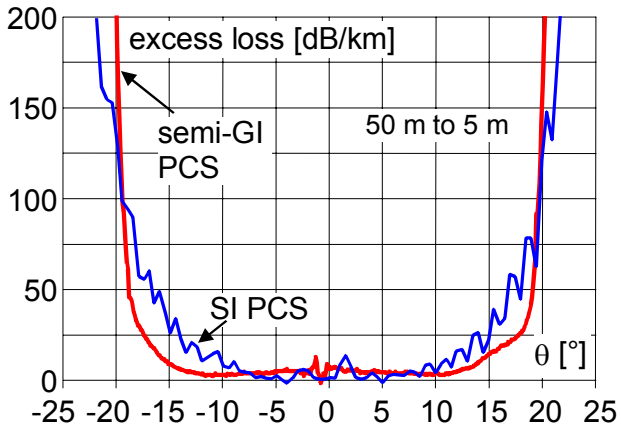

Fig. 3: Influence of the cladding absorption on the loss ([3]), left
Fig. 4: Mode dependent loss in 200 mm PCS ([3]), right

There is a wide range of consequences. The attenuation and much stronger the bandwidth depends on the launching and the detection conditions. Experimental results are given in Fig. 5 (length dependent loss for 4 sources with different emission angles, see [9]) and Fig. 6 (length and launch dependent bandwidth, [10]).

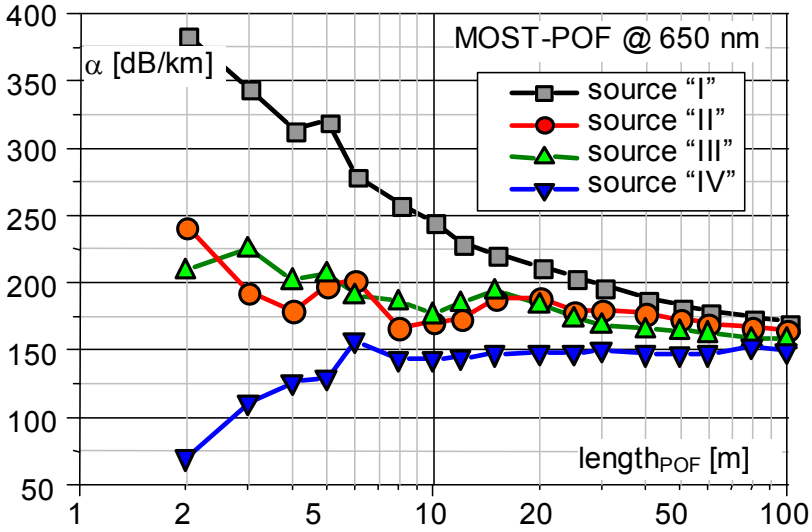

Fig. 5: Length dependent loss for 4 sources with different emission angles

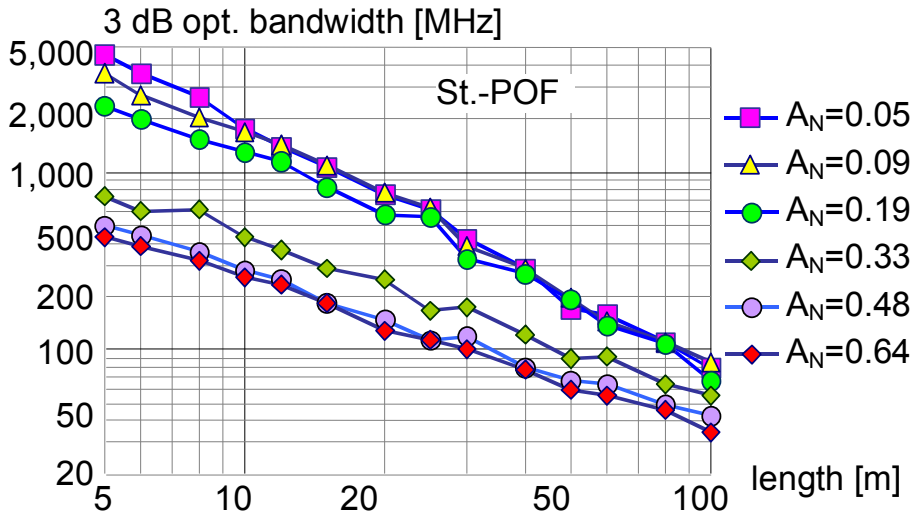

Fig. 6: POF length and launch dependent bandwidth

It can be seen clearly, that it is very important to define and to guarantee the launching and detection conditions for correct and reproducible measurements. The same situation is true for other parameters, like bending loss, connector loss and OTDR measurements.
A second effect besides the mode dependent loss can be seen in both figures as well. The curves are not parallel, but the converge for higher lengths. The reason is the internal mode mixing (mainly on the core cladding interface). The mode mixing is very strong for SI-POF but also important for GI-POF and PCS. In theory, it is sufficient to take a fiber in front of the test object, with is much longer than the mode coupling length to be launch independent. In the reality it is not possible, because of the high loss of the required length. The influence of mode mixing can be seen again in Fig. 7. A collimated light beam is coupled into a St.-POF under an angle of 10°. The far field is measured after 10 m (left) and 100 m (right).

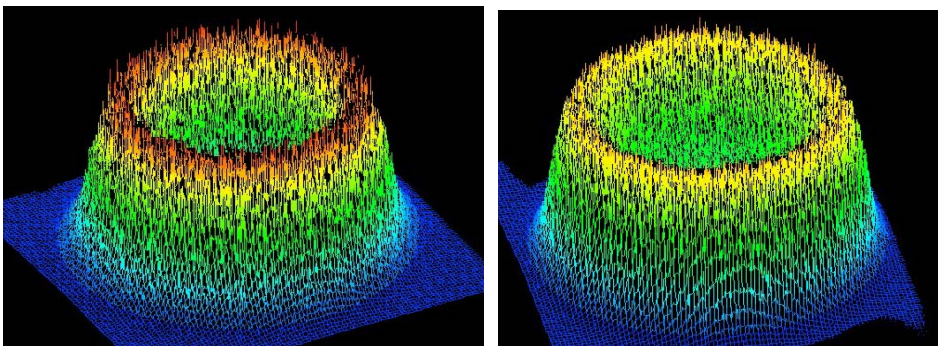

Fig. 7: Far field pf a St.-POF (collimated light, 10 m and 100 m fiber)

3. Examples for available solutions

A lot of special devices have been developed, which can be used for POF and other thick fibers. We will present some of them. A major problem is the bandwidth limitation due to the large area of the required photo diodes. For a Si-pin photo diode with about 1 mm diameter, the possible bandwidth is about 1 GHz. This is not sufficient to measure the bandwidth of GI-POF even for short distances. Figure 8 shows a setup combined from a special red laser source (70 ps pulse width) and a Hamamatsu optical oscilloscope (20 GHz bandwidth) for measurements in the time domain (e.g. [11]).

Fig. 8: Fast laser pulse source and Optical Oscilloscope Hamamatsu OOS-01/VIS

The correct measurement of spectral attenuation can be made, if the launching conditions are close to EMD (Equilibrium Mode Distribution, see [12]). A possible setup is shown in Fig. 9. The core elements are the monochromator with a high NA and the special optics for adapting the launching conditions to the POF. The integration sphere enables the detection of all modes. This principle is now part of the European standardization.

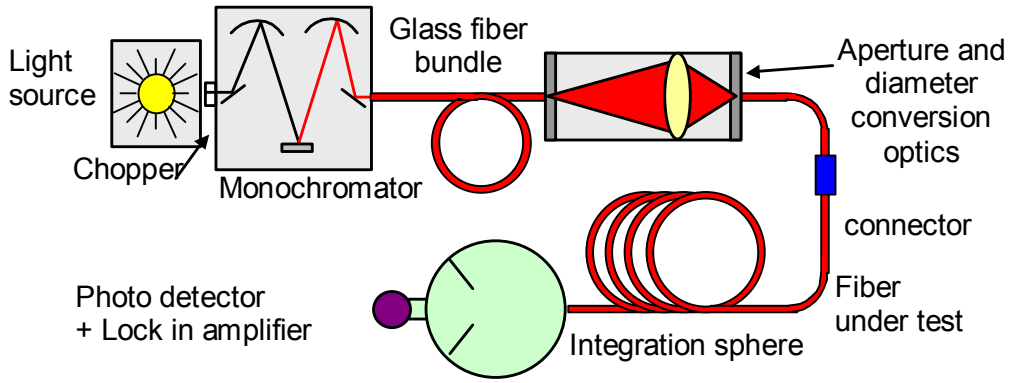

Fig. 9: Setup for spectral loss measurements under EMD conditions

One of the most powerful methods for the investigation of optical fibers is the OTDR (Optical time Domain reflectometer). Two different devices for POF and/or PCS are on the market (Fig. 10, [13], [14]).

Fig. 10: Available POF OTDR

We have shown in [14] that an ODTR can be used for bandwidth measurement with some restrictions (see also [15]). New principles and improved devices are under development. For details for the measurement of index profiles, lifetime and far field see [16], [17] and [18].

4. Open Problems and Summary

The principles of optical measurements on thick optical fibers are the same as for conventional communication glass fibers. The higher diameter and NA and the different operation wavelength, together with the influence of mode dependent effects requires new and adapted solutions. We have developed several setups for measuring the different optical parameters like spectral attenuation and bandwidth.
The biggest task for the future is the definition of parameters in the standardization and the production of devices based on these standards.

References

[1] W. Daum, J. Krauser, P. E. Zamzow, O. Ziemann: „POF - Polymer Optical Fibers for Data Communication", Springer, Berlin 2002
[2] H. Poisel: „POF Measurement Techniques", WorkPOF 2006, Rio de Janeiro, 27.04.2006
[3] W. Daum, J. Krauser, P. E. Zamzow, O. Ziemann: „POF - Polymer Optical Fibers for Data Communication - Handbook for thick Optical Fibers", 2nd edition, Springer, Berlin to be published 2007
[4] J. Warrelmann, R. Schnell: „GF-Bündel für Datenkommunikation", 15. ITG-Fachgruppentreffen 5.4.1, Offenburg, 25./26.03.2003
[5] M. Luber, A. Bachmann, J. Vinogradov, O. Ziemann, H. Poisel: „Comparison of glass fiber bundles and step index POF", POF'2004, Nürnberg, 27.-30.09.2004, pp. 393-398
[6] O. Ziemann, C.-A. Bunge, H. Poisel, K.-F. Klein: „Bandwidth of thick glass and polymer optical fibers", POF'2004, Nürnberg, 27.-30.09.2004, pp. 140-146
[7] O. Ziemann, H. Poisel, A. Bachmann, K.-F. Klein: „Bandwidth measurements on SI- and Semi-GI-PCS", POF'2005, HongKong, 19.-22.09.2005, pp. 251-254
[8] T. Ishigure: „POF Test & Measurement", Tutorial, POF'2003, Seattle, 14.-17.09.2003
[9] M. Luber, O. Ziemann, A. Dröge, J. Hanson, R. Hengl, R. Renk: „Characterisation of EMD Quality for Different Light Sources", POF'2002, Tokyo, 18.-20.09.2002, pp. 161-164
[10] C.-A. Bunge, O. Ziemann, M. Bloos, A. Bachmann: „Theoretical and Experimental Investigation of FF and Bandwidth for Different POF", POF'2002, Tokyo, 18.-20.09.2002, pp. 217-220
[11] A. Bachmann, K.-F. Klein, H. Poisel, O. Ziemann: „Differential mode delay measurements on graded index POF", POF'2001, Amsterdam, 27.-30.09.2001, pp. 57-62
[12] D. Peitscher, G. Schulte, H. Mühlen, O. Ziemann, J. Krauser: „Correct Definition and Measurement of Spectral Attenuation for Step Index Polymer Optical Fibers", POF´2000, Boston, 05.-08.09.2000, pp. 214-220
[13] J. Brendel: „Applications of optical time-domain reflectometry for POF test and measurement", POF'2001, Amsterdam, 27.-30.09.2001, pp. 45-50
[14] O. Ziemann, M. Bloos, K.-H. Friedrich, L. v.-d. Vegt: „Measurement of pulse broadening in SI- and GI-PMMA-POF with an OTDR", POF'2005, HongKong, 19.-22.09.2005, pp. 57-60
[15] R. Gaudino, E. Capello, G. Perrone: „POF bandwidth measurements using OTDR", POF'2004, Nürnberg, 27.-30.09.2004, pp. 153-158
[16] C.-A. Bunge, G. Kramer, H. Poisel: „Measurement of refractive-index profile by lateral illumination", Poster, POF'2004, Nürnberg, 27.-30.09.2004, pp. 513-520
[17] B. Günther, W. Czepluch, K. Mäder, S. Zedler: „Multiplexer for Attenuation Measurements During POF Durability Testing", POF´2000, Boston, 05.-08.09.2000, pp. 209-213
[18] K.-F. Klein, A. Bachmann, M. Bloos, O. Ziemann: „Comparison of Different FF-Measurement Setups", POF'2002, Tokyo, 18.-20.09.2002, pp. 259-262

Characterization of Hole-Assisted Fibers as Single Polarization Fibers and Polarization Maintaining Fibers

Xin Chen, Joohyun Koh, Ming-Jun Li, and Daniel A. Nolan
Science and Technology Division, Corning Incorporated, Corning, NY14831
Chenx2@corning.com

Abstract

Hole-assisted single polarization fibers (SPFs) and polarization maintaining fibers (PMFs) have attracted significantly interest recently due to its wide range of applications. Hole-assisted SPF and PMF also have special properties that require understanding for proper fiber deployment. In this paper, we review the novel properties of a hole-assisted fiber that we recently implemented as either a SPF or PMF. We measured the fiber birefringence and the fundamental mode cutoff wavelengths, which directly determine the performance of such fiber as a SPF. We also comprehensively explored other unique characteristics of these fibers such as the length dependence of the fundamental mode cutoff, the effects of bending on the fiber cutoff wavelengths, and the performance of such fiber over a wide range of temperatures. To address the issue of selecting target fiber in a non-destructive and cost effective manner, we developed a novel method to distributedly measure the cutoff wavelength drifting along the entire length of the fiber.

1. Introduction

Recently there has been increasing interest in using single-polarization fibers in applications such as fiber lasers, fiber-optic gyroscopes, and fiber sensors to deal with unwanted and detrimental polarization effects. As a result, different approaches in achieving single polarization operation in optical fibers have been explored [1-4]. Although a solid type single polarization fiber was studied in details in early times [1], more recent studies focused on single polarization fiber with air holes either in hole-assisted fibers or microstructured fibers [2-6].

In the past few years, we have proposed, implemented and commercialized a hole-assisted single polarization fiber [5-6]. In studying this new type of fiber, we have identified many novel properties that require special attention in order to use the fiber properly. In this paper, we focus on the characterization of the single polarization fibers based on the dual air hole design. We review the novel properties of a hole-assisted fiber that we recently implemented as either a SPF or PMF including some very recent results. In Section 2, we study the fiber birefringence and the fundamental mode cutoff wavelengths, which directly determine the performance of such fiber as a SPF. We also comprehensively explored other unique characteristics of these fibers such as the length dependence of the fundamental mode cutoff, the effects of bending on the fiber cutoff wavelengths, and the performance of such fiber over a wide range of temperatures. To simplify the task of selecting target fiber, in Section 4, we describe a novel method to distributedly measure the cutoff wavelength drifting along the entire length of fiber in a non-destructive and cost effective manner.

2. Hole-assisted Single Polarization and Polarization Maintaining Fibers

Figure 1 shows a schematic of the proposed dual air hole fiber structure. The fiber consists of an elliptical core with two air holes placed next to the core and along the minor axis of the ellipse. The two air holes play critical roles. They induce form birefringence through a high index

contrast between the core and the air holes. The air holes also create fundamental mode cutoffs. The fundamental cutoff wavelengths between the two polarization modes are different because of the high birefringence; in between the fiber is a SPF. In order to have sufficiently high birefringence and single polarization bandwidth, which is defined by the difference of the fundamental mode cutoff wavelengths between the two polarization modes, the core delta should be sufficiently high and appropriate dimension of the core especially the minor core dimension should be chosen so that the single polarization operation window is located at the desired wavelength range. At the wavelength range below the first fundamental cutoff and higher than the higher order cutoffs, the fiber is highly birefringent, behaving like a PMF. Therefore, depending on the wavelength that the fiber is operated, the dual air hole fiber can serve either as a PMF or a SPF.

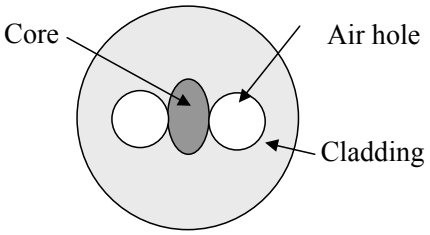

Figure 1. Cross section of a dual air holes fiber as SPF and PMF.

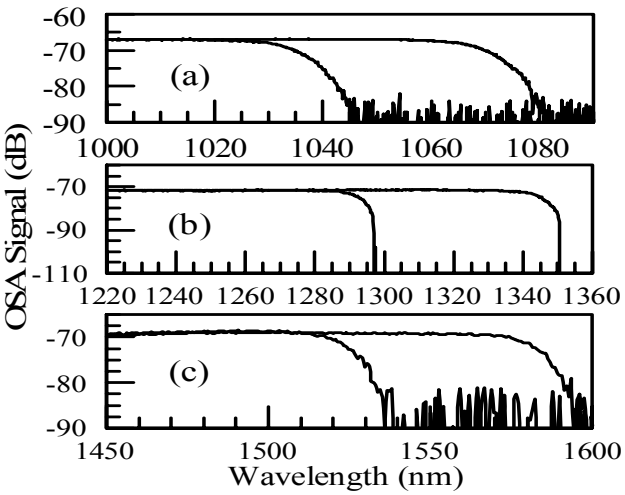

Figure 2. Measured cutoff wavelengths of the two polarization modes.

3. Characterization of Hole-Assisted Fibers

Over the past few years, we have fabricated many fibers according to the design in Fig. 1 by outside vapor deposition and with different parameters. With these fibers, we have experimentally studied many aspects of the fiber characteristics.

First we study several transmission characteristics of the fibers. An experimental setup that is capable of measuring the transmission signals over a wide range of wavelengths and that uses a white light source and an optical spectrum analyzer was constructed. We used a polarizer to obtain the transmission spectrum of each polarization mode by aligning the polarizer with the birefringent axis of the fiber. In Fig. 2 we show the transmitted signal for three fibers which have single polarization operations at 1060nm (Fig. 2a), 1310nm (Fig. 2b), and 1550nm (Fig. 2c). The bandwidths of the fibers in Fig. 2 judged at the 3dB down from the plateau region are 35nm, 53nm, and 59nm respectively for 1060nm, 1310nm and 1550nm wavelength windows. The ability to control the center of a single-polarization window offers flexibility for applications operating at different wavelengths.

In early experiments, to explore experimentally the relation between the core Δ and the bandwidth of single-polarization operation, we used two core Δ values in the fiber fabrication. Subsequent measurements were conducted to characterize several properties of the fibers. Results for five fibers are summarized in Table 1. We compare the bandwidth of each fiber to the core Δ

and group beat length. The beat length is measured by a wavelength scanning method in the PM regime by using a broadband light source, placing the fiber between two cross polarizers and observing the modulation pattern in the spectrum. We have found that, in general, a higher core Δ is linked to higher fiber birefringence and a higher single polarization bandwidth. This observation agrees with the results of the theoretical modeling we conducted.

Fiber	Delta (%)	Cutoff1 (nm)	Cutoff2 (nm)	Bandwidth (nm)	Beatlength (mm)	Loss (dB/m)
1	1.1	1147.8	1177.4	29.6	3.0	0.03
2	1.1	1066.6	1098	31.4	2.8	0.03
3	1.1	911.2	935.5	24.3	*	0.08
4	2	972.0	1014.0	42.0	1.1	1.76
5	2	1477.7	1533.1	55.4	*	0.1

Table 1. Measurement results of the single polarization fibers. Beatlength is normalized to value at 980nm.

We then studied the dependence of the cutoff wavelength on the fiber length. Figure 3 plots the measured cutoff wavelengths of the two polarization modes as a function of fiber length for fiber 2 of Table 1. When the fiber length was cut from 5 to 1 m the cutoff wavelengths of both polarization modes were shifted higher by 14 nm. This suggests that one can fine tune the center wavelength for the single-polarization operating window in a given wavelength range by adjusting the fiber length, which offers additional flexibility for dedicated applications. We also looked into the loss properties of the fibers. One can measures loss by obtaining the transmission powers at a longer length (3 m), followed by a cutback to a shorter length (1 m). Typical losses of the preferred polarization listed in Table 1 are less than 0.1dB/m. More accurate attenuation measurement by OTDR of certain fibers has shown attenuation of less than 0.02dB/m. As single-polarization fiber is used mostly in short lengths, the current loss level is sufficient for most applications, although lower loss is desired.

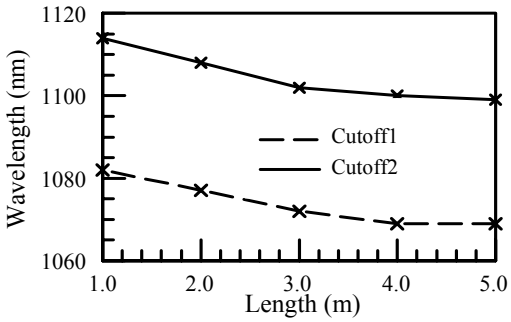

Figure 3. Measured fiber cutoff wavelengths for different fiber lengths.

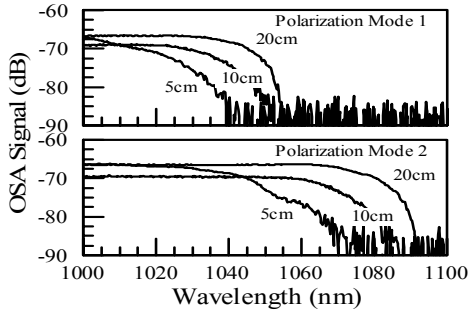

Figure 4. Fundamental cutoff wavelengths shift at different bending diameter.

We also studied the effect of the bending by measuring the transmission spectrum of each polarization mode at different bending diameters. Although the bending even at several millimeters in diameter has very minor effect to the fiber attenuation in wavelength region below the fundamental mode cutoff, it has larger effect to the cutoffs. The results are shown in Fig. 4. As the bending diameter decreases, the spectrum curve shifts toward lower wavelengths, resulting in the down-shift of the fundamental mode cutoffs. The effects apply to both polarization modes. The results in Fig.4 vary with the orientation of the bending, which is not controllable. Larger distortion of the transmission spectrum has been observed for smaller bending diameter. Knowing the bending property can be very useful in selecting fibers for proper deployment.

Another important property of single-polarization fibers is the extinction ratio for single-polarization operation, which is defined by the relative strength in decibels of the power transmitted through the fiber between the two polarization modes. As our concern is with the two linear polarization modes, the standard measurement of polarization-dependent loss10 (PDL) can be interpreted as the extinction ratio measurement of a single-polarization fiber. We measured fiber 5 by using a PDL meter (Profile PAT-9000B) with a tunable laser source. In Fig. 5 we show the measured PDL for three lengths of fiber 5 across the single-polarization wavelength window. No significant difference among the three lengths was found. Even when the fiber length was as short as 27.8 cm, the average PDL, i.e., the extinction ratio, was 60 dB. Note that the measurements may be constrained by the dynamic range. The actual extinction ratio could be higher. The PDL results suggest that compact fiber-polarizer applications with short pieces of fiber are feasible. The ability to reach a high extinction ratio in a short length of fiber is a significant advantage over other single-polarization fibers, which were reported to have lower extinction ratios with linear length scaling.

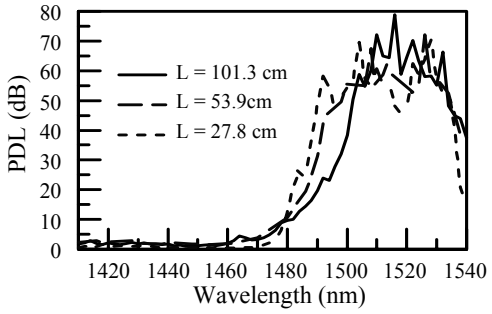

Figure 5. Measured PDL for different fiber lengths.

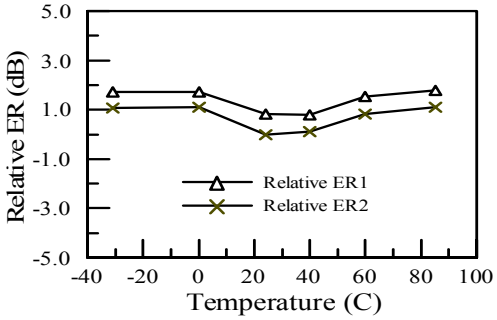

Figure 6. Relative ER as a function of temperature.

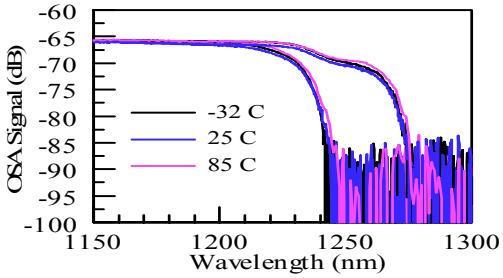

Figure 7. Transmission spectrum for both polarization modes measured at three different temperatures.

Recently, we studied the temperature related properties of dual air hole fibers as either a PMF or SPF. As a PM fiber, the main concern is if the extinction ratio can be maintained throughout the range of temperatures that the fiber can be operated at, such as from -35°C to 85°C. For 500m long dual air hole fiber, we measure the PM extinction ratio (ER) to be around 25 dB at room temperature. We then prepared 100m portion of it in loose coil condition and measure the extinction ratio as a function of the temperature. Two slightly different ERs are obtained because there are two polarizer alignment conditions as related to two birefringent axes of the fiber. The change of the ERs relative to one ER at room temperature is shown in Fig. 6. It is found the ER is maintained rather stable for the wide range temperature. We also measure the fiber over the range of temperature to see how the cutoff shifts with the temperature with the results shown in Fig. 7. Over 117 degree of temperature change, the cutoff wavelength shifts in general upward and by less than 3nm. This suggests that the fiber optical properties are largely independent of the temperature, and the birefringence is primarily contributed by form birefringence. Our further

numerical model, which can take into account the thermal and stress effect is in reasonably good agreement with the experimental observation.

4. Distributed Cutoff Measurement

The location of the fundamental mode cutoff wavelength of single polarization fibers is very sensitive to the geometry of the fiber as laid out in Figure 1. A minor change in the fiber geometry can alter the fundamental mode cutoff significantly. In practice, the air pressures within air holes applied during the fiber drawing process has most of the effect to alter the core dimension. The shift can move somehow randomly and gradually upward or download in wavelength over the entire fiber span. However, for a given portion of the fiber, the shift typically stays in one direction.

Because of the fluctuation of the cutoff wavelengths, the selection of the target fiber can be a difficult and cumbersome task. Many 2 meter length of fiber samples are cut from different regions of the fiber to determine the cutoff wavelength of the fiber at a specific location, and further prediction is made by linearly interpolate the measured results. This method is labor intensive and the frequent cutback incurs loss of useful fibers.

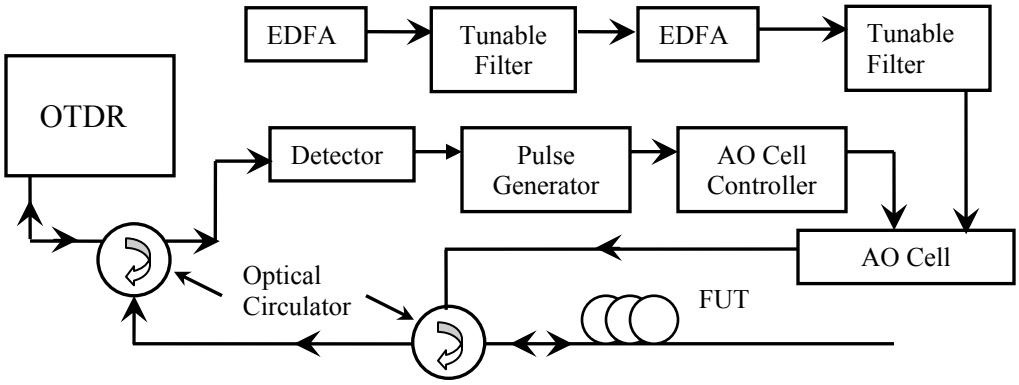

Figure 8. Schematic of the tunable OTDR used for measuring the cutoff wavelengths distributed.

In order to simplify the fiber selection process, we have developed a novel distributed cutoff measurement method based on the use of a wavelength tunable optical time domain reflectometer (OTDR), which measures the cutoff shift of the fiber along the fiber. Figure 8 illustrate the scheme of the method. A commercial OTDR working at a fixed wavelength such as 1550nm is first converted into a wavelength tunable OTDR over the wavelength range of between 1530nm and 1560nm. The tunable light source is obtained through a two stage amplification of EDFA working at the C-band with wavelength selection done by a fiber Bragg-grating based tunable filter. The pulsed light output from the commercial OTDR is detected by a detector and used as a triggering source for a pulse generator. The pulse generator further chops the CW light from the EDFAs into pulsed light at a specified wavelength through the use of an acoustic-optic modulator (AO Cell). Two optical circulators are used to loop the light into the fiber under test (FUT) and the back-scattered light back into the OTDR.

In the actual test, we launched the light from the fiber end with higher fundamental mode cutoff wavelength, which can be found by measuring two short fiber samples taken from both end of the fibers. In the scheme of Fig. 8 where no polarizer is used, the light will propagate till no light can propagate further, or when the cutoff or complete extinction of the light is reached. The reached cutoff is for the second polarization mode, which has a longer cutoff wavelength than the other polarization mode. Since the cutoff wavelength shift toward a lower wavelength along the fiber,

depending on the wavelength of the light launched into the fiber, the length of the fiber that light can propagate varies. The information is captured by a series of OTDR traces taken at different wavelengths. We illustrate the results from one fiber samples in Figure 9. It is shown that when the wavelength increases, the OTDR traces fall at a shorter distance from the light launching end. By choosing a proper threshold level, we can obtain the wavelength of the second cutoff as a function of the position as in Fig. 9(b). Since the fiber has a single polarization bandwidth of 55nm, we can pick the right portion of the fiber based on a specified requirement. For example, for fiber that operates as SPF between 1540 nm and 1560nm, the first 60m of the fiber meets the requirement. In this example, we illustrate the measurement of second cutoff wavelength. Should we insert a polarizer into the light launching end and proper align it, we can gain sole access to the first cutoff. The measurement scheme above can then be used to each polarization mode separately.

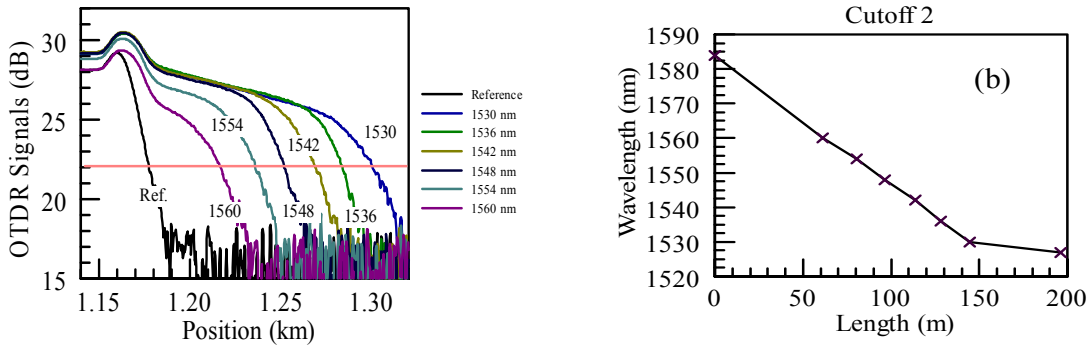

Figure 9. (a) OTDR traces at different wavelengths. The fiber under test starts at around 1.16km. (b) The wavelength of the second cutoff as a function of the fiber position.

5. Conclusion

We comprehensively studied various properties of the dual air hole fibers both as a PMF and as a SPF. We also developed a novel method to measure the fiber fundamental mode cutoff distributed along the fiber in a non-destructive and cost effective manner. The understanding gained from the measurement efforts not only helps to facilitate the deployment the fibers in different environment but also helps us to verify theoretical model which strengthens our further research capability in this area.

References

1. M. J. Messerly, J. R. Onstott, and R. C. Mikkelson, “A broad-band single polarization optical fiber”, J. Lightwave Technol. 9, 817 (1991).
2. H. Kubota, S. Kawanishi, S. Koyanagi, M. Tanaka, and S. Yamaguchi, “Absolutely single polarization photonic crystal fiber”, IEEE Photonics Technol. Lett. 16, 182 (2004)
3. J. R. Folkenberg, M. D. Nielsen, and C. Jakobsen, “Broadband single-polarization photonic crystal fiber”, Optics Lett. 30, (2005)
4. T. Schreiber, O. Schmidt, F. Roser, J. Röthhardt, J. Limpert, “High power operation of a low-nonlinearity single polarization photonic crystal fiber”, Photonics West 2006, WA3.
5. D. A. Nolan, G. E. Berkey, M.-J. Li, X. Chen, W. A. Wood, and L. A. Zenteno, “Single-polarization fiber with a high extinction ratio”, Optics Lett. 29, 1855 (2004)
6. D. A. Nolan, M.-J. Li, X. Chen, and J. Koh, “Single polarization fibers and applications”, in Optical Fiber Communication Conference and Exposition and The National Fiber Optic Engineers Conference on CD-ROM (Optical Society of America, Washington DC, 2006) OWA1

Micro-Tomographic Reconstruction for Arbitrary Refractive Index Profiling of Optical Fibers

N.M. Dragomir[1], X. M. Goh[1], G. Baxter[2] and A. Roberts[1]

[1]School of Physics, The University of Melbourne, Melbourne, Vic, 3010, Australia
[2]School of Electrical Engineering, Victoria University of Technology, Melbourne, 8001, Victoria, Australia

Tel: +61 03 8344 5985, Fax: +61 03 9347 4783

n.dragomir@physics.unimelb.edu.au

Abstract: We demonstrate a micro tomographic method to measure arbitrary refractive index profiles of optical fibers and grating structures. The method involves the use of a traditional bright field microscope in conjunction with Quantitative Phase Microscopy. The fiber is rotated through 180 degrees and the phase data is collected, then the filtered back projection technique is used in the computed two-dimensional profile distribution. The complete micro tomographic method makes it possible to reconstruct the optical fiber index distribution without *a priori* knowledge of the optical fiber.

1. Introduction

Optical fibers, especially those with complex internal structure require a non-destructive technique for a full determination of the three-dimensional refractive index (RI) distribution. In addition, knowledge of the refractive index distribution in many photonic devices including long period gratings and fiber Bragg gratings is fundamental to modeling their behavior and optimizing their performance.

Roberts *et al* reported the use of a non-destructive method to measure the two-dimensional (2D) refractive index distribution of circularly symmetric optical fibers [1] using Quantitative Phase Microscopy (QPM) [2]. A single transverse phase image of an optical fiber is measured, from which the refractive index profile is calculated by using the Abel inversion method [3]. In addition, QPM has been used with polarized light to determine the retardation introduced by a specimen [4], which permits the simultaneous mapping of the refractive index and birefringence in an optical fiber. Furthermore, it has also been demonstrated that a comprehensive measurement of the distribution of residual axial stress within an axially symmetric fiber [5] is possible when polarized light is used. Recently, differential longitudinal evolution in the fiber refractive index profile in the vicinity of a fusion splice has been quantified using QPM [6]. The method has also been proved for the tomographic reconstruction of asymmetric fibers [7], whereby the three-dimensional (3D) refractive index distribution of a double core fiber has been reconstructed via a Radon transform from a series of transverse phase images obtained for different angular orientations.

We illustrate here new experimental results demonstrating the reconstruction of the three-dimensional refractive index distribution of a section of an ion implanted long period grating structure incorporated in a graded-index multimode fiber. This method is very timely as a wide selection of new optical fibers with complex structures and various enter the telecommunication and sensors market [8,9].

2. Quantitative Phase Tomography

A significant number of previously published articles have discussed the principle of QPM [1, 7]. Here, it is sufficient to note that in the context of non-destructive fiber characterization it is based on the measurement of the phase shift introduced into an optical wavefield when it is transmitted transversely through an optical fiber. Thus its phase is uniquely determined by using an algorithm based on the transport of intensity equation for a set of intensity images at known defocus.

Since a transverse phase measurement of the fiber represents a projection through the refractive index distribution within the fiber, by obtaining a series of phase measurements as the fiber is rotated around its axis through 180 degrees, standard tomographic techniques can be used to reconstruct the three-dimensional refractive index distribution.

Figure 1 shows the coordinate system and the micro tomographic geometry based on a conventional transmission microscope where the fiber sample is rotated within the field of view of a lens. The *z*-axis of in the Cartesian coordinate system *(x ,y ,z)* defines the axis of rotation of the fiber sample; the rotated coordinate system is defined by (r, q, z) and is related to the reference system through the angle of

rotation θ, measured from the positive *x*-axis. A miniature stepper motor turns the fiber sample which is placed between a glass slide and coverslip.

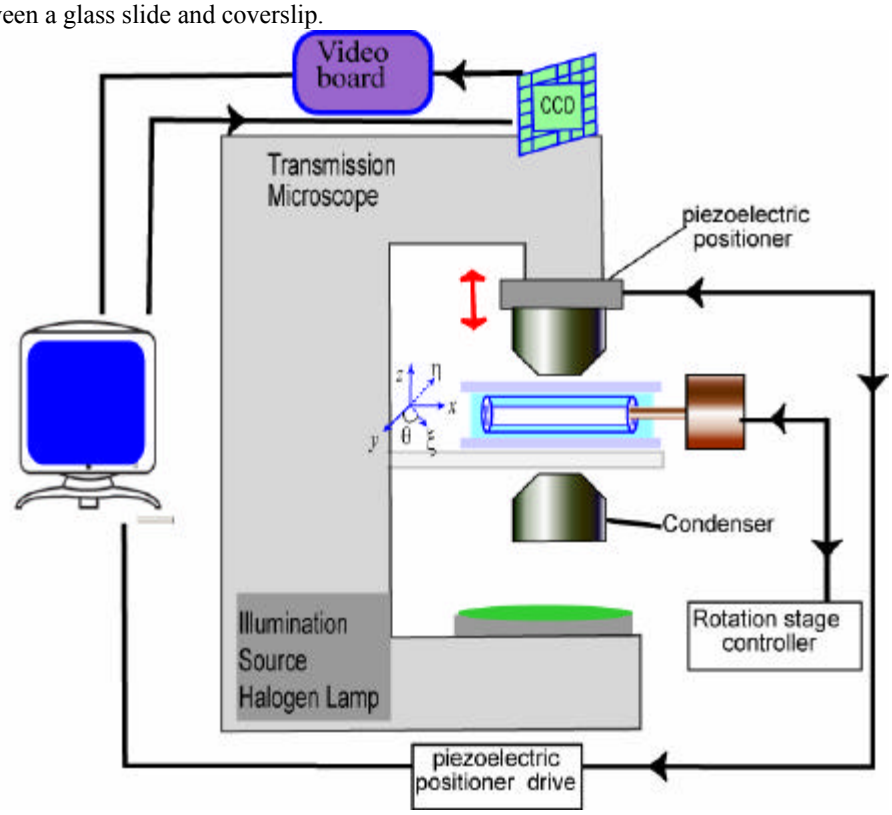

Fig. 1. Schematic of the micro tomographic imaging setup. The fiber (8 cm length) without its plastic jacket is mounted side-on in the tomographic mount using a standard fiber chuck. The fiber chuck is mounted on a micro stepper motor that permits a full 360° rotation. The fiber is placed in a pool of index matching fluid (Cargille Laboratories) formed between two other identical fibers located on either side of the specimen, acting as spacers to minimize the introduction of spurious tilts into the phase images.

Let $D\,n(x, y, z)$ denote the refractive index distribution of the optical fiber, the measured phase of the optical fiber, $j\ (r, q, z)$ for a distinct position, q , is proportional to the integration of the refractive index distribution through the fiber specimen and can be expressed as a Radon transform [10]:

$$j(r,q,z) = k\int_{-\infty}^{\infty} \Delta n(r\cos q - s\sin q,\ r\sin q + s\cos q, z)ds \qquad (1)$$

where the wavenumber $k = 2p / l$ and l is the wavelength.

A number of mathematical algorithms to reconstruct a quantitative map of the RI distribution from a series of projections, $j\ (r, q, z)$, as q is varied through 180º are available. Here filtered backprojection was used [10].

3. Experiments and Results

The fibre sample used in this work was a section of a graded index multimode fibre (Corning 62.5/125 µm) containing a long period grating (LPG) (500 µm period). The LPG was fabricated by an ion-implantation process [11] carried out using a focused ion beam of singly charged light ions (H^+ ions at a concentration of 10^{16} ions/cm^2) accelerated through a 2.4 MeV potential). Upon entering the fibre the protons travel to a depth which is determined by their energy, mass and the nature of materials in the fibre cladding and core. This produces a compaction leading to a significant increase of the RI in both the cladding and the core.

Images of the optical fiber were obtained using a conventional bright field microscope (Olympus BX60) equipped with a commercial implementation of QPM [12]. Intensity images were recorded with a

cooled camera (Roper Scientific CoolSNAP), a 12-bit camera with a 1392 × 1040 pixel CCD image sensor (Sony ICX285AL) and a 6.45 µm pixel size. The subsequent intensity images of the optical fiber samples under investigation were magnified by a lens system consisting of objectives lenses (UplanApo 20×/0.70 NA for the LPG) and a 0.5× relay lens to couple the microscope intermediate image into the camera CCD chip, Fig.1. The numerical aperture (NA) of the condenser was chosen to be less than the NA of the objective lens being used and it was set to 0.2 to improve spatial coherence. The illumination, provided by a 100W halogen lamp was filtered using a band pass filter centered on 521±10 nm. Control of the defocus positions at either side of the plane of interest was achieved using a piezo-driven nanopositioning system (PIFOC, Physik Instrumente, Germany).

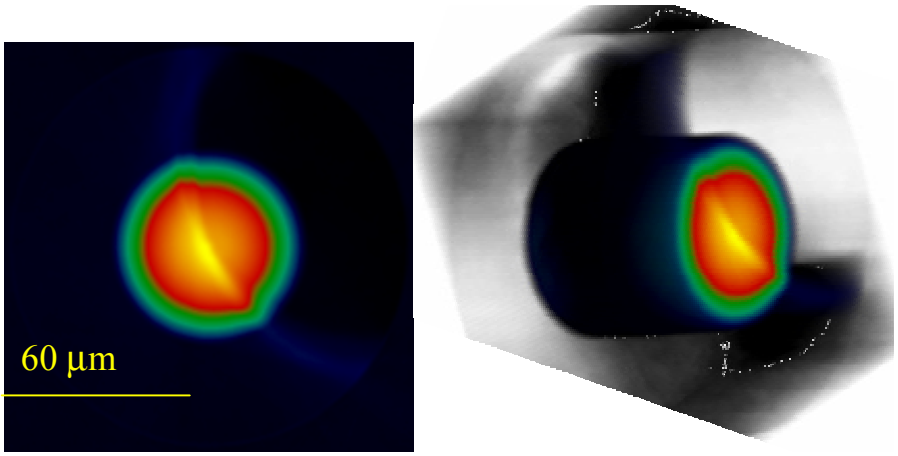

Fig. 2. Reconstructed refractive index distribution obtained from transverse phase images collected over 180º in 2º steps. (a) transverse 2D slice through the ion implanted region of a graded-index multi-mode fiber; (b) rendered three-dimensional tomography plot for a 60 µm length of the fiber.

A total of 90 transverse phase images of the fiber were acquired at an angular interval of 2º using a defocus of ±3 µm. The phase images were first aligned using an algorithm based on centering on the maximum phase. The RI of a series of slices through the fiber was obtained using filtered backprojection. This was achieved by applying the IDL (V6.1) RADON function to 'ramp' filtered data. These slices through the fiber were then fused together to produce a 3D RI distribution of the sample. Figure 2 (a) illustrates a transverse section through the reconstructed RI corresponding to the irradiated region of the multi-mode fiber. In Fig. 2(a) a parabolic index variation of the fiber itself is apparent as is an index enhanced arc through the fiber corresponding to the end-of-range of the ions. As predicted prior to implantation, the end-of-range passes close to the centre of the core of the fiber.

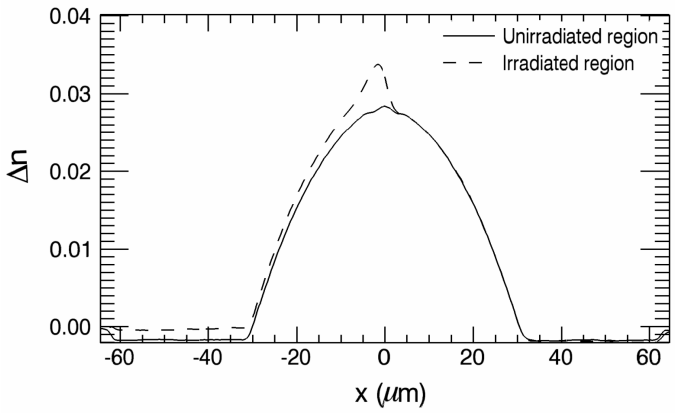

Fig. 3. Comparison of reconstructed RI through the central region of unirradited (solid line) and irradiated (dashed line) for LPG data. An increase of the RI with ~0.005 can be observed through the irradiated section.

A 3D volume rendering of the RI distribution of the LPG is illustrated in Fig. 2 (b), where changes in the RI distribution along the fiber length can be seen. A line profile through the centre of the fiber of the unirradiated region (solid line) and through the irradiated region (dashed line), is shown in Fig. 3. This shows that the index increase at the end-of-range is of the order of 0.005, while a more subtle increase in index of approximately 0.002 is apparent between the irradiated surface and the end-of-range, while, as expected there is no change in index below the end-of-range.

3. Conclusions

This paper illustrates a micro tomographic method to measure the refractive index distribution using phase information of an optical fiber section with arbitrary refractive index distribution. It can be seen that QPM is a powerful tool for the characterization of optical fibers and photonic devices. In the case of non-symmetric distribution of the RI of optical fiber micro tomographic reconstruction of the 3D RI distribution of optical fibers was obtained. Ongoing research is aimed at a more comprehensive assessment of the accuracy and sensitivity of the technique as well as the development of an improved rotation mount.

Acknowledgement
The Financial support from the Australian Research Council and the provision of the samples by OFTC are acknowledged.

References

[1] A. Roberts, E. Ampem-Lassen, A. Barty, K. A. Nugent, G. W. Baxter, N. M. Dragomir, and S. T. Huntington, "Refractive-index profiling of optical fibers with axial symmetry by use of quantitative phase microscopy," *Opt. Lett.*, 27: 2061-2063, 2002.
[2] A. Barty, K. A. Nugent, D. Paganin, and A. Roberts, "Quantitative optical phase microscopy," *Opt. Lett.*, 23: 817-819, 1998.
[3] M. Kalal and K. A. Nugent, "Abel inversion using fast Fourier transforms," *Appl. Opt.*, 27: 1956-1959, 1988.
[4] A. Roberts, K. Thorn, M. L. Michna, N. M. Dragomir, P. M. Farrell, and G. W. Baxter, "Determination of bending-induced strain in optical fibers by use of quantitative phase imaging," *Opt. Lett.*,27: 86-88, 2002.
[5] N. M. Dragomir, G. W. Baxter, and A. Roberts, " Phase sensitive imaging techniques applied to optical fibre characterisation," 7th Optical Fibre Measurements Conference, Teddington, UK, 107-111, 2005.
[6] N. M. Dragomir, E. Ampen-Lassen, G. W. Baxter, P. Pace, S. T. Huntington, A. J. Stevenson, P. Farrell and A. Roberts " Analysis of Changes in Optical Fibres during Arc-Fusion Splicing by Use of Quantitative Phase Imaging" *Microsc. Res. Techn.* (accepted), 2006.
[7] A. Barty, K. A. Nugent, A. Roberts, and D. Paganin, "Quantitative phase tomography," *Opt. Comm.*, 175: 329-336, 2000.
[8] X. Feng, M. T. Monro, P. Petropoulos, V. Finazzi, D.J. Richardson, "Extruded single-mode high-index-core one-dimensional microstructured optical fiber with high index-contrast for highly nonlinear optical devices " *Appl. Phys. Lett*. 87: 08110, 2005.
[9] A. Wang, A. George, J. Liu, J. Knight, "Highly birefringent lamellar core fiber", *Opt. Exp*. 13(16):5988-5993, 2005.
[10] F. Natterer, *The Mathematics of Computerized Tomography*. Stuttgart: John Wiley and B G Teubner, 1986.
[11] M. L. von Bibra, A. Roberts, and J. Canning, "Fabrication of long-period fiber gratings by use of focused ion-beam irradiation," *Opt. Lett.*, 26: 765-767, 2001.
[12] QPm V2.1 Iatia Ltd. Australia, *http://www.iatia.com.au*.

Fictive temperature distribution in highly Ge-doped multimode optical fibers

M. Lancry[1], I. Flammer[2], D. Simons[3], B. Poumellec[1], C. Depecker[4], P. Nouchi[2] and M. Douay[5]

[1]ICMMO/LPCES, UMR CNRS-UPS 8182, Université Paris Sud (XI), 91405 Orsay, France
[2]Draka Comteq France, Site Alcatel de Marcoussis, Route de Nozay, 91460 Marcoussis, France
[3]Draka Comteq Fiber BV, Zwaanstraat 1, 5651 CA Eindhoven, Netherlands
[4]LSPES, UMR 8008, Université des Sciences et Technologies de Lille, 59655 Villeneuve d'Ascq, France
[5] PhLAM, UMR 8523, Université des Sciences et Technologies de Lille, 59655 Villeneuve d'Ascq, France

Abstract:
In this study, FTIR FPA (Focal Plan Array) detector was used to image the 'bond-stretching' vibration mode observed near σ=1120 cm^{-1} of highly Ge-doped graded index multimode optical fibers (GI-MMF). Next, as calibration curves between σ and the fictive temperature T_f are not available in the literature for highly Ge-doped glasses (above 7 w %), we have determined our own calibration curves from 1 to 30 w% in Ge. Then, we have applied these corrections to our σ measurements in GI-MMF in order to estimate, for the first time to our knowledge, the fictive temperature distribution within MMF cross section.

1. Introduction

It is well known that the fictive temperature characterizes the glass structural state and is linked to glass properties such as density [1], mechanical fatigue resistance [1] or Rayleigh scattering loss [2]. In general, a glass sample can exhibit a fictive temperature T_f of its surface different from that of its bulk. This situation can occur, for example, when a glass is rapidly cooled from the liquid as it is done in fiber production. In this case, a higher T_f is expected on the fiber surface than in the bulk due to a faster cooling rate at the surface. One objective of the present work is to examine this occurrence in multimode optical fibers. In this view, the 'bond-stretching' vibration observed near 1120 cm^{-1} in the IR reflection spectra was monitored to determine the fictive temperature distribution in MMF cross sections.

However, the radial variation of T_f has been studied before with some divergent results [2-5]. One problem is that the reflection peak position varies not only with T_f but also with the material composition [2 and 5]. This is a problem as optical fiber has different composition in the core and in the cladding surrounding the core. Therefore, calibration curves between T_f and the IR band peak position must be available for each material composition. Unfortunately, the fictive temperature of highly Ge-doped glasses (> 6.3 w %) cannot be reliably estimated due to the lack of calibration curves between T_f and σ_{1120}.

In the following, after a brief description of the experimental procedure, we determine here calibration curves for germanosilicate glasses from 1w% to 30w% using only one sample. Next, using these curves, we are able to determine the T_f of Ge-doped optical fibers whatever the Ge content may be.

2. Experimental procedure

It has been shown that the fundamental asymmetric vibration band located near 1120 cm^{-1} is the most sensitive to structural change and thus to the T_f changes. Thus, this band was monitored in the IR reflection spectra to determine the fictive temperature for GI-MMF. Furthermore, this method is well adapted to realize T_f cross-section profile in optical fibers [2-5] whereas IR transmission measurements are less precise (lower slope of the calibration curve) and imply to prepare thin sample (around 100 µm). FTIR reflectance spectra were thus recorded by means of a FTIR Spotlight 300 Perkin Elmer equipped with the new technology FPA (Focal Plane Array) MCT (Mercury Cadmium Telluride) detector. The instrument provides 6:1 imaging on MCT detector, resulting in nominal resolution of 6.25 µm. The

spectra have been recorded in the 800 cm^{-1} to 2000 cm^{-1} spectral range. The reproducibility of our measurements of the IR peak wavenumber is around 0.1 cm^{-1}.

3. Determination of calibration curves between the IR peak wavenumber σ and the fictive temperature T_f in GI-MMF stretched preform rods

3.1. Samples preparation and treatments

The main objective of this study is to determine calibration lines for the Si-O-Si asymmetric stretching band position versus fictive temperature for highly Ge-doped glasses. This study has never been reported to our knowledge because it is too difficult to cut a highly Ge-doped preform rod into slices without breaking it due to the high stress level. We have thus circumvented this tricky point by reducing the preform diameter by a factor of 100. The preform was indeed stretched into smaller rods called capillaries in the following. Next, we have cut these capillaries to the desired length to realize the calibration standards. In order to achieve different uniform fictive temperatures in the calibration standards, the samples were held at various temperatures for long time periods, long enough to ensure full structural relaxation (up to a few 100s hours). The typical temperatures selected were between 1223 K and 1523 K. After heating treatment, these samples were rapidly quenched in water to fix the uniform fictive temperature at the heating temperature. Then, the capillaries were polished and the IR reflection spectra were measured as a function of the radial position (and thus the Ge content).

3.2. 2D distribution of the IR peak wavenumber σ in GI-MMF stretched preform heated at various temperature

Figure 1 displays the 2D distribution of the peak wavenumber σ related to the Si-O-Si asymmetric stretching band recorded in reflection. The circle (black solid line) corresponds to the core part within the capillary. In this figure, the stronger the blue color (or the darker in gray levels), the higher the peak wavenumber σ (in cm^{-1}). These results indicate that the concentric distribution of σ is quite uniform for a fixed radial position r whereas it changes strongly according to the radial position r.

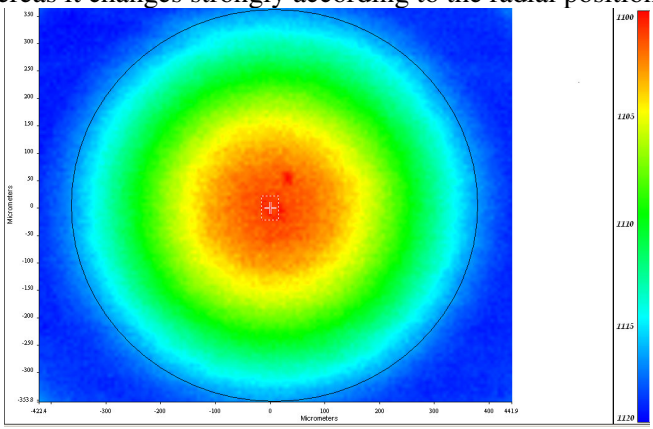

Fig. 1: 2D distribution of the reflectance peak wavenumber σ in the core of the MMF capillary cross section

Figure 2 shows the IR peak wavenumber profiles σ = f (r) of a silica asymmetric stretching band around ~1120 cm^{-1} as a function of the radial distance. In this Figure, one can clearly see that the IR wavenumber follows a parabolic profile in the core region. Furthermore, the higher the heating temperature (i.e. T_f); the lower the IR wavenumber along the whole profile. Now, as the germanium concentration profile follows a well-known parabolic law (from 0 to 30 w % in Ge), we are able to determine calibrations curves for several Ge concentrations.

3.3. Determination of calibration curves: influence of the Ge concentration

In this part, we will extract the data obtained above in order to determine calibration curves between the fictive temperature and the IR reflection peak wavenumber for Ge concentrations up to 30 w %. Figure 3 displays several of these calibration curves for various Ge contents from 1w% to 30w%. The least

square regression analysis reveals the following relationship between fictive temperature and IR peak position: $\sigma(Ge, T_f) = a(Ge) - b(Ge) \times T_f$, where the coefficients a and b could depend on the Ge content. Based on those calibration curves, the fictive temperatures of the highly Ge-doped (up to 30 w %) optical fibers can be estimated once the composition of the core is known.

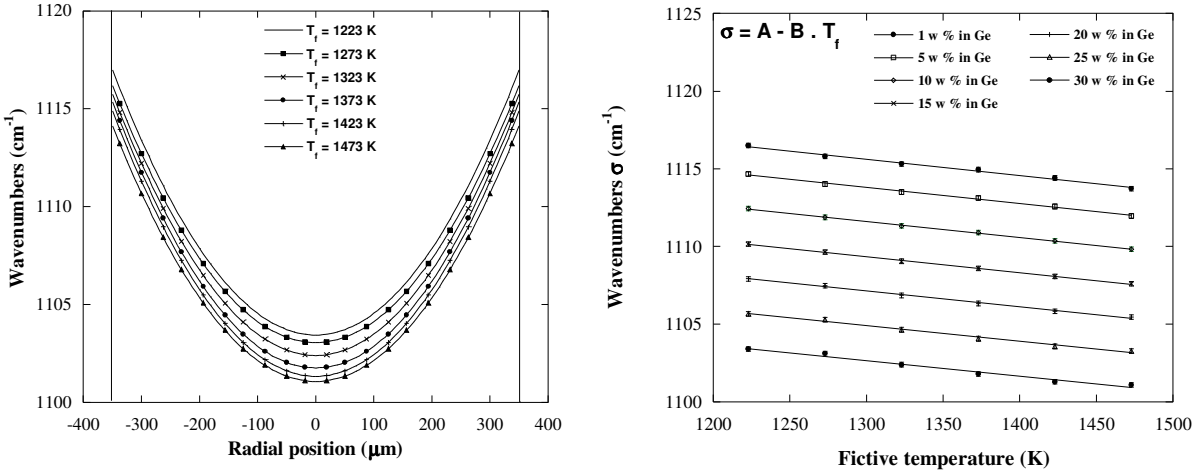

Fig. 2: Radial profiles of the reflectance peak wavenumber σ for MMF stretched preforms heat treated at various temperatures. Fig. 3: The relationship between IR peak wavenumber and the fictive temperature for GeO_2-doped bulk silica for various Ge concentrations.

In the following, we will investigate more precisely the effect of the Ge content on the calibration curves parameters: i.e. the ordinate at the origin (coefficient a) and the slope b. We have thus extracted these values from the above linear regressions for various Ge concentrations up to 30 w%. We found that the coefficient a follows a linear relationship with the Ge content: a = 1129.8 – 0.469 x [Ge] with an uncertainty Δa around ± 0.1. In contrast, the slope b appears to be independent on [Ge] when compared to our measurements uncertainty: b = 0.0102 ± 0.0002.

Now, we have extracted relation (1) from these results to estimate the fictive temperature profile from the IR peak wavenumber σ. This allows us to estimate the fictive temperature for any radial position r provided that the Ge concentration [Ge] is known. Using the above reported uncertainties on a, b and σ, we can estimate an uncertainty around 2 % in the fictive temperature determination.

$$T_f(r) = \frac{a(Ge) - \sigma(r)}{b} = \frac{1129.8 - 0.469.[Ge](r) - \sigma(r)}{0.0102} \qquad (1)$$

4. Application: measurements of fictive temperature distribution in multimode optical fibers

Graded index multimode prototype fiber (GI-MMF) P1 was realized for these experiments by Draka Comteq using internal deposition process (CVD based). Fiber has silica outer cladding with a diameter of 125µm and a GeO_2-doped core with a diameter of 50µm. The typical refractive index profile follows a parabolic law within the core. The maximum Ge concentration of the investigated fibers is around 15 ± 0.05 w%. Next, fiber was cleaved and then mounted in epoxy resin at 90 ± 1 degrees off the horizontal direction using a V-groove metal support. Finally, the mounted fiber was etched for 30s in 10% HF-10% H_2SO_4 solution and the IR reflection spectra were recorded by means of a FTIR spectrometer.

Figure 4 shows the estimated fictive temperature distribution on the cross section of the P1 fiber. The T_f along the entire cross-section varied with radial position. Firstly, the determined fictive temperatures of the P1 fiber at the near-surface region are ≈ 200 K higher than the lowest in the interior of the fiber. Secondly, there is an increase (≈ 150 K) of the fictive temperature from the tube towards the center of the core.

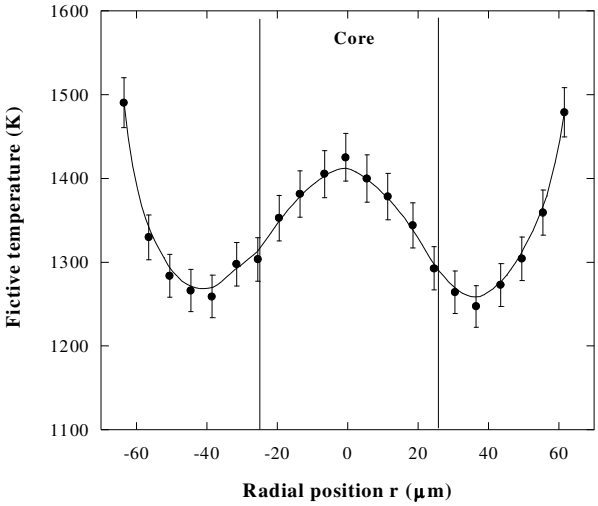

Fig. 4: Estimated fictive temperature as a function of the radial position for GI-MMF fiber. The solid lines are guides for eyes.

In the GI-MMF fiber, pure silica used for the outer cladding has the highest viscosity while the Ge-doped core has the lowest viscosity. Typically when cooled at a constant rate, a glass with higher viscosity is expected to acquire a higher fictive temperature. Therefore, the core is expected to have 1/ a non uniform T_f due to the Ge profile (lower T_f in the center) and 2/ a lower fictive temperature than the outer-cladding. However, in our measurements, the fictive temperature of the core is higher in the center (higher Ge content) and even higher than in the interior (e.g. from -50 to –25 μm) of the outer-cladding. One explanation could be that during the fiber cooling, the outer-cladding becomes rigid before the core. Thus, when the core changes from the supercooled liquid to the glass state, it is constrained by the outer-cladding and cannot change its volume freely. This might produce a higher fictive temperature state in the core when compared with unconstrained cooling. Another possibility will be that the stress distribution influences our σ measurements resulting in non-reliable calibration curves. Indeed, the stress distribution is different in the calibration capillaries and in the fiber samples.

5. Conclusion

New technology FTIR detector (FPA) allows us to perform rapidly fictive temperature radial profile within optical fiber cross-section with 6.25μm spatial resolution. Firstly, we have determined the calibration curves between fictive temperature and the IR peak wavenumber related to the Si-O-Si asymmetric stretching band for high Ge-content (from 1 to 30 w%) silica glasses. Next, using these curves, we have estimated for the first time to our knowledge the fictive temperature radial profile in GI-MMF. We show that T_f is higher at the fiber edges presumably due to the faster cooling and there is also an increase of T_f in the center of the core.

6. Bibliography

[1] A. Agarwal and M. Tomozawa, J. of Non-Cryst. Solids 209, 1997
[2] D.L. Kim et al., J. of Non-Cryst. Solids 286, 2001
[3] D.L. Kim et al., J. of Light. Technol. 19 (8), 2001
[4] P. Helander, J. of Mat. Science 39, 2004
[5] J.W. Hong, PhD thesis, Rensselaer Institute, NY, 2003

Monitoring OSNR in Dynamic WDM Network

Y. C. Chung
Korea Advanced Institute of Science and Technology
Department of Electrical Engineering and Computer Science
373-1 Guseong-dong, Yuseong-gu, Daejeon 305-701, Korea
ychung@ee.kaist.ac.kr

Future optical networks are envisioned to be dynamically reconfigurable – optical channels are added/dropped or cross-connected directly in the optical layer using wavelength-division-multiplexing technology. However, for the efficient operation and maintenance of these networks, it is essential to monitor various parameters including the channel power, optical frequency, OSNR, Q-parameter, and optical path, etc [1]. In this paper, we will review the current status of these monitoring techniques with an emphasis on the OSNR monitoring techniques.

Previously, OSNR has been measured by using the linear interpolation technique, in which the ASE noise was measured in between the channels and then interpolated into the signal's wavelength. However, in dynamically reconfigurable networks, WDM signals are added/dropped or cross-connected directly in the optical layer. Thus, each channel could traverse through different routes and different number of optical amplifiers. As a result, the accumulated noise level could be quite different from channel to channel. However, these noises located within the signal's bandwidths (and consequently the "true" value of OSNR) cannot be measured by the conventional linear interpolation technique [1].

Recently, a unique OSNR monitoring technique has been proposed by utilizing the different polarization properties of signals and ASE noises [2]-[4]. Up till now, this polarization-nulling technique appears to be the only practical solution capable of measuring the in-band ASE noise. However, the performance of this technique could suffer from PMD, PDL, nonlinear birefringence, in-band crosstalk (caused by FWM or multi-path interference), and polarization fluctuation [2], [5]-[6]. To overcome this problem, it has been proposed to improve the polarization-nulling technique by using an additional optical bandpass filter or measuring the noise power at the slope of the signal's spectrum [3]-[4]. It has also been reported that this technique could endure the fast fluctuation of the state-of-polarization (SOP) of optical signal in the aerial fiber caused by wind and electrical current in the neighboring power lines [5], [7].

To evaluate the possibility of using the polarization-nulling technique in the real systems, we investigated the effects of PMD, nonlinear birefringence, PDL, and fast polarization fluctuation. The results showed that this technique could monitor the OSNR with accuracy of better than ±1 dB, even when DGD and in-band crosstalk were as large as 60 ps (@ OSNR ≤ 27 dB) and 20 dB (@ OSNR=20 dB), respectively. The effect of the signal depolarization caused by nonlinear birefringence was measured to be negligible even in a highly nonlinear transmission link. We also investigated the effect of the partially polarized ASE noise caused by PDL. The results showed that, as long as the PDL/span was smaller than 0.2 dB (as in most current systems [8]), the OSNR could be monitored accurately by using the polarization-nulling technique even in a long-distance system. For example, when the PDL/span was 0.2 dB, the probability that the error in the measured OSNR became larger than 1 dB was merely 10^{-4} in the transmission link made of 50 amplifier spans. To verify the practicality of the polarization-nulling technique, we measured the OSNR of the optical signals transmitted through a 120-km long aerial fiber link for a week. In this aerial fiber link, the SOP of the optical signal was measured to be fluctuated at ~0.3 Hz and 60 Hz due to winds and electric currents in the neighboring power lines, respectively. Despite of these slow and fast fluctuations, the polarization-nulling technique could monitor OSNR with accuracy better than ±1 dB (@ OSNR = 19 ~ 28 dB). No significant degradation in the monitoring accuracy was observed during this long-term measurement. We also evaluated the performance of the polarization-nulling technique in an ultra long-distance transmission link by using a 640-km long recirculating loop. The results showed that this technique could measure the OSNR accurately even in the transmission link longer than 3200 km.

In summary, we reviewed the current status of various optical monitoring techniques for WDM networks with an emphasis on the OSNR monitoring technique. The results show that the polarization-nulling technique could be used in modern dynamic WDM networks and enhance their operation and maintenance.

References

[1]. Y. C. Chung, "Performance monitoring in optical networks (Tutorial)", *Proc. APOC 2003*, 5282-46, 2003.

[2]. J. H. Lee, D. K. Jung, C. H. Kim, and Y. C. Chung, "OSNR monitoring technique using polarization-nulling method", *IEEE Photon. Technol. Lett.* 13, 88–90, 2001.

[3]. J. H. Lee and Y. C Chung, "Improved OSNR monitoring technique based on polarization-nulling method", *Electron. Lett.* 37, 972–973, 2001.

[4]. H. Y. Choi, J. H. Lee, S. B. Jun, and Y. C. Chung, S. K. Shin and S. K. Ji, "Improved polarization-nulling technique for monitoring OSNR in WDM network," *Proc. OFC* 2006, paper OThP2, 2006.

[5]. C. H. Kim, Y. B. Lee, S. K. Ji, S. D. Choi, S. P. Hamn, M. S. Kim, M. W. Park, S. K. Shin, I. B. Kim, J. H. Lee, D. H. Hyun, and Y. C. Chung, "Performance of an OSNR monitor based on the polarization-nulling technique", *OSA Journal of Optical Networking*, 3, 388–395, 2004

[6]. J. H. Lee and Y. C. Chung, "Effect of polarization-dependent loss on optical signal-to-noise ratio monitoring technique based on polarization-nulling method", *Optics Express*, 13, 5045-5049, 2006

[7]. J. Wuttke, P. M. Krummrich, and J. Rosch, "Polarization oscillations in aerial fiber caused by wind and power-line current", *IEEE Photon. Technol. Lett.* 15, 882–884, 2003.

[8]. T. Lima, A. O. Lima, Y. Sun, H. Jiao, J. Zweck, C. R. Menyuk, and G. M. Carter, "A receiver model for optical fiber communication systems with arbitrarily polarized noise," *J. Lightwave Technol.,* 23, pp. 1478-1490, 2005

Optical signal quality monitoring based on asynchronous amplitude histogram for DPSK systems

H. Takara, T. Ohara, and B. Kozicki*

NTT Network Innovation Laboratories, NTT Corporation, 1-1 Hikari-no-oka, Yokosuka, Kanagawa, 239-0847 Japan
* Currently at Osaka University, 2-1 Yamadaoka, Suita, Osaka, 565-0871 Japan.
e-mail: takara.hidehiko@lab.ntt.co.jp

Abstract

We propose a method of monitoring the optical signal quality of NRZ-DPSK and RZ-DPSK systems that utilizes asynchronous amplitude histogram. It is shown that the proposed method can provide information about the level of noise and the amount of chromatic dispersion for DPSK systems.

1. Introduction

Optical signal quality monitoring is an important issue in optical networks and should satisfy a number of general requirements [1, 2]. There are several approaches for this purpose including both digital and analog techniques. Those receiving most attention are optical spectrum monitoring [3], pilot tone monitoring [4], polarization nulling [5], and RF spectrum analysis [6]. These methods can provide information about signal parameters. However, they are limited either to a certain signal format or to a particular degradation.

In this paper, we propose an extension of the optical signal quality monitoring method based on asynchronous amplitude histogram to cover a wide range of signal formats. To confirm our approach, we apply it to DPSK signals. Amplitude histograms have been shown to provide information about the level of noise through the averaged Q-factor and about the amount of residual dispersion [7] for intensity-modulated signals at bit rates from 2.5 to 40 Gbit/s. It has been verified that the same device can support both NRZ and RZ modulation. In order to provide even greater flexibility of the asynchronous amplitude histogram method, we investigate its application in monitoring of dispersion and noise level of NRZ-DPSK and RZ-DPSK signals. The following sections describe the theoretical and experimental results of application of asynchronous amplitude histogram method to the monitoring of DPSK signals.

2. Asynchronous amplitude histogram

Asynchronous amplitude histogram optical performance monitoring consists of two parts: the sampling device and the algorithm extracting the desired information about the signal quality. Sampling is performed asynchronously. Therefore, the key advantages of this method are that the same device can be used to monitor a wide variety of optical signals and that the expensive clock recovery circuit can be eliminated. The sampler modeled and used in this research consists of an internal clock, electrical pulse generator, electro-absorption modulator (EAM), O/E converter, and a signal processing unit with analog-to-digital (A/D) converter, as shown in Fig. 1.

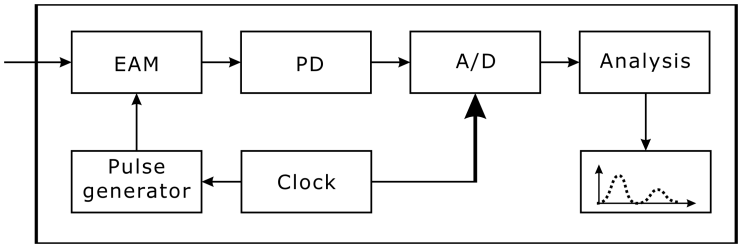

Fig. 1 Fundamental configuration of optical signal quality monitor

The clock operates at a frequency of 100 MHz and is not synchronized to the incoming bit stream. It stimulates the pulse generator, which, in turn, drives the electro-absorption modulator to provide a narrow optical gate for sampling the signal waveforms. The sampled signals are received by a photodetector and processed electronically. This arrangement is simpler than the traditional electronic sampling, because the photodetector bandwidth can be lower than the bandwidth of the incoming signal as the signal is sampled in the optical domain. The electrical signal is processed to form an amplitude histogram. Signal parameters can be calculated from histogram details.

3. NRZ-DPSK monitoring

When an asynchronous amplitude histogram is constructed from an NRZ-DPSK signal, a single peak is created with the mean value equal to the average power of the signal. Considering the fact, that the ASE noise affects the intensity of the signal in the same fashion as in the case of IM signals, we adopted a similar measure of noise for the phase-modulated signal. With the single peak present, the modified Q-factor is:

$$Q_{avg} = \frac{\mu_{avg}}{\sigma_{avg}} \tag{1}$$

where μ_{avg} and σ_{avg} are the average mean and average standard deviation of the histogram peak, respectively. An example of NRZ-DPSK histogram and the corresponding values are shown in the inset of Fig. 2.

The performance of asynchronous amplitude histogram for measuring noise in a 10 Gbit/s NRZ-DPSK signal was estimated by simulation and experiment. Light from a tunable laser diode, emitted at 1550.2 nm, is modulated by a phase modulator and, subsequently, attenuated and amplified. The tunable attenuator allows to modify the optical signal-to-noise ratio (OSNR) of the signal. The optional span of fiber is used for adjusting the level of dispersion (as explained in the following paragraphs). The power reaching the monitor is kept at a constant level of -2 dBm. The value obtained by the monitor is compared to the OSNR measured by the optical spectrum analyzer whose resolution is 0.1 nm.

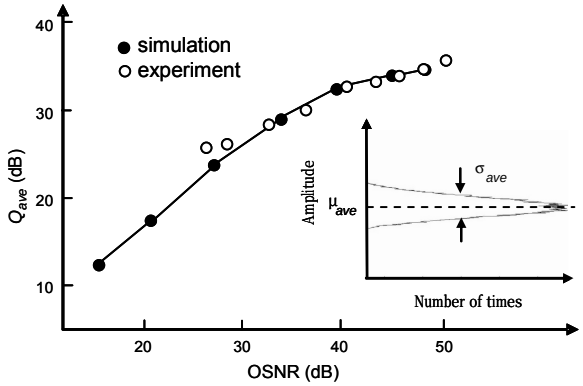

Fig. 2 Relationship between averaged Q-factor and OSNR for NRZ-DPSK signal

The results of the averaged Q-factor measurement are plotted as a function of OSNR in Fig. 2. The experimental results are compared to the simulation results (line). In the experiment, the OSNR was changed from 27 to 49 dB. In that range the agreement between the simulation and the experiment results is very good. Moreover, the simulation considered OSNR values down to 15 dB. As can be observed in the figure, the relation between the averaged Q-factor and the signal OSNR is linear in the range 15 to 40 dB OSNR.

In addition to monitoring the noise level, the asynchronous amplitude histogram method can provide information about the level of acquired dispersion. We propose an extension of this method. An NRZ-DPSK signal is a constant-amplitude signal with phase transitions between the bits. The temporal transitions in phase cause frequency chirp. When the signal is transmitted through a dispersive medium, the chromatic dispersion produces the phase-to-amplitude modulation, which manifests itself as a variation from the constant amplitude at the bit transitions. This can be observed in the asynchronous amplitude histogram, as shown in the inset of Fig. 3. The effect yields a pedestal with peaks at both ends, whose width is proportional to the acquired

chromatic dispersion; without affecting the standard deviation of the central peak. This measurement was demonstrated in [8]. However, for large levels of dispersion (>200 ps/nm), the standard deviation of the pedestal peaks cannot be calculated because of the excessive spread. We propose to calculate the level of dispersion by the following equation,

$$F_{dis,nrz} = \mu_{90} / \mu_m \quad (2),$$

where μ_{90} is the level of 90% of cumulative histogram distribution and μ_m is the mean level of the entire histogram; $F_{dis,nrz}$ is obtained by normalizing μ_{90} with μ_m.

Using the factor $F_{dis,nrz}$, verification tests were done using simulations and experiments by employing a number of dispersion compensating modules. The results for a 10 Gbit/s NRZ-DPSK signal are plotted in Fig.3. The asynchronous amplitude histogram method provides a way to measure residual dispersion within the range -1000 to +1000 ps/nm. This range is much broader than the one presented in ref [8] (-170 ~ +320 ps/nm).

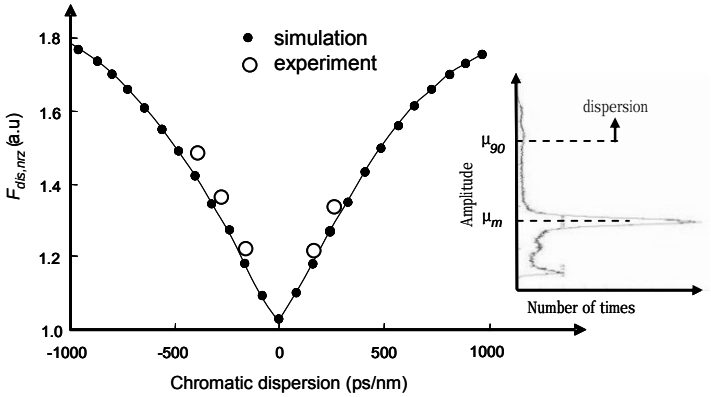

Fig.3 Relationship between $F_{dis,nrz}$ and chromatic dispersion for NRZ-DPSK signal

4. RZ-DPSK monitoring

We also propose a simple way to measure the noise and dispersion in RZ-DPSK signals by using asynchronous amplitude histograms.

Similar to the NRZ-DPSK case, the information in the RZ-DPSK signal is encoded in the phase of the signal. However, the phase transitions, clearly visible in the former one, in the latter format occur when the intensity reaches the "0" level. Therefore, the dispersion does not develop a pedestal in the histogram due to the phase-to-intensity conversion. The actual asynchronous amplitude histogram of an RZ-DPSK signal is shown in the inset of Fig. 4(a). The two peaks are formed because of the return-to-zero intensity modulation. The dispersion influences the signal (and the histogram) through chirp created by intensity modulation, thereby reducing the spacing between the histogram peaks without a change in average power. Moreover, as the signal traverses the amplifiers, the ASE broadens the histogram peaks and effectively reduces the rate between the height of histogram peak and the height of histogram valley. These observations allow us to derive the parameters needed for estimating the level of noise and dispersion in the RZ-DPSK signal.

In order to verify the applicability of the above effects, the following two parameters, $F_{snr,rz}$ and $F_{dis,rz}$ are proposed; a confirming simulation was performed on a 10 Gbit/s RZ-DPSK signal.

$$F_{snr,rz} = N_1 / N_m \quad (3)$$

$$F_{dis,rz} = (\mu_1 - \mu_0) / \mu_{,m} \quad (4),$$

where N_1 is the number of sampling points of the higher histogram peak. Parameter N_m is the number of sampling points of the histogram valley at the middle level, while parameters μ_1 and μ_0 are the levels of higher and lower histogram peak, respectively.

The simulation results of OSNR dependence assuming constant dispersion are presented in the graph in Fig. 4(a). Noise parameter $F_{snr,rz}$ is plotted versus OSNR. For a wide range of noise levels (OSNR 15 – 40 dB), the parameter provides a clear relation to the OSNR. We also estimated the relation between the dispersion parameter $F_{dis,rz}$ and the actual acquired dispersion. The results are plotted in Fig. 4(b). The parameter also shows a good relationship to the chromatic dispersion. It is found that signal quality monitoring can be performed in the range from -600 to +600 ps/nm. From these results, it is expected that the proposed parameters, $F_{snr,rz}$ and $F_{dis,rz}$, can be applied to evaluate the signal quality of RZ-DPSK signals.

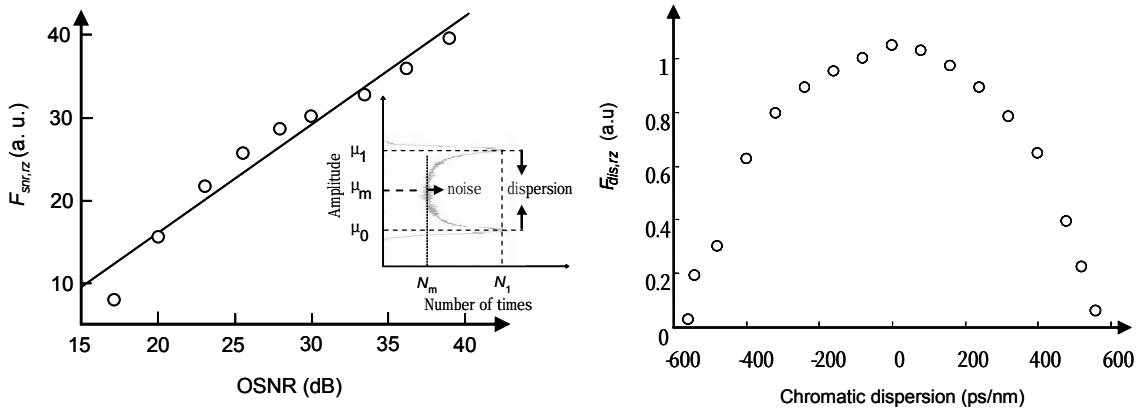

(a) (b)

Fig. 4 Characteristics of parameters for RZ-DPSK signal
(a) OSNR dependence of $F_{snr,rz}$, (b)dispersion dependence of $F_{dis,rz}$

5. Summary

This contribution proposed a method of monitoring the optical signal quality of DPSK systems based on asynchronous amplitude histograms. Parameters are derived from the histograms and shown to be in a close relation to the actual performance of the signal in terms of dispersion and noise level. The asynchronous amplitude histogram method has been proven to be a flexible method for optical performance monitoring of both intensity- and phase-modulated signals.

This work was supported in part by the National Institute of Information and Communications Technology (NICT) of Japan.

References

[1] G. Bendelli, C. Cavazzoni, R. Girardi, and R. Lano, ECOC 2000, vol. 4, pp. 113-116, Sep. 2000.
[2] R. Giles, SOFM2002, pp. 19-24, 2002.
[3] K. Park, S. Shin, and Y. Chung, Electronics Letters, vol. 35, pp. 415-417, 1999.
[4] H.C. Ji, K.J. Park, J.H. Lee, H.S. Chung, E.S. Son, K.H. Han, S.B. Jun, and Y.C. Chung, J. Optical Networking, vol. 3, pp. 510-533, 2004.
[5] J. Lee, D. Jung,, C. Kim, and Y. Chung, IEEE Photonics Technology Letters, vol. 13, pp. 88-90, 2004.
[6] C. Dorrer, and X. Liu, IEEE Photonics Technology Letters, vol. 16, pp. 1781-1783, 2004.
[7] I. Shake, and H. Takara, IEEE J. Lightwave Technology, vol. 20, pp. 1367-1373, 2002.
[8] Z. Li, C. Lu, Y. Wang, and G. Li, IEEE Photonics Technology Letters, vol. 17, pp. 1998-2000, 2005.

New methods for investigating mode coupling in multimode fiber: Impact on high-speed links and channel equalization

Stephen E Ralph and Arup Polley
School of Electrical and Computer Engineering
Georgia Institute of Technology, Atlanta, Georgia 30332

K. D. Pedrotti, R. P. Dahlgren and J. A. Wysocki
Department of Electrical Engineering
University of California, Santa Cruz, CA 95064-1077

Introduction

Multimode fiber has reemerged as a potentially high performance optical transport media with under exploited capabilities. By examination of the impulse response of MMF with large temporal resolution and large dynamic range, enabled by measurements with sub-picosecond jitter, we quantify the impact on the impulse response and determine the mode coupling. These results together with numerical models enable us to accurately depict the transmission of ultrafast data streams, and thereby quantify system performance increases in the context of adding optical and electronic signal processing to legacy and modern multimode fiber.

We first provide an overview of the mode coupling theoretical results, which lead to the fiber impulse response for various levels of coupling strength. This provides a motivation for the new experimental methods which are subsequently discussed. The experimental results are then fit to the mode coupling theory, providing a measure of mode coupling strength in modern multimode fiber. We then discuss the impact of mode coupling on the performance of electronic equalization methods. Lastly we outline our new results which exploit Raman gain to selectively amplify only one mode group and thereby improve the fiber impulse response.

Mode coupling theory

A set of coupled equations describing the power flow in a waveguide with N modes can be derived via a perturbation approach [1].

$$\frac{\partial P_n}{\partial z} + \tau_n \frac{\partial P_n}{\partial t} = -\gamma_n P_n + \sum_k d_{n,k}\left(P_k - P_n\right) \tag{1}$$

where, P_n is the power in the n^{th} mode at time t at a distance z. γ_n is the attenuation coefficient for nth mode and $d_{n,k}$ is the coupling coefficient between two modes n and k. In deriving (1) a number of assumptions are made: a) the imperfections in the waveguide such as changes in diameter, elliptical core deformations, or random bends of the axis lead to coupling of modes; b) these imperfections appear in a random fashion along the length of the waveguide and a statistical ensemble average can be taken; c) the waveguide perturbation is uncorrelated to the field amplitude beyond a certain correlation length; d) the distance required to create any change in field amplitude is large compared to correlation length. The assumptions c) and d) essentially make the waveguide perturbation function and field amplitudes uncorrelated over the entire waveguide. It should be noted that the perturbation interacts strongly with the phases of the field and the effect is integrated over the length of the waveguide. The spatial frequencies of the perturbation are determined via a Fourier analysis and are used to quantify the interaction with the propagation phase difference of the modes. The contribution is contained in the mode coupling coefficient $d_{n,k}$ given by

$$d_{n,k} = A \cdot \left[\frac{\left(\pi k_0 c \varepsilon_0\right)^2}{8} \cdot \rho_{n,k}^2 \cdot \frac{1}{\left(\Delta\beta_{n,k}\right)^8} \right] \tag{2}$$

$$\rho_{n,k} = \int_0^\infty r E_n(r) E_k(r) \frac{\partial \tilde{n}^2}{\partial r} dr \tag{3}$$

where, E_n is the radial electric field profile of the n^{th} mode, n(r) is the refractive index profile, $\Delta\beta_{n,k}$ is the difference in propagation constant of mode n and k and A is the mode coupling strength. The electric field

profiles and the propagation constants as well as the group delays used later are all numerically determined using our mode solver which allows arbitrary core index profiles. The electric field profiles in (3) are normalized such that:

$$\int_0^\infty rE_n^2(r)dr = \frac{k_0}{\pi}\sqrt{\frac{\mu_0}{\varepsilon_0}}\cdot\frac{1}{\beta_n} \tag{4}$$

There are wave vector degeneracies among the modes and complete mode coupling is assumed between the these modes which form a mode group as suggested by (2). Furthermore, since the adjacent mode groups have the smallest $\Delta\beta_{n,k}$, coupling is dominated by them. Considering this the average power P_g of the mode group g is found by solving the equations:

$$\frac{\partial P_g}{\partial z}+\tau_g\frac{\partial P_g}{\partial t}=\begin{cases}-\gamma_g P_g + d_g\left(P_{g+1}-P_g\right) + \left(\dfrac{g-1}{g}\right)d_{g-1}\left(P_{g-1}-P_g\right) & \text{for } g \text{ even}\\ -\gamma_g P_g + \left(\dfrac{g}{g+1}\right)d_g\left(P_{g+1}-P_g\right)+\left(\dfrac{g-1}{g+1}\right)d_{g-1}\left(P_{g-1}-P_g\right) & \text{for } g \text{ odd}\end{cases} \tag{5}$$

The coupling coefficient d_g between two adjacent mode groups g and g+1 can also be found using an approximate analytical solution [2] and we find that it matches well with the exact value obtained using (2), (3) and (4) directly

$$d_g = \frac{1}{2}\left(\frac{nk_0}{a}\right)^2\Delta^2\left(\frac{g}{g_{TOT}}\right)\frac{A}{\left(\Delta\beta_{g,g+1}\right)^8} \tag{6}$$

where, g_{TOT} is the total number of mode groups present and a is the radius of the fiber. A split step method [3] is used to evaluate (5) for a range of mode coupling strengths A.

Figure 1 depicts the impulse response for a 62.5μm multimode fiber (MMF) subject to a center launch Gaussian spot excitation consistent with the mode size of single mode fiber. The intrinsic bandwidth is that of a 10Gbps channel. The nature of the channel response is strongly dependent on mode coupling. For A< 10^4 the coupling has negligible effect and we observe the arrival of the distinct mode groups. On the other hand, for A≥10^{12} the response becomes Gaussian due to strong mode coupling. For intermediate coupling, energy is seen to "fill in" the valleys between the primary mode groups. Essentially, some energy propagates with a group velocity correspond to some average of other distinct groups.

This observation suggests the new experimental method; observe the impulse response with sufficient temporal resolution and dynamic range to observe this fill-in effect. Then the coupling coefficient can be estimated by fitting the results to the numerical model.

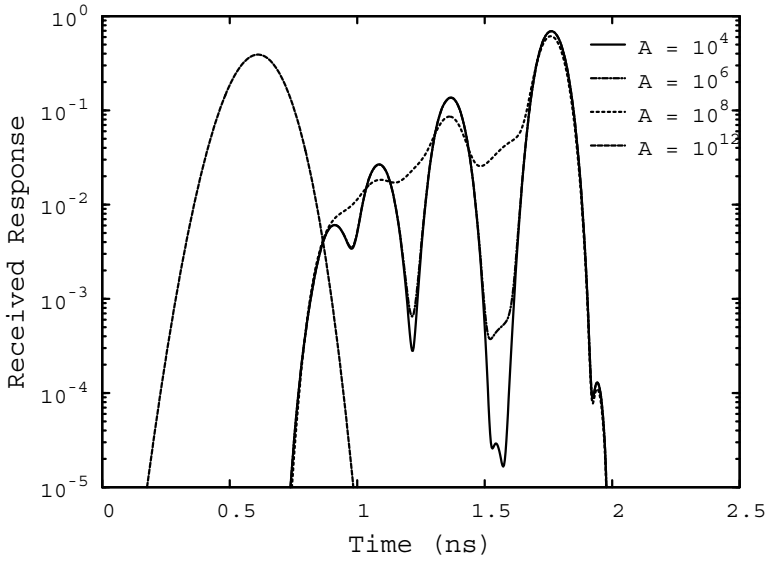

Fig. 1. Numerical estimate of the effects of mode coupling on received pulse shape for an 8km MMF. For weak coupling (A ≤ 10^4), the arrival of distinct mode groups is observed. For strong coupling (A ≥ 10^{12}), the received pulse is nearly Gaussian. For intermediate coupling, energy exchange between the modes results in energy arrival at times other than that of the distinct mode groups and the "valleys" are gradually filled in. [Ref. 3]

Measurement methods

Previous methods to determine the mode coupling strength in (MMF) are essentially based on comparing the evolution of mode power distribution (MPD) observed experimentally with that predicted by the mode coupling theory [1]. The far field analysis method is used to determine the mode power distribution at the end of the fiber. Our method relies more on comparing the evolution of temporal impulse response of the fiber with that predicted by a MMF model including the mode coupling. Apart from the change in MPD, the other obvious effect of mode coupling is the energy filling between the distinct mode groups and the corresponding change in the temporal response. The MPD at launch is dependent on the excitation and the specific fiber and is not directly measurable. Therefore, instead of comparing the change in MPD, we focus on the impulse response, which is sensitive to the mode coupling coefficient and, more importantly, is directly related to the channel performance.

Impulse response measurements of the MMF are done with sufficient temporal resolution and dynamic range to separate the mode groups distinctly and quantify the energy arriving between them. To minimize the chromatic dispersion, 16 ps FWHM pulses at 1550 nm are launched. A mode locked laser followed by bandpass filters is used to generate the nearly transform-limited pulses. A detector-sampling module with net bandwidth of 20 GHz is used as the receiver. A GRIN lens couples all modes of 50 μm MMF in the detector with nearly 100% efficiency. The signal is launched into the MMF core with a single mode fiber (SMF) at different offsets which allows control of the power distribution in the excited modes. To reduce the noise, the response is effectively averaged for 32 minutes and 3 orders dynamic range is obtained. Care is taken to minimize the jitter and drift in the acquired waveforms.

The use of 1550 nm helps to insure that the primary modes are temporally separated due to large differential modal delay (DMD) at 1550 nm for fibers optimized at 1310 nm. Coupling strength A, which is a function of micro-bending perturbation and mechanical properties of fiber, is expected to be only slightly dependent on the wavelength of operation. By comparing the measured impulse responses of 4.4 km 50 μm MMF with numerically generated impulse response we estimate a coupling strength A of $1x10^8$. The observed uniformity of arrival of the mode groups suggest that the fibers examined can be described by an alpha profile [4] without any major index profile defects. Hence, in the numerical model, we assume the $\Delta\beta$'s to be that of a fiber with a pure alpha index profile. The modal delays and the mode power distribution at the launch are adjusted for different correlation length to match the received waveform. We also estimate the coupling strength A of typical 62.5 μm FDDI grade fiber to be $5x10^7$.

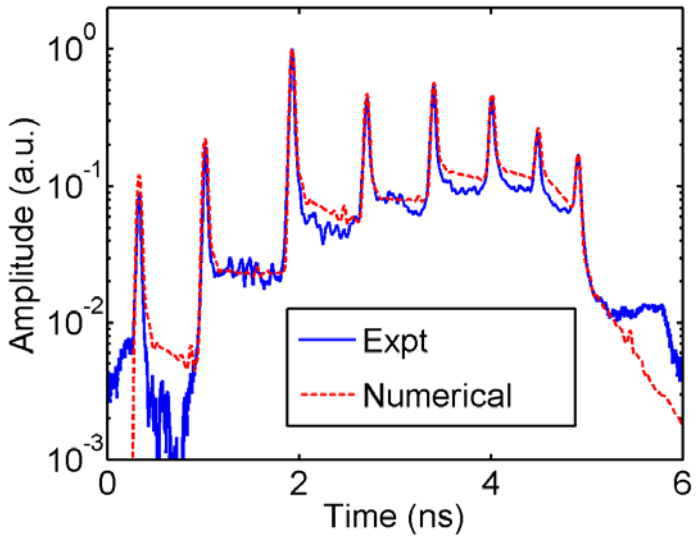

Fig. 2. Comparison of measured MMF response and the numerical estimate using a mode coupling strength of $A=1x10^8$. Energy arriving between the primary mode groups is due to mode coupling. For this fiber, at 1550nm, the lower order modes arrive later. The lower order modes are seen to exhibit lower coupling compared to the higher order mode groups as predicted by the theory.

The method described above is specifically suitable for MMFs with relatively low mode coupling strength and therefore, requires relatively long fiber lengths in order to observe the effects of coupling. In that regime, modes can be resolved temporally and the estimation of mode coupling strength is accurate and the impulse response is useful in estimated the efficacy of mitigation methods. We note that for smaller lengths of fiber, the temporal resolution may be made sufficient by using shorter launch pulses and a receiver with larger bandwidth. However, the dynamic range of the measurement is often limited by the tail of the detector response and an appropriate length of fiber should be chosen to clearly observe the mode coupling effects. Nonlinear methods of measuring optical pulses such as autocorrelation and cross-correlation may also be used. However, the nonlinear interaction between different modes needs to be quantified and hence extracting the information quantitatively from the observed response is challenging.

In plastic optical fibers (POFs) strong mode coupling is observed and complete mode coupling is observed within 10-30 m of fiber length [6]. A method suitable in this regime illuminates the fiber end at an angle to preferentially excite higher order modes (HOMs) [7,8], mode coupling changes the MPD to couple power into the lower order modes (LOMs). The far field patterns of LOM and HOM are disk-like and annular-shaped respectively. For an appropriate length of fiber, where mode coupling effect is intermediate, transition of far field image from disk to annular shape occur at a particular angle. From the measured angle and fiber length, the mode coupling strength can be found to a first order approximation. The extracted mode coupling strength can be used in the numerical model for verification and prediction. Figure 3 illustrates the impulse response of POF over 200m, no structure is observed, indicative of the strong coupling regime. However, the response is suitable for >10Gbps links.

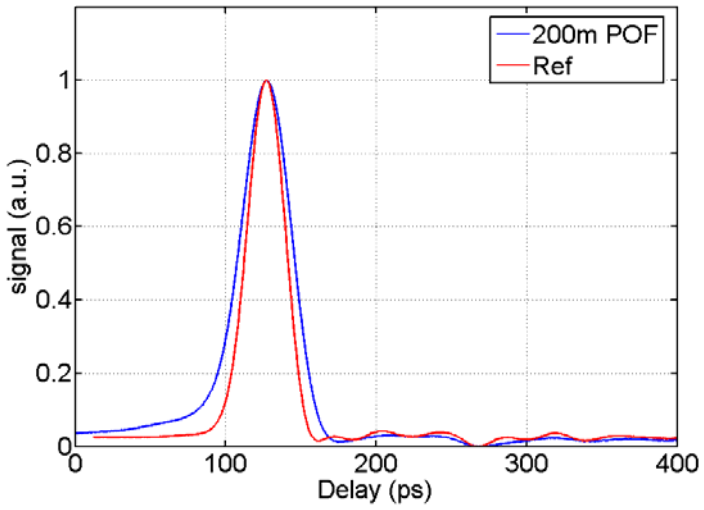

Fig. 3. Response of 200 m of 50 μm core perfluorinated polymer based POF (GigaPOF-50SR from Chromis Fiberoptics). Absence of any modal structure and nearly Gaussian response indicate a strong mode coupling regime.

Electronic Equalization Analysis

Different electronic equalization methods to mitigate channel impairments are extensively used for copper and wireless links. For 10 Gbps data transmission via optical channels less complex structures such as feedforward equalizer (FFE) and decision feedback equalizer (DFE) architectures are implemented. FFE, which is essentially a linear filter, attempts to invert the channel and in the process necessarily increases the noise-to-signal ratio of channel. DFE partially avoids the problem by removing the post-curser inter symbol interference (ISI) estimated from the previously detected bits, using a feedback filter. However, for both cases the equalization process incurs a signal-to-noise (SNR) penalty which can be translated to an optical power penalty. Though the equalization penalty depends on the specific filter architecture, number of filter taps etc., the ideal equalization penalty for infinite length DFE (PIE-D) can be computed which provides a lower limit for the penalty of specific implementations [5].

We compute the ideal equalization penalty for the 10 Gbps, 62.5μm MMF links with and without mode coupling for different fiber lengths and two launch conditions: center launch (0-3 μm offset) and offset launch (17-23 μm offset). The range of each launch condition accounts for the fiber coupler misalignment tolerance and the offset launch is under consideration as a part of an IEEE standard [9]. Based upon the measured results a coupling strength $A = 5\text{x}10^7$ is assumed. We examine two fiber index profiles, a pure alpha profile and a profile characterized by a dip in the index on center. This irregularity is common in some legacy MMF.

Figure 4 depicts the equalizer penalty for these cases and shows that coupling systematically increases the residual equalizer penalty. Additionally, the increase depends strongly on fiber index profile. This can be understood by first considering the equalizer penalty in the absence of coupling. Initially, the penalty linearly increases with fiber length. This results from the temporal spreading of the mode groups. As the energy slowly spreads outside of a single bit slot the penalty increases. After some fiber length only the dominant mode group is left in one bit slot and all others mode groups contribute to ISI. In this regime the infinite equalizer penalty no longer increases. The transition point depends on the relative DMD of the fiber and since the center dip has larger DMD it shows that it has already reached this saturated penalty regime by 300m for center launch, Fig. 4a.

Now consider the action of mode coupling. First we note that the DMD dominates the equalizer penalty. However, once the saturated penalty regime is reached coupling increases the penalty, in some cases by substantial amounts. This results from the slow coupling of energy out of the dominant mode group into the other groups which contribute to ISI. The center dip profile is more susceptible to this due to the larger mode coupling found with center dip profiles. Similarly, the effect of mode coupling is larger for offset launch, Fig. 4 b since the higher order modes, which are preferentially exited with offset launch, exhibit larger coupling than the lower order mode groups.

We note that though the general observations remain unchanged, larger coupling strength as measured for 50 μm MMF will have larger impact on the equalization penalty.

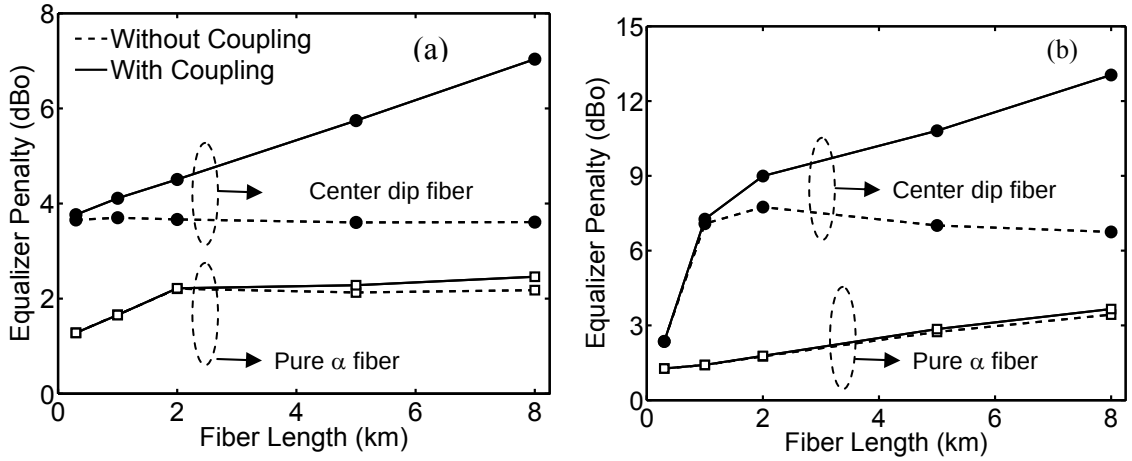

Fig. 4. Impact of mode coupling on equalizer penalty as the fiber length is increased: (a) Center launch (b) Offset launch. For each launch condition, both the pure alpha and center dip fibers are shown [4].

Raman amplification in MMF

We use Raman amplification in MMF as an optical signal processing technique to boost the signal strength as well as improve upon the signal integrity. Numerical calculations show that Raman gain of the lowest order mode LP_{01} in 62.5 μm MMF is comparable to that of SMF. This results from the larger GeO2 concentration in the core and hence the larger Raman gain coefficient which offsets the somewhat larger effective area of the lowest mode group compared to SMF [10]. Furthermore, the larger effective area of the higher order modes reduces the Raman gain of the higher order modes compared to that of LP_{01}. This enables Raman gain to selectively amplify the LP_{01} mode and thereby reduce the inter symbol interference

from higher order modes. We experimentally show for co-propagating pump set up and for near-center launch with a SMF, the response of MMF is improved via mode selective gain.

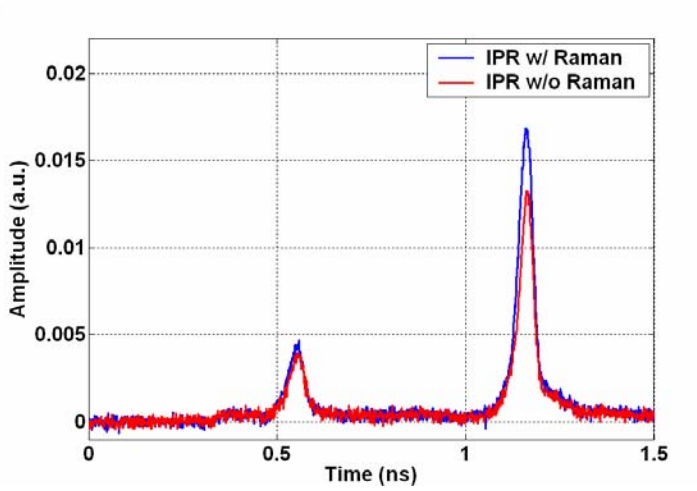

Fig. 5. Improvement in the impulse response via mode selective Raman amplification. 200 mW of 1450 nm pump and 16 ps pulses at 1500 nm are launched in 9 km of 62.5 μm MMF via SMF at 3 μm offset from the center of the core.

Conclusions

We have shown that mode coupling effects in multimode fiber can be readily observed and quantified using a new high temporal resolution, high dynamic range impulse response characterization method. The effects of coupling are shown to increase the power penalties for subsequent electronic filtering. We also demonstrate an optical signal processing method using mode selective Raman gain that effectively reduces intersymbol interference and enables high speed long reach MMF links.

Acknowledgements

We thank Kasyapa Balemarthy for some of the numerical calculations, and we thank Chromis Fiberoptics Inc for POF fiber samples.

References:

[1] D. Marcuse, *Theory of Dielectric Optical Waveguides*, Academic Press, 1991.
[2] R. Olshansky, "Mode Coupling Effects in Graded-Index Optical Fibers," *Applied Optics*, vol. 14, no. 4, pp. 935-945, April 1975.
[3] K. Balemarthy, A. Polley, and S. E. Ralph, "Electronic Equalization of Multi-km 10Gb/s Multi-Mode Fiber Links: Mode Coupling Effects," submitted to *JLT*.
[4] J.A. Buck, *Fundamentals of Optical Fibers*, John Wiley & Sons, 1995.
[5] J. G. Proakis, *Digital Communications*, McGraw-Hill, 1995.
[6] S. Zheng, X. Jin, and X. Zhang, "Analysis of the effects of mode coupling on the bandwidth characteristics of step-index plastic optical fiber," *Microwave and Optical Technology Letters*, vol. 48, no. 3, March 2006.
[7] W. A. Gambling, D. N. Payne, and H. Matsumura, "Mode conversion coefficients in optical fibers," *Applied Optics*, vol. 14, no. 7, pp. 1538-1542, July 1975.
[8] K.D. Pedrotti, R. P. Dahlgren, J. A. Wysocki, S. E. Ralph, R. Gandhi and A. Polley, "Multi-gigabit Transmission over POF", POF World West, Santa Clara CA, June 21-22, 2006.
[9] IEEE 802.3aq 10G-LRM Task Force http://www.ieee802.org/3/aq
[10] A. Polley and S. E. Ralph, "Raman amplification in multi-mode fiber: Reduction of inter-symbol interference via mode selective gain," *OAA* 2006.

A differential mode delay measurement for a multimode optical fiber with Fourier-domain low-coherence interferometry

J.Y. Lee, T-J. Ahn, and D.Y. Kim

Department of Information and Communications, Gwangju Institute of Science and Technology

1 Oryong-dong, Buk-gu, Gwangju 500-712, Republic of Korea

We present a novel differential mode delay (DMD) measurement technique for a conventional multimode fiber (MMF) using Fourier-domain low-coherence interferometry (fLCI) with a modified Mach-Zenhder interferomter. An optical spectrum analyzer and a broadband source were used to obtain time resolved optical interference signal. The measured interference signal is Fourier transformed to obtain time delay information. A scanning offset launching method is used to excite every available mode in an MMF. A conventional MMF with its length of 9 m is tested to demonstrate the validity of our proposed method. The experimental results of our proposed method agree well with results obtained using a conventional time-domain measurement method. Our proposed measurement method can measure a short length multimode optical fiber with temporal DMD resolution better than 0.11 ps / m.

1. Introduction

An MMF is an essential component for 10 Gb/s next generation local area network (LAN) transmission system. Differential mode delay (DMD) of an MMF is a decisive factor in determining the bandwidth of an optical transmission system [1]. The concepts of DMD and the study of its measurement method have still been under development. The conventional time-domain DMD measurement system uses complicated and expensive instruments such as a pulsed laser and a fast detection system with a sampling oscilloscope in order to measure broadening in a transmitted optical pulse [2]. Even though this method is an industry standard, it is not easy for the time-domain measurement technique to obtain the DMD of an optical multimode fiber with large chromatic dispersion. It is also hard to measure a short length MMF or a multimode PCF with the time-domain technique. Therefore, there is a need for an alternative DMD measurement method that can be used for a sample with a short length or high chromatic dispersion. In this study, we present an alternative novel differential mode delay (DMD) measurement technique for an MMF using Fourier-domain low-coherence interferometry (fLCI) [3]. A Mach-Zehnder interferometer is used with a broadband source, and an optical spectrum analyzer is employed to detect spectral interference signal. A conventional MMF with its length of 9 m was tested to demonstrate the validity of this proposed method.

2. Experiment and results

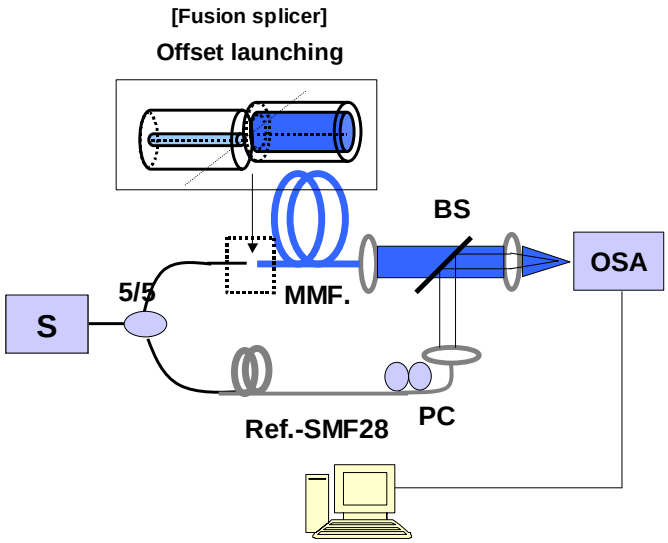

Fig.1 Our proposed experimental setup based on fLCI

The experimental apparatus of our proposed technique is illustrated schematically in Fig. 1. The basic configuration is a modified Mach-Zehnder interferometer with an optical broadband source and an optical spectrums analyzer (OSA) for a spectral detection. The main body consists of a fiber type 3 dB coupler and a beam splitter (BS). An amplified spontaneous emission (ASE) light source made of an Erbium doped fiber was used as an optical source. ASE light is launching into the interferometer and is split by a fiber coupler (50:50) into both a reference arm and a sample arm. The output through a sample MMF and another output through a reference fiber are collimated with two lenses and combined with a bulk beam splitter. The combined beam is coupled into an OSA with another lens. A 9 m long commercially available MMF (InfiniCor. SX +50/125, Coring Inc.) is inserted into one arm of an interferometer as a test fiber. A single mode fiber whose length is also about 9 m is inserted into another arm of an interferometer as a reference delay line. The output end of the reference single mode fiber is aligned with a 3-axis linear translation stage to obtain maximum visibility in a spectral interferogram. The length of a single mode fiber is matched to those of MMF to cancel out the chromatic dispersion effect of the sample fiber, which is the major obstacle in a time-domain DMD measurement system. This allows us to extend the capability of the measurement range of our proposed measurement method dramatically.

A scanning offset launching method with a butt-coupled single mode fiber is used for an excitation of all possible modes in an MMF [2]. All scanning launching processes are operated with a commercially available fusion suplicer. After a precision horizontal alignment between a center position of a single mode fiber and an MMF, the single mode fiber whose core diameter is about 9 micron is scanned vertically with a step size of 1um. The gap between the end faces of a SMF and a MMF have been sustained within 10 μm during a complete measurement. An OSA detects a spectral interference signal for each offset position. The spectral sweeping range of the OSA is 20 nm, and its sweeping time is less than a second. A fiber polarization controller (PC) is put in the reference arm of interferometer to acquire the maximum visibility of a spectral interferogram. A captured interference signal is transferred to a computer via a GPIB interface. All processing is done by a specially made LabView program automatically. Detailed theoretical expressions about a differential mode delay measurement method with fLCI can be found in Ref. [4]

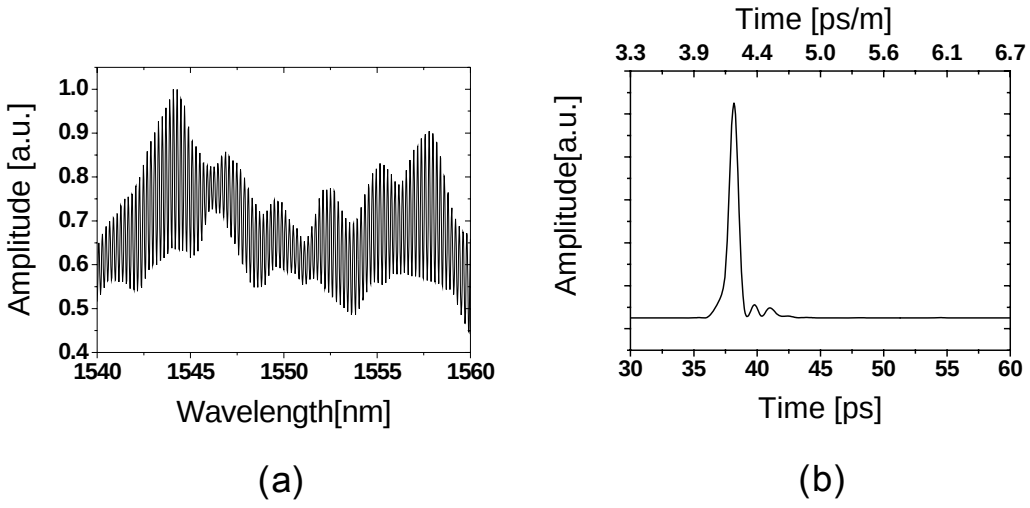

Fig. 2. (a) A measured spectral interferogram by using our proposed method when the offset between the launching SMF and an MMF is zero. (b) Calculated relative time delay graphs obtained from Fourier transformation of the spectral interferogram shown in Fig. 2(a)

A measured spectral interferogram at zero offset position between the launching SMF and the sample MMF for a conventional MMF is shown in Fig. 2(a). This spectrum contains the information of a relative modal delay between the fundamental mode of the reference SMF and a mode group of the test fiber excited by a given offset launching position. In order to obtain modal delay information from this interferogram, we need to do a numerical Fourier transformation. We have first converted the wavelength axis of Fig. 2(a) into a frequency axis and used a cubic spline fitting algorism to obtain a regularly spaced data in frequency domain before doing a numerical Fourier transformation. Then, the rescaled spectrum is Fourier transformed to obtain the mode delay distribution of the test sample [5]. Fig. 2(b) is a calculated modal delay from the interferogram shown in Fig. 2(a). The top axis of the graph shows the modal delay normalized by the length of the fiber.

Fig. 3 shows measured modal delays for all available mode groups of the sample MMF excited by the single mode coupled offset launching method. There is 1 μm difference in offset launching position between adjacent waveforms in this figure. The horizontal axis is normalized by the length of the fiber. The top graph is when the offset position is +25 μm while the bottom one is when the offset position of the launching SMF is -25 μm. The intensity of each waveform was normalized by its maximum peak. From those measured modal delay profiles in Fig. 3 we can calculate the DMD of the sample MMF, which is defined by the 25% threshold level between the first leading edge and the last trailing edge of all waveforms. The DMD of this MMF is obtained to be 1.65 ps/m. From the Full width at half maximum of peaks in Fig. 3, the temporal resolution of our proposed measurement method is estimated to be about 0.98 ps for 9 m sample length. Therefore, the minimum measurable DMD in our measurement system is about 0.11 ps/m (= 0.98 ps / 9m). The experimental results of our proposed method agree well with the results obtained from a conventional time-domain measurement method [6]. Comparing with the results obtained with a time-domain method, our measured DMD profiles shows asymmetric shape with respect to offset launching positions around the center of the sample MMF. We think that this asymmetric shape comes from mismatches in polarization state and overlap integral between the transmitted reference signal from an SMF and an excited high order optical signal from a sample MMF.

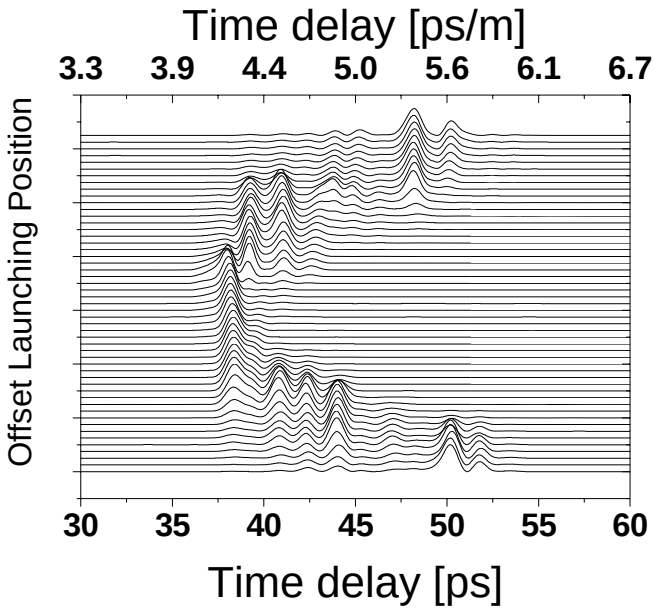

Fig. 3. Differential mode delay profile by our proposed method

3. Conclusion

We have demonstrated a new, powerful DMD measurement method using fLCI for a conventional multimode fiber. We have shown that offset launched DMD profiles can be obtained with subpicosecond accuracy for a conventional MMF with less than 10m length. Measurement results have good agreement with a conventional time-domain DMD measurement method. Our proposed DMD measurement technique as several advantages compared with conventional time-domain techniques; it has a high sensitivity and a good temporal resolution (< 0.11 ps/m), and it can be used for a short length MMF. We expect our technique to be an alternative practical method for determining the modal dispersion of a conventional multimode optical fiber.

References

[1] Mechels, S.E.; Schlager, J.B.; Franzen, D.L, "High-resolution differential-mode delay measurements in optical fibers using a frequency-domain phase-shift technique" PTL, Vol 9, pp.794 –796, (1997)

[2] TIA-455-220-A, Differential Mode Delay Measurement of Multimode Fiber in the Time Domain, Telecommunication Industry Association (2003)

[3] Adam Wax, Changhuei Yang, Joseph A. Izatt, "Fourier-domain low-coherence interferometry for light-scattering spectroscopy", Opt. Lett. 28, 1230–1232, (2003)

[4] J.Y. Lee, T-J Ahn, S Moon, Y. C Youk, Y. M Jung, K. Oh, and D. Y Kim, "Fourier-domain low coherence interferometry for differential mode delay analysis of an optical fiber", Opt. Lett. (accepted)

[5] C. Dorrer, D. Belabas, J. P. Likforman, and M. Joffre, "Spectral resolution and smapling issues in Fourier-transform spectral interferometry", J. Opt. Soc. Am. B, **17**, 1795-1802, (2000)

[6] T. -J. Ahn, and D. Y. Kim, "High resolution differential mode delay measurement for a multimode optical fiber using a modified optical frequency domain reflectometer", Opt. Express, vol.13, No. 20, 8256–8262, (2005)

AUTHOR INDEX

SOFM 2006 PROGRAM

A NIST symposium for photonic and fiber measurements
September 19-20, 2006 – Boulder, Colorado

Tuesday, September 19, 2006

8:30 **Opening Remarks:** Paul Williams, NIST, Symposium Co-Chair

Session I. Fiber Sensors, Chair: Gordon Day, NIST

8:45 **INVITED:** Photonic Sensor Market Evolution, Opportunities and Metrology Needs, David Krohn, *Light Wave Venture LLC*

9:15 Modulation Function Study of Coupling Based Intensity Modulated Fiber-Optic Sensors, Johan Jason[1,2], Hans-Erik Nilsson[1], Bertil Arvidsson[1,3], Anders Larsson[2], [1]*Department of Information Technology and Media, Mid-Sweden University,* [2]*Fiberson AB,* [3]*Ericsson Network Technologies AB*

9:30 Characteristics of Spun Fiber Grating Sensors, Yong Wang and Chang-Qing Xu, *Department of Engineering Physics, McMaster University, Canada*

9:45 Metrology of Integrated Waveguide Devices and Systems Using Near-Field Scanning Optical Microscopy, Guangwei Yuan and Kevin L. Lear, *Electrical and Computer Engineering Department, Colorado State University*

10:00 **BREAK**

Session II. Power-Related Metrology, Chair: Alan McCurdy, OFS

10:30 Return Loss Measurement in the Presence of Variable Insertion Loss Using Optical Frequency Domain Reflectometry, Stephen Kreger, Mark Froggatt, Dawn Gifford, Matthew Wolfe, and Brian Soller, *Luna Technologies*

10:45 High-Power Nonlinearity of Optical Fiber Power Meters for Pump Lasers at 980 and 1480 nm, I. Vayshenker and S. Yang, *NIST,* R. Swafford, *OZ Optics Ltd.*

11:00 Novel Approach for Non-Intrusive "Clip-On" Fiber Monitoring, Gang He, Daniel Gariépy, Hongxin Chen, Jean Théberge, and Gregory W. Schinn, *EXFO Electro-Optical Engineering, Inc.*

11:15 Measurement Technique for Stimulated Brillouin Scattering Threshold, Per Olof Hedekvist and Anne Andersson, *SP, Swedish National Testing and Research Institute*

11:30 Butt-Joint Splice with Refractive Index Matching Material for High Power Light in Optical Fiber Communications, Ikutaro Ogushi, Hisashi Izumita, Kuniaki Tanaka, Fumihiko Ito, and Masahito Arii, *NTT Access Network Service Systems Laboratories, NTT Corp., Japan*

11:45 High Speed PRBS for Detection of Defects in Fibers and Fiber Connectors, S. Rangaswamy, D. Lao, and E. van Doorn, *Intelligent Automation Inc.*

12:00 Experimental Investigation on Special Shaped Fibers Coupling with InP-Based Planar Lightwave Circuit Chips, Xu Liu, Jinbiao Xiao, Xiaohan Sun, *Department of Electronic Engineering, Southeast University, P.R. China*

12:15 **LUNCH**

Session III. Spectroscopic and Frequency Metrology, Chair: Janet Jackel, Telcordia

1:45 **INVITED:** Fiber Frequency Combs: Development and Applications, N. R. Newbury, W. C. Swann, I. Coddington, and J. J. McFerran, *NIST*

2:15 Generation of a Frequency Comb by FWM in SOAs Enhanced by Raman, Ana Carrasco-Sanz[a], Sonia Martín-López[a], Miguel González-Herráez[a,b], Pedro Corredera[a], Maria Luisa Hernanz[a] and Laura Abrardi[a], [a]*Departamento de Metrología, Instituto de Física Aplicada, (CSIC) Madrid,* [b]*Departamento de Electrónica, Universidad de Alcalá, Spain*

2: 30 Comparison of Saturated Absorption Spectra of Acetylene Gas Inside Photonic Bandgap Fibers, K. Knabe, R. Thapa, O. L. Weaver, B. R. Washburn, and K. L. Corwin, *Dept. of Physics, Kansas State University*

2:45 CW Supercontinuum Generation in Standard Optical Fiber over the O, E, S and C Communication Bands, Laura Abrardi[a], Sonia Martín-López[a], Ana Carrasco-Sanz[a], Miguel González-Herráez[a,b], Pedro Corredera[a] and Maria Luisa Hernanz[a], [a]*Departamento de Metrología, Instituto de Física Aplicada, (CSIC), Madrid,* [b] *Departamento de Electrónica, Universidad de Alcalá, Spain*

3:00 A C-Band Optical Frequency Synthesizer Using 1.5 Micron NICE OHMS Frequency Standards and an Optical Frequency Comb Generator, C. S. Edwards[1,2], H.S. Margolis[1], G.P. Barwood[1], P. Gill[1,2], and W.R.C. Rowley[1], [1]*National Physical Laboratory,* [2]*Blackett Laboratory, Imperial College, UK*

3:15 **BREAK**

Session IV. Dispersion Metrology, Chair: Greg Schinn, EXFO

3:45 **INVITED:** PMD: Measurement Method Linkages, T.A. Hanson, *Corning Inc.*

4:15 PMD Measurements Using Fixed-Analyzer Technique on a 1000km Amplified Link that Includes ROADMs, Vincent Lecoeuche[1], Fabien Sauron[1] and André Champavère[1], Alexey Turukhin[2] and Enrico Gonzales[2], [1]*JDSU Commtest Division,* [2]*JDSU Optical Network Research*

4:30 Chromatic Dispersion Measurement Technique Utilizing an Unstable Supercontinuum Pulse Source, Sucbei Moon and Dug Y. Kim, *Gwangju Institute of Science Technology (GIST), Republic of Korea*

4:45 Accurate Measurement of Chromatic Dispersion Distribution along Dispersion Managed Transmission System, Mirza Imran Baig, Tohru Miyauchi and Masaaki Imai, *Dept. of Electrical & Electronic Engineering, Muroran Institute of Technology, Japan*

5:00 Assessment of the Potential Accuracy of a Four Wavelength OTDR to Measure Chromatic Dispersion, David Ives, Joan Hall and Christian Hart, *National Physical Laboratory, UK*

5:15 **SESSION CLOSE**

6:30 **CONFERENCE RECEPTION / DINNER - RED LION INN**

Wednesday, September 20, 2006

Session V. Tutorial – FTTx Measurement Issues, Chair: André Champavère, JDSU

8:30 **INVITED**: Critical Issues Relating to FTTH/PON Testing, Andre Girard, *EXFO E.O. Engineering, Inc.*

9:00 **INVITED**: WDM-PON for FTTx, Wayne V. Sorin[1], Chang-Hee Lee[2], Byoung Y. Kim[1], [1]*Novera Optics, Inc.,* [2]*Korea Advanced Institute of Science and Technology*

9: 30 **INVITED**: FTTx Deployment Issues, Jimmy Salinas, *AT&T*

10:00 **BREAK**

Session VI. Specialty Fibers, Chair: Tom Hanson, Corning Inc.

10:30 **INVITED:** Special Requirements for Measurement Techniques Used for POF and Thick Glass Fibers, Olaf Ziemann, *Polymer Optical Fiber Application Center, University of Applied Sciences Nürnberg, Germany*

11:00 **INVITED:** Characterization of Hole-Assisted Fibers as Single Polarization Fibers and Polarization Maintaining Fibers, Xin Chen, Joohyun Koh, Ming-Jun Li, and Daniel A. Nolan, *Corning Inc.*

11:30 Micro-Tomographic Reconstruction for Arbitrary Refractive Index Profiling of Optical Fibers, N.M. Dragomir[1], X. M. Goh[1], G. Baxter[2] and A. Roberts[1], [1]*School of Physics, The University of Melbourne,* [2]*School of Electrical Engineering, Victoria University of Technology, Australia*

11:45 Fictive Temperature Distribution in Highly Ge-Doped Multimode Optical Fibers, M. Lancry[1], I. Flammer[2], D. Simons[3], B. Poumellec[1], C. Depecker[4], P. Nouchi[2] and M. Douay[5], [1]*ICMMO/LPCES, Université Paris Sud (XI),* [2]*Draka Comteq France,* [3]*Draka Comteq Fiber BV, Netherlands,* [4]*LSPES, Université des Sciences et Technologies de Lille, France,* [5]*PhLAM, Université des Sciences et Technologies de Lille, France*

12:00 **LUNCH**

Session VII. Systems Metrology, Chair: Dug Young Kim, GIST

1:30 **INVITED:** Monitoring OSNR in Dynamic WDM Network, Y. C. Chung, *Korea Advanced Institute of Science and Technology, Department of Electrical Engineering and Computer Science*

2:00 Optical Signal Quality Monitoring Based on Asynchronous Amplitude Histogram for DPSK Systems, H. Takara[1], T. Ohara[1], and B. Kozicki[2], [1]*NTT Network Innovation Laboratories, NTT Corp.,* [2]*Osaka University, Japan*

2:15 **INVITED**: New Methods for Investigating Mode Coupling in Multimode Fiber: Impact on High-Speed Links and Channel Equalization, Stephen E. Ralph, Arup Polley, *Georgia Institute of Technology,* K. D. Pedrotti, R. P. Dahlgren, J. A. Wysocki, *Dept. of Electrical Engineering, University of California, Santa Cruz*

2:45 A Differential Mode Delay Measurement for a Multimode Optical Fiber with Fourier-Domain Low-Coherence Interferometry, J.Y. Lee, T-J. Ahn, and D.Y. Kim, *Department of Information and Communications, Gwangju Institute of Science and Technology, Republic of Korea*

3:00 **BREAK**

Session VIII. Workshop

3:30 – 5:00 Fiber and Photonic Metrology Roadmapping

5:00 **SYMPOSIUM CLOSE**

SYMPOSIUM COMMITTEE

P.A. Williams, NIST, Co-Chair, T.J. Drapela, NIST, Co-Chair

A. Barlow, *PerkinElmer*
A. Champavère, *JDSU*
G.W. Day, *NIST*
S.C. Fleming, *Univ, of Sydney*
D. Franzen, *NIST*
N. Gisin, *Univ. of Geneva*
M. Hackert, *U.S. Navy*
T.A. Hanson, *Corning*
D. Humphreys, *NPL*
J. Jackel, *Telcordia*
D.Y. Kim, *GIST*
P. Kolesar, *SYSTIMAX Solutions*
D. Krohn, *Light Wave Venture*
G. Kuyt, *Draka Comteq*
A. McCurdy, *OFS*
G. W. Schinn, *EXFO*
C. Shaar, *Photon Kinetics*
H. Takara, *NTT*

Sponsored by the:
National Institute of Standards and Technology
in coopertation with the
IEEE Lasers and Electro-Optics Society
And the **Optical Society of America**

OSA Optical Society of America

NIST

IEEE LEOS LASERS & ELECTRO-OPTICS SOCIETY

National Institute of Standards and Technology
Technology Administration, U.S. Department of Commerce

NIST Technical Publications

Periodical

Journal of Research of the National Institute of Standards and Technology—Reports NIST research and development in metrology and related fields of physical science, engineering, applied mathematics, statistics, biotechnology, and information technology. Papers cover a broad range of subjects, with major emphasis on measurement methodology and the basic technology underlying standardization. Also included from time to time are survey articles on topics closely related to the Institute's technical and scientific programs. Issued six times a year.

Nonperiodicals

Monographs—Major contributions to the technical literature on various subjects related to the Institute's scientific and technical activities.
Handbooks—Recommended codes of engineering and industrial practice (including safety codes) devel- oped in cooperation with interested industries, professional organizations, and regulatory bodies.
Special Publications—Include proceedings of conferences sponsored by NIST, NIST annual reports, and other special publications appropriate to this grouping such as wall charts, pocket cards, and bibliographies.
National Standard Reference Data Series—Provides quantitative data on the physical and chemical properties of materials, compiled from the world's literature and critically evaluated. Developed under a worldwide program coordinated by NIST under the authority of the National Standard Data Act (Public Law 90-396). NOTE: The Journal of Physical and Chemical Reference Data (JPCRD) is published bimonthly for NIST by the American Institute of Physics (AlP). Subscription orders and renewals are available from AIP, P.O. Box 503284, St. Louis, MO 63150-3284.
Building Science Series—Disseminates technical information developed at the Institute on building materials, components, systems, and whole structures. The series presents research results, test methods, and performance criteria related to the structural and environmental functions and the durability and safety characteristics of building elements and systems.
Technical Notes—Studies or reports which are complete in themselves but restrictive in their treatment of a subject. Analogous to monographs but not so comprehensive in scope or definitive in treatment of the subject area. Often serve as a vehicle for final reports of work performed at NIST under the sponsorship of other government agencies.
Voluntary Product Standards—Developed under procedures published by the Department of Commerce in Part 10, Title 15, of the Code of Federal Regulations. The standards establish nationally recognized requirements for products, and provide all concerned interests with a basis for common understanding of the characteristics of the products. NIST administers this program in support of the efforts of private-sector standardizing organizations.

*Order the **following** NIST publications—FIPS and NISTIRs—from the National Technical Information Service, Springfield, VA 22161.*

Federal Information Processing Standards Publications (FIPS PUB)—Publications in this series collectively constitute the Federal Information Processing Standards Register. The Register serves as the official source of information in the Federal Government regarding standards issued by NIST pursuant to the Federal Property and Administrative Services Act of 1949 as amended, Public Law 89-306 (79 Stat. 1127), and as implemented by Executive Order 11717 (38 FR 12315, dated May 11,1973) and Part 6 of Title 15 CFR (Code of Federal Regulations).
NIST Interagency or Internal Reports (NISTIR)—The series includes interim or final reports on work performed by NIST for outside sponsors (both government and nongovernment). In general, initial distribution is handled by the sponsor; public distribution is handled by sales through the National Technical Information Service, Springfield, VA 22161, in hard copy, electronic media, or microfiche form. NISTIR's may also report results of NIST projects of transitory or limited interest, including those that will be published subsequently in more comprehensive form.

U.S. Department of Commerce
National Bureau of Standards and Technology
325 Broadway
Boulder, CO 80305-3328